Linkage between Dust Cycle and European Loess in the Last Glacial Maximum Determined by Atmospheric Model Simulations

Inaugural Dissertation

zur

Erlangung des Doktorgrades

der Mathematisch-Naturwissenschaftlichen Fakultät

der Universität zu Köln

vorgelegt von

Erik J. Schaffernicht

aus Köln

Berichterstatter, Gutachter:

Prof. Dr. Yaping Shao, Universität zu Köln

Prof. Dr. Joaquim G. Pinto, Karlsruher Institut für Technologie

Mündliche Prüfung am 24. Juli 2018

Abstract

The Last Glacial Maximum (LGM) is a turning point of the Earth's climate and the human dispersal. Yet, the then prevailing atmosphere dynamics over Europe and the North Atlantic as well as the mineral dust cycle in Europe are not well understood. This dissertation improves understanding the LGM climate and its dust cycle. Based on global climate simulations, it compares the LGM climatologies, jet stream, Circulation Weather Types (CWTs), and Combined Empirical Orthogonal Functions (CEOFs) with their present analogues. The dust cycle was reconstructed for Europe based on statistic dynamic downscaling using CWT frequency-conform regional Weather Research and Forecasting Model (WRF) simulations for the LGM. Proxies and reanalyses served to evaluate all simulations; among them a comprehensive compilation of loess-based reconstructed mass accumulation rates for the LGM. By comparing the simulated LGM depositions with these rates, a linkage was established between the LGM dust cycle and the present loess.

For the North Atlantic and Europe, the CEOFs suggest a lower LGM than present climate variability. The jet stream was narrower and partly more than 10 m/s faster there. Possible subsequent jet stream paths ran over and along the Nordic Seas, eastwards along the onset of the Central German Uplands or over the Mediterranean. The North Atlantic Oscillation (NAO) was 50% stronger combined with a 6° wider (westward) Azores High. The latitude-deviating LGM temperatures indicate that the North Atlantic Current extended up to Norway. Precipitation reduced by more than 150 mm/yr over the proglacial European areas; including a reduction of more than 300 mm/yr over the North Sea Basin. Near the EIS coast, periods of precipitation and temperatures that ranged below their climatological average synchronized with above-average precipitation periods over the Azores; both likely correlating with a below-average NAO. Similarly, stronger EIS High periods correlated with reduced precipitation and temperatures in western and central Europe. Combined with strong dry northeast sector winds, they favored erosion along the proglacial areas. Consistently, more frequent southerlies, cyclones, and east sector winds occurred in central and eastern Europe. This agrees with katabatic winds and the EIS-induced blocking that shifted the storm tracks southward. In contrast to the present westerlies, east sector winds (36%) and cyclones (22%) dominated central Europe. The east sector winds dominated the dust transport from the proglacial EIS areas to central Europe. In particular over western Europe, cyclones and strong — yet rare — west sector winds contributed in addition to the dust transport. Most dust was emitted from the Alps-, Black Sea- and EIS-bounded area. Its emissions culminated in proglacial central Europe with peaks of more than 100 kg m^{-2} yr^{-1}. The LGM dust plumes mainly ran westwards along the EIS margin. The highest aeolian depositions covered West Poland, the German Bight, and the North German Plain (between 1 and 100 kg m^{-2} yr^{-1}). The significance of the east sector winds for the LGM is corroborated by the consistency of the simulated depositions and the mass accumulation rates reconstructed from more than 70 distinct loess sites across Europe.

Zusammenfassung

Das letzte glaziale Maximum (LGM) ist ein Wendepunkt des Erdklimas und der Menschheitsausbreitung. Dessen ungeachtet ist das Verständnis für die damalige europäische und nordatlantische Atmosphärendynamik sowie den Mineralstaubzyklus in Europa wenig ausgeprägt. Diese Dissertation trägt zu einem besseren Verständnis beider bei. Basierend auf globalen Klimasimulationen werden die Klimatologien, der Jetstream, die Zirkulationswetterarten (CWTs) und die kombinierten empirischen Orthogonalfunktionen (CEOFs) des LGMs und der Gegenwart miteinander verglichen. Zudem wird der Staubzyklus in Europa rekonstruiert mittels statistisch dynamischem Downscaling, welches CWT-Frequenz-konforme, regionale Weather Research and Forecasting (WRF) Modellsimulationen nutzt. Unabhängige Referenzen für die Simulationsergebnisse bieten Reanalysen und Proxies. Im Rahmen Letzterer wurden ca. 100 lössbasierte Masse-Akkumulationsraten zusammengestellt. Deren Vergleich mit den simulierten Raten setzt den LGM-Staubzyklus in Beziehung zum gegenwärtigen Löss.

Für Europa und den Nordatlantik suggerieren die CEOFs eine geringere Klimavariabilität als heute. Der Jetstream war dort schmaler und teilweise mehr als 10 m/s schneller; mögliche Strömungspfade verliefen vor der Küste des eurasischen Eisschildes (EIS), ostwärts über den deutschen Mittelgebirgen oder über dem Mittelmeer. Die Nordatlantische Oszillation (NAO) war 50% stärker verbunden mit einem 6° westwärts ausgedehnteren Azorenhoch. Der Nordatlantikstrom reichte gemäß Breitengrad-abweichender Temperaturen bis nach Norwegen. Niederschläge fielen über Europas proglazialen Gebieten um mehr als 150 mm/a geringer aus; über dem Nordseebecken um mehr als 300 mm/a. Unterdurchschnittliche Niederschläge und Temperaturen über dem arktisnahen Atlantik und dem westlichen EIS sychronisierten mit überdurchschnittlichen Niederschlägen über den Azoren; wahrscheinlich korrelierend mit einer unterdurchschnittlichen NAO. Phasen eines stärkeren EIS-Hochs gingen einher mit Niederschlags- und Temperaturrückgängen in Europa. Verbunden mit starken, trockenen Nordostsektorwinden begünstigten diese Rückgänge die Erosion der proglazialen Gebiete. Konsistent dazu traten häufigere Südwinde, Zyklonen und Ostsektorwinde über Mittel- und Osteuropa auf. Dazu passen die katabatischen Winde und das EIS-erzeugte Blocking, das die Sturmzugbahnen südwärts verschob. In Mitteleuropa überwiegten während des LGMs Zyklonen (22%) und Ostsektorwinde (36%). Die Ostsektorwinde dominierten den Staubtransport von den proglazialen EIS-Gebieten nach Mitteleuropa. Besonders über Westeuropa trugen auch Zyklonen und starke — aber seltene — Westsektorwinde zum Staubtransport bei. Die stärksten Staubemissionen stammten von dem durch Alpen, Schwarzmeer und EIS begrenzten Gebiet. Dessen Raten gipfelten im proglazialen Mitteleuropa in vereinzelt mehr als 100 kg m^{-2} a^{-1}. Auftretende Staubwolken zogen hauptsächlich westwärts entlang des EIS-Rands. Die größten äolischen Sedimentationsraten (zwischen 1 und 100 kg m^{-2} a^{-1}) traten in Westpolen, der norddeutschen Ebene und der Deutschen Bucht auf. Die Bedeutung der Ostsektorwinde wird durch die Konsistenz der für das LGM simulierten Ablagerungs- und der von mehr als 70 verschiedenen Lössfundstellen rekonstruierten Masse-Akkumulationsraten bestätigt.

Contents

Preface

The key to abbreviations, terms, and non SI units is in Sec. 10; it contains also the commonly known acronyms that are not expanded on their first occurrence.

1 Introduction

1.1 Motivation

The paleo climate and environment affected the migration of *Homo sapiens* to and within Europe during the last 200 000 years[1,2]. Yet, robust knowledge on their migratory conditions and routes lacks[3–6]: How, where, and under which conditions were settlements chosen in Europe? For example, settlements disintegrated repeatedly on the Iberian Peninsula[7], possibly due to Heinrich Events[8]; yet, a well-established theory is still missing. Also, the central European settlement hiatus[7,9,10] related to the Last Glacial Maximum (LGM, 21 000 ± 3 000 years ago[11,12]) is not completely understood and contradictory assumptions have been published: either the western European population withdrew to refugia in southern France and on the Iberian Peninsula at that time[10,13]; or the European population expanded considerably at 23 ka ago according to mitochondrial DNA analyses[14,15]. In this case, it possibly affected vulnerable fauna[16].

To improve the understanding of human migration to and within Europe, the Collaborative Research Centre 806 (CRC806) 'Our Way to Europe' was established[7] consisting of three phases. The research leading to this dissertation formed part of its second phase, during which the CRC806 encompassed the following collaborating disciplines (*marked* are *those*, which closely relate to data, methods or findings of this dissertation): *physical geography*, *sedimentology*, *geology*, geomorphology, speleology, archaeology, anthropology, palynology, *paleobotany*, and *meteorology* including mineral dust modeling. Within the CRC806 framework, this dissertation implements an interdisciplinary research approach and perspective.

Almost all these disciplines focus on fieldwork. Yet, the scope of fieldwork is usually limited to addressing one or a few sites; each extending between some meters up to a few kilometers at maximum. Sampling, excavation or core drilling is rarely carried out at high spatial resolution for areas of a 100 km^2 or larger. Therefore, it often remains unanswerable whether fieldwork-based reconstructions represent more than a local site-specific finding — in particular when focusing on fieldwork only. Fieldwork alone can either not or only fragmentarily provide the surrounding three dimensional spatial context on regional to continental scales.

This dissertation provides this missing context. It focuses on the LGM climate including the reconstruction of the mineral dust cycle for the LGM. Its findings base on analyzing global[17–20] and performing regional climate-dust simulations to reconstruct the dust cycle. These findings are evaluated by relating them to climate proxies. This referencing advances the interpretation of the fieldwork results and the climate simulations, as it establishes the complementary paleoclimatic context to fieldwork.

This dissertation establishes a more complete multidisciplinary understanding of the Earth's past climate; its analyses and reconstructions serve to understand the interaction between the atmo-, oceano-, cryo-, bio-, and pedosphere. Their relevance is not limited to the CRC806; on the contrary, they show connections that also serve soil scientists, atmospheric chemists, and climatologists. Its climate analyses enable to assess the regional significance and to establish the supra-regional understanding of fieldwork results.

1.2 The Past Climate is a Key to Respect our Future

In this dissertation, the LGM is analyzed and compared to the present climate. The LGM represents a fundamentally different state of the Earth's climate (Sec. 2). However, it is not the only time when a global temperature trend resulted in a fundamentally different climate. Since the industrialization and more vigorous since the 1950s, the humans force global warming, which affects the Earth's climate drastically[21–23]. Though the current human-induced global warming trend is inverse to the cooling trend during the LGM onset, both trends modify the Earth system dynamics and severely affect the genera[24–26]. However, in contrast to the pace of the temperature trend leading to the LGM, the driving pace of the human-induced global warming is much faster than any previous well-understood global temperature trend during the existence of *Homo sapiens*[21–23].

During the Earth's past, similar or even faster climate changes were only caused by major asteroid impacts followed by mass extinctions[27]. So far, severe mass extinctions on Earth have been rare: only five in the last 540 million years[24]. After the most recent impact 65 million years ago 70% of the Earth's marine invertebrate species vanished; 50% of all genera perished[27,28]. Despite this being published in 1980, and despite the serious number of species that already died out in the last decades, almost all humans, who cause the ongoing greenhouse gas emissions, decide—by sticking to their behavior—to continue loosing biodiversity[24–26,28]. The first human-induced mass extinction is very likely, as it has already begun[29].

The survival of species has depended and will continue to depend on feedback and tipping points that control, balance or torpedo the Earth's climate system — depending on the immanent non-linear dynamics of this system. Their understanding is crucial to be aware of present and upcoming global warming hazards[23,30–32]. The accomplishment of our near future depends critically on both, the best possible understanding of the non-linear climate dynamics, and our swift action now to stop any additional human-induced global warming[21–23]. In addition, our rapid societal action is needed to mitigate the already inevitable and ever-increasing impact of the existing climate crisis.

This dissertation enhances knowledge of the climate dynamics and variability beyond the average quasi-stationary state that lasted for at least the last two to three millennia before industrialization. The comparison of the LGM with this state emphasizes the different and thus characteristic dynamics and variability of each of them. Improving their understanding is crucial to recognize the changing patterns during the transient, globally warming climate today and in the near future.

1.3 Importance and effects of the Last Glacial Maximum for our Ancestors

In the Earth's past climate, the LGM is the most recent turning point (Sec. 2). Although it offered new potential human habitats and migration routes, such as the narrowed Strait of Sicily, the dry Bosporus and northern Adriatic, the restriction by the atmosphere, the cryosphere, and their interactions with the pedosphere during the LGM dominated human mobility[33,34]. As a result of the increased aridity[35], particular in central to eastern Europe[36–40], the pre-glacial biomes including their specific fauna deteriorated or shifted[40], thereby reducing their human carrying capacity.

The LGM reduced the European megafauna considerably[16]. The woolly mammoth and several other species disappeared across central Europe[10,41]. The giant deer withdrew from western and central Europe[10]. Many other species withdrew to refugia[42]; for example, reindeer remains dated to the LGM were mainly found south of 50°N indicating the southward retreat of the reindeer population[41]. This exemplifies the effects of the LGM on the megafaunal range dynamics[40,41].

Phylogeographic patterns indicate isolated populations in southern European LGM climate refugia[42]. Mitochondrial DNA of pre-LGM bears evidences almost no such patterns. This presumably applies also to many European species[42]. It indicates the significant impact of the LGM climate on the fauna evolution[41].

In Eurasia, the reindeer probably was the main human resource[41]. Its retreat presumably reduced the human carrying capacity of northern central Europe during the LGM, which probably reversed the human expansion, i.e. the decreasing human population withdrew to the glacial megafauna refugia. To interrelate how the varying human population density and climate affected the megafaunal species, an improved understanding of the LGM climate is needed[16]. This dissertation provides this by analyzing the LGM climate in Europe and over the North Atlantic (Sec. 4, 5, and 6) as well as by reconstructing the LGM environment with a particular focus on mineral dust (Sec. 7). Ultimately, the accomplished LGM climate analyses and dust cycle reconstruction pave the way for modeling the human mobility during the LGM.

1.4 Glacial Dust Cycle, Climate Proxies, and Present Loess

Despite the importance of the LGM in the Earth's past climate, its regional atmospheric characteristics including the aeolian mineral dust cycle are not well known. For this cycle, the boundary layer winds and their directions are of particular importance. On the local scale, wind proxies enable the reconstruction of the then prevailing surface wind directions. Yet, these reconstructions are often ambiguous and their extrapolation to regional or continental scales is controversial.

Many studies assume that westerlies continuously dominated Europe during the LGM similar to present-day westerlies[43–45]. However, plenty of evidence exists for prevailing north and east sector winds during the LGM in Europe: Central and eastern European sediments indicate north sector winds[46]. Easterlies are evidenced by several proxies across Europe: grain size records in northern central Europe[46], Eifel sediments[47], heavy minerals and carbonate peaks[48], Harz Foreland loess[49], and wind-polished rocks[45] in central Europe near the margin of the Eurasian ice sheet. Danish proxies in addition evidence southeasters[45]. In Hungary and the Carpathian Basin, sediments evidence north sector winds, westerlies, and southeasters[46,50–52]. Ukrainian sand deposits evidence north sector winds[46,52].

To evaluate these proxy-based, yet partly opposing wind direction reconstructions, and to overcome the absence of instrumental observations, the wind distribution in Europe during the LGM was analyzed in this dissertation based on global climate simulations. At the regional scale, the simulated pressure patterns were classified into Circulation Weather Types[53–55] (CWTs) . The GCM quality was assessed by comparing the CWT frequencies that result from their simulations for the recent climate with those resulting from reanalyses. Key characteristics of the regional wind distribution during the LGM were revealed by comparing the CWT frequencies calculated from the LGM simulation with those calculated from the simulations of the recent climate. Compiling the western, central, eastern, and southern European distributions establishes a pan-European reference for the LGM wind system. This enables relating the distinct kinds of local wind proxies with the pan-European wind system and serves to reconstruct the LGM dust cycle for Europe by statistic dynamic downscaling.

The dominant LGM wind directions directly affected the aeolian mineral dust cycle in Europe at that time. This cycle is of particular interest because mineral dust is a core theme in Earth system science and climate sciences[56]: For example, aeolian dust enhances or suppresses precipitation[57]; it alters the radiation budget; its deposits evidence changing aridity[58] and paleo wind systems[59].

Compared to the present, reduced LGM wet depositions[35], the more vigorous atmospheric circulation, and stronger cyclones at the upper mid-latitudes[60,61] relate to the at least ten times greater dust loads during the LGM[62]. Over erodible areas, strong winds presumably transformed to dust storms hindering humans by reducing the visibility to zero[63]. Increased aridity[35], severe cold[64–71], huge ice sheets[17,72,73], and the lower sea level[12,74–77] led to more dust sources[35]; many of them probably near the southern or eastern margin of the Eurasian ice sheet[44].

This dissertation improves the understanding of the high-resolved spatial distribution of dust emission rates by taking into account effects of vegetation, snow, ice, and soil moisture on the emissions. Although the LGM temperatures and greenhouse gas concentrations were lower than today[78], understanding how extreme aridity, strong winds, and steep topography affected aeolian erosion allows to improve the projections of erosion dynamics for the upcoming climate.

Dust is relevant to paleo sciences, as it is frequently found in all kinds of climate archives, which are the only in situ fragments for reconstructing the local paleoclimate. Some of these archives such as sediments and ice cores record in addition also regional and global paleoclimate properties. Therefore, it is important to understand these archives in the best possible way. Yet, transforming climate archives to meaning- and insightful climate proxies is in some cases not at all, in most cases not well or not completely understood. Improvement is needed on extracting data and converting it to statements, understanding, and context — which corresponds to learning from the fragments of the 'book' written by nature at times far beyond the individual and societal memory.

In this dissertation climate proxies for the LGM are compared to simulation results for temperature, precipitation, and wind (Sec. 4, 5, and 6). The dissertation provides the complementary spatial context and reveals the unknown dynamics that explains the encountered patterns of, and the reconstructed values from the proxies. It reveals and establishes the linkage between the LGM dust cycle in Europe and one of its most important proxy — the loess.

Loess is particularly appropriate for validating spatially resolved dust simulations, because it is on land the most prominent, widely, and abundantly distributed dust deposition proxy in Europe; it has been sampled and analyzed for decades[79]. In Europe, loess covers large areas[79] (Fig. 41); its creation began 75 kyr ago, followed by the enhanced built-up during the last glacial, and ended 15 kyr ago[80]. In the eastern European history, the LGM represents the most substantial phase of loess accumulation[81]. Its thickest layers form the European loess belt at about 50°N. They extend from France to the eastern European Plain[82], which stretches from Slovakia to the Caspian Mountains. This belt includes the large loess sheets of the southern proglacial EIS regions, which are optimal for studying the paleoclimate[79,83–85].

This dissertation contributes a concise, new, and otherwise missing overview (Tab. 1) of all (~100) from loess for the LGM reconstructed mass accumulation rates (MARs) for the domain that was defined to reconstruct the dust cycle for the LGM. This state-of-the-art overview enables the quantitative, independent, and spatially resolved verification of the simulated LGM dust deposition rates for Europe.

1.5 Linkage between the Glacial Dust Cycle and the Current Loess

Although most of the present-day loess-paleosol sites in Europe include a sequence that potentially originated from dust accumulations during the LGM, the linkage to their corresponding LGM dust sources is not well known. This has seriously compromised their value as climate proxies. As large amounts of dust were transported during the LGM, it is particular important to establish this linkage for this period[80].

Laboratory analyses of European sediment samples are one attempt to restore this linkage. For the LGM, they result in European dust source locations up to the littoral of the Aral Sea[86]: The Lower Rhine Embayment loess likely originated from sources further west[87]. Central European sediments refer to sources south or southeast of the EIS, north or east of the Alps, and around the Carpathians[46,57,88,89]. The Carpathian loess refers to various sources[46]. Aeolian contributions to the loess in the Lower Danube Basin come from the dry-fallen Black Sea littoral[90].

Drawbacks of the proxy-based reconstructed linkages are their dating dependence and, for some types of proxies, their dependence on assumptions on the past atmospheric circulation that do not necessarily apply homogeneously to all locations or past periods. In addition, these linkages are fragments of knowledge; they do not explain the atmospheric dust dynamics nor do they abstract from the individual sediment to the general context. To overcome these fieldwork-inherent shortcomings, this dissertation contributes to reveals the linkage between the dust cycle during the LGM and the present-day loess distribution in Europe based on climate-dust simulations for Europe (Sec. 7).

A few fieldwork-based studies of sediments offer a reconstruction of the dust transport direction(s) that caused the respective sediment: For the LGM, aeolian sediments in the Eifel evidence easterlies[47]. For the Late Pleniglacial, proxies evidence westerlies and southwesters near the Polish-Ukrainian border[46], northerlies and northwesters in the Carpathian Basin[46], and north sector winds that transported dust and sand from the proglacial plains to Ukraine, Romania, and the eastern Carpathians[46,52]. Serbian and Ukrainian loess sites evidence east sector winds[46,91]. The central and eastern European loess partly originated from the Aral Sea implying dust-transporting easterlies and southeasters[86].

These proxy-inferred directions usually base solely on (a few) samples taken only from one site or sediment core. The resulting MARs and wind directions often vary considerably for neighboring sites[46]. Their temporal scope is generalized to long time spans such as the Late Pleniglacial, which itself consisted of distinct atmospheric circulation periods due to the varying Eurasian and Laurentide ice sheets[69]. The reconstruction of the LGM wind dynamics and dust cycle exclusively from sediments is problematic because the samples do not contain any indicators to distinguish dust contributions of rare storms from those of the frequent wind directions[45].

These discrepancies and uncertainties of the dust proxies show the need for state-of-the-art paleo dust modeling, which is provided by this dissertation. The therefore accomplished climate-dust simulations serve to establish the linkage between the LGM dust cycle and the loess records. They contribute to an improved understanding of the LGM dust cycle in Europe.

For glacial climates, only a few simulation-based studies have been published that researched on the mineral dust cycle[43,44,92–98]. Two of them[43,44] limited their domain to a sub-European region during the Marine Isotope Stage 3. Due to their domain extent (8° latitude, 20°–40° longitude) and non LGM-compliant ice sheets[43,44], it is very unlikely that they approximate well the real dust cycle during the LGM in Europe[69]. The deposition rates that are calculated for the LGM by the GCMs[92–98] (between 1 and 100 g m^{-2} yr^{-1}) significantly underestimate the loess-based reconstructed MARs for Europe[46,57,59,99].

This GCM deficiency to represent the real dust cycle during the LGM is corroborated by failing GCM dust simulations[100] for 1982 to 2005. These present-day dust simulations run by 23 GCMs systematically underestimate the dust emissions and transport that is obtained independently from fieldwork and satellite observations[100]. These underestimated dust processes presumably result from the insufficient resolution, dust schemes, dust size and source distributions of the GCMs[35,100,101]. In summary, up to now, GCMs fail to represent the dust cycle for both, the present and the LGM. As a consequence, both, appropriate global and regional climate-dust simulations are missing for Europe during the LGM.

This dissertation provides the more appropriate reconstruction of the dust cycle. It overcomes the existing discrepancy of fieldwork- and simulation-based rates for the LGM. To this aim, high-resolved regional climate-dust simulations were run using the WRF-Chem-LGM. The WRF-Chem-LGM is a version of the Weather Research and Forecasting Model coupled with Chemistry[102–105] (WRF-Chem) that was slightly upgraded for this purpose to respect the effects of a glacial environment on the dust emissions, and to consider LGM-specific boundary conditions (Sec. 7.3). The WRF-Chem-LGM simulations avoid several and reduce considerably the remaining deficiencies compared to the previous[43,44,92–98] simulations by others. The LGM upgrade of the WRF-Chem takes into account glacial vegetation, topography, and dust sources. It hinders dust emissions proportionally to the areal fraction covered by snow or ice sheets.

It is unprecedented in the LGM climate-dust modeling to combine the online[102] atmosphere-dust interaction, the high resolution over the whole European domain, and the dust cycle completeness. This completeness comprises the dust emissions by aerodynamic entrainment, saltation bombardment, and aggregate disintegration[106]; the dust transport, the gravitational settling[102], the dry and the wet deposition[102,107].

In contrast to most dust simulations[92,96,108], the performed WRF-Chem-LGM simulations are neither tuned nor otherwise manipulated towards any predefined outcome, which distinguishes the current approach from many others. The consistency of the fieldwork-based MARs[46,57,59,99] and the simulated deposition rates shows the quality of the simulations contributed by this dissertation.

Independent findings provide a complementary perspective on my results and assess their relevance. These independent references comprise other simulations[43,69,96–98,109–113], geomorphological, biological, and geological climate proxies, such as marine sediments[114], pollen[70,115–117], coleoptera[71], sand deposits[52], equilibrium line altitudes[66], as well as the spatial distribution and the rates of about a hundred local fieldwork-based reconstructed mass accumulations of loess sites in Europe (Sec. 7 and Tab. 1).

1.6 Goal and Methods

This dissertation creates the linkage between the mineral dust cycle during the LGM and the present-day loess deposits in Europe. To achieve this goal, a comprehensive understanding of the LGM climate dynamics and its differences to the present climate dynamics is sought. This encompasses the recognition of atmospheric patterns that dominated the LGM in contrast to the present climate. To accomplish this, the analyses based on different kinds of scientific data: first and foremost on climate and climate-dust simulations; for the verification of the simulations, the analyses also base on various climate and dust proxies, among others pollen[70,115–117], rocks[45], fossils[71], marine sediment cores[114], glacier equilibrium line altitudes[66], sand deposits[45,52], and loess[46,57,85,92,99,118–125]. The verification of the simulation-based dust depositions is facilitated by a comprehensive mass accumulation rate compilation based on loess deposits all across Europe (Tab. 1).

The pattern recognition includes the analysis of and the comparison between the LGM and the present climatologies for the principle variables of the atmosphere: pressure, temperature, and precipitation. It also includes the subclimatological decomposition of these variables using combined empirical orthogonal functions[126] to understand the variables' reciprocal dependency, feedback, and interaction. The combined empirical orthogonal functions provide insights into the synchronous spatial atmosphere dynamics patterns generated by the variables' interaction and their feedback to the remaining Earth system components and dynamics.

In addition to the effects of this reciprocal climate dynamics on the mineral dust cycle, the dust transport is determined by the prevailing winds. This is taken into account for Europe by classifying the daily simulation-based weather variability using the CWT analysis[36,53–55]. This classification enables the statistic dynamic downscaling based reconstruction of the LGM dust cycle. This reconstruction requires regional episodic climate-dust simulations for the LGM. These were created by running a LGM-adapted version of the Weather Research and Forecasting Model coupled with Chemistry[102–105] (WRF-Chem). The domain boundaries of these simulations were driven by the LGM simulation of the Max-Planck-Institute Earth System Model[18–20,127] (MPI-ESM). The CWT-based dust simulations enable to establish the linkage between the current loess deposits and their LGM dust sources.

2 The Last Glacial Maximum

2.1 Earth's orbit triggered the Last Glacial Maximum

The LGM (21 000 ± 3 000 years ago[11,12]) is a milestone of the Earth's past climate. Within the Quaternary, it is the most recent major climatic turning point that marks the transition from the Pleistocene to the Holocene.

The astronomical theory of paleoclimate[128] explains the onset of the Last Glacial by the favorable period of the Earth's orbit and rotation. The superposition of the different cyclic variabilities that describe the configuration of the Earth towards the Sun limits the conditions to cyclic and discrete time slots that allow for glaciation. The dynamics of the Earth leads to a continuous realization of Earth Sun configurations that are different from their predecessor within the cyclic variability range. Thus, each realization of a successive configuration potentially leads to a change of the seasonal and latitudinal distribution of the Earth's insolation.

During the Quaternary, ice ages began when successive low northern hemisphere insolation configurations prevailed[129], which enabled the growth and rise of vast northern hemispheric ice sheets during a few millennia. The mechanisms that allowed the onset of the Last Glacial can be reduced to three changes in the Earth's orbit. The eccentricity e of the Earth's orbit varies during the 100 kyr cycle and determines the total amount of energy received by the Earth[128–130]. The Earth's axis inclination ε (obliquity or tilt) varies about 1.5° during the 41 kyr tilt cycle, which affects the latitudinal distribution of the incoming radiation, hence the seasonality[73]. The spatial distribution and the seasonal pattern of the insolation depends on ε and $e \sin \bar{\omega}$, with $\bar{\omega}$ as the longitude of the perihelion[128]. The latter term describes the changing insolation due to the 21 kyr precession cycle, which takes into account the times of maximum and minimum Earth Sun distance combined with the effect of the changing insolation angle during the year. Hence, the term $e \sin \bar{\omega}$ describes the precession effects that modify the seasonal partitioning of the insolation. Thus, the superposition of both, $e \sin \bar{\omega}$ and ε, determines the Earth's spatiotemporal surface distribution of the incoming energy. In accordance with this theory, the northern hemispheric boreal summer insolation density was lower than average during the onset of the Last Glacial. Moreover, mid-month and monthly mean insolation can explain long term climatic changes that have occurred during the Quaternary. Particularly, the mid August and the daily autumnal equinox insolation showed negative deviations about 20 kyr ago, coinciding with the LGM[131].

2.2 Sea level, Ice sheets, and Lakes

During the LGM, the sea level was distinctly lower[12,74–77] than today (compare Fig. 1 and Fig. 75, for example). It decreased by ~134 m according to about 1000 inverted observations[74]. An Earth mantle finite volume model[75] found a ~130 m sea level decrease, in agreement with an ice sheet model[12]. A coherent LGM sea level decrease range of 127.5 ± 7.5 m resulted from the assessment[76] of sea level records, modeling, geochemical proxies, and reconstructed ice sheet extents. According to observations[77] at Barbados and the Australian Bonaparte Gulf, the ice-volume equivalent LGM sea level was between 130 and 135 m lower.

Figure 1: Present-day orography and bathymetry of Europe; from Wikipedia[132]. Shelves, which mostly fell dry during the LGM (Fig. 75), are colored in light blues. To reconstruct the mineral dust cycle for the LGM in Europe (Sec. 7.4), an analysis of the wind regime frequencies (Sec. 6) is required. These Circulation Weather Type frequencies were calculated for a region labeled *Transdanubia* (Sec. 7.4, p. 98) that is centered around 47.5°N, 17.5°E (red dot). Transdanubia encompasses the Eastern Alps, the northern Dinarides, the Balkans, and the Carpathians (cf. also Fig. 18).

The Laurentide[72] (LIS, up to ~3600 m height), Greenland (GIS), and Eurasian ice sheet (EIS) covered[72] large parts of the Northern Hemisphere during the LGM. On northern Europe, the EIS margin was several hundred meters thick, and the EIS thickness increased up to ~2400 m at its center[72]. The EIS encompassed the Scandinavian ice sheet (SIS, also called Fennoscandian ice sheet), the British-Irish (BIIS), the Svalbard, the Barents Sea, and Kara Sea ice sheet. It covered[11] Europe from the Arctic (~80°N) to ~50°N, thereby increasing the northern European topography distinctly[133]. Moreover, the southeast sector of the SIS and the Alpine ice sheet reached their maximum about coterminously to the global LGM[134].

The LGM lake levels differed[135] from today. An Italian lake and a lake in southern France were drier, whereas two lakes, one at the Balkans and one in southern Turkey, were much wetter[135].

2.3 Temperature distribution

Compared with today, the LGM atmosphere was colder and drier[136–140]. The mean global LGM near-surface air temperature differed[49,129,141,142] by $\Delta T = -4.5 \pm 0.5\,^{\circ}\mathrm{C}$ from its present value. Compared to today, during the average European LGM winter, the simulated 2 m air temperature decreased[64] between 8 and 16 °C in agreement with a pollen-reconstructed annual mean temperature decrease[116] of $\Delta T = -12 \pm 3\,^{\circ}\mathrm{C}$ in western Europe. There, the coldest month cooled[116] by $\Delta T = -30 \pm 10\,^{\circ}\mathrm{C}$ and the precipitation north of the Mediterranean decreased[116] by $\Delta P = -800 \pm 100$ mm, i.e. -60 ± 20 %, compared to today. Over the ice-sheet free central European regions, the annual average temperatures decreased between −5 and −10 °C according to a regional simulation[111]. According to paleobotany[116], the cooling and drying at the LGM was more pronounced in western than in southeastern Europe. This gradient of decreasing temperatures was in line with more severe western than eastern European cooling, which was reported[140] as necessary for reproducing the LGM glaciers. Coherently, the polar front[66] and the westerlies[73] were shifted southward causing a drier climate[116,140,143]. For regions south of the Pyrenees–Alps line, temperature decreased by $\Delta T = -10 \pm 5\,^{\circ}\mathrm{C}$ according to pollen records[116]. For central Poland between 26 and 24 kyr ago, the mean annual temperature was −4 °C, the intra annual temperature ranged between −27 and 8 °C, both reconstructed from coleoptera[71]. Nearby the EIS margin at the NW Russian plains, ice wedges[136] indicated an average annual temperature below −6 °C. The average simulated LGM summer temperature decreased[64] by at least -16 to -8 °C over the Scandinavian ice sheet compared to modern day summer temperatures in Scandinavia.

The Eurasian Arctic climate between 20 and 15 kyr ago was extremely cold and dry[136]. Similarly, during the LGM, the northeastern Mediterranean was very cold and extremely dry[80]; pollen evidence even for the whole Mediterranean strong dryness[116]. Also, the Carpathian Basin was drier[51].

2.4 Greenhouse gas concentrations during the LGM and until today

Greenhouse gas concentrations were considerably lower during the LGM[78,144] than at present time. For the present (2018), CO_2 concentration observations result in more than 400 ppmv. This value is strictly increasing at increasingly high rates on the multi annual scale since the onset of direct measurements[145].

The most prominent continuous direct measurement of the CO_2 concentration is represented by the Mauna Loa Observatory (Hawaii, United States) time series[145] that was started by David Keeling in March 1958. Laboratory analyzes of the Vostok ice core (Fig. 2) resulted[78] in a mean CO_2 concentration of ~185 ppmv (CH_4: ~360 ppbv) for the LGM, i.e. until today, the CO_2 concentration has more than doubled compared to the LGM.

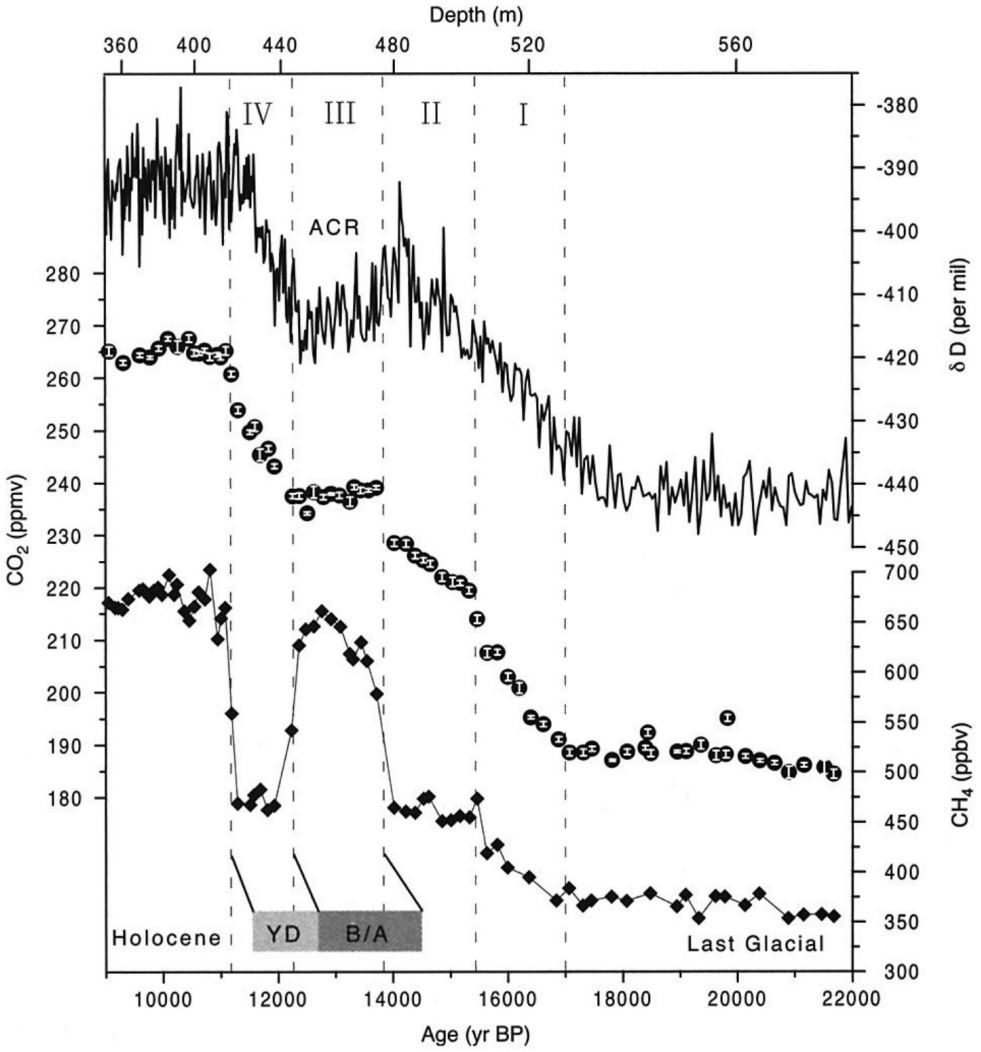

Figure 2: LGM to Holocene CO_2 (circles), CH_4 (diamonds), and deuterium (δD, solid curve, not discussed) concentrations based on the Vostok Dome C ice core measurements. The depth (top axis) is only valid for the CO_2 and CH_4 records. Younger Dryas (YD), Bølling/Allerød warm phase (B/A). From Monnin et al.[78] © AAAS (p. 195).

From the LGM to the present, the CO_2 concentration has increased by more than 215 ppmv (CH_4 by more than 1485 ppbv). Based on numerous evidence, such as the Vostok ice core[78] and the Mauna Loa measurements[145], this increase occurred at considerably varying rates including short periods of CO_2 decrease during the last 18 kyr.

Between 17 and 10 kyr ago, the CO_2 concentration increased monotonically[78] by 75 ppmv reaching ~268 ppmv[146]. For the industrialization onset (1760), Antarctic climate archive CO_2 concentration reconstructions[147,148] resulted in ~278 ppmv. This implies a total, yet not necessarily monotonic, increase of about 15 ppmv over ~10 kyr. This increase is explainable by forest clearance through humans, first evidenced[146] for China (9400 years ago), then India (8500 years ago), then southern-central Europe (between 8000 and 7000 years ago).

At about 5000 years ago, the methane (CH_4) concentration started rising, as the Antarctic climate proxies show[146]. Synchronously, humans started irrigating rice[146] and it is well known, that farming and irrigating rice releases methane[149]. The methane concentration increase found in ice cores for the subsequent millennia can be explained as a direct consequence of ongoing rice irrigation and farming[146]. This methane release amplified the greenhouse effect. Though the lifetime of methane is shorter, its greenhouse effect per molecule is far larger[22,23,150] than that of CO_2. As the exponential human population density increase occurred first in southeastern Asia, it is also most likely that the extensive anthropological land use changes, which considerably transformed the previously ecosystems (shaped by hunters and gathers), also remain traceable in the cryospheric CH_4 and CO_2 concentration archives.

From 1760 to 1958, during about 200 years only, the CO_2 concentration rose by ~40 ppmv, from ~278 to 316 ppmv[147,148]. This strong acceleration of CO_2 increase is directly related to the human-induced industrialization starting in Britain, then expanding over western Europe and subsequently over most mid-latitude regions of high population densities around the globe. From 1958 to the present[145], the CO_2 increase accelerated dramatically: The CO_2 concentration rose by another 84 ppmv within only 60 years, according to all direct measurements[145] (Fig. 3).

Such a high rate is unprecedented during the existence of *Homo sapiens* on this planet. The severe impacts of this global, human-induced greenhouse gas release exposes the essential planetary resources at high risks of destruction. In the past, humans could rely on and benefit from an enormous amount of 'services' provided by the ecosystems of the Earth 'for free'. These included the availability of potable water, fertile soils for farming, and sophisticated element cycles taking care of the human waste including the repair of local, human-induced ecosystem damages.

However, the accelerated human-induced greenhouse gas increase implies the human decision to expose their current existence at risk in the upcoming years to centuries by increasing the likelihood for systematic destruction. The acidification of the oceans, which take up one quarter of the released anthropogenic CO_2, leads to the collapse of key organisms[151–156] such as corals, crabs, oysters, and some plankton (calcifiers) — just to mention one of many current ecosystem threats.

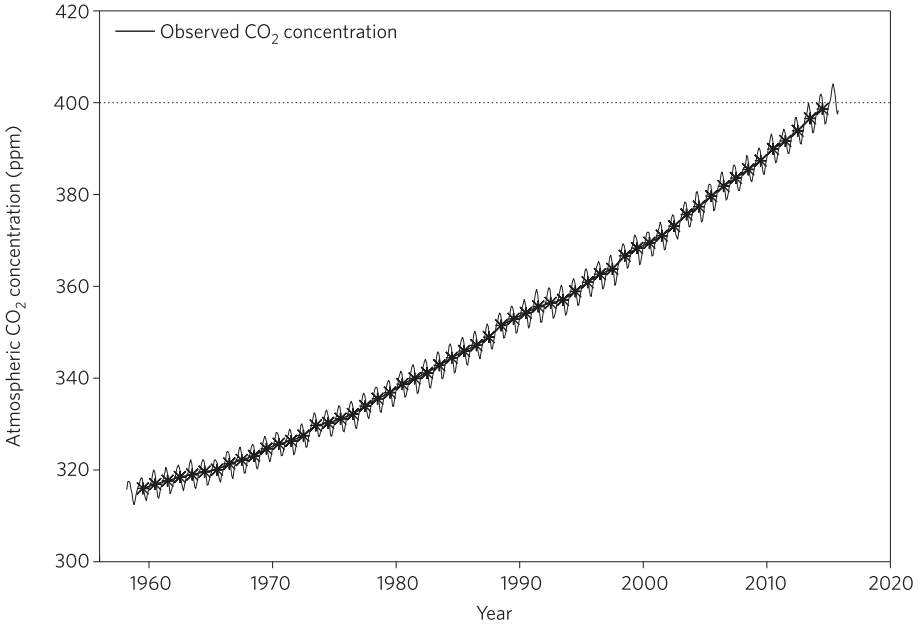

Figure 3: Atmospheric CO_2 concentration, observed since 1957. From Betts et al.[145]. Extrapolated CO_2 concentration has been removed. © Macmillan Publ. Ltd (p. 195)

2.5 Biosphere

Generally, a lower CO_2 concentration, such as during the LGM, favors the photosynthesis of C_4 vs. C_3 plants[157,158]. Yet, to determine the actual change of specific biomes, the precipitation and temperature that affects them must also be factored in[158,159]. If photosynthesis is not limited by water stress nor by temperature, then the C_4 outperform the C_3 plants if both are subjected to a lower CO_2 concentration[158–161]. According to the Chinese Loess Plateau records, the temperature has to be higher than 15 °C for the existence of C_4 plants in an originally C_3-dominated plant biome under lower CO_2 concentration[162]. Also, the precipitation increase needed by grasses is less than by trees under reduced CO_2 conditions[161]. As a result, open vegetation such as steppe, tundra, or grassland, replaced forests[67,163]; in particular grasses expanded their ecological range during the LGM[161]. For example, C_3 grassland was favored instead of shrubs in eastern Europe, according to modeling results[161] for the LGM. Besides grassland, central and eastern Europe was partly covered by taiga or montane woodland containing isolated pockets of temperate trees during the last full glacial[164]. Simulations[165] and pollen[166] confirm more extensive herbaceous- and reduced shrub-tundra, which favored erosion and detrital sedimentation[80,167], in particular on grassland.

In Spain, southern France, Italy, Greece, Turkey, and southern Ukraine, cool[116] steppe prevailed, according to pollen[70,168]. Consistently, in Italy, the Carpathian Basin, Dinarides, Balkans, northern France, the Benelux, the percentage of trees was below 20% during the LGM, while it could have been up to 40% in Spain and southern France, according to a principle component analysis[166] of pollen. At Monticchio in southern Italy, steppe prevailed[117], according to a Mediterranean sediment core and lake sediments. Tropical semi-desert existed[167] in Turkey and Lebanon during the LGM. Northern France, the Benelux and unglaciated regions of Denmark, Germany, western Poland, and the United Kingdom were partially polar deserts[167].

On the Russian Plain, subarctic tundra (nearby the EIS) and steppe (nearby the Black Sea) dominated — whereas forest occurred fragmentarily[169]. Particularly the northwestern Russian Plain was shaped by very dry climate[36] and (sub-)Arctic vegetation[136]. In the zone from western Ukraine to western Siberia, steppe graded into tundra[115].

Taiga prevailed at the north coast of the Sea of Azov during the LGM[115]. Thus, it expanded about 1500 km southwards of its current limit in west Russia. Broadleaved trees were confined to small refuges[115], such as the east coast of the Black Sea (cool mixed forest) and western Georgia (cool conifer forests). Their interglacial Caucasian-Georgian habitat was offset during the LGM by more than −1000 m in height[115].

During the LGM, the Danube-region was relatively warmer than other European regions[170]. The grass-covered east Carpathians were characterized by burning biomass, according to loess-charcoal analyzes[171]. These are in contrast to the globally decreasing trend of fires during the LGM[171]. However, they coincide with humans present in that region at the LGM[171]. The Carpathian Basin (CB) was much drier, particularly in its south, according to palaeopedology and loess[91] (Surduk, 45.1°N, 20.3°E). On the river flood plains in the CB, wet or mesic grassland dominated, whereas outside of them, dry steppe prevailed[171]. Woods occurred in the river valleys and on wet, north-facing hillsides of the CB[171]. Scattered trees were likely present on the CB loess plateaus[171]. Consistently, grassland and taiga was reported[57] for the CB between 28 and 12 kyr ago.

3 Climate and Proxy Data

3.1 Reanalyses and Global Climate Model Simulations

To understand the climate during the LGM in Europe, global, 100-year long, stationary simulations for the LGM run by the MPI-ESM-P[18–20] (MPI), the CCSM4[172] (CCSM), the MIROC-ESM[173] (MIROC), and the MRI[174] are analyzed. These GCM simulations conform to the Paleoclimate Modelling Intercomparison Project Phase 3 (PMIP3)[17] standards. Atmosphere and land surface conditions, such as the Eurasian ice sheet or the CO_2 concentration of 185 ppmv are adapted according to the PMIP standards for the LGM.

Since 1765, gaseous concentrations are recorded (ozone since 1850). Therefore, stationary reference runs of the *recent* global climate shortly before the onset of the industrialization are either initialized with the observed values for 1750 or 1850. These runs are termed *Preindustrial* (PI) or *control runs*. The Preindustrial ensemble of the four PMIP3-conforming GCM runs is abbreviated PMIP-PI and analogously the LGM ensemble PMIP-LGM. For instance, in the MPI-PI[127], the orbital parameters of 1850 determine the forcing: the spectral solar irradiance, averaged over 1844–1856, and the greenhouse gas concentrations of 1850 are applied. The latter are assumed to be homogeneously distributed *(well-mixed)* in the Earth's atmosphere. The monthly ozone concentration in the MPI-PI[127] is set to the average concentration of 1850–1860, aerosol forcing accounts only for tropospheric natural aerosols, while volcanic aerosols are not considered.

To analyze the recent transient climate from 1850 to 2005, additional simulations were run that are commonly labeled Historical (Hist; unfortunately a rather general term). In all subsequent sections of this dissertation, the individual as well as the ensemble of GCM runs are referenced by attaching a unique postfix (Hist, PI, or LGM) to the model name. To create easy and short to read acronyms, for example, the MPI-ESM-P-LGM will be simply called MPI-LGM. Analogously, the other model and time slice references will be simplified, if their newly created simplified reference are still unique.

Besides these GCM simulations, reanalyses, which consist of assimilated observation data, provide independent climate data, in particular from the 1950s onward. During the 1950s, the spatial density of weather observations around the northern hemisphere had increased sufficiently to assimilate these pointlike measurement data and to calculate two or more dimensional global spatiotemporal distributions for meteorological variables such as temperature and pressure.

The two most prominent global reanalyses are provided by the NCEP-NCAR (National Centers for Environmental Prediction and the National Center for Atmospheric Research) and the ECMWF (European Centre for Medium-Range Weather Forecasts). The NCEP-NCAR Reanalysis 1[175] (NCEP) encompasses assimilated observations since 1948. The NCEP-DOE Reanalysis 2[176] (NCEP2) and the ERA-Interim[177] (European Reanalysis Interim) provide assimilated observations since 1979; the time when weather satellite observations became available. In contrast to NCEP1, NCEP2 has upgraded assimilation algorithms and fixed human processing errors.

The reanalyses are an independent, at least three dimensional, observation-based reference to compare the climate simulations with for the recent past. This allows to assess the climate model quality. The simulation-to-reanalyses comparison can also reveal any climate model-specific drifts or bias. Such drifts or bias most likely affect all simulations of that model, including projections, hindcasts, and paleo climate simulations.

3.2 Boundary Conditions for Regional Climate Simulations

For running regional climate simulations with the WRF, prescribed static, initial, and boundary conditions are necessary. While static geographical data for the present climate exist for WRF, they are missing for past climate periods, such as the LGM. To fill this gap, reconstructed LGM conditions based on PMIP3[17] and CLIMAP[178] were included and if necessary adapted to refine the WRF configuration for the LGM. These encompass for example the reconstructed vegetation, land use, ice sheets, mean sea level, and straits of the LGM. Initial and boundary conditions for the regional LGM simulations were provided using the available MPI-LGM. More details, particularly on the prescribed static data of the bio-, cryo-, and pedosphere, as well as on the developed methods to adapt them to the WRF requirements, are provided in Sec. 7.3 (p. 94).

3.3 Climate Archives and Proxies

Climate archives, such as pollen[115], rocks[45], fossils[71], marine sediment cores[114], glacier equilibrium line altitudes[66], and lake sediments[117] served as an independent reference to validate the global climate simulations and the regional climate-dust simulations.

Loess Mass Accumulation Rates Among the climate archives, loess is one of the most abundantly available and widespread proxies for the LGM wind directions and its dust cycle in Europe. Based on laboratory analyses of sampled loess deposits, mass accumulation rates (MARs) are reconstructed for the LGM. These MARs represent an independent data source to evaluate climate-dust simulations. For this dissertation, a state-of-the-art MAR table has been compiled (Tab. 1). For some loess sites, MAR ranges were published. These ranges are taken into account in Tab. 1 by listing their upper and lower limits as separate entries. This representation is chosen since the suitability of a summarizing statistical conversion, e.g. the arithmetic mean, can not be assumed to represent a more realistic MAR measure per se.

Table 1: Loess mass accumulation rates; encompassing all particle sizes (MAR) or only particles with less than 10 µm diameter (MAR10). Reconstructed from fieldwork samples dated to the LGM or to a period encompassing the LGM. Proportion of particles smaller than 10 µm in diameter (Frac10). MAR ranges itemized by their limits. For sites with more than one reconstructed MAR each rate is shown separately. Missing value (0.00); country codes (CC) conform with ISO 3166.

Site	CC	Lat °N	Lon °E	MAR g m^{-2} yr^{-1}	MAR10 g m^{-2} yr^{-1}	Frac10
Achenheim[179]	FR	48.35	7.38	331.00	82.75	0.25
Achenheim[99]	FR	48.35	7.38	257.00	0.00	0
Albertirsa[118]	HU	47.26	19.64	386.00	96.50	0.25
Albertirsa[99]	HU	47.26	19.64	841.00	0.00	0
Albertirsa[57]	HU	47.26	19.64	587.00	134.00	0.23
Am Bingert Wiesbaden[99]	DE	50.12	8.28	361.00	0.00	0
Arapovychi (Arapovichi)[92]	UA	51.95	33.31	666.00	166.50	0.25
Basaharc[57]	HU	47.80	18.84	348.00	79.00	0.23
Batajnica[57]	RS	44.92	20.32	329.00	75.00	0.23
Böckingen[99]	DE	49.13	9.18	3300.00	0.00	0
Bodrogkeresztúr 1[57]	HU	48.13	21.40	381.00	87.00	0.23
Bönnigheim A[99]	DE	49.04	9.14	131.00	0.00	0
Bönnigheim B[180]	DE	49.04	9.14	242.00	60.50	0.25
Bönnigheim B[99]	DE	49.04	9.14	283.00	0.00	0
Bönnigheim B[99]	DE	49.04	9.14	1500.00	0.00	0
Bryansk[92]	RU	53.15	34.06	394.00	98.50	0.25
Crvenka[57]	RS	45.66	19.48	197.00	45.00	0.23
Csorgókút 1[57]	HU	48.13	21.40	284.00	65.00	0.23
Csorgókút 2[57]	HU	48.13	21.40	453.00	103.00	0.23
Debrecen (Alföldi brickyard)[57]	HU	47.53	21.57	237.00	54.00	0.23
Dolní Vestonice[180]	CZ	48.89	16.66	758.00	189.50	0.25
Dolní Věstonice[99]	CZ	48.89	16.66	754.00	0.00	0
Dolní Věstonice[99]	CZ	48.89	16.66	1100.00	0.00	0
Dunaszekcső[57]	HU	46.07	18.75	707.00	161.00	0.23
Dunaújváros[57]	HU	46.97	18.94	1238.00	282.00	0.23
Dybawka[46]	PL	49.79	22.69	1195.00	0.00	0
Erdut[57]	HR	45.53	19.06	215.00	49.00	0.23
Gololobovo[85]	RU	55.05	38.57	272.00	68.00	0.25
Gorokhov[92]	UA	50.31	24.50	435.00	108.75	0.25
Grubgraben Kammern Niederösterreich[99]	AT	48.50	15.80	2100.00	0.00	0
Gunderding Oberösterreich[99]	AT	48.26	13.23	10340.00	0.00	0

Table continues

Table 1: *Continued*

Site	CC	Lat °N	Lon °E	MAR g m^{-2} yr^{-1}	MAR10 g m^{-2} yr^{-1}	Frac10
Halytsch (Halyc)[119]	UA	49.10	24.80	226.00	56.50	0.25
Harmignies[181]	BE	50.41	4.02	412.00	103.00	0.25
Harmignies[99]	BE	50.41	4.02	1467.00	0.00	0
Harmignies[99]	BE	50.41	4.02	3135.00	0.00	0
Irig[57]	RS	45.08	19.87	192.00	44.00	0.23
Katymár[46]	HU	46.02	19.20	1005.00	0.00	0
Katymár[57]	HU	46.02	19.20	632.00	144.00	0.23
Kesselt[120]	BE	50.84	5.60	446.00	111.50	0.25
Kesselt[99]	BE	50.84	5.60	825.00	0.00	0
Kesselt[99]	BE	50.84	5.60	330.00	0.00	0
Korostelevo (Korostylievo)[121]	RU	51.84	42.42	181.00	45.25	0.25
Lakitelek 1[57]	HU	46.88	20.02	254.00	58.00	0.23
Látókép[57]	HU	47.56	21.49	212.00	48.00	0.23
Likhvin (Chekalin)[85]	RU	54.10	36.27	272.00	68.00	0.25
Madaras[57]	HU	46.04	19.29	375.00	86.00	0.23
Mende[182]	HU	47.42	19.45	456.00	114.00	0.25
Mende[99]	HU	47.42	19.45	519.00	0.00	0
Mende[57]	HU	47.42	19.45	761.00	173.00	0.23
Mezyn (Mezin)[92]	UA	52.20	33.30	788.00	197.00	0.25
Molodova V[122]	UA	48.50	26.89	369.00	92.25	0.25
Mosorin[46]	RS	45.26	20.28	545.00	0.00	0
Mošorin[57]	RS	45.26	20.28	395.00	90.00	0.23
Nussloch[123]	DE	49.35	8.72	2114.00	528.50	0.25
Nussloch[99]	DE	49.35	8.72	1213.00	0.00	0
Nussloch[99]	DE	49.35	8.72	6129.00	0.00	0
Otkaznoe (Otkaznoye)[124]	RU	44.32	43.85	336.00	117.60	0.35
Paks[182]	HU	46.64	18.88	1325.00	331.25	0.25
Paks[99]	HU	46.64	18.88	2662.00	0.00	0
Paks[57]	HU	46.64	18.88	1422.00	324.00	0.23
Patkóbánya Kopasz Hill Tokaj[125]	HU	48.22	20.45	395.00	98.75	0.25
Petrovaradin[57]	RS	45.27	19.87	174.00	40.00	0.23
Prymors'ke (Primorskoje)[183]	UA	45.94	30.20	654.00	163.50	0.25
Pyrogove[46]	UA	50.36	30.53	1659.00	0.00	0
Radymno[46]	PL	49.96	22.81	538.00	0.00	0
Remicourt[99]	BE	50.67	5.40	560.00	140.00	0.25
Remicourt[99]	BE	50.67	5.40	453.00	0.00	0

Table continues

Table 1: *Continued*

Site	CC	Lat °N	Lon °E	MAR g m^{-2} yr^{-1}	MAR10 g m^{-2} yr^{-1}	Frac10
Rocourt [184]	BE	50.68	5.54	257.00	64.25	0.25
Rocourt [99]	BE	50.68	5.54	93.00	0.00	0
Ruma [57]	RS	45.01	19.85	192.00	44.00	0.23
Sables d'Or les Pins [99]	FR	48.65	-2.39	354.00	0.00	0
Ságvár [57]	HU	46.83	18.09	176.00	40.00	0.23
Sanzhijka [46]	UA	46.23	30.61	808.00	0.00	0
Schwalbenberg [99]	DE	50.57	7.24	560.00	140.00	0.25
St.-Pierre-les-Elbeuf [185]	FR	49.60	1.23	242.00	60.50	0.25
St.-Romain-de-Colbosc [184]	FR	49.54	0.36	687.00	171.75	0.25
Stari Bezradychy [46]	UA	50.18	30.55	440.00	0.00	0
Stari Slankamen [57]	RS	45.13	20.27	168.00	38.00	0.23
Stillfried Gänserndorf Niederösterreich [99]	AT	48.42	16.84	229.00	0.00	0
Strelitsa [186]	RU	51.60	38.90	290.00	72.50	0.25
Surduk [57]	RS	45.07	20.33	434.00	99.00	0.23
Susek [57]	RS	45.22	19.53	150.00	34.00	0.23
Süttő [51]	HU	47.74	18.45	1009.00	0.00	0
Süttő [57]	HU	47.74	18.45	584.00	133.00	0.23
Szeged-Öthalom I [57]	HU	46.28	20.10	332.00	76.00	0.23
Tápiósüly [57]	HU	47.45	19.52	504.00	115.00	0.23
Titel [46]	RS	45.23	20.30	591.00	0.00	0
Titel [57]	RS	45.23	20.30	510.00	116.00	0.23
Tokaj (Kereszt Hill II) [57]	HU	48.13	21.40	222.00	51.00	0.23
Tokaj (Patkó-quarry) [57]	HU	48.12	21.40	332.00	76.00	0.23
Tokaj Kopasz Hill Patkó-bánya [125]	HU	48.22	20.45	395.00	98.75	0.25
Tönchesberg Tönches-Berg Kruft [187]	DE	50.35	7.35	779.00	194.75	0.25
Tönchesberg Tönches-Berg Kruft [99]	DE	50.35	7.35	1249.00	0.00	0
Trindorf Oftering [99]	AT	48.24	14.14	2970.00	0.00	0
Üveghuta-2 borehole [57]	HU	46.20	18.61	338.00	77.00	0.23
Volgodonsk [188]	RU	47.56	41.99	245.00	98.00	0.40
Vyazivok [189]	UA	49.33	32.98	202.00	50.50	0.25
Willendorf II Niederösterreich [99]	AT	47.79	16.05	372.00	0.00	0
Willendorf II Niederösterreich [99]	AT	47.79	16.05	886.00	0.00	0
Zmajevac [57]	HR	45.81	18.82	437.00	100.00	0.23

4 Climatologies of the European and Atlantic Atmosphere

Preamble In this section and in Sec. 6 (p. 70), some figures have been adapted from a publication by the author and his colleagues[36]; legal details on the co-authorship are stated in the Supplementary (p. 195).

4.1 Introduction

Jet stream To better understand the LGM wind dynamics, the simulated polar-front jet stream is analyzed. The jet stream is the main driver of the winds between the surface and the 200 hPa level. It is strongly related to cyclone activity[36]. A possible displacement of the LGM jet stream will be analyzed. It might explain the southward shift of the polar front[66] and westerlies[73] at that time.

Pressure Sea level pressure (pressure) is one of the most common meteorological variables. Its distribution provides the basis to understand the wind dynamics that are most relevant at the Earth's surface and for near surface atmospheric processes. It is important to understand these wind dynamics as the winds dominate the advection of heat and the transport of mineral dust and/or moisture. Today, there are well-known pressure distribution patterns, such as the North Atlantic Oscillation (NAO) that largely affect the European weather and, on a larger time scale, its climate. Whether and if so how they changed during the LGM compared to the present is an important research question. Understanding the wind dynamics is directly related to understanding the Earth's climate variability, which is an important question also in the current globally warming climate.

Temperature The near-surface air temperature (temperature) distribution describes relevant properties of the Earth system, such as the 0 °C freezing and melting threshold. As the near-surface soil temperatures are usually closely dependent on the near-surface air temperature, the latter directly determines the permafrost extent. The timberline depends in most cases directly on the temperature, as the other limiting factors, such as the available humidity, sunlight, and nutrients are usually fulfilled. Numerous biotic proxies exist for the LGM climate. As temperature is the limiting factor for many species during a cold-dominated climate, the existence of biotic proxies and their abundance allows to reconstruct a corresponding local or regional temperature range. Hence, these biotic temperature proxies are an independent mean to evaluate the simulated LGM temperatures. This evaluation also provides evidence for the general quality of the LGM simulation. If deviations between the reconstructed and simulated temperatures exist, they could indicate a deficiency in the proxy-based reconstructions. This could lead, in turn, to a re-evaluation and improvements in the responsible scientific disciplines.

Precipitation The *precipitation rate(s)* (precipitation) are part of the hydrological cycle on the Earth, required for ice sheet and glacier formation, and most important for water-limited biosphere regimes. Precipitation also affects the *mineral dust* (dust) entrainment of the atmosphere, as it considerably reduces or suppresses aeolian soil erosion. It shortens the mean aeolian dust transport distance due to more wet deposition. In the hydrological cycle, it is the linkage that redistributes moisture and affects dust movements between the atmo-, bio-, cryo-, pedo-, and oceanosphere. Simulated LGM precipitation is assessable using independent reconstructions from lake sediments and biotic proxies.

4.2 Hypotheses

During the Last Glacial Maximum:

(1) The jet stream differed from its current (Preindustrial) path, was regionally faster and partly latitudinally narrower.

(2) The pressure gradient of the NAO was larger, including the shrinkage and westward shift of the Icelandic Low and the expansion of the Azores High.

(3) The highest sea level pressure centered over the EIS and the eastern LIS.

(4) The North Atlantic Current reached to the Norwegian Sea.

(5) Over the Eurasian plains, temperatures were considerably lower and favored permafrost.

(6) Over Baffin Bay, precipitation was almost absent. Over the proglacial central European areas including the North Sea Basin and the unglaciated Eurasian plains east of the EIS, precipitation was lower implying their increased potential for aeolian erosion.

4.3 Methods

Jet stream The input data for the jet stream analysis is extracted from the global Preindustrial and the LGM simulation ensembles (PMIP-PI and -LGM). The jet stream analysis includes also the individual simulations of the MPI[18–20] and MRI[174] model (Fig. 4). Of all four GCMs, they reproduce best the recent transient climate (Sec. 6, p. 70). The jet stream speed is calculated by annually averaging the 300 to 200 hPa vertical average of the monthly mean wind speed records.

Climatologies for pressure, temperature, and precipitation The analyses focus on Europe and the extended North Atlantic region, referred to as the EurAt Domain (90°W to 70°E, 20 to 80°N). For both, the LGM and PI, the average pressure, temperature, and precipitation climatologies were calculated based on the last 30 simulation years of the 1.875° horizontally and daily resolved, stationary MPI-LGM and -PI. Based on the temporal averages of the LGM and PI climatologies, the respective climatology differences (LGM minus PI) were calculated. The climatologies and their LGM to PI differences were analyzed, compared, and assessed using independent simulation- and proxy-based results.

4.4 Results and Discussion

Jet stream The jet stream was fastest (40 to 45 m/s) over and along the southeastern LIS coastline, consistent with the LGM simulations run by a model of intermediate complexity[190]. While it crossed the subpolar North Atlantic in (north-)eastward direction, its speed decreased uniformly. At the southwestern EIS tip, it had decreased to between 20 and 25 m/s (Fig. 4).

According to the more reanalysis-conform MPI- and MRI-LGM (Fig. 5), it was even slower there, i.e., less than 20 m/s. The results provided by the MPI and MRI are assumed to be more relevant than those of the other GCMs because the MPI (MRI) is the (second) most capable in approximating the control case, i.e. the reanalyses, among all four GCMs (Sec. 6.4, p. 74). Though the maximum glacial MPI and MRI jet speeds differ, MPI 35 to 40 m/s vs. MRI 30 to 35 m/s, their maxima are located congruently. According to the MRI, the jet stream was more zonally oriented heading towards France, in contrast to the MPI, in which it bent northeastwards towards the Nordic Seas. Over the North Atlantic, the jet stream core was faster during the LGM than during the PI (Fig. 4). This is consistent with the CCSM-based jet stream analyzes[191,192] under glacial conditions. In addition, the latitudinal jet stream extent was thinner, consistent with the storm track energy found in other models[110].

Jet stream according to MPI simulations According to the MPI, the LGM jet stream speed increased by more than 10 m/s over the southeast coast of the LIS compared to the PI. An increase of 5–10 m/s occurred along but off the southeast coast of the LIS, inland over and across the southeastern topographical gradient of the LIS, and over the western subpolar Atlantic to the margin of the Iceland ice sheet (IIS). Even further northwards over the GIS, the IIS, and the likely ice-covered Nordic Seas, the velocity increased by between 2 and 5 m/s compared to the PI, yet their total velocity remained below 20 m/s. As a result, the jet stream vanished over the eastern subpolar Atlantic, according to the MPI-LGM. The wind velocities also decreased over the central North Atlantic at about 30°N by 2 to 10 m/s compared to the PI, according to the MPI.

Jet stream according to MRI simulations According to the MRI, the LGM jet stream was only about 5 to 10 m/s faster over and along the southeastern LIS margin than the PI jet stream. An increase of 2 to 5 m/s was calculated for a zone from the outer radius of the jet stream core running eastwards over and beyond Iberia to about Sicily. This zone is consistent with the reported[110] southeastward extension of the jet stream and the southward shifted storm tracks. Yet, the LGM jet stream vanished already west off Iberia and Ireland, near 10°W, according to the MRI. LGM wind velocities decreased compared to the PI by 2 to 5 m/s at the northern flank and by 2 to 10 m/s at the southern flank of the jet stream.

Summary In summary, evidence indicates a stronger jet stream, partly strengthened by more than 10 m/s, whose propagation direction differed from today. Likely, the increased topography of the LIS, GIS and EIS affected its propagation direction over the North Atlantic, a finding that is confirmed by others[69,110] as well.

The LGM jet streams agree well among the MPI and MRI, though, according to the MPI, the jet stream flowed farther northeast, whereas according to the MRI, it favored a path directed towards France. The ice sheets affected the path of the jet stream markedly.

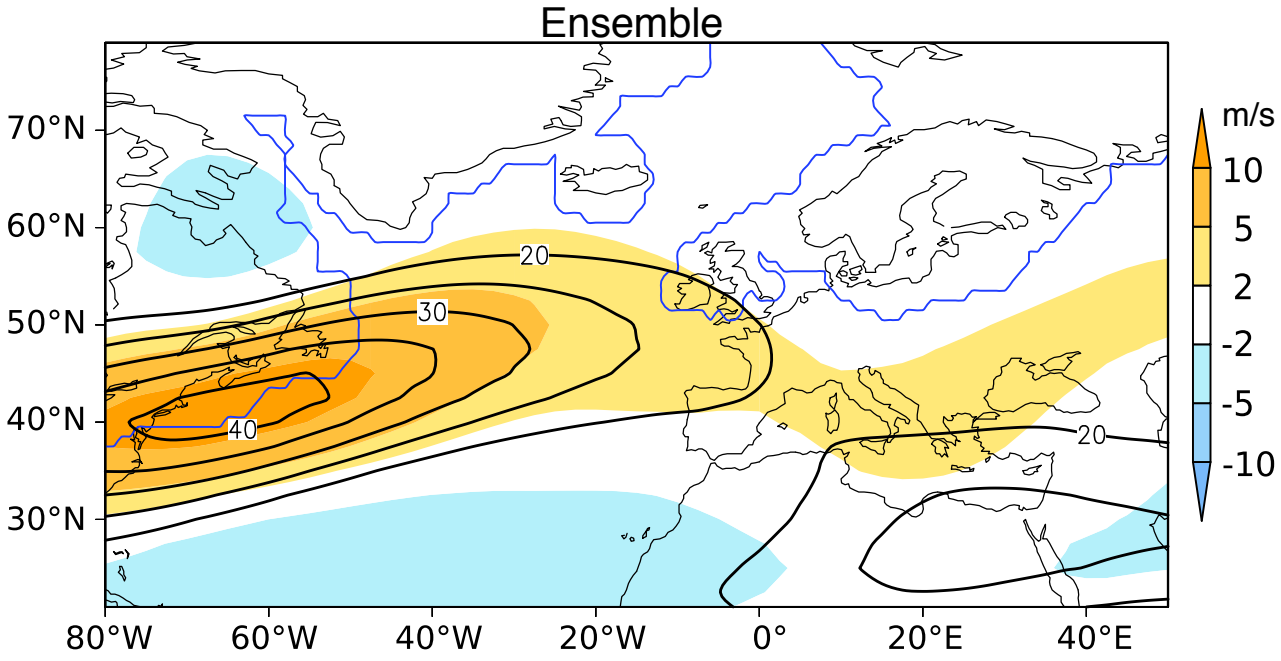

Figure 4: The Last Glacial Maximum (LGM) jet stream and the differences from its present characteristics. The spatial speed distribution (labeled contours) during the LGM and deviations from the present (color-shaded) base on the global climate model ensemble mean of the MPI-ESM-P, MRI, MIROC, and CCSM4. The contours (starting at 20 m/s, 5 m/s spacing) show the temporal and 300 to 200 hPa LGM average of monthly wind speed records. Higher *(Lower)* LGM than PI wind speed areas are sunny *(blueish)* tinted. *Adapted from Ludwig,* Schaffernicht, *Shao, and Pinto*[36] *© Wiley (p. 195).*

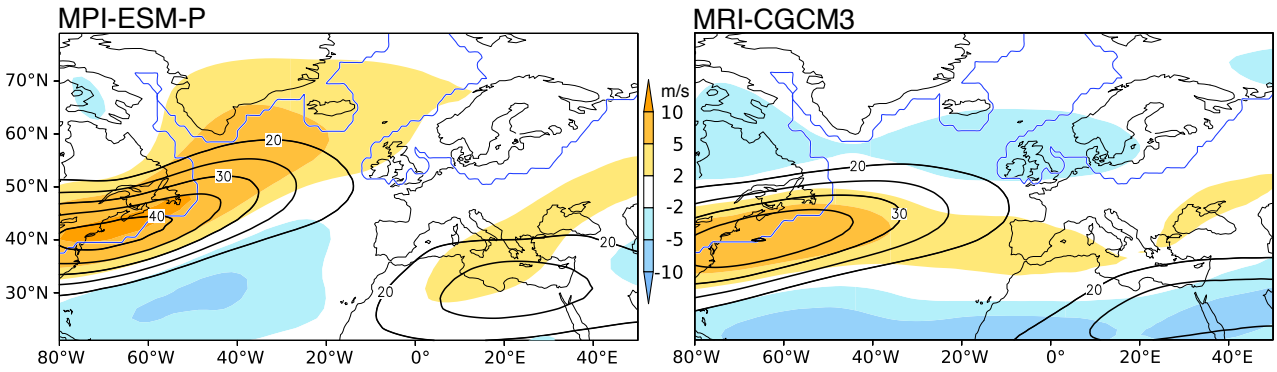

Figure 5: The Last Glacial Maximum (LGM) jet stream and the differences from its present characteristics. The spatial speed distribution (labeled contours) during the LGM and deviations from today (color-shaded) simulated with the MPI-ESM-P and the MRI-CGCM3. The contours (starting at 20 m/s, 5 m/s spacing) show the temporal and 300 to 200 hPa LGM average of monthly wind speed records. Higher LGM than PI wind speed areas are sunny tinted, blueish for the reverse case. *Adapted from Ludwig,* Schaffernicht, *Shao, and Pinto*[36] *© Wiley (p. 195).*

North Atlantic Oscillation and high pressure systems The NAO[193–201] is the dominant pressure distribution pattern during the LGM and PI (Fig. 6). The average LGM NAO pressure gradient was about 1.5 hPa/deg compared to only 0.95 hPa/deg during the present. This corresponds to a on average 50% stronger NAO during the LGM compared to today.

This strengthening and the estimated LGM pressure gradient agree with the LGM results based on a climate model beyond the PMIP3 ensemble[141]. Likely, the stronger NAO led to stronger westerlies over the North Atlantic and western Europe. Both, the NAO increase and the assumption that this caused stronger westerlies, agree with the IPSL[141] GCM results[112]. In meridional direction, the LGM Azores High covered the North Atlantic from 20 to 50°N. In contrast to the PI, the LGM Azores High extended about 4° further northwards and 6° further westwards (Fig. 6). According to the reconstructed[66] equilibrium line altitude of the European glaciers, the northward extension of the Azores High is favored. Regarding the westwards extension of the Azores High, it thus dominated not only over the eastern but also over the central North Atlantic.

Apart from the Azores High, two further high pressure centers existed during the LGM (Fig. 6a). The strongest prevailed over the LIS (LIS High). The EIS High, which was about as strong as the Azores High, prevailed over the EIS-covered central-eastern Scandinavia, where the EIS was at least 1 km thick.

In the EurAt Domain, after the Azores High, the second strongest and only remaining high pressure in the present climatology is the Greenland ice sheet High (GIS-High). The contiguous high pressure extends from the United States, Canada, across the Atlantic to the Maghreb, continuing via the Mediterranean region, central, and eastern Europe. It includes the Saharan Hoggar Mountains, the Zagros Mountains, and the West Siberian Plain (Fig. 6b).

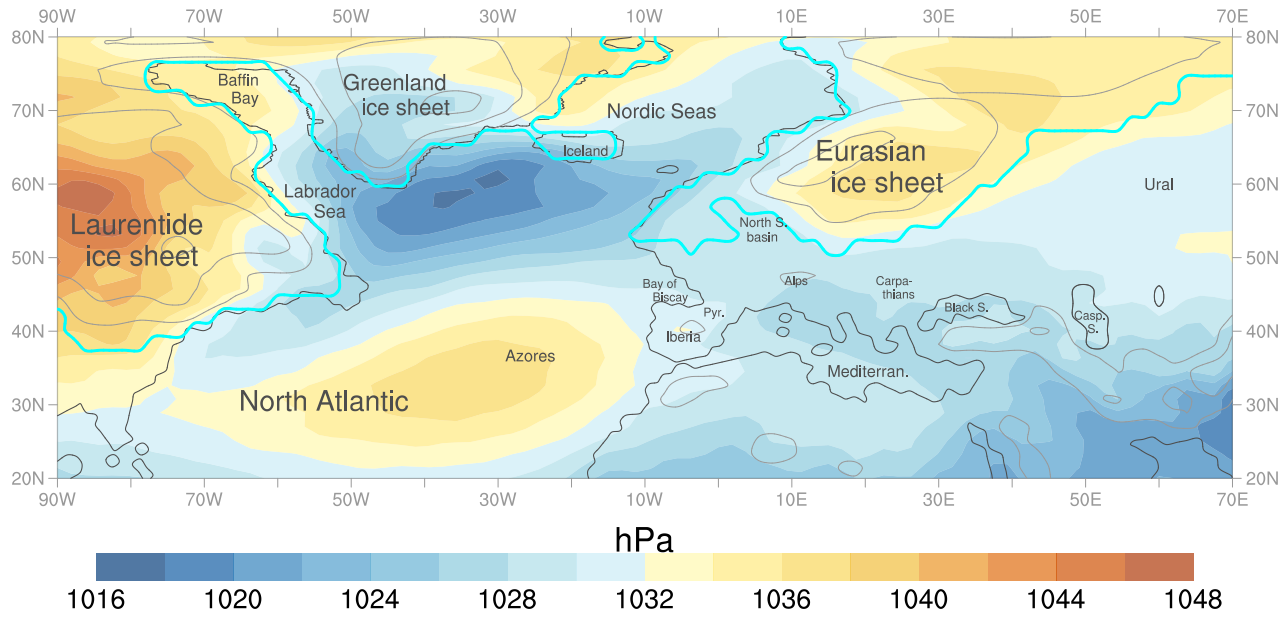

(a) LGM SLP climatology

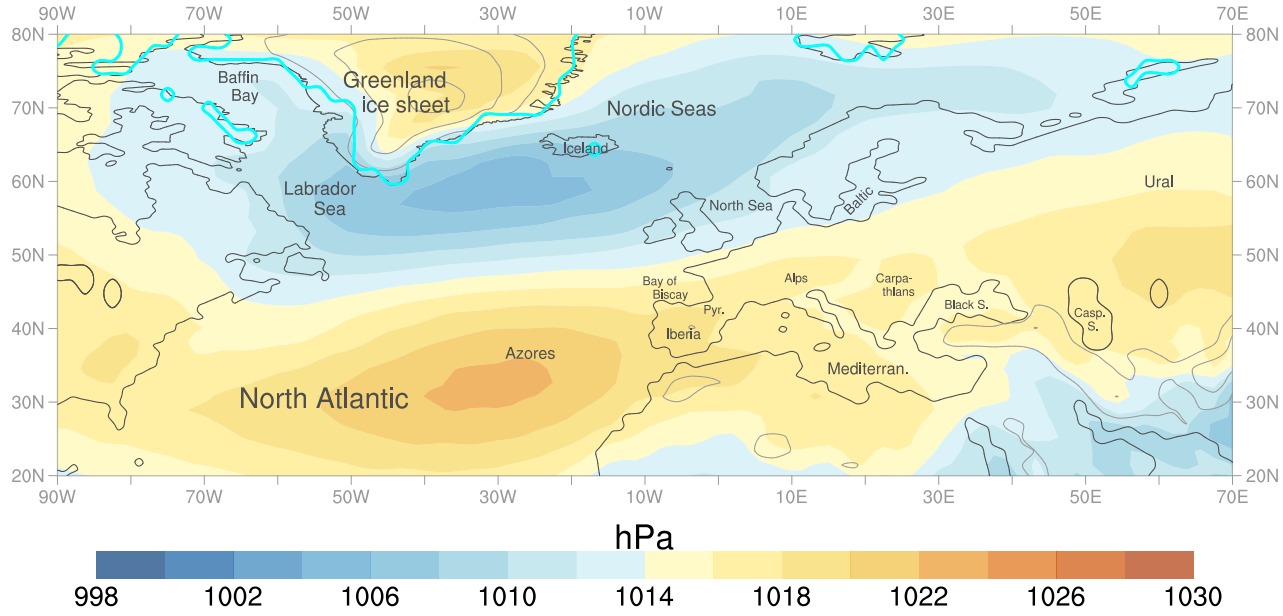

(b) Preindustrial SLP climatology

Figure 6: Pressure at sea level climatologies based on simulations for (a) the Last Glacial Maximum (MPI-LGM) and (b) the recent present climate (MPI-PI). Ice sheet extent (cyan lines) extracted from the atmospheric model realm. Coastlines (black) extracted from the oceanic realm except for the Caspian Sea, whose coastline was extracted from the atmospheric realm. Topographic isohypses (grey, extracted from the atmospheric realm) mark the 1000, 2000, and 3000 m levels; the latter two being relevant only to the ice sheets.

The general 14 hPa pressure difference between the LGM and the present results from the lower LGM sea level (Fig. 7). Compared to the present, the by far largest 32 hPa LGM increase occurred over the LIS followed by 24 hPa over the EIS. Even after taking into account the effect of sea level decrease on pressure, a 18 hPa increase over the LIS and a 10 hPa increase over the EIS resulted.

As shown in Sec. 6.4, particularly for central and eastern Europe as well as westernmost Russia, the EIS High likely caused northeasters and easterlies over the proglacial surfaces along the eastern and southern EIS margin (Tab. 11). Similarly, along the southern margin of the LIS, northeasters and easterlies are likely. For Europe, this hypothesis of easterlies is supported notably during DJF by the 10 m wind and 200 hPa zonal wind changes simulated[112] by two different IPSL GCMs.

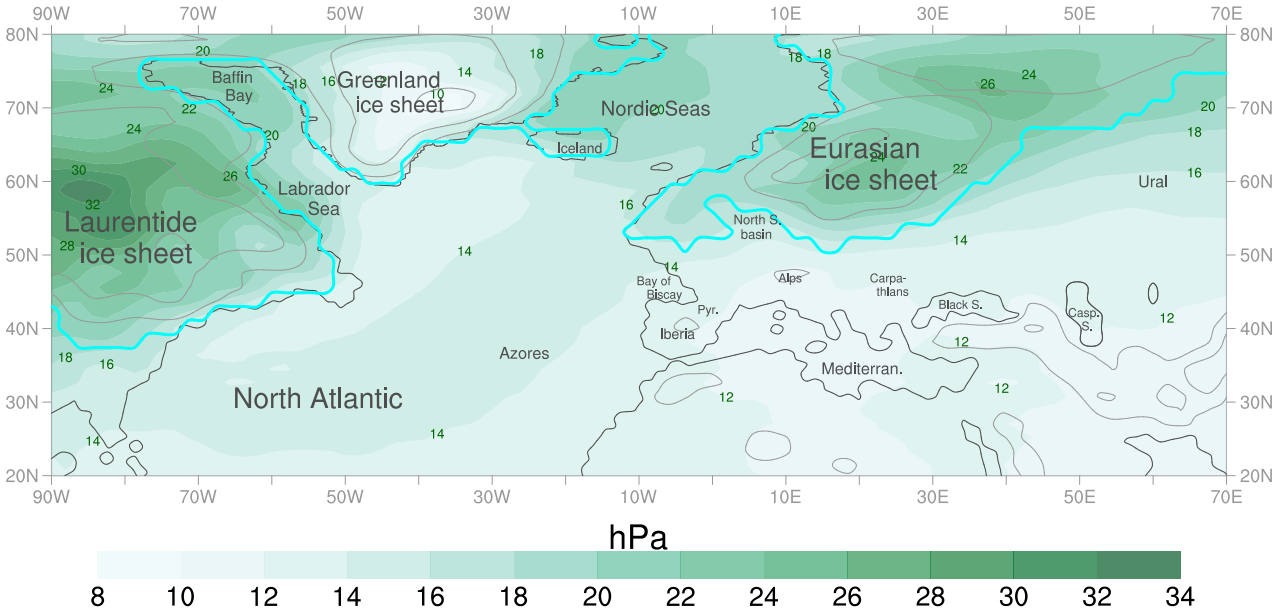

Figure 7: Climatological differences of the sea level pressure between the LGM and the present (LGM minus PI pressure) according to the MPI-LGM and -PI simulations (Fig. 6). Contours as in Fig. 6.

According to the LGM climatology (Fig. 6a), only one low pressure center prevailed, located between Newfoundland and Iceland over the subpolar gyre. The pressure over southeastern Europe is slightly lower, yet it continues southeastwards beyond Europe without reaching a well-defined pressure minimum within the analyzed domain. The pressure at the unglaciated regions of central Europe and northern Africa equals about the mean spatial pressure for the whole domain.

According to today's climatology (PI, Fig. 6b), low pressure extended from Labrador and Baffin Bay to Scandinavia, the Barents and Kara Seas. Its most pronounced part, the Icelandic Low, covers in Europe only Scandinavia and the British Isles.

Temperatures For the LGM, the average near-surface air temperatures ranged between −45 and 30 °C in the analyzed domain (Fig. 8a). To improve readability, the shortening *temperature* will be used subsequently, which always represents *near-surface air temperature(s)*. For the PI (Fig. 8b), the domain temperatures range between −35 and 30 °C, with the minimum over the GIS and the maximum at the southern margin of the domain.

During the LGM, the minimal temperature in the domain (Fig. 8a) occurred over the most elevated LIS surfaces of the domain. The temperature gradients anticorrelate with the topographic gradients over the LIS, the GIS, and the EIS. The land east of the EIS was characterized by temperatures below 0 °C (Fig. 8a) favoring permafrost[202].

Sea ice likely prevailed in Baffin Bay, on the Labrador, and on parts of the Nordic Seas given their less than 0 °C temperatures (Fig. 8a). Heat was advected to the mid-latitude Atlantic, the subpolar gyre, and the Norwegian Sea (Fig. 8a). It is inferred from the climatological temperature gradient, which deviates northwards from an exclusively latitude-conform decrease. These deviations are likely caused by heat advection through the North Atlantic Current[203]. The reconstructed LGM GLAMAP (Glacial Atlantic Ocean Mapping) SST gradient[203] suggests a more latitude-conform cooling.

For off the Mauritian and Moroccan coast (20–32°N), 15 to 20 °C were reconstructed (Fig. 8a), in line with the 14 to 18 °C SST reconstructions[114] that resulted from two Atlantic sediment cores drilled off the Mauritian coast. For off the Western Sahara coast, the simulated temperatures and the reconstructed SSTs[114] differ by only 1 °C. Over the Alboran Sea, the LGM simulation calculated temperatures between 10 and 15 °C. Off the southern and western Iberian coast, in the region located at about 38°N and extending to about 40°W, the simulated 10 to 15 °C and 15 to 20 °C ranges adjoined, which agrees with Mg/Ca-reconstructed SSTs[114] (14 to 18 °C) from three Atlantic and one Alboran cores that were drilled at 38°N. Further north (45°N,27°W), the simulation calculated 10 to 15 °C; a result, which is supported by the Mg/Ca SST reconstruction[114] (10 to 14 °C). Also at 60°N, 23°W, the calculated 5 to 10 °C match with the reconstructed SST[114] (6 to 10 °C).

For southern Europe, the temperatures over the Bay of Biscay and the north coast of the Mediterranean Sea ranged between 5 and 10 °C, over the central Mediterranean Sea between 10 and 15 °C, and over the southern Mediterranean Sea between 15 and 20 °C. This agrees well with foraminifera[65]- and alkenone[66]-based SST reconstructions for the LGM. The SST to temperature comparison is warranted for the Mediterranean Sea as SSTs are closely related[66,204] to the temperature. Conforming annual temperatures for these areas but also for the Black Sea region and central to eastern Europe are reported[205] on the basis of a regional atmospheric simulation.

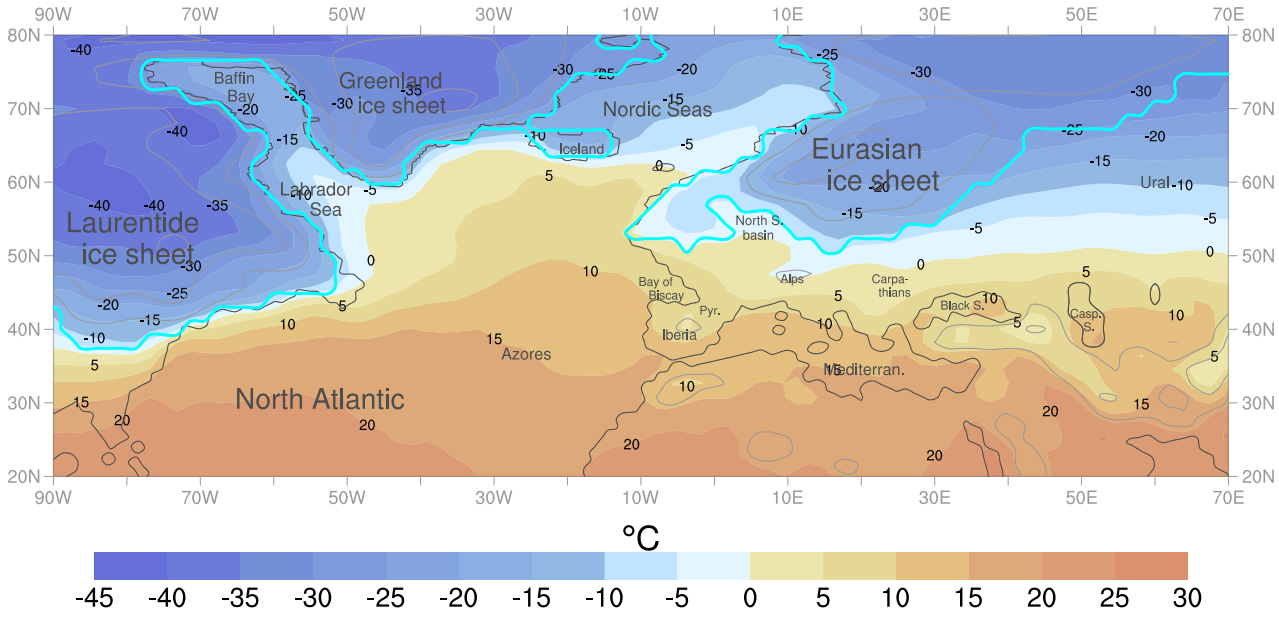

(a) Last Glacial Maximum

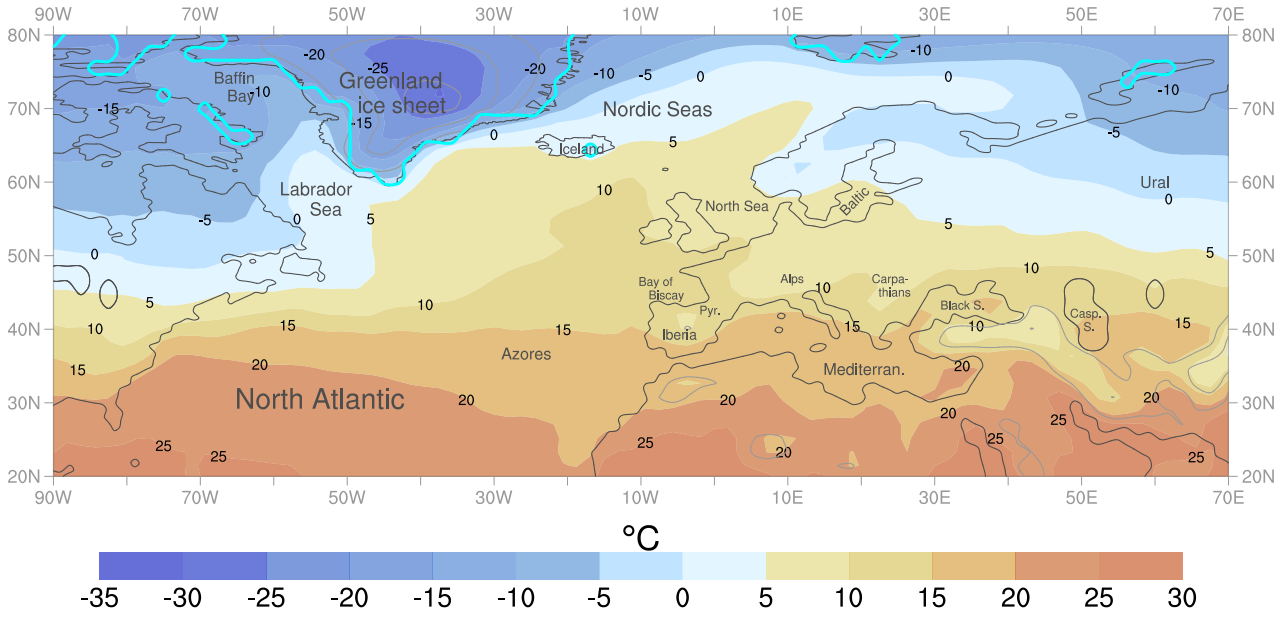

(b) Preindustrial

Figure 8: Near-surface air temperature climatologies. Based on simulations for the (a) Last Glacial Maximum (MPI-LGM) and (b) recent climate (MPI-PI). Contours as in Fig. 6

LGM-to-present comparison Compared to the PI, the LGM temperature decrease was at maximum (ΔT = 32 °C) over the ice sheet tops (Fig. 9) in agreement with other GCM simulations[109]. The largest EurAt Domain LGM temperature decrease over the unglaciated land surface was over the Eurasian plains northeast of the Alps (ΔT = −8 to −16 °C) supported by other GCM simulations[109]. The largest decrease over the sea surface occurred over the Nordic Seas (ΔT > 16 °C) consistent with other simulations[64] that indicate a ΔT > 16 °C reduction for the LGM winter over the subpolar gyre, the Labrador, and the Nordic Seas. The 4 to 6 °C temperature decrease over the northern and central Mediterranean Sea as well as the 2 to 4 °C decrease over the southern and eastern part agree with proxy-based SST reconstructions[65,66] and simulation-based temperature differences[69,109]. The advection of warm desert air possibly[66] accounts for this minor LGM cooling over the eastern Mediterranean Sea. The decrease by about 3 to 5 °C over the western Mediterranean and Iberia is less than that found[112,141] by the IPSL GCM (5 to 10 °C). However, the IPSL GCM calculated an unusually homogeneous temperature over the whole Mediterranean basin in contrast to many other studies[65,66,204]. It calculated a 20 to 25 °C decrease over the Norwegian Sea, much larger than the 8 to 16 °C decrease found here (Fig. 9). For the remaining EIS-free parts of Europe, western Russia, and the North Atlantic, the IPSL GCM temperature decreases[112] conform to the results presented here (Fig. 9).

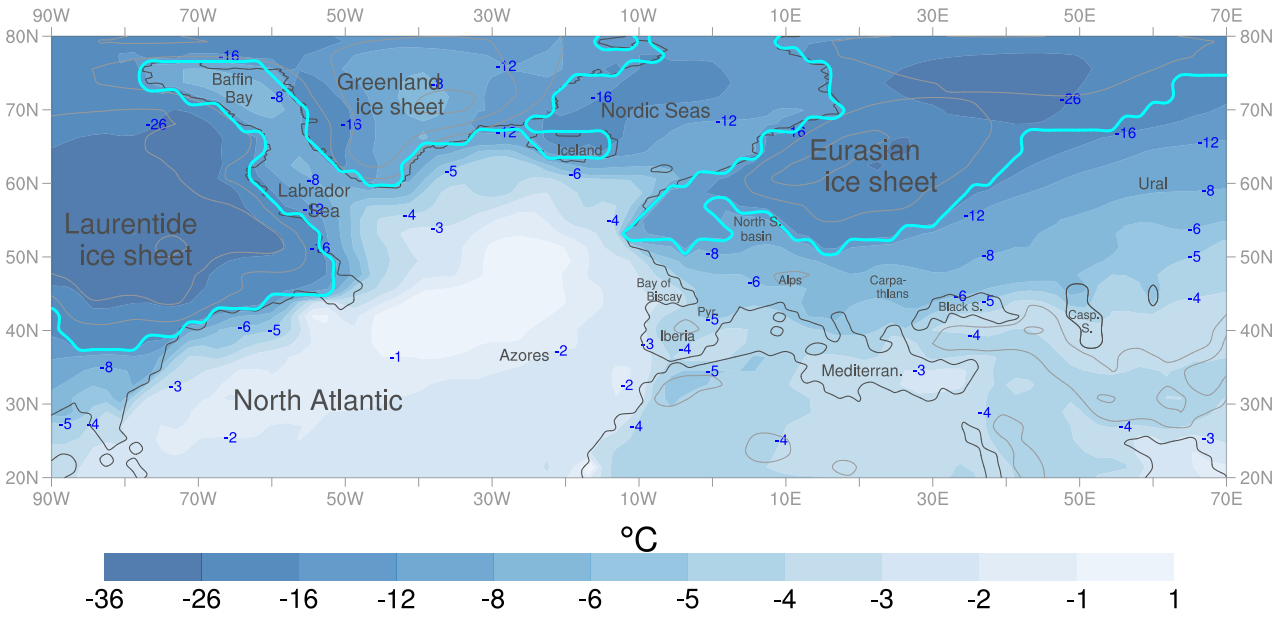

Figure 9: Near-surface air temperature differences (−36 to 0.6 °C) according to the simulated Last Glacial Maximum (MPI-LGM) minus the recent (Preindustrial, MPI-PI) climate. Contours as in Fig. 6.

Botanical reconstructions[68] validate the simulated temperature decreases for Eurasia. In particular, the 8 to more than 16 °C temperature decreases over western Russia agree with decreases between 8 and 17 °C reconstructed from botany[68]. Near 60 °N over Eurasia and at the eastern EIS margin, the 8 to 16 °C temperature decrease is supported by a pollen-reconstructed[67] decrease of 5 to more than 10 °C.

For Ukraine, a decrease between 6 and 12 °C was calculated. This is less than the 12 to 17 °C decrease that had been reconstructed[68] from botany. Nevertheless, it agrees with the 5 °C to more than 10 °C decrease, reconstructed by a different pollen study[67]. The temperature decrease during the LGM is supported only for southern Ukraine by a CCSM4-based[69] temperature decrease of 7.5 to 10 °C. Over northern Ukraine, the CCSM4 results in a larger, 10 to 12.5 °C temperature decrease[69].

For the southern Urals, 5 to 8 °C decreases resulted in agreement with the proxy-based reconstructed decreases[68] between 4 and 8 °C. East of the Urals (60–70°E), between 54°N and 68°N, the 5 to 12 °C temperature decrease corresponds to the 5 to 10 °C pollen-reconstructed[67] decrease. For the West Siberian Plain, along about 70°E, a 5 to 12 °C decrease resulted, supported by botany reconstructions[68] that had found a decrease of 4 to 12 °C.

For Georgia, a 3 to 5 °C decrease is found concordant with a botany-reconstructed 4 to 12 °C decrease[68]. Over Turkey, the 4 °C decrease conforms to the pollen-reconstructed[67] decrease of 2 to 5 °C. At steep, heterogeneous topographies, such as the Alps and Caucasus, the simulated temperature decrease is less than its pollen-reconstructed[67] value. There, pollen indicate a temperature decrease larger than 10 °C. The spatial resolution is likely too low to resolve the effects of such topographies well enough.

Over southern France, Italy, the Balkans, and northern Greece, the 5 to 6 °C and the bontany-reconstructed[67] 5 to 10 °C temperature decreases are in line. Over southern France, Italy, Greece and at the western Black Sea coast, the temperature decreases also conform quantitatively well with pollen-based reconstructed temperature decreases[66,70]. Additionally, a CCSM4 LGM simulation[69] supports these decreases. Over the coastal areas of Iberia, the 2 to 4 °C temperature decrease is slightly smaller than the pollen-reconstructed[67] 5 to 10 °C decrease. Likely, these areas were affected by an indicated MPI-LGM SST overestimation[37]. Over the Norwegian Sea including the bordering EIS margin, the 8 to 12 °C temperature decrease overlaps well with the pollen-reconstructed[67] (5 to 10 °C) decrease for this EIS margin.

Over the Atlantic between 20 and 35°N, the (up to) 3 °C temperature decrease is supported by the foraminifera and dinoflagellate cysts based GLAMAP SST reconstructions[203,206], and by the simulation-based[109] 2 to 4 °C decrease. Over the mid-latitude Atlantic (about 35–60°N), the temperature decrease of maximal 4 °C, with a major part only subjected to a maximum decrease of 2 °C, is smaller than their reconstructed[203,206] SST decrease of 4 to 14 °C during JJA and 2 to 12 °C during DJF. It is questionable, whether the temperature and SST are tightly coupled over the mid-latitude Atlantic. The strong cooling[206] of the Atlantic surface near the south-westernmost part of the EIS also differs from the MPI-based results presented here.

In summary, the distribution of LGM to present temperature differences is supported by most of the independent evidence.

Though beyond the scope of this dissertation, the understanding of the LGM temperature distribution corroborated by botanic proxies allows to extrapolate the fauna. Based on this, human LGM population density and dispersal concepts could be developed[6].

Precipitation The spatial distribution of the precipitation rates (shortening: precipitation), in particular their regional minima and maxima, is similar for the LGM and the PI (Fig. 10). During both, the EurAt Domain maxima occurred between Florida, Iceland, and the British Isles; a region that largely corresponds to the subpolar gyre. Precipitation maxima were found over the Gulf Stream, the North Atlantic Current, and off the east coast of the GIS tip.

During the LGM, the highest EurAt Domain precipitation occurred in the cloud lifting zone proglacial of the eastern GIS margin near the southern GIS tip (7–8 mm/d, Fig. 10a). This agrees with more than 7 mm/d based on another GCM simulation[110]. Near the bottom of the GIS topography gradient, high precipitation rates were likely due to the steep GIS barrier and the implied lifting of moist southerlies, southeasters, and easterlies, which likely released enhanced precipitation. At the American east coast, where the LIS margin separated from the coastline (Fig. 10a), 5–7 mm/d precipitation occurred in agreement with the CNRM results[110]. Also, major precipitation areas were in front of the south coast of Iceland (5–6 mm/d), at the southwestern-most extent of the 1000 m contour line of the EIS (4–5 mm/d), over Galicia and at the western onset of the Alps (both 3–4 mm/d). The latter three precipitation areas are supported by a regional LGM simulation[111]. For the Atlantic and Europe, a modeling study[207] supports the previously mentioned precipitation ranges, reporting 2–8 mm/d over the western Atlantic and central Europe.

Particularly low precipitation occurred inland over the high elevated ice sheet surfaces. This is expected as low to zero evaporation occurred from the ice sheets and the there prevailing air had lost its moisture during its previous topographical lift. In agreement with modeling studies[110,207], low precipitation was found over Baffin Bay and the Norwegian Sea, likely caused by sea ice (Fig. 8a) which inhibited or suppressed evaporation and moisture transfer to the atmosphere. Low to zero precipitation occurred east of the Caspian Sea, over Arabia and the Sahara-dominated part of northern Africa including the adjacent Atlantic up to 35°W. The shape of this low-to-zero region remains almost identical during the LGM and the present (Fig. 10).

During the recent climate (PI), the highest precipitation occurred off the American east coast over the Gulf Stream and the North Atlantic Current (6–8 mm/d, Fig. 10b), supported by more than 7 mm/d calculated by two (HadCM and CNRM) out of four other GCMs[110]. Though the MIROC and the IPSL-CM4 simulations resulted in lower precipitation[110] (5–6 mm/d and 4–5 mm/d), still, their highest EurAt Domain precipitation occurred over the Gulf Stream region, which shows the relative MPI-PI precipitation distribution consistency (Fig. 10b).

LGM to present comparison Compared to the PI, the LGM precipitation was up to 600 to 750 mm/yr (2 mm/d) lower over the center of the EIS (Fig. 11) in agreement with the simulation results[112]. Similarly, they decreased by up to 2 mm/d (150 to 450 mm/yr) over the North Sea Basin and northwestern Russia, and by up to 1 mm/d (150 to 300 mm/yr) over the unglaciated areas north of the Alps and European Plain. These findings are in line with HadRM[113] climate model results[208] for the whole domain.

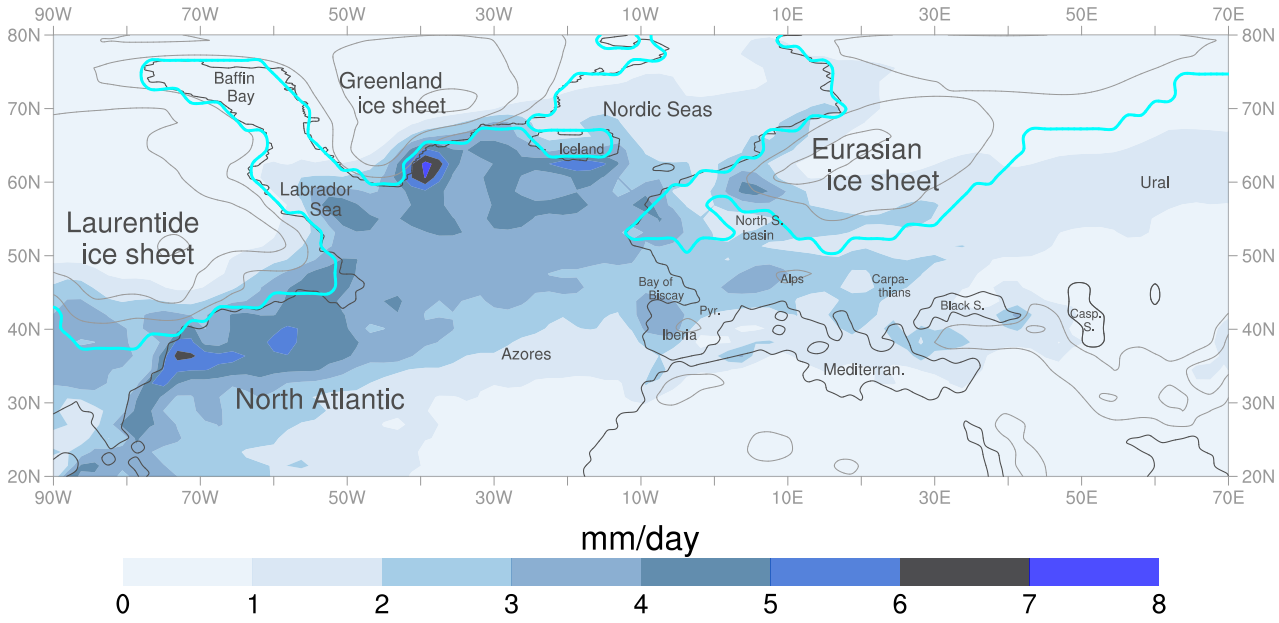

(a) Last Glacial Maximum

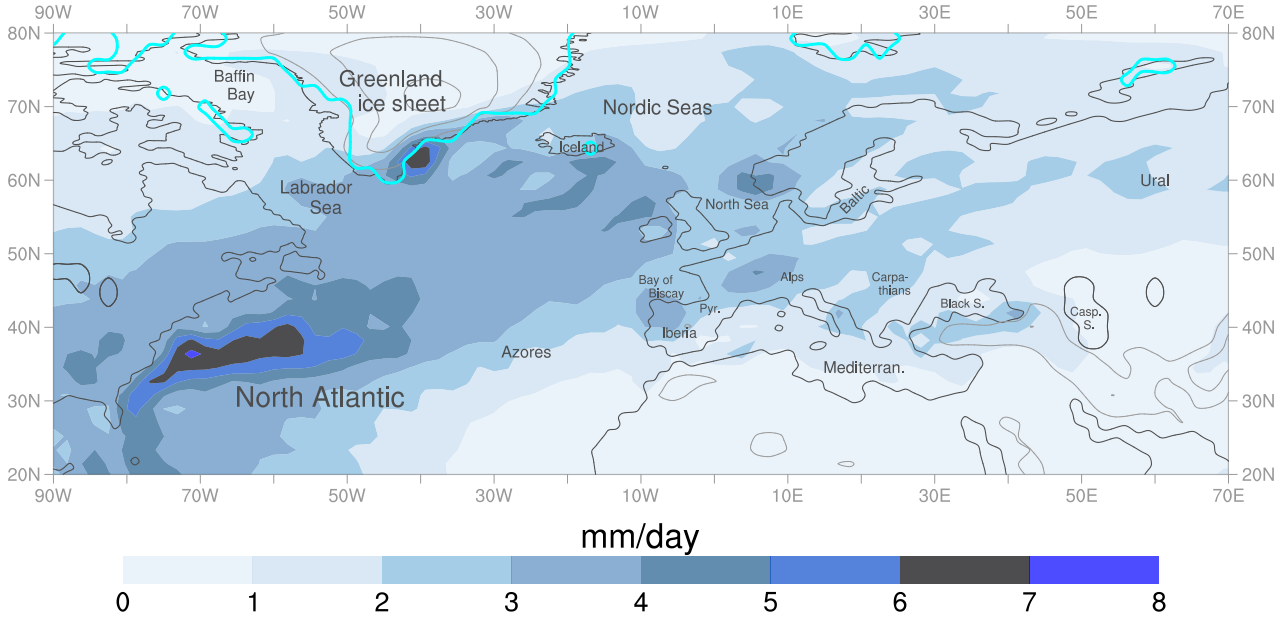

(b) Preindustrial

Figure 10: Precipitation rate climatologies based on simulations (MPI-LGM, -PI) Contours as in Fig. 6

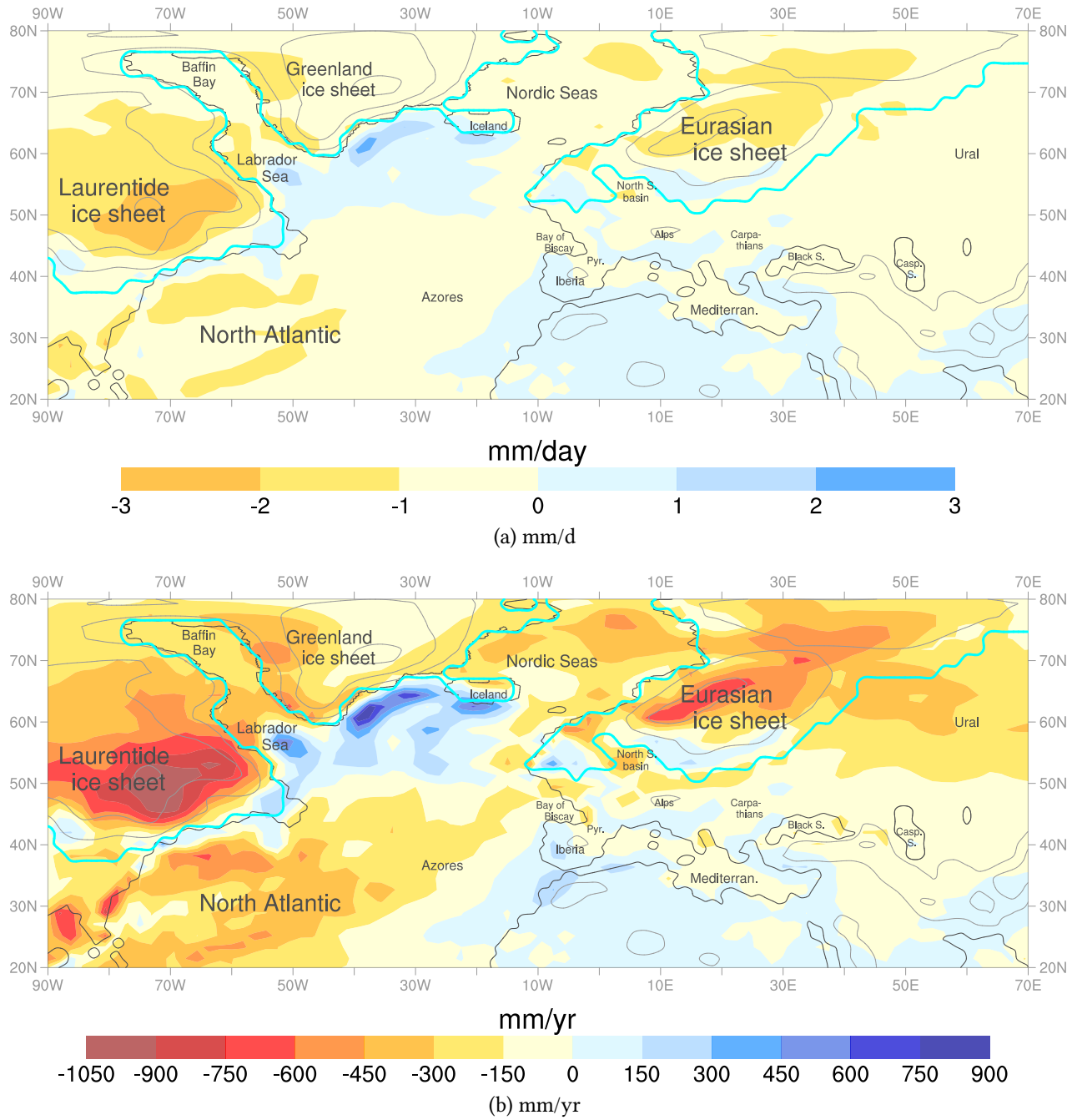

(a) mm/d

(b) mm/yr

Figure 11: Climatological precipitation differences, *Last Glacial Maximum* minus *Preindustrial*, (a) in mm/day (values ranging between −2.8 and 2.4), (b) in mm/year. Climatologies (Fig. 10) calculated from the MPI-LGM and -PI simulations. Contours as in Fig. 6.

The expected precipitation decrease is evident over the Nordic Seas and the ice sheets (Fig. 10). Over the most elevated ice sheet surfaces that were oriented towards the Atlantic, precipitation decreased by up to 3 mm/d. This, as well as the precipitation decreases over the eastern margin of the EIS and the subsequent continental regions of Eurasia conform to the IPSL model results[112].

The 150 to 300 mm/yr decrease over western Russia in the zone from about the EIS margin to 70°E and 50–60°N is partly coherent with the decrease of 200 to 500 mm/yr reconstructed from at least four botanical records[67,68]. During the LGM, the precipitation decrease near the southern and eastern EIS margin favored dry soil surfaces that in turn allow for mineral dust emissions. The condition of the soil surfaces is relevant, as strong, cold, and dry northeasters[68], which likely originated from the EIS, prevailed frequently over central and eastern Europe along the EIS margin (Tab. 11 in Sec. 7.4.1). Such a hypothesis of dry and strong easterlies generated by the EIS (compare Tab. 11 in Sec. 7.4.1) is also supported by botanical reconstructions[68].

The precipitation was lower by up to 1 mm/d over northern and eastern Iceland during the LGM, in accordance with an Icelandic thermo-mechanical[209] and a climate[112] model. The precipitation decreased by up to 150 mm/yr north of the Black Sea (Fig. 11b), affirmed by the 40 to 450 mm/yr decrease according to botany[68]. Between the Black and Caspian Seas, the botanically reconstructed[68] decrease (200 to 750 mm/yr) partly overlaps but is also much larger than the simulated decrease (0 to 300 mm/yr). Given the GCM resolution, the topographic gradients[208] of the Caucasus are likely not well enough represented. Hence, their effect on the simulated precipitation near and over the Caucasus is too small. The simulated decrease directly at the eastern margin of the Black Sea, between Black and Caspian Seas (both 150 to 300 mm/yr) conforms slightly better to the pollen-reconstructed[67] temperature decrease of 200 to 500 mm/yr.

An increase of up to 1 mm/d (300 mm/yr) occurs over southern and western Iberia, the Alboran Sea, Morocco, Algeria and southern Turkey in agreement with a 5 level scale (dry–wet) based on lake records[210] and the IPSL model results[112]. Six out of eight PMIP3-GCMs show[211] a similar LGM increase for Portugal, five of them also for Galicia, and four also for Morocco, the Alboran Sea and parts of Algeria. At the Western Alps, the up to 300 mm/yr precipitation decrease overlaps with the pollen-reconstructed[67] 200 to 500 mm/yr decrease. Over central Italy and the Zagros Mountains southwest of the Caspian Sea, the precipitation was up to 150 mm/yr lower. This decrease is affirmed by lake data[210], reporting higher aridity for central Italy and no change in the Zagros Mountains according to the Zrebar or Zarivar Lake. Over almost all of Greece, slightly higher precipitation (up to 150 mm/yr) occurred except for its southwest coast where the precipitation decreased by up to the same value. However, the reconstruction[210] based on one lake record indicates much wetter local LGM conditions.

The simulated precipitation decreased less in Galicia, the Pyrenees, northern Italy, Ukraine, Greece, and Turkey than according to pollen-based reconstructions[67]. In case the pollen-based reconstruction is correct, then the deviation likely occurs because of the locally unresolved[212] topographic gradients and their effect on the precipitation. Whether or not pollen reconstructed precipitation reasonably approximates the average precipitation during the LGM or rather the lower or upper precipitation thresholds is still an arguable question in the field of botanical climate proxy research.

4.5 Conclusions

Jet Stream The simulation results confirm the hypothesis on the from the present differing LGM jet stream paths. Instead of crossing the British Isles and southern Scandinavia, they ran along the Nordic Seas, between the EIS and the Alps, or over the western Mediterranean. The results confirm the hypothesis on the regionally faster (10 m/s) and narrower LGM jet stream. These LGM jet stream characteristic were most likely caused by the Northern Hemisphere ice sheet elevations.

Pressure The LGM NAO and in consequence most likely the westerlies were stronger. This was confirmed by the simulations that resulted in a larger LGM region affected by the Azores High. Additionally to the present Azores and GIS High, the LIS and the EIS High shaped the LGM climate. Both highs likely caused combined with the ice sheet topographies proglacial northeasters and easterlies. In contrast to the present, low pressure systems prevailed over the subpolar gyre between Newfoundland and Iceland.

Temperature The average LGM temperatures ranged between −45 and 30 °C in the domain, compared with between −35 and 30 °C during the PI. Sea ice likely prevailed in Baffin Bay, on the Labrador, and the Nordic Seas. Permafrost characterized the unglaciated land east of the EIS. Northward heat transport from the low latitudes to the Norwegian Sea by the North Atlantic Current was likely. The GCM results indicate slightly more warmth than the GLAMAP reconstruction over areas, where heat was transported northward in the oceans. Near the Mauritian coast, the temperature ranges simulated by the GCM (between 15 and 20 °C) and reconstructed from sediment cores (between 14 and 18 °C) agree well. The simulated temperatures are confirmed by Mg/Ca SST reconstructions, foraminifers, and alkenone data for different locations in and near Europe.

Apart from over the ice sheets, the strongest temperature decrease occurred over the Eurasian plains northeast of the Alps (between 8 and 26 °C). In the Mediterranean area, temperatures were between 2 and 6 °C lower and their differences were spatially heterogeneously distributed. For the unglaciated parts of central and eastern Europe, such as western Russia, Ukraine, the Urals, Georgia, and Turkey, botanic (pollen) temperature reconstructions validate the simulation-based results. Also, simulated temperature reductions in southern France, Italy, and Greece were confirmed by proxy data. For Iberia, the simulated temperature decrease is lower than the pollen-indicated. This possibly indicates too warm SST in the eastern North Atlantic.

Precipitation The LGM to present climate precipitation similarity indicates a low sensitivity of precipitation to the glacial conditions. Known present precipitation interaction with other Earth system components, such as precipitation generated during topographic lifting, also shaped the LGM precipitation distribution. This applies particularly to the LGM ice sheet margins; for example, off the east coast of the GIS tip, some of the highest EurAt Domain precipitation rates occurred. Vast LGM sea ice covers hindered and suppressed atmospheric moisture uptake; thereby reducing the fresh water transport to subpolar regions, such as Baffin Bay. Less precipitation over the proglacial central European areas and the North Sea Basin favored their aeolian erosion. This applied also to the unglaciated Eurasian plains east of the EIS, north of 55°N. The agreement between simulation- and botany-based precipitation reconstructions evidences the quality of the simulation-based LGM reconstruction.

5 Atmospheric Variability beyond Climatologies

5.1 Introduction

To reveal the hidden dynamics and to recognize the patterns and interaction of the atmosphere, it is necessary to analyze the atmosphere using appropriate, objective, and reproducible methods. To this aim, the spatiotemporal distributions of the sea level pressure, the near-surface temperatures, and the precipitation rates have been analyzed for the recent climate for distinct regions using combined empirical orthogonal functions[126,199,213] (CEOFs). CEOFs are also known as combined principal components[126], as joint, as mixed-field, or as extended empirical orthogonal functions. The CEOF analysis extends the empirical orthogonal function (EOF) analysis by combining distinct variables into a single numerical array.

EOFs, also known as eigenvectors or as principal components, result from the linear transformation of multidimensional data from one to another reference system. This transformation aims at finding a different set of algebraic basis vectors under the constraint that each vector represents the maximum possible variance that is not yet represented by any of the precedent basis vectors. In some cases, the first few resulting basis vectors are sufficient to represent most of the source data variability. For large multidimensional meteorological fields, the EOF analysis can reveal meteorological patterns that would otherwise remain invisible. As the EOF decomposition is a purely mathematical tool, any physical meaning of the resulting EOFs is not guaranteed per se. The requirement of mutually independent EOFs and maximal variability represented by all subsequent EOF imposes a non-physical restriction on the possible EOF outcomes[214].

EOFs have been applied to research numerous meteorological and geoscientifical questions. Their application[215–218] to the recent and present-day spatiotemporal distributions of the North Atlantic surface pressure revealed the NAO (North Atlantic Oscillation) as the most significant modern climatological pressure pattern over the North Atlantic. They have also been applied to the sea surface temperature (SST) distribution of the Pacific[219], which contributed to reveal the PDO (Pacific Decadal Oscillation), and the ENSO (El Niño Southern Oscillation)[220].

The study of the peer-reviewed publications that rely on statistics and multidimensional climate data to analyze the atmospheric dynamics revealed that CEOF results for the EurAt Domain are missing for the LGM. To bridge this gap, the subclimatological dynamics of the LGM and of the recent climate are analyzed and compared in this dissertation by calculating their CEOFs. The CEOFs offer the potential to reveal subclimatological patterns and dynamic relationships between the distinct variables for the LGM and for the recent climate that would otherwise be ignored and remain unknown. The results reveal potential cause-effect mechanisms, dependencies, and feedback between the pressure, temperature, and precipitation dynamics.

Independent climate models[208], reconstructions for the recent climate based on measurements[199], and LGM climate proxies[66] serve to evaluate the obtained CEOF patterns.

5.2 Hypotheses

(1) The cumulative explained variance of the leading CEOFs for the LGM is larger than that for the PI raising the question whether the atmospheric dynamics of the LGM were characterized by fewer degrees of freedom.

For the Last Glacial Maximum:

(2) Frequent NAO minus phases potentially caused above average temperatures over the Labrador Sea and the subpolar gyre as well as above average precipitation over Iberia, the northern Mediterranean, the Azores, the Labrador Sea, and the southwestern GIS. Simultaneously, temperatures and precipitation were below average over the EIS coast.

(3) Frequent subclimatological pressure variability created anti-phased pressure dynamics over the EIS with regard to Baffin Bay, the Labrador Sea, and the Sahara that likely correlated with above average temperatures and precipitation over the eastern GIS and its adjacent areas. Synchronously, below average precipitation likely prevailed over Europe and below average temperatures prevailed over western Asia and the northern Mediterranean.

(4) Frequent anti-phased pressure variability dynamics distinguished France, Spain, and Bermuda from the Caspian Sea and the low latitude eastern Atlantic; likely correlating with above average temperatures over western Iberia and precipitation over the Azores, the subpolar gyre, western Iceland, the EIS coast, the Black Sea, Turkey, and the southernmost Mediterranean. Simultaneously, below average temperatures prevailed over central eastern Europe, the Mediterranean, Tunisia, Libya, and the Hoggar Mountains while below average precipitation prevailed over France, western Iberia, Italy, the Bay of Biscay, the southeastern EIS, and the Maghreb coasts.

(5) Compared to the PI, the subclimatological LGM variability was larger over Baffin Bay, Iceland, southwestern Scandinavia, eastern Germany, and most parts of the Mediterranean. It was similar over central Asia, the Middle East, and northern Africa including the bordering Atlantic. It was smaller over Scotland, the Urals, and southeastern Finland.

5.3 Methods — Combined Empirical Orthogonal Functions

The CEOF analysis encompasses *sea level pressure* (pressure), *near-surface air temperature* (temperature), and *precipitation rate* (precipitation) fields extracted from the MPI-LGM and MPI-PI to analyze the spatiotemporal relation between pressure, winds, temperature, and precipitation. Details on these simulations are provided in Sec. 3.1 (p. 23). The simulation-to-reanalyses comparison based on their respective CWT distribution showed that the MPI-ESM-P simulated the recent European climate more realistically than the other GCMs (Sec. 6.4, p. 74).

Different test domain sizes and time slices were extracted from the complete MPI-LGM and MPI-PI to test the applicability, robustness, and limitations of the CEOF method. They also served to select an appropriate subset of the input data for the main analysis. Taking into account the test results, the CEOFs were implemented by extending the available standard routines[221,222] for numerical EOF decomposition. For the main analysis, the last 30 years of the daily-resolved pressure, temperature, and precipitation fields of the EurAt Domain were extracted from the MPI-LGM and MPI-PI. The daily-resolved pressure, temperature, and precipitation climatologies that base on the same 30 years were subtracted from each record to obtain the subclimatological per-day anomalies. These anomalies were weighted by latitude according to their respective location in the EurAt Domain. The resulting weighted subclimatological anomalies were decomposed into CEOFs.

After re-separating the decomposed combination into pressure, temperature, and precipitation anomalies, the obtained (separate) fields were analyzed to find their dominant subclimatological variability. To this aim, a tendency score that can be either negative, undefined or positive, was calculated. It summarizes the expansion coefficient variability per expansion coefficient series by regarding their major positive and negative amplitudes (e.g. Fig. 13a and 13b). The amplitude selection criteria was defined relatively to the maximum absolute amplitude of the respective expansion coefficient series, i.e. only amplitudes were summed whose absolute value was larger than 0.2 times the respective maximum absolute amplitude of the whole series. For the subsequent interpretation of the obtained eigenvectors, only the resulting sign of each tendency score is considered. A positive sign indicates that the corresponding eigenvector dominates during most of its major contributions as indicated by the colored contour plot. A negative tendency score implies that the signs of all values of the respective eigenvector have to be multiplied by −1 to generate the dominant variability pattern for this eigenvector. Separate plots of these additive inversion are not shown, nevertheless this inversion has been taken into account during all subsequent parts of this dissertation. The resulting LGM eigenvectors were analyzed and compared to those of the PI as well as to MPI-ESM-P-independent climate proxies.

5.4 Results and Discussion

The first LGM CEOF encompasses 7.2% of the total variability, the second 5.8%, and the third 3.5% (Fig. 12a, 14a, and 16a). While the first PI CEOF represents the same variability as its LGM analogue, the second (4.3%) and third (3.2%) PI CEOFs represent less of the total PI variability compared to their LGM analogues (Fig. 12b, 14b, and 16b). This raises the question of whether the total LGM variability can be represented by fewer CEOFs than the total PI variability. Also the cumulative explained variances by the first 40 or 60 CEOFs are larger for the LGM than for the recent climate (Tab. 2) — a finding that points in the same direction. Analyzing the obtained eigenvalues using North's rule of thumb[223], the first three LGM and the first three PI CEOFs as well as more than 90% of the first 40 and the first 60 CEOFs result to be mutually significantly different.

Table 2: Cumulative explained variances (%) taking into account the first (#) combined empirical orthogonal functions for the LGM and the recent climate (PI).

	Cumulat. variance (%)	
#	LGM	Recent/PI
3	16.5	14.7
40	57.3	54.2
60	63.9	60.9

North Atlantic Oscillation variability The north-to-south-oriented sea level pressure (short: *pressure*) anomaly dipole of the first LGM CEOF indicates a varying NAO strength during the LGM (Fig. 12a, top panel). The southern dipole center is located over the Azores with an in-phase variability extending eastwards up to the Carpathians. The northern center prevails over Greenland, Iceland, and the Nordic Seas with the equal-phased variability reaching from the eastern margin of the LIS to the western margin of the EIS (Fig. 12a, top panel). Thus, the EIS center separates the synchronous zones of negative and the positive pressure anomalies. The location of this separation was likely determined by the highest topography, which existed over Scandinavia due to the EIS. Most frequently during pronounced contributions of this eigenvector (Fig. 12a and 13a, top panels), the pressure increased over Baffin Bay, the GIS, and the Nordic Seas. Synchronously, it decreased at its southern center of variability, i.e. over the Azores, the Mediterranean, and southern Europe. Regarding the averaged LGM pressure (Fig. 6a), these pronounced contributions weakened the NAO gradient, i.e. the pressure distribution was shifted towards its NAO minus state.

The variability of *the temperature of the near-surface air* (short: *the temperature*) that is represented by the first LGM CEOF consists of a west-east oriented dipole. Its western pole is centered over the Labrador Sea; its eastern along the EIS coast (Fig. 14a and 15a, top panels). Most frequently during major contributions of this eigenvector, the temperatures increased over the Labrador Sea and synchronously decreased over the western EIS. For the Labrador and the Nordic Seas, this variability was possibly related to oscillating sea ice changes. Thus, during major contributions of the first CEOF, the Labrador Sea ice cover was probably smaller (if at all present), while the sea ice on the Nordic Seas was larger. Possible drivers were changes in the atmospheric and/or in the Atlantic circulation. In particular, the spatiotemporal deflection of the drifting warm North Atlantic Current could have been relevant. Very likely, heat advection disfavored or even prohibited large sea ice covers. In addition, cold northerlies, originating from the ice-covered Arctic, might have reached the coastal EIS margin during such phases. As an effect, the ice cover probably closed possible gaps on the Nordic Seas and expanded to lower latitudes.

Also, Arctic air might have reached the southwestern tip of the EIS. Consequently, this icy air advection could have enforced the southwestern tip of the EIS, which was surrounded by climatologically warmer environments (Fig. 8a), such as the North Atlantic Current and the proglacial Channel. Beyond, the increase of the LGM jet stream over the subpolar gyre and the Nordic Seas is supporting this effect (Fig. 4, left panel). This might explain the frequent cooling along the coastal EIS margin.

The *precipitation rate* (short: *precipitation*) variability of the first LGM CEOF is characterized by a fragmented spatial distribution of enhanced and reduced precipitation anomalies. The recognizable dipole structure in the pressure or temperature does not appear in the precipitation anomalies. The largest in-phase precipitation variability occurred over or near the coastal EIS margin and Nordic Seas. Synchronously, two major and one minor opposite-phased varying precipitation areas existed: one was located over the Labrador coastline and extending via the southern GIS tip over the whole western GIS; the other major was centered over the Azores and extended to Iberia. Precipitation extended also from northern Corsica via the Carpathians to the southeastern EIS margin.

During major contributions of this first precipitation eigenvector, precipitation over the Nordic Seas was lower than its average climatological value (Fig. 10a). Synchronously, the precipitation was higher over the three opposite-phased regions. Possibly, this can be related to an atmospheric tendency towards a NAO minus state. Likely, prevailing northerlies and/or sea ice cover could explain this precipitation reduction over the Nordic Seas and the coastal EIS margin. The presence of sea ice suppresses the atmospheric moisture supplies, i.e. the evaporation of water from the sea surface.

The synchronous precipitation increase over the Azores could be related to the southward shifted track of the westerlies[66] consistent to the NAO minus tendency. The synchronous precipitation increase over and along the Labrador coastline was likely related to a high pressure system over the GIS that supported easterlies and southeasters over the Labrador Sea. Also, the possible Atlantic meridional overturning circulation distributary into the Labrador Sea might have prevented an extensive sea ice cover thereby allowing the uptake of moisture by surface winds that crossed the Labrador Sea to head towards the LIS.

Reconstructed glacier equilibrium line altitudes[66] in the Mediterranean based on ^{10}Be exposition dating and also biological climate proxies[66] support considerable precipitation over northern Corsica, the Gulf of Genoa and the Apennines, which are found in both, the first LGM CEOF (Fig. 16a, top panel) and the LGM precipitation climatology anomalies (Fig. 11). The HadRM results[208] also support the precipitation increase over the French Mediterranean coast, northern Italy, the west coast of the Black Sea, while a common precipitation decrease is found over the unglaciated regions north and east of the Alps.

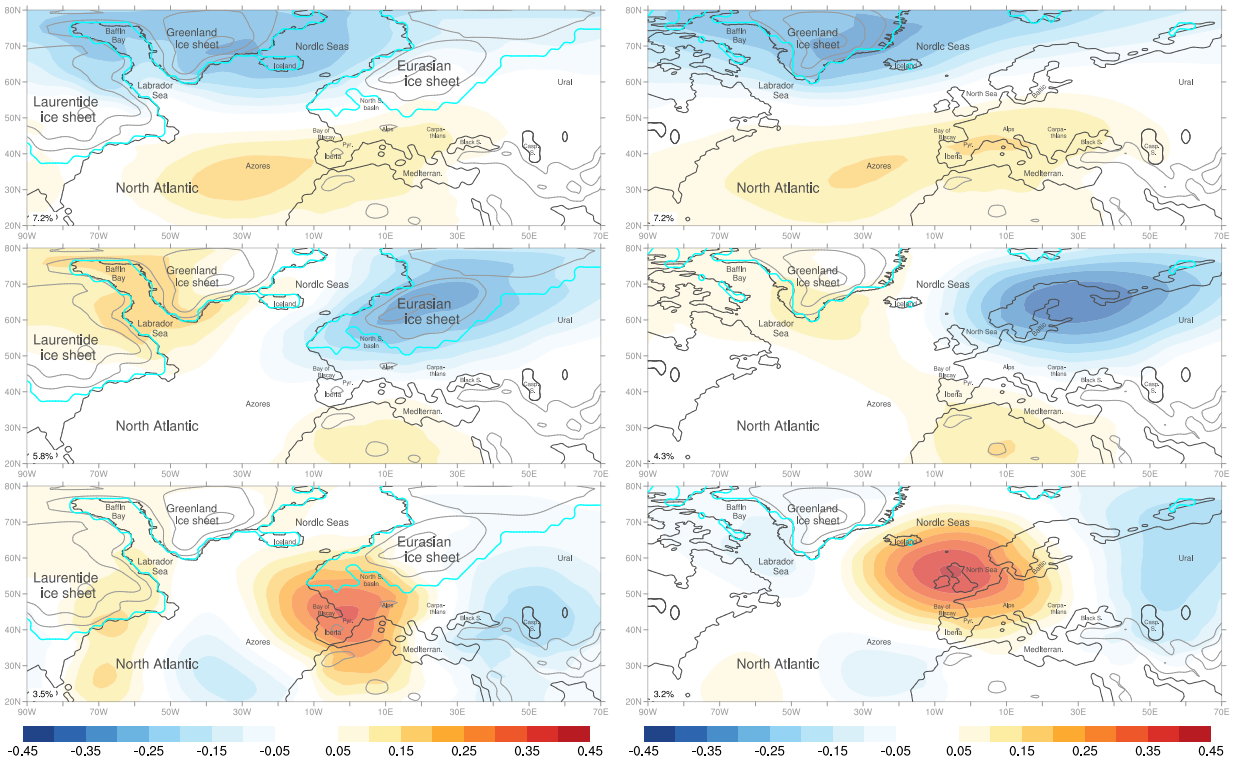

(a) Last Glacial Maximum (b) Preindustrial

Figure 12: First three sea level pressure anomaly eigenvectors. They resulted from the combined empirical orthogonal functions analysis of the sea level pressure, the near-surface air temperature values, and the precipitation rates that were extracted from the MPI-ESM-P simulation for (a) the Last Glacial Maximum and (b) the Preindustrial. The variability that they represent is stated at the bottom left of each panel. Contours as in Fig. 6

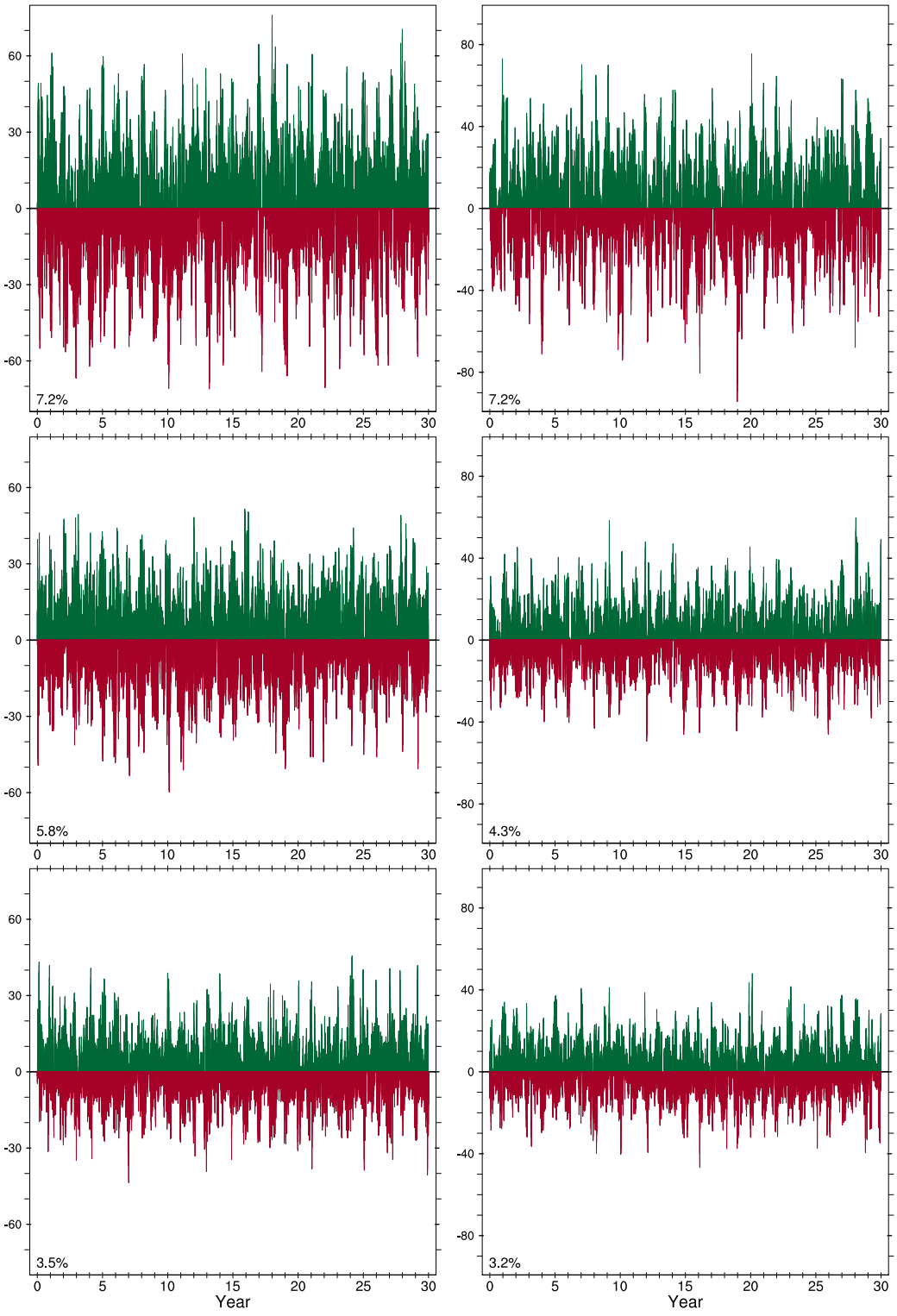

(a) Last Glacial Maximum (b) Preindustrial

Figure 13: Expansion coefficients for the sea level pressure anomaly eigenvectors (Fig. 12)

The first PI CEOF explains the same variability fraction (7.2%) as its LGM analogue and also its pressure and temperature eigenvectors are similar to their LGM analogues (Fig. 12 and 14, top panels). Its temperature pole over northern Europe (Fig. 14b, top panel) is similar to one of the maxima found in the probability density function of a principal components decomposition of a station-based reconstruction for 1766–2000 for Europe[199]. The amplitude of the precipitation variability in the first PI CEOF is only about half that of the LGM (Fig. 16 and 17, top panels). The only notable PI precipitation variability synchronizes the western part of the Nordic Seas and Iceland with the Norwegian west coast (Fig. 16b, top panel).

Second CEOF: EIS High and ice-related pressure variability The second LGM CEOF represents 5.8% of the total LGM variability. Its pressure eigenvector contains three regions of variability (Fig. 12a, center panel). The strongest in-phase pressure variability is located over the higher elevated EIS surfaces. The opposite-phased variability is split: higher variability is found over Baffin Bay, the Davis Strait, Labrador Sea, and adjacent topographical GIS and LIS gradients, while lower variability is observed over the Sahara.

Generally, pronounced contributions of this mode occurred during winter (Fig. 13a, center panel). During most of them, the EIS High, which was centered as a characteristic feature over the Scandinavian ice sheet (the major and center part of the EIS) enhanced itself in all directions. Thereby, it covered and extended beyond the EIS, likely merging into the Azores High.

The extended EIS High favored strong and dry northeasters and easterlies (Tab. 11) that ran about parallel to the EIS margin over the unglaciated areas in eastern and central Europe (Sec. 7.4). They likely resulted from katabatic winds descending from the EIS. Synchronously with the EIS High enhancement, the pressure decreased over Baffin Bay, the Labrador Sea, and the adjacent LIS and GIS surfaces, which implied the westward displacement of the Icelandic Low towards the Labrador Sea.

The synchronous Saharan pressure decrease that was most pronounced around the Hoggar Mountains possibly resulted in a low pressure system over the zone that is limited in the north by about the northern margin of the Hoggar Mountains. Climatologically, this zone is already characterized by low pressure (Fig. 6a). The Saharan pressure decrease is consistent with the simulated increase of the cyclonic 10m-wind flow over the northwestern Sahara and the adjacent Mediterranean[112].

During most of the pronounced phases of the second CEOF temperature eigenvector, the near-surface air became warmer over the eastern GIS, Iceland, and along the Nordic Seas up to the Arctic (Fig. 14a and 15a, top panels). This coincided well with the extended EIS High and the Labrador Sea Low (i.e. the westward displaced Icelandic Low). At the western flank of the EIS High and the eastern flank of the Labrador Sea Low, warm air from the mid-latitudes was entrained northwards causing this warm pool over the Nordic Seas.

Synchronously, the air over Europe and northwestern Asia cooled. The strongest cooling occurred over Germany and Poland, while major cooling extended from the Alboran Sea via the Balearics, the Gulf of Lion, the North Sea Basin, the Alps, and the Carpathians to about today's location of Moscow. Frequent cold air incursions, advected from the EIS and Arctic, can explain these prevailing cold anomalies; in particular over the northwestern Mediterranean, where in situ proxies provide additional evidence[66,224].

During most of the pronounced phases of the second CEOF precipitation variability, the precipitation mainly increased along the east coast of the GIS including Iceland and the western parts of the EIS north of 70°N, as well as the western Mediterranean Sea (Fig. 16a and 17a, center panels). This conforms well with the prevailing low pressure system over the Labrador Sea, which transports moist air northwards from the western North Atlantic to the shore of the GIS. There, the lifting of moist air over the steep topographic GIS gradient led to precipitation. The moisture originated off the Newfoundland shore coinciding with a warm sea surface, which was probably caused by the North Atlantic Current. Jointly with the precipitation, this could explain the positive temperature anomalies (the warmth) that occurred between the GIS and the east coast of Iceland (Fig. 14a and 15a).

Over the Mediterranean Sea, increased precipitation anomalies likely resulted from the prevailing low pressure system over northern Africa (Fig. 12a). On the eastern and northeastern flank of this system, warm winds (southerlies and southeasters) prevailed over the Red Sea and the eastern Mediterranean Sea, where they presumably became moister.

Synchronously, the strongest precipitation decrease, likely indicating a drier atmosphere, was centered over the North German Plain and major decreases extended from the Pyrenees up to the southern edge of the 2000 m EIS contour. Favored by the EIS High, prevailing dry easterlies can explain this (Tab. 11). They were shaped by dry continental land surfaces of northwestern Asia and (north)eastern Europe. Their effect appeared particularly over western and central Europe as this region was alternately affected by both, the dry east sector winds and the moist Atlantic (south)westerlies. Prevailing negative temperature anomalies over Europe and northwestern Asia including the southern EIS (Fig. 14a) corroborate the inference of a drier, icy, and easterly-shaped LGM atmosphere during the most pronounced variability phases of the second CEOF.

Second PI CEOF The second PI CEOF represents 4.3% of the total PI variability (Fig. 12b, center panel), which is less than that of its LGM analogue (5.8%). This tendency applies also to the third PI CEOF with 3.2% vs. its LGM analogue (3.5%).

According to the second PI CEOF, pressure that was most frequently below its climatological average occurred synchronously over northern Sweden, Finland, and northwestern Russia (Fig. 12b, center panel). This area of negative pressure anomalies is shifted north-eastwards compared with the position of the largest pressure anomalies of the second LGM CEOF (Fig. 12a, center panel). Its total area extends from the Faroe Islands to the Urals including northern Ukraine (Fig. 12b, center panel). In contrast to the second LGM CEOF pressure anomalies, in phase anomalies with Scandinavia hardly occurred over Ireland, France, Belgium, the Bay of Biscay, and the Western Alps (Fig. 12a and 12b, center panels).

Modest positive pressure anomalies occurred over northern Africa with the highest variability over the Hoggar Mountains and over southern Greenland (Fig. 12b, center panel). Compared the second LGM CEOF (Fig. 12a, center panel), they are smaller over Baffin Bay and the western Labrador Sea; likely due to the absent LIS.

When the second CEOF pressure eigenvector for the PI contributed distinctly, most frequently, the Icelandic Low weakened, particular at its west (Fig. 6b). Simultaneously, new pressure centers formed corresponding to an eastward enlargement of the NAO: low pressure over northern Eurasia and high pressure over the Sahara.

The second PI CEOF temperature variability is similar to its LGM analogue, except for two aspects occurring during periods of pronounced contributions by the second temperature eigenvector (Fig. 14, center panel): The displacement of the negative anomalies from central Europe to the Urals and the lesser cooling *(warming)* over Labrador *(the central GIS)*.

During pronounced contributions of the second PI CEOF precipitation eigenvector, above average precipitation occured at the southeastern GIS margin (Fig. 16b, center panel), whose climatology is already dominated by high precipitation (6–7 mm/d, Fig. 10b). The precipitation is likely caused by the reduced moisture capacity of the air masses, which is controlled mostly by the topographic gradient across the GIS margin. Slightly increasing precipitation is also found over the c-shaped zone, that runs from Svalbard along the eastern GIS margin, then crosses the Atlantic to end over the western Mediterranean Sea.

Synchronously, precipitation decreases over the Benelux, western Germany, the Norwegian west coast, and from the Baltic Sea to the West Siberian Plain (Fig. 16b, center panel). This decrease might be explained by drier than average air masses — possibly of continental origin. In general, the amplitude of this mode is lower compared to its LGM analogue (Fig. 17b, center panel). During the PI, these centers formed a joined zone of synchronous variance.

Third LGM CEOF: Franco-Iberian variability affecting central Europe The third LGM CEOF consisted of four synchronous pressure variances: the Franco-Iberian was the strongest, the Caspian (50°E), the Bermudan (70°W), and the east Atlantic (35°W) were subordinated (Fig. 12a, bottom panel). Among these four variances, any two direct neighbores in latitude-parallel direction (at about 30°N) modified their respective climatological pressure in opposite directions. The Franco-Iberian, the Bermudan, and the Caspian extended from 20–60°N whereas the east Atlantic variance extended only from 20–40°N.

During most of the pronounced contributions of this pressure eigenvector, the Franco-Iberian variance indicated distinctly above climatological pressure. It extended from the west of the Bay of Biscay to the Carpathians and from the Hoggar Mountains to the EIS, where it possibly merged into the EIS High. This implied a negative or absent NAO with regard to the present-day NAO pattern. It also hindered the propagation of the westerlies over France and Germany. Instead, these phases likely favored southwesters over the eastern mid-latitude Atlantic that continued over and along the Nordic Seas towards the Arctic.

Coincidentally, the Bermudan variance indicates above climatological pressure over the west Atlantic up to the LIS. These Bermuda Anomalies probably moved warm and moist air from the Gulf of Mexico to the southern LIS margin while favoring northerlies from the Labrador Sea via Newfoundland to the subtropical Atlantic. However, the amplitude of the east Atlantic Anomalies was only about half as large as that of the Franco-Iberian. Simultaneously, the Caspian variance indicates below climatological pressure from the Black via the Caspian to the Aral Sea, including Turkey, Iran, the Middle East, major parts of Arabia, and western Russia. At the same time, the east Atlantic variance indicates a weakened Azores High.

Pressure eigenvector expansion coefficients of negative sign and large absolute values were more seldom. When they occurred, below climatological pressure characterized southwestern and western Europe up to western Poland (20°E). It favored the propagation of the westerlies over France. This is inline with one—i.e. the central European—of the two southwards shifted paths of the LGM jet stream that the climatological LGM jet stream analysis indicated (Sec. 4.4). It is also consistent with the southwards shifted LGM storm tracks. It also indicates a weakened southwestern part of the EIS High and northeastern part of the Azores High. It favored warm and moist southerlies propagating from the central Mediterranean Sea towards the EIS margin.

The positive Franco-Iberian and the negative Caspian pressure anomalies occurred most likely combined with below climatological temperatures over central-eastern Europe, the Carpathians, the Dinarides, the Balkans, the central Mediterranean, Tunisia, Libya, and the Hoggar Mountains (Fig. 14a, bottom panel). They were likely caused by frequent icy northerlies, northeasters, and cold air outbreaks that originated from the EIS margin and extended from there beyond Libya and Tunisia (Fig. 14a bottom panel). For Italy and the Dinarides, the reconstructed LGM glacier equilibrium line altitudes[66] support these frequent southward advances of polar air ‚masses.

The synchronously existing cold air masses south of Newfoundland likely resulted from polar northerlies flowing along the Labrador Sea and the LIS margin. Synchronously, the air over the African and European Atlantic coast (up to 70°N) warmed with the largest warming occurring over the Atlantic near the south-westernmost EIS margin. Also, the air over Portugal and Galicia warmed more than over the remaining coastal regions. During pronounced periods of the first and second LGM CEOFs, temperature anomalies over these coastal regions of the Atlantic were likely affected by colder zonal winds. However, during most of the pronounced temperature eigenvector contributions of the third CEOF, warmer southerlies and southwesters likely dominated over the same regions due to the positive Franco-Iberian Anomalies. The Bermuda High-related warm southerlies could explain the warming at about 75–90°W and 20–50°N, extending from the Gulf of Mexico northwards beyond the 2000 m LIS isohypse.

Most frequently, the pronounced anomalies of the third CEOF precipitation eigenvector indicate distinctly below climatological precipitation over the Iberian Atlantic coast; most likely due to the positive Franco-Iberian anomalies that impeded the passage of moisture-advecting westerlies. Below climatological precipitation occurred also over a meridionally shaped region between 55–70°W that includes parts of the low to mid-latitude Atlantic and the eastern LIS margin up to the southern coast of Baffin Bay. This decrease was likely related to the LIS and the Bermuda High, which favored (along their eastern flank) dry and cold northerlies originating from the Arctic and the northernmost LIS. The coldness over the LIS and the Labrador Sea as well as the probably prevailing sea ice on the Labrador Sea hindered the moistening of the near-surface air, which then became part of the northerlies. Subsequently, these northerlies blew along the rather dry and cold LIS margin. Thus, they consisted of very dry southward moving air masses with little or no potential for precipitation over the North Atlantic.

Above climatological precipitation occurred adjacently around the positive Franco-Iberian pressure anomalies and over northern Turkey due to the orographic lifting of north sector winds that released the moisture they had previously aquired over the Black Sea (Fig. 12a and 16a). Warm Saharan southeasters incorporated moist air masses while passing over the Atlantic between the positive Franco-Iberian Anomalies and the negative east Atlantic Anomalies. As they reached higher latitudes, their temperature and thus moisture capacity decreased continuously leading to moisture release through precipitation. This explains the c-shaped area of above climatological precipitation from the Azores via Iceland to the EIS coast (Fig. 16b bottom panel). The positive precipitation anomalies over southwestern Iceland likely resulted from topographic lifting of southwesters that probably issued from the southeasters. Northeast of Iceland, the main winds turned into westerlies. As they reached and lifted over the steep Norwegian EIS coast, they released most of their moisture as precipitation .

Synchronously, below climatological precipitation occurred over the topographic gradient of the inland-, lee- or Asia-facing EIS margin where dry and cold fall winds prevailed. This decrease is in line with the anticyclonic circulation around the common pressure zone of the EIS High and the positive Franco-Iberian Anomalies. Subsequently, these winds likely eroded the proglacial Eurasian soils by entraining mineral dust — in particular from bare soil areas (Sec. 7.4). Meanwhile, they turned into northerlies and northeasters that overflowed eastern and central Europe.

Third PI CEOF Above climatological pressure prevailed over the British Isles during most of the major contributions of the pressure eigenvector of the third PI CEOF (Fig. 12b, bottom panel). This likely hindered or blocked the westerlies from running over the British Isles. It favored NAO minus phases as the pressure anomalies increased the climatological pressure of the eastern part of the Icelandic Low. Coincidently, below climatological pressure prevailed over the Urals, the Labrador Sea, and the east Atlantic at ~30°N. Compared to the climatological position of the Icelandic Low, this implied the westward shift of the low to the Labrador Sea (Labrador Low). The Labrador Low, i.e. the former Icelandic Low, favored westerlies that gradually turned into southerlies, then southeasters, and easterlies while they blew along the eastern and northern margin of the Labrador Low towards the coast of Greenland. Alternatively, former westerlies turned into southerlies, then southwesterlies, and westerlies over the Nordic Seas, while they blew along the margin of the positive British Anomalies towards the Arctic and northernmost Europe.

Simultaneously, below climatological pressure occurred over the Urals and their surrounds likely causing northerlies over Finland, the East European Plain, and the Black Sea. Over the Carpathians, northeasters were favored by the combined effect of these negative Urals Anomalies and the positive British Anomalies. Compared with the third LGM CEOF pressure eigenvector, the anomalies are shifted northwards; likely due to the lower PI topography.

The temperature eigenvector of the third PI CEOF indicates two major areas of variance (Fig. 14b and 15b, bottom panels). Most frequently, below climatological temperatures occurred over central to eastern Europe and the western Mediterranean. These cold anomalies result most likely from the prevailing northerlies and northeasters during the positive British and the synchronously negative Urals Anomaly phases. During these phases, the north sector winds advected the cold from Finland, northern Russia, and the Arctic.

Coincidently, above climatological temperatures occurred over, between, and south of Greenland and Iceland (Fig. 14b, bottom panel). The Labrador Low likely advected energy (i.e. moisture and heat) from the temperate latitudes along its northeastern flank to this region. This northwards advected warmth possibly originated, apart from the westerlies, also from the southeasters that are favored by the positive British Anomalies. Along the topographic gradient of the GIS, the condensating moisture led to precipitation whose formation released additional heat.

Correspondingly, during most of the pronounced phases of the 3. PI CEOF precipitation eigenvector, above climatological precipitation occurred along the topographic gradient of northwestern Norway, northern Turkey, and the southeastern GIS (Fig. 16b, bottom panel). For the southeastern GIS, over which the largest anomaly amplitudes prevail, this increase occurred likely due to the topographic lifting of southeasters. These southeasters flowed between the negative Labrador and the positive British Anomalies, advecting moist from the temperate latitudes to the GIS. For northwestern Norway, moist westerlies and northwesters that either orignated from the Arctic or from the temperate latitudes but had flowed around the western edge of the positive British Anomalies likely caused these positive anomalies.

Simultaneously, below climatological precipitation occurred over northwestern Europe, from Ireland and the Bay of Biscay to southern Sweden, most likely during and due to the positive British Anomalies.

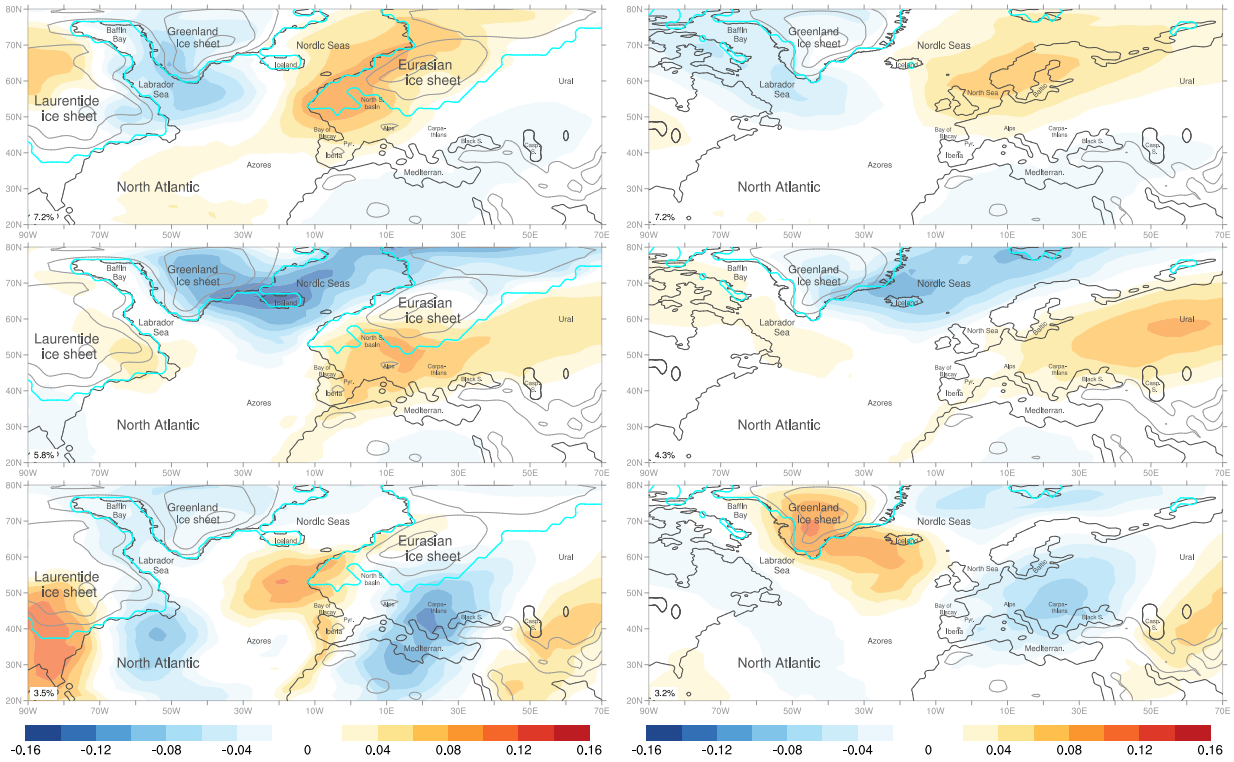

(a) Last Glacial Maximum (b) Preindustrial

Figure 14: First three near-surface air temperature eigenvectors. Resulting from a combined EOF analysis of the precipitation rates, the sea level pressure, and the near-surface air temperature values extracted from the MPI-ESM-P simulations for (a) the Last Glacial Maximum and (b) the Preindustrial.

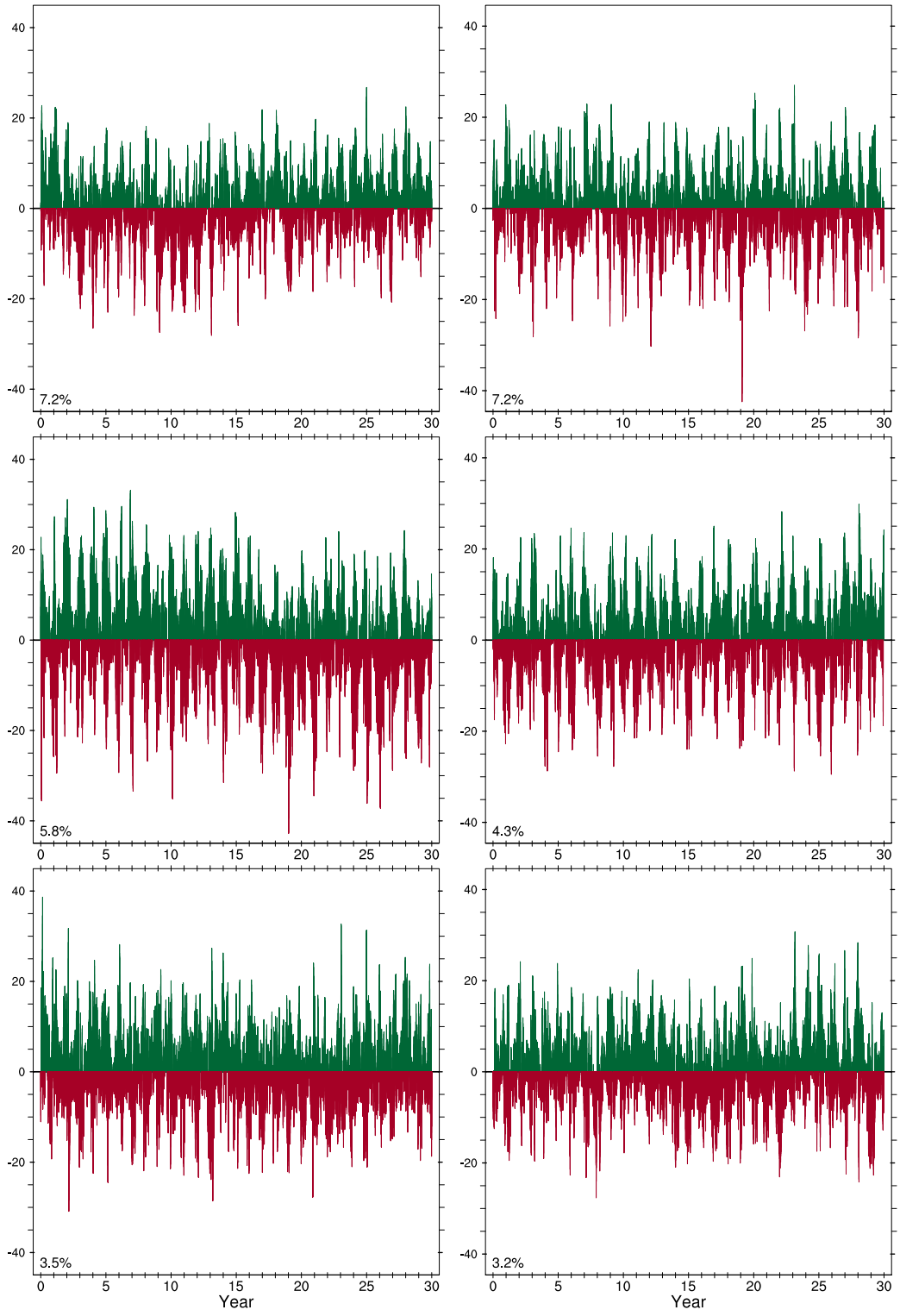

(a) Last Glacial Maximum (b) Preindustrial

Figure 15: Expansion coefficients for the near-surface air temperature eigenvectors (Fig. 14).

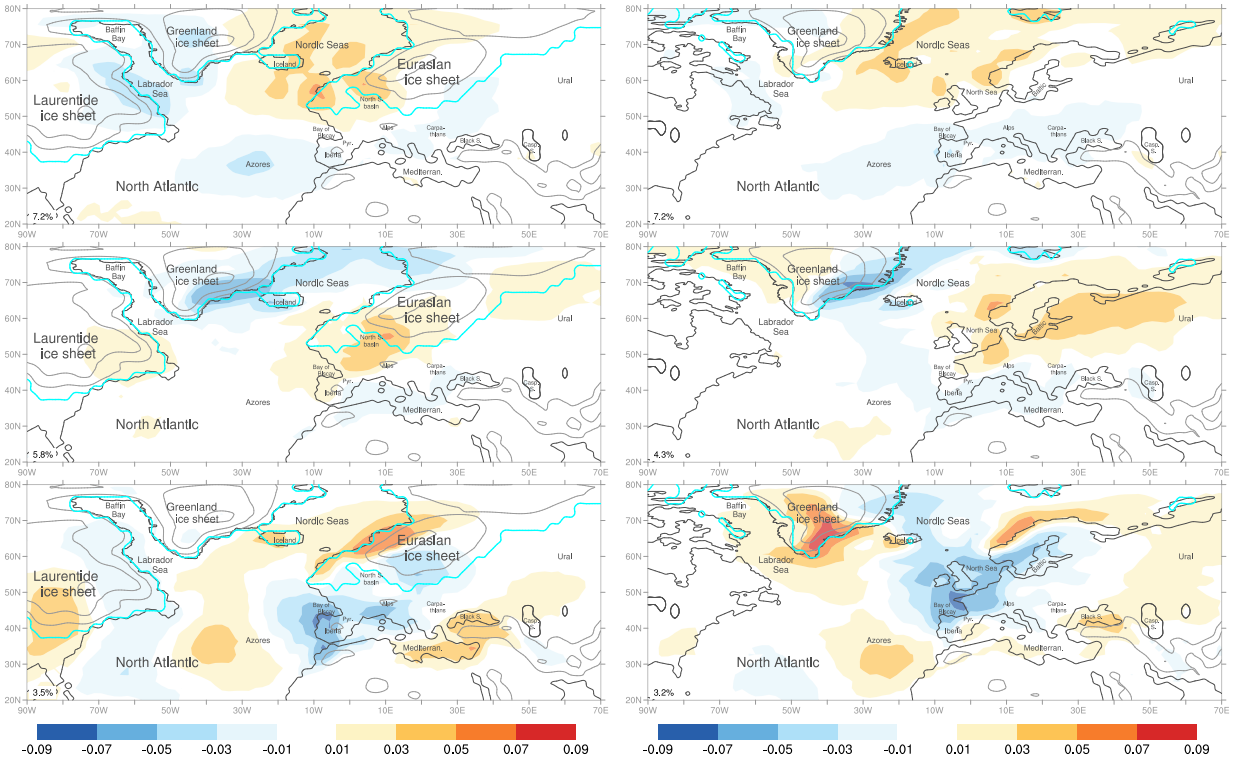

(a) Last Glacial Maximum (b) Preindustrial

Figure 16: First three precipitation rate eigenvectors resulting from the combined empirical orthogonal function analysis based on the precipitation rate, the sea level pressure, and the near-surface air temperature values that were extracted from the MPI-ESM-P simulations for (a) the Last Glacial Maximum and (b) the Preindustrial.

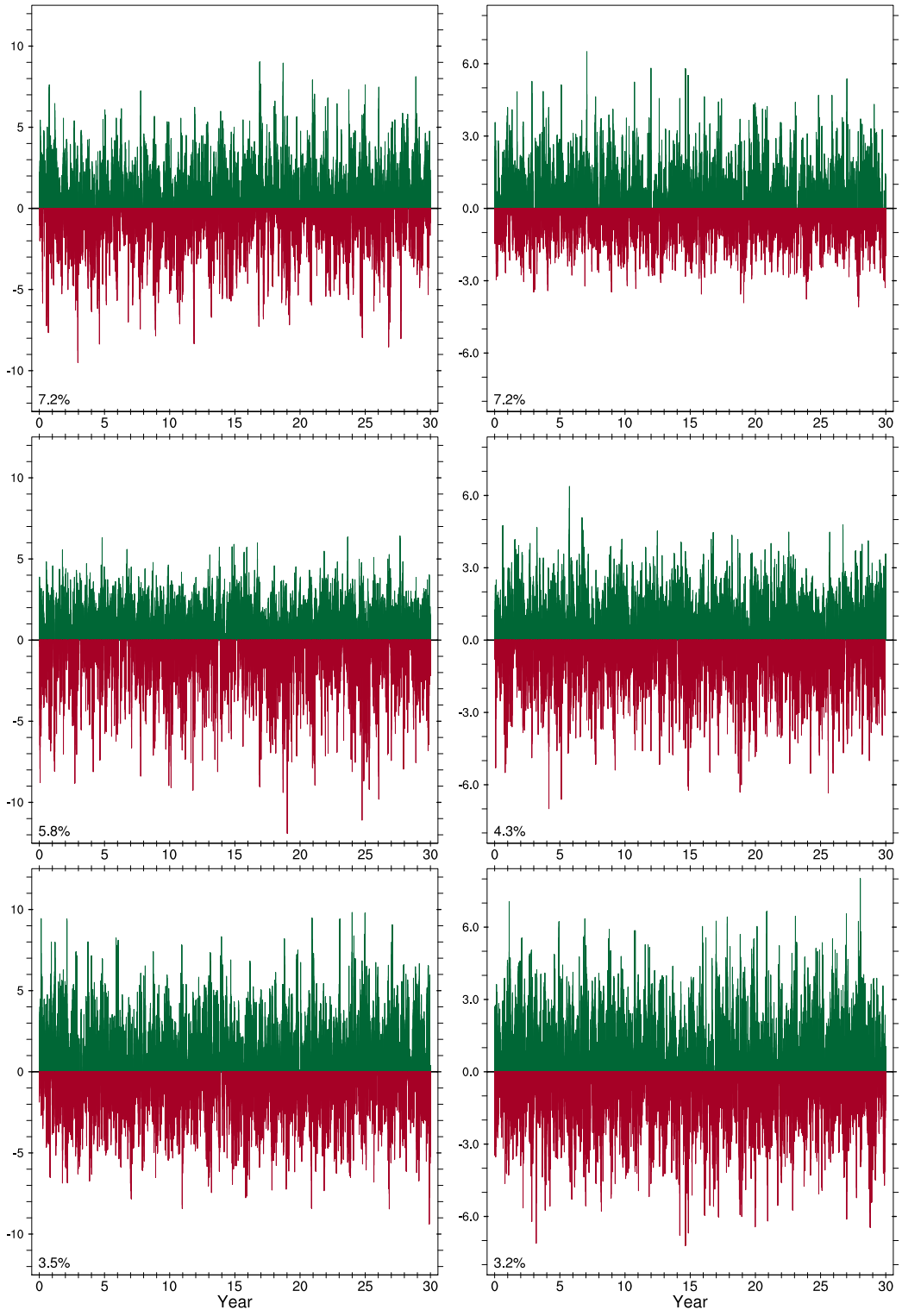

(a) Last Glacial Maximum (b) Preindustrial

Figure 17: Expansion coefficients for the precipitation rate eigenvectors (Fig. 16).

Spatiotemporal correlation of anomaly poles For a complementary representation focusing on the aspect of the spatiotemporal correlation, the variability regions were grouped (Tab. 3–6) according to their prevailing subclimatological effects. These prevailing subclimatological effects were inferred from Fig. 12 to 17. The comprehensive description of these effects was one purpose of the previous paragraphs. The description of these effects provided the basis for the analysis that also focused on the inference of their causes, probable drivers, forcings, and implications.

Here, the main areas of synchronous but opposite subclimatological anomalies were juxtaposed, grouped by meteorological variables (Tab. 3). This first representation focuses on the field-internal spatial structure of the dynamics of the basic meteorological variables.

To understand potential trans-variable correlations, a modified representation grouping regions according to the prevailing sign of their atmospheric anomalies was compiled (Tab. 4). With respect to the climatology, the sign indicates whether the anomaly represents a higher or a lower value during most major contributions of its CEOF.

To research the LGM characteristics concerning the modern reference climate (the PI), the regions are grouped according to the result of comparing the maximal absolute amplitude of their atmospheric LGM anomalies with their spatially corresponding absolute PI anomaly amplitude (Tab. 5 and 6). To focus on the locations and structure of the LGM variability within each separate meteorological field, the synchronous atmospheric variability during the PI is primarily grouped by variable (Tab. 5). To research the trans or inter quantity patterns in the relative LGM variability, the respective regions are primarily grouped based on the same relative LGM variability characteristic, i.e. they were subjected to more, equally, or less variability compared to the PI (Tab. 6).

Table 3: Overview on subclimatological anomalies. Row-wise grouped by pressure at sea level (SLP), temperature (T), precipitation rate (PR), column-wise by CEOF cardinality. Anomalies mainly increase (↑) or decrease (↓) the climatological value over central (c.), southern (s.), northern (n.), western (w.), eastern (e.), southeastern (s.e.), southwestern (s.w.), northwestern (n.w.), northeastern (n.e.) parts or low latitudinal (lat.) areas.

		LGM CEOFs		
		1.	2.	3.
SLP	↑	Iceland, GIS, Nordic Seas	EIS	France, n. Iberia, Bermuda
	↓	Azores, NAO	Baffin Bay, Labrador Sea, Sahara	Caspian Sea, low lat. e. Atlantic
T	↑	Labrador Sea, subpolar gyre	Iceland, e. GIS, Nordic Seas	w. Iberia
	↓	EIS coast	Europe, w. Asia, n. Mediterranean	c.e. Europe, Mediterranean, Tunisia, Libya, Hoggar Mountains
PR	↑	Labrador Sea, s.w. GIS, Azores, s. Iberia, n. Mediterranean	s.e. GIS margin	Azores, subpolar gyre, w. Iceland, EIS coast, Black Sea, Turkey, s. Mediterranean
	↓	EIS coast, Nordic Seas	w.c. Europe	France, Italy, Bay of Biscay, s.e. EIS, coasts of Morocco, Algeria, and w. Iberia

Table 4: Regrouped version of Tab. 3, the caption of which applies mostly, too. However, here, the regions are grouped (row-wise) by their prevailing subclimatological LGM anomaly signs.

		1. LGM CEOF	2.	3.
↑	SLP	Iceland, GIS, Nordic Seas	EIS	France, n. Iberia, Bermuda
	T	Labrador Sea, subpolar gyre	Iceland, e. GIS, Nordic Seas	w. Iberia
	PR	Labrador Sea, s.w. GIS, Azores, s. Iberia, n. Mediterranean	s.e. GIS margin	Azores, subpolar gyre, w. Iceland, EIS coast, Black Sea, Turkey, s. Mediterranean
↓	SLP	Azores, NAO	Baffin Bay, Labrador Sea, Sahara	Caspian Sea, low lat. e. Atlantic
	T	EIS coast	Europe, w. Asia, n. Mediterranean	c.e. Europe, Mediterranean, Tunisia, Libya, Hoggar Mountains
	PR	EIS coast, Nordic Seas	w.c. Europe	France, Italy, Bay of Biscay, s.e. EIS, coasts of Morocco, Algeria, and w. Iberia

Table 5: Subclimatological LGM minus PI anomaly amplitudes. For the first three CEOFs and the three atmospheric variables, the analyzed regions are classified whether they were subjected to *more*, *similar* (sim.), or *less* subclimatological variability during the LGM than during the PI. Here, the rows are grouped by variable to focus on the spatial dynamics of one meteorological quantity. Abbreviations are explained in Tab. 3.

		1. LGM CEOF	2.	3.
SLP ↕	more	Iceland	s.w. Scandinavia, France, British Isles, Bay of Biscay, Benelux, Alps, Davis Strait, Baffin Bay	France, n. Iberia, Caspian Sea
	sim.	non-Icelandic areas	Sahara	low lat. e. Atlantic
	less	–	e. Finland and adjacent Russia	British Isles, Urals
T ↕	more	s.w. EIS, subpolar gyre, e. LIS	c. Europe, Iceland, Nordic Seas, GIS	Atlantic, e. Atlantic coast, Mediterranean
	sim.	n. Africa, Middle East, Turkey	n.e. Africa	c. Asia
	less	–	Urals, w. Russia	GIS, subpolar gyre, e. Europe
PR ↕	more	in general	e. LIS, Denmark, s. Sweden, e. Germany	British Isles, Turkey, s. Mediterranean
	sim.	s. Iberia and adjacent Atlantic	Mediterranean, GIS, Iceland	Norwegian west coast
	less	–	s. Finland, n.w. Russia, Norwegian west coast	France, n. Iberia, s. GIS

Table 6: Rearrangement of Tab. 5; caption of Tab. 3 applies. The regional LGM anomalies are grouped row-wise by their deviation: *more*, *equal* or *less* subclimatological variability compared to the PI anomalies at the respective location. This highlights regions that are subjected to similar anomaly ranges between the LGM and the PI. It emphasizes relations between precipitation, pressure, and temperature.

		1. LGM CEOF	2.	3.
More ↕	SLP	Iceland	s.w. Scandinavia, France, British Isles, Bay of Biscay, Benelux, Alps, Davis Strait, Baffin Bay	France, n. Iberia, Caspian Sea
	T	s.w. EIS, subpolar gyre, e. LIS	c. Europe, Iceland, Nordic Seas, GIS	Atlantic, e. Atlantic coast, Mediterranean
	PR	in general	e. LIS, Denmark, s. Sweden, e. Germany	Scotland, Turkey, s. Mediterranean
Sim. ↕	SLP	non-Icelandic areas	Sahara	low lat. e. Atlantic
	T	n. Africa, Middle East, Turkey	n.e. Africa	c. Asia
	PR	s. Iberia and adjacent Atlantic	Mediterranean, GIS, Iceland	Norwegian west coast
Less ↕	SLP	–	e. Finland and adjacent Russia	Scotland, Urals
	T	–	Urals, w. Russia	GIS, subpolar gyre, e. Europe
	PR	–	s. Finland, n.w. Russia, Norwegian west coast	France, n. Iberia, s. GIS

Robustness of combined pressure, temperature, and precipitation variability The spatial robustness of the CEOF results was evaluated by calculating the CEOF for various sub domain sizes (not shown). As a result, the same patterns also re-occurred for slightly modified total extents of the domain. The outcomes converge to a stable and robust solution that is independent of minimal domain extent modifications. This is important as it corroborates the validity of the CEOF method to result in valid and reproducible patterns for about the same regions when analyzing the same input variables.

Temporal sub spans, i.e. 5, 10, 20, 30, and 40 years of consecutive daily-resolved data were analyzed as well. As a result, for more than about 10 to 20 years of input data, the corresponding CEOF pattern does not change markedly. The same is true for extracting different 30-year time slices of the available, stationary 100-year encompassing MPI-LGM as well as of the MPI-PI. According to the definition of the WMO, 30 years are considered as a climate normal period. Hence, the presented results base on the last 30 simulated years extracted from the MPI-LGM and -PI.

5.5 Conclusions

The results imply the successful numerical implementation and application of the CEOF analysis to the MPI-LGM and -PI. The analysis of the subclimatological atmospheric variability over the North Atlantic and Europe revealed distinct LGM patterns compared to the modern PI reference climate. The cumulative explained variance of the first three, 40, and 60 CEOFs for the LGM is larger than that of the corresponding number of PI CEOFs. This result favors the thesis that the LGM variability can be represented by fewer CEOFs than the PI variability. If this thesis is true, it implies that the LGM had fewer degrees of freedom than the PI atmosphere. The first three CEOFs for the LGM and for the PI are mutually independent; this has been indicated by North's rule of thumb.

During most major contributions of the first LGM CEOF, the prevailing NAO weakened; above climatological temperatures occurred over the Labrador Sea and the subpolar gyre; while the opposite applies to the coast of the EIS and its surrounds. There, icy Arctic northerlies and northeasters likely prevailed while warm southerlies reached synchronously the Labrador Sea. Ice melt on and ice discharge from the Labrador Sea, as well as ice formation and thickening in the EIS coast vicinity might have been significant. These processes were coherent with below climatological precipitation over the EIS coast and the Nordic Seas while above climatological precipitation occurred synchronously over the southwestern GIS, the Labrador Sea and its coastal areas. Moisture condensed and precipitated over the Labrador coast as winds lifted moist air masses along its topographic gradient. The synchronous above climatological precipitation centered over the Azores and extending to southern Iberia was possibly related to the southward shifted track of the westerlies, which is consistent with a NAO minus tendency. The above climatological precipitation over the northernmost Mediterranean is coherent with reconstructed glacier equilibrium lines, biological climate proxies, and regional climate simulation results.

The variability centers of the first PI and LGM pressure CEOFs are similar, except for Iceland, which is subjected to higher variability during the LGM. The first LGM temperature CEOF indicates much higher variability over the southwestern EIS tip, the subpolar gyre, and the easternmost LIS, in contrast to the PI. During the LGM, the dominant precipitation variability amplitude was about twice as large as during the PI. During both, the LGM and the PI, the Nordic Seas possessed an opposing precipitation variability phase compared to Labrador and the Azores.

The pressure variability over the EIS center, which is particularly pronounced during winter, was synchronous yet contra-phased with that over Baffin Bay, the Labrador Sea, and the Sahara. During times of very high positive pressure anomalies over the EIS, the Azores and the EIS High likely merged to one continuous high pressure zone. Synchronously, strong and dry katabatic northerlies, northeasters, and easterlies were favored over eastern and central Europe. Coincidentally, the major pressure decrease over the central Sahara likely forced cyclonic flows over the northwestern Sahara and the adjacent Mediterranean territories.

Strong temperature variability occurred over Iceland, the eastern GIS, and the Nordic Seas. Above climatological temperatures likely resulted from south sector winds, coherent with the stronger EIS High and the enforced Labrador Low. At the same time, below climatological temperatures prevailed over western to eastern Europe and western Asia coherent with katabatic winds descending from the EIS and proxy evidence for cold air incursions entering the northwestern Mediterranean.

Synchronously, the large precipitation variabilities in western-central Europe and across the GIS gradient were opposite-phased to each other. The above climatological precipitation at the GIS margin was likely a consequence of the below climatological pressure over the Labrador Sea. This low pressure presumably favored south sector winds over the central subpolar gyre, which in turn advected moisture to the southeastern GIS margin. Meanwhile, the above climatological pressure of the EIS High favored dry northeast sector winds over France, Germany, and adjacent areas, where coherently much less precipitation and cool anomalies.

The high Scandinavian pressure variability existed also during the PI; yet, smaller in extent and shifted northeastwards to eastern Finland and the bordering Russian areas. Additionally, below climatological pressure dominated in and near the Finnish-Russian region, which possessed a low pressure climatology already. Over the Davis Strait, the extent of the subclimatological pressure anomalies was smaller, while it was larger over the southern GIS during the PI; both likely a consequence of the absent LIS. Synchronous to the below climatological pressure in Finland, above climatological prevailed over the southern GIS, which shifted the NAO centers eastwards and is opposed to the below climatological pressure during the LGM over the Davis Strait and the Labrador Sea.

The subclimatological LGM temperature variability in central Europe had shifted eastwards to center over the Urals during the PI. Also the LGM temperature variability over Labrador prevailed farther east, i.e. over the Labrador Sea while that over the GIS had vanished during the PI.

The locations of the synchronous anti phase LGM precipitation variabilities between the southern GIS and mid-western Europe had shifted eastward during the PI. Additionally, the European variability center of lower than average precipitation fragmented into three areas during the PI: the westernmost Norwegian coast, the Benelux, and northwestern Russia. This implies almost no precipitation over northwestern Russia, little precipitation over the Benelux, and some over the Norwegian coast.

The CEOF decomposition suggests four synchronously varying pressure areas during the LGM. The sign of these four pressure anomaly amplitudes always alternated between direct neighbors. Among these four, the most frequently positive Franco-Iberian Anomalies dominated in extent and amplitude. They likely deflected the westerlies. As a result, the westerlies probably turned into southwesters that propagated over the Nordic Seas. Synchronously, positive Bermuda and negative Caspian Anomalies occurred; the former caused southerlies advecting warm moist air from the Gulf of Mexico to the LIS margin, coherent with northerlies from the Labrador Sea towards the subtropical Atlantic. The latter caused northeasters advecting cold air from the Urals to eastern Europe.

The less frequent negative Franco-Iberian Anomalies likely related to cyclones prevailing over and crossing France or Iberia consistent with the southwards shifted storm tracks and jet stream.

Channeled between the positive Franco-Iberian and the negative Caspian Anomalies, northeasters advected colder than average air masses to central-eastern Europe, the central Mediterranean basin, Tunisia, Libya, and the Hoggar Mountains. These cold Arctic air outbreaks into the Mediterranean are coherent with proxy results. At the same time, western Iberia was warmer than its climatological average; likely caused by prevailing warm-dry south sector winds instead of cold-wet westerlies. The positive Franco-Iberian Anomalies also caused below climatological precipitation over France, Italy, the Bay of Biscay, the southeastern EIS, the Maghreb coasts, and western Iberia. In particular in proglacial pedospheric regions, the drier atmosphere favored aeolian erosion. Synchronously, precipitation increased over the Azores and the subpolar gyre, western Iceland, the EIS coast, the Black Sea, Turkey, and the southern Mediterranean basin. This increase likely resulted from advected moisture by southerlies over the Azores and the subpolar gyre, by westerlies over Iceland and the EIS coast, and by northerlies over Turkey.

The third CEOF PI eigenvectors differed distinctly from their LGM analogues, e.g., over the North Atlantic, synchronous pressure variability was almost absent while two larger centers, the most frequently positive British and the negative Urals Anomalies prevailed synchronously 15° farther north favoring NAO minus phases. In line with this pressure eigenvector, synchronous temperature variabilities were quasi absent between 20 and 50°N over the Atlantic and its surrounds — instead, during major eigenvector contributions, temperatures were above average over the GIS and southwest of Iceland, synchronous to below average cold that centered over the northern Carpathians. This cold anomaly was weaker and 15° farther north than during the LGM. Consistently, above climatological precipitation dominated during most major contributions over northwestern Norway and the southeast GIS coast synchronous to below climatological precipitation over the Bay of Biscay, France, the British Isles, and the North Sea. In contrast to the LGM, synchronous anomalies were quasi absent over southern Iberia, southern Turkey, and the southern Mediterranean. For the latter, this is possibly a consequence of the absent Caspian pressure anomalies. The LGM-to-PI eigenvector differences result most likely from the lower PI topography.

6 Dominant Eastern Sector Winds over Europe

6.1 Introduction

The LGM surface winds in Europe are poorly understood. In some regions, even different prevailing directions of surface winds are found. Knowledge on the prevailing regional to continental wind dynamics is missing, which provides the complementary context for the locally recorded surface wind directions in Europe.

Wind proxies in Europe indicate rather different local wind directions for the LGM: Sediments in the Benelux indicate north and west winds[46]. Alpine, western, and southern European proxies indicate that southerlies, which originated from the southward shifted storm tracks, ran past the Eastern Alps[143]. Sediments in central and eastern Europe indicate north sector winds[46]. Easterlies are evidenced by northern central European grain size records[46], Eifel sediments[47], heavy minerals, and carbonate peaks[48]. The Harz Foreland loess[49], and wind-polished rocks[45] near the EIS margin indicate a shift to prevailing easterlies. Danish proxies in addition evidence southeasters[45].

Changing winds were found for Hungary (N, NE, W, WSW)[46,50] and for the Carpathian Basin (CB; N, NW, SE)[46,51,52]. In addition, Serbian loess indicates southwesters[57]. In Romania, the north sector winds including WNW-winds prevailed[46,81,170]. Ukrainian sand deposits indicate northerlies and northeasters[52] that transformed to northwesters in western Ukraine[46]. Part of the dust that was deposited in central and eastern Europe came from the partially dry-fallen Caspian and Aral Sea[86]. Its presence implies easterlies and southeasters during the LGM[46]. All these separate pointlike proxy results lack the context and the overall wind dynamics structure that explains their formation.

To overcome the shortcomings of the LGM climate proxies in the absence of instrumental observations, climate simulations are the only remaining data source for LGM climate research. In addition, to reconstruct the regional LGM dust cycle, it is required to reveal the prevailing wind directions for Europe. This encompasses classifying, understanding, and analyzing the best way possible the differences between the LGM and the present climate.

Although GCMs exist for at least two decades, the reliability of their simulations varies due to model-inherent bias: GCMs are too zonal, they underestimate blocking over Europe[225]; the MPI-LGM possibly overestimates the sea surface temperatures[37]. To be aware of potential model-specific bias, the reliability of the models is analyzed based on their simulations for a period for which a reference climate is available through instrumental observations.

This is accomplished by comparing the GCM simulations for the 20th century to reanalyses[175–177] consisting of independently assimilated weather observations since the 1950es. The extent to which the simulated atmospheric dynamics, patterns, and variables for the 20th century climate deviate from the reanalyses indicates an upper quality limit, which is most likely also true for the LGM simulation of the same GCM. Therefore, any simulated 20th century incoherence requires a careful pertinence assessment of potentially similarly occurring LGM dynamics.

For this assessment and to provide the missing context that explains the dynamics leading to these wind proxies, the spatial distribution of the sea level pressure (pressure) is analyzed using Circulation Weather Types[53–55] (CWTs) as an objective method. The CWTs have already been successfully applied to recent climate data; e.g. to research European potentials of wind energy[55]. Apart from my coauthored publication[36], no other peer-reviewed publication has up to now used CWTs or weather typing methods to analyze the regional wind dynamics in Europe for the LGM. This dissertation is the first to analyze the LGM wind dynamics for five European regions.

This analysis of the LGM pressure distribution reveals the frequency distributions of the regionally prevailing wind directions. Analyzing them for the different European regions leads to a comprehensive reconstruction of the wind dynamics structure. This structure is the context that relates the local proxy-inferred wind directions with each other and with the regional to continental wind dynamics; thus establishing an improved understanding of the LGM wind proxies. The frequency distribution is also the prerequisite to use statistic dynamic downscaling for the reconstruction of the LGM dust cycle.

6.2 Hypotheses

(1) The CWT analysis is capable to classify the atmospheric circulation of the LGM for different European regions. This is new because except for the work[36] that I coauthored, the applicability and outcome of the CWT analyses of the regional atmospheric circulation during the LGM has not been shown previously.

(2) In contrast to the present, the southerlies and the east sector winds (NE, E, SE) prevailed in sum over central Europe (Franconia) during the LGM. In sum, they occurred more often in all analyzed regions during the LGM compared to the present.

(3) Accompanied by less frequent anticyclonic regimes, cyclones occurred more often over Europe during the LGM.

(4) The MPI-ESM-P is the most capable model out of the four PMIP3-conform GCMs to simulate European climate for the present according to the CWT classification. According to the actualism[226,227] principle, it is therefore most appropriate to postdict the LGM climate in Europe.

6.3 Methods — Circulation Weather Types

This analysis bases on the regional sea level pressure (pressure) distribution that was simulated by four different PMIP3-conform GCMs for the present, the Preindustrial, and the LGM climate (Sec. 3). To compare the GCM simulations to the reanalyses, all horizontal grid resolutions were standardized to the highest common resolution, in this case the 2.5° horizontally resolved NCEP reanalyses. Each remapped daily record was classified to one or at maximum two Circulation Weather Types (CWTs)[53]. This classification bases on its regional pressure distribution, which determines its prevailing near-surface wind. More precisely, the pressure gradient and the vorticity in a region covered by 16 grid cells that surround a pre-defined central point determine the CWT of each record[53].

This CWT analysis is applied to five different European regions (Fig. 18): Franconia, a region influenced by its proximity to the EIS; Galicia, a costal region at the southwestern edge of Europe under North Atlantic influence; Campania, in the centre of the Mediterranean; Volgograd, representing continental, eastern Europe, and western Asia; and Transdanubia, focusing on the major European loess deposits that resulted from aeolian dust deposition in the Carpathian Basin in Central Europe. The center and boundary coordinates of all regions are provided in Tab. 7.

Table 7: Boundary and center coordinates of the CWT-analyzed regions

	West (°E)	East (°E)	South (°N)	North (°N)	Center (°E, °N)
Campania	−1.25	31.25	28.75	51.25	15.0, 40.0
Franconia	−6.25	26.25	38.75	61.25	10.0, 50.0
Galicia	−26.25	6.25	33.75	56.25	−10.0, 45.0
Transdanubia	1.25	33.75	36.25	58.75	17.5, 47.5
Volgograd	28.75	61.25	38.75	61.25	45.0, 50.0

As a result, the dynamics were summarized per region in a frequency distribution of ten standard wind classes. Each simulation and each reanalysis record was classified into at least one of the following classes based on its pressure distribution in the respective region: anticyclonic (A), cyclonic (C), northeast (NE), east (E), southeast (SE), south (S), southwest (SW), west (W), northwest (NW), and north (N); anticyclonic and cyclonic are circular, the remaining are directional classes or regimes. Records that are classified to be hybrid, i.e. half circular and half directional, are fully assigned to their directional class ignoring their circular part.

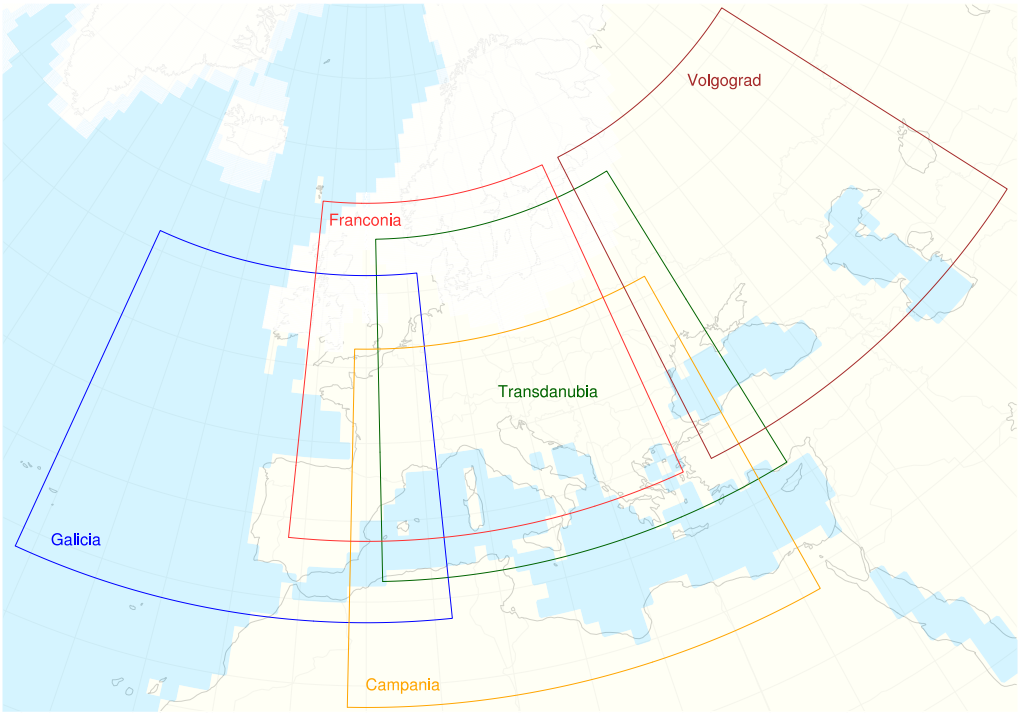

Figure 18: Naming and extent of the Circulation Weather Type analyzed regions. Schematically shown are the Last Glacial Maximum ice sheet extent (white) and its the land-sea distribution (slightly modified) based on the PMIP3. Only for guidance of the viewer, present-day coastlines (gray) and national borders (light-gray) are marked.

6.4 Results and Discussion

At present, central Europe is dominated by westerlies, in particular during the occurrence of a strong pressure gradient between the semi permanent Icelandic Low and the Azores High. This pressure gradient, on average Δp = ~14 hPa (Fig. 19a), determines the North Atlantic Oscillation[54] (NAO), which in turn affects the strength and permanence of westerlies over Europe.

During the LGM (Fig. 19), the pressure difference between the Azores High and the Icelandic Low is larger (~18 hPa) and the pressure poles are located closer together, as the Low is southward displaced by about 5°, from 62 to 57°N, compared to 1970–1999. As a result, the pressure gradient between this High and Low is stronger (NAO plus) compared to the average gradient during 1970–1999. Supporting results were reported for the LGM winter[228]. The pressure isobars at the North Atlantic are more zonal than today, which could result from the stronger NAO plus as well as the more zonal Atlantic jet stream[112,229] during the LGM (Fig. 4). Stronger westerlies approach the Bay of Biscay, Brittany (le Bretagne) and the dry-fallen Channel, given the stronger pressure gradient and more zonal isobars at the North Atlantic, consistent with stronger wind predictions[190].

High pressure over the Eurasian ice sheet At the end of the Channel, the pressure contours diverge distinctly, half of them sharply turn off northwards continuing along the west coast of the EIS. High pressure prevails semi-permanently over the EIS (p = ~1032 hPa), which was only ~4 hPa lower than the pressure of the Azores High. This characteristic atmospheric feature[190,230] over northern Europe during the LGM is termed the EIS High. It blocked, enhanced by the topographic gradient of the EIS margin, the Atlantic cyclones on their eastwards track over Europe. Because of the steep topographic EIS margin gradient, the cyclones either avoided this obstacle by directing their track towards the NE, off the Norwegian coast, or they propagated on a southward displaced track over the Mediterranean Sea or along the corridor between the Alps and the southern EIS margin. The tracks over the Mediterranean Sea are inferable from the pressure contours that bend south-eastwards over Iberia and southern France, then continuing over the Mediterranean. In summary, the more zonal pressure field for today's climate, running from the Atlantic over the British Isles, the Northern European Plain, Scandinavia, the Baltic Sea, and Northern Russia, was distinctly modified by the topography of EIS and its atmospheric effect, e.g. the persisting cold anticyclones.

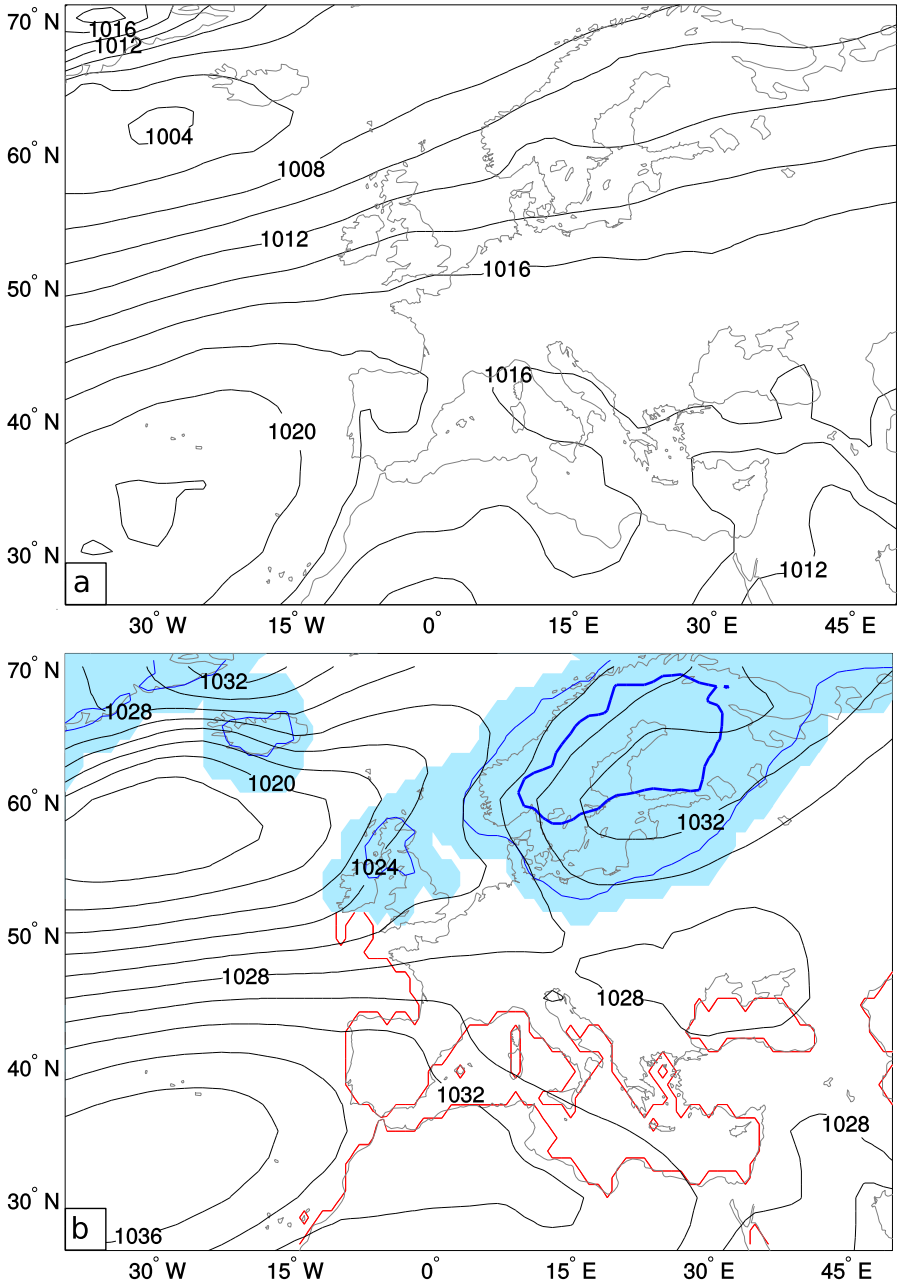

Figure 19: Sea level pressure, averaged: (a) NCEP Reanalysis 1, 1970–1999. (b) GCM simulations (MPI-ESM-P, CCSM, MIROC, MRI) for the Last Glacial Maximum, boundary conditions conform to the Paleoclimate Modelling Intercomparison Project Phase 3, sea level pressure contours (black lines, 2 hPa spaced), approximate extent of the ice sheets (shaded), ice elevation (500 m thin/1500 m bold blue line), approximate LGM coast line[17] (red) shown. *Adapted from Ludwig,* Schaffernicht, *Shao, and Pinto*[36] *© Wiley (p. 195).*

Sea level pressure patterns of LGM Circulation Weather Types During the LGM, CWT-E (Fig. 20a) and -C (Fig. 20b) occurred twice as much over Franconia, according to the LGM ensemble and compared to their respective PI frequencies (Fig. 24). The increased prevailing east sector winds (NE, E, SE) frequency was particularly relevant to the mineral dust cycle (Sec. 7.4, p. 98).

The Franconian CWT-E consisted of high pressure over Scandinavia and the Baltic Sea, whereas low pressure was located over Italy, both is expected for easterlies (Fig. 20a). Compared with the averaged, non-classified LGM ensemble pressure, the pressure increased by more than 10 hPa over Scotland, the North Sea, Norway, and Sweden, all of them either glaciated or dry-fallen. Thus, for easterlies (CWT-E) over Franconia, the per se existing anticyclone over Finland and the northern Baltic extended on average further westwards to Ireland. Thereby, the semi permanent Icelandic Low weakened and was westwards displaced. These easterlies flow over the low-elevated topographic corridor of central Europe between the southern EIS margin and the Alps. On average, the Franconian CWT-C implies a low pressure area centered over Franconia that extends from the North Sea Basin to western margin of the Carpathians and the Gulf of Genoa (Fig. 20b). Similar to the CWT-E, it weakens the Icelandic Low.

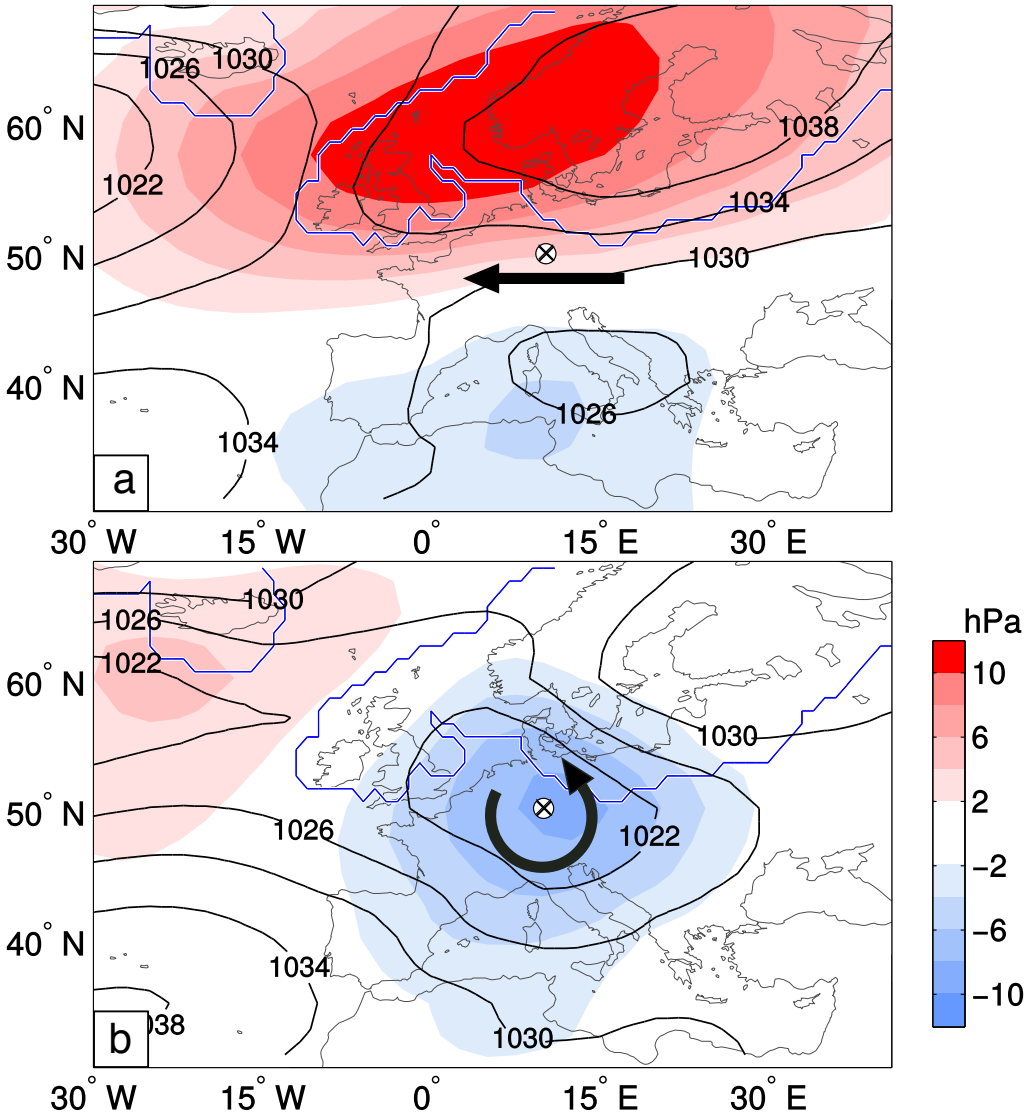

Figure 20: Average sea level pressure (pressure) for all as east (a) and cyclonic (b) classified records of the Last Glacial Maximum (LGM). Each record was classified according to its Circulation Weather Type (CWT). The records are taken from the ensemble mean of 4 daily-resolved GCM simulations over 30 simulated LGM years. CWT class and prevailing wind direction (arrow), pressure (in hPa, black contours), pressure deviations of the respective class from the temporally averaged, non-classified pressure for the LGM-ensemble (red to blue gradient; Fig. 19b shows the non-classified pressure for the LGM ensemble), extent of the ice sheets (blue lines), 20th century coastlines (gray) only for illustration. In fact, the LGM simulations were run with LGM-adapted coastlines. *Adapted from Ludwig,* Schaffernicht, *Shao, and Pinto*[36] *© Wiley (p. 195).*

Simulation assessment by reanalyses The CWT frequency distribution percentages are rounded. The CWT frequency differences are reported as absolute values unless otherwise indicated. To assess the MPI-ESM-P's capability to simulate climate, 52 years (1954–2005) of sea level pressure extracted of its transient run (1850–2005) were analyzed and compared to the synchronous NCEP/NCAR Reanalysis 1 (NCEP1)[175]. Already for the year 1954, NCEP1 includes 60–120 observations[231] per 2.5° lat-lon box and month within the latitudinal belt located at 30–60°N. Subsequently, the observation density for the NCEP1 continuously increased: 120–240 observations since 1965 — more than 240 observations since 1998.

For 1954–2005, based on CWTs and compared to the NCEP1, the transient MPI-ESM-P reproduced the occurrence frequencies of the dominant wind direction sectors acceptably (Fig. 21). In the transient MPI-ESM-P and in the NCEP1, the CWT-A prevailed with more than 19%, followed by -W with more than 15%, and -SW with more than 10%. Less frequent are the CWT-N, -NE, -E, and -SE. The agreement between the transient MPI-ESM-P and NCEP1 is best for CWT-N and -C. The transient MPI-ESM-P overestimates the CWT-SW by 3.3 percentage points (pp), the CWT-W by 2.3 pp, and the CWT-NW by 2.9 pp. Thus, NW, W, and SW are too frequent at the expense of the remaining directional winds and the anticyclonic weather regimes. According to the NCEP1, most underrepresented in the MPI-ESM-P are: CWT-A with a deficit of −3.8 pp, -NE with −1.9 pp, -E with −2.9 pp, and -SE with −2 pp. The overestimation of CWT-NW, -W and -SW is not solely a problem of the MPI-ESM-P, rather GCMs underestimate atmospheric blocking in general at higher latitudes[225] — particularly pronounced for Europe[225]. E.g., compared to the ERA-40 reanalysis[232], the MPI underestimates[225] 4% of the number of blocked days.

Comparing the more recent period, 1979–2005, allows to strengthen the informativeness and reliability of the comparison by additionally considering ERA-Interim Reanalysis[177] and NCEP-DOE Reanalysis 2 (NCEP2)[176]. NCEP2 is an improved (errors fixed, updated parameterizations of physical processes) version of the NCEP1. All three reanalyses are very similar for Franconia, i.e. they differ maximally by 1 pp (Fig. 22). According to the CWT classification, the MPI-ESM-P results for 1979–2005 are almost identical to those for 1954–2005. The reanalyses that start 1979 (Fig. 22) differ from the 1954 starting NCEP1 (Fig. 21): Their CWT-NE, -E, and -SE are less frequent. Thus the MPI-Hist deviates less from them. The MPI-ESM-P distinctly overestimates the prevailing of western winds and cyclones at the expense of the anticyclones and the east sector winds.

Nevertheless, the MPI-ESM-P reproduces the general wind frequency distribution well enough for the present to statistical dynamically downscale its LGM simulations. However, the so obtained results are to be discussed by taking into account its general, model-inherent under- and overestimation of some of the wind directions.

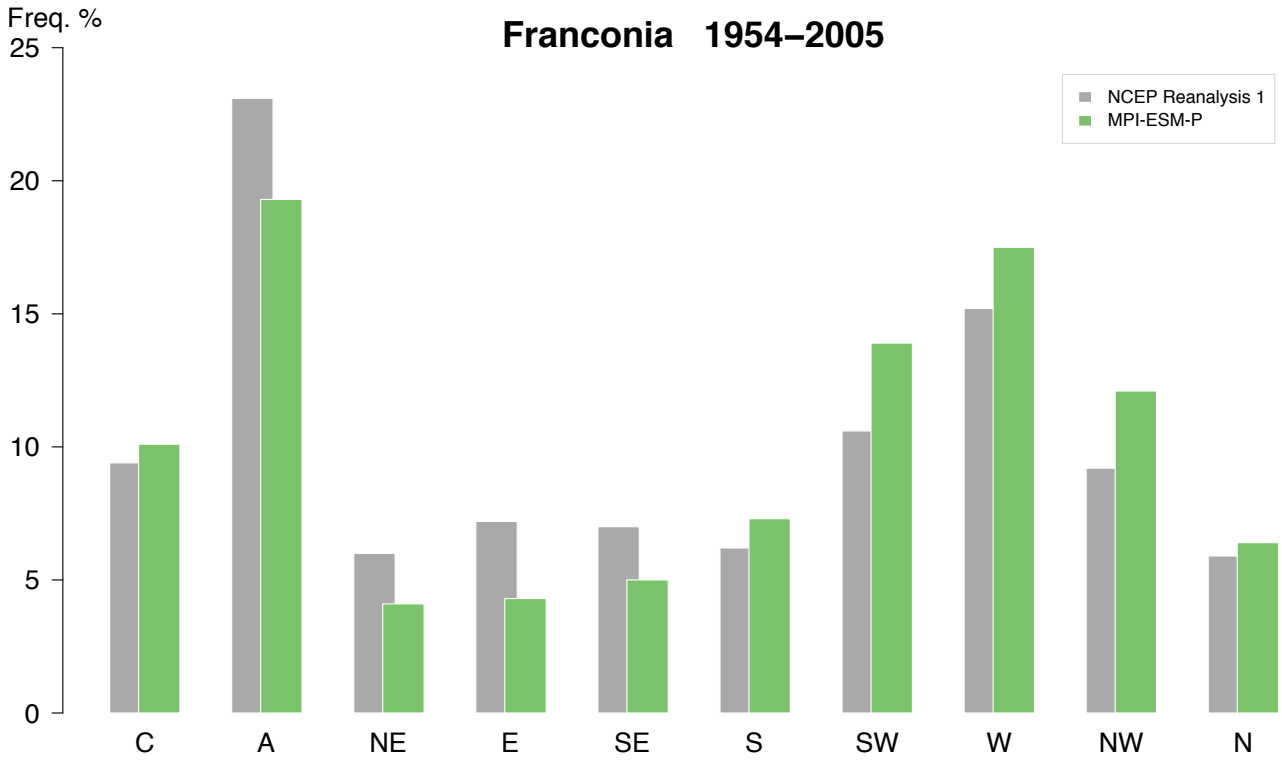

Figure 21: Occurrence frequencies according to the Circulation Weather Type classification of the transient MPI-ESM-P simulation and NCEP Reanalysis 1 for the region Franconia (Fig. 18) from 1954 to 2005; records classified as half circular and half directional are counted as directional only; cyclonic (C), anticyclonic (A).

The CWT occurrence frequencies of the stationary MPI-PI, the transient MPI-ESM-P-Hist 1850–2005 and its subset 1954–2005 are very similar (Fig. 23). Seven out of ten classes differ by less than 1 pp, and for the remaining, the largest difference is 1.4 pp. Therefore, it is possible to characterize the MPI-ESM-P simulation of the modern day climate by only referring to one of its simulations, without loosing much of its relevant variability. Remarkably, the different MPI-ESM-P boundary conditions, transient or in equilibrium, produce no major difference according to the CWT analysis. The CWT frequency distribution of the MPI-PI is even closer to the reanalyses, as its western winds prevail more seldom, whereas CWT-SE, -A, -E and -NE more often. Hence, in the following, for the purpose of weather typing and comparison, only the MPI-PI will be considered to represent the recent GCM-simulated climate.

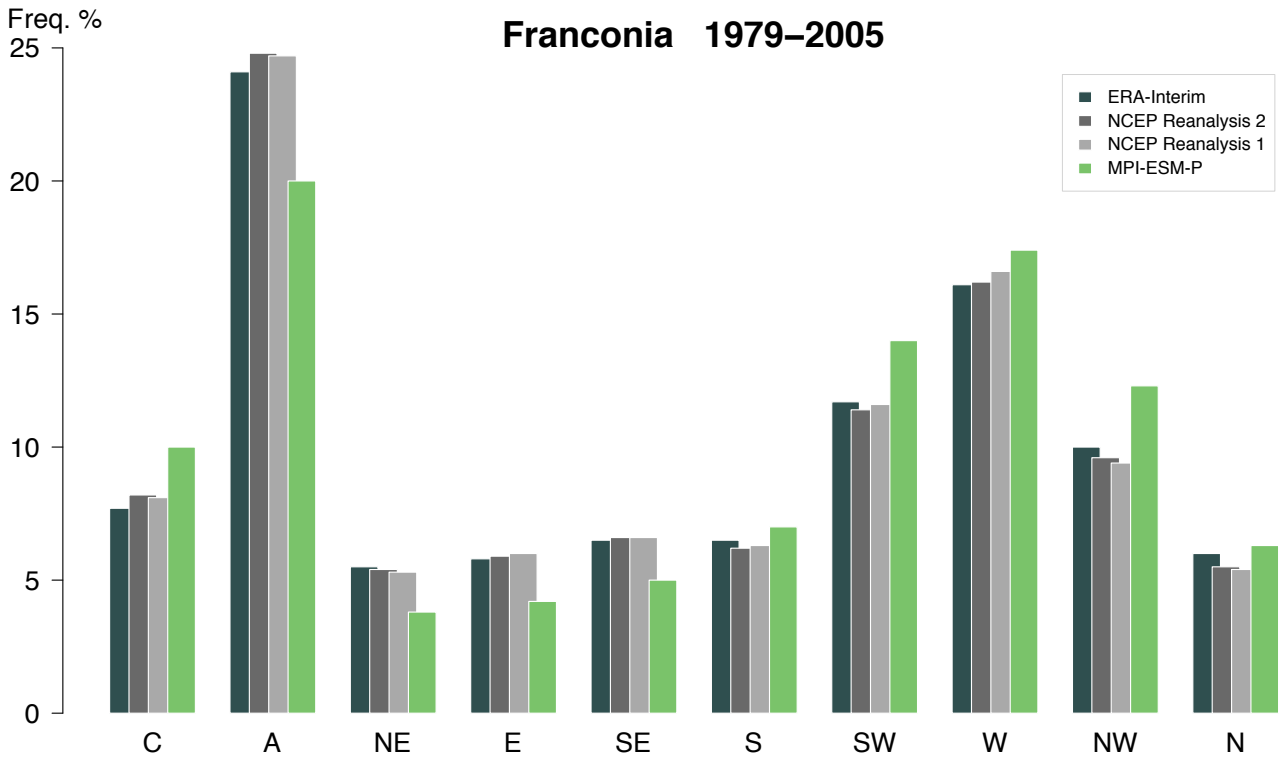

Figure 22: MPI-ESM-P simulation for 1979–2005 (transient) compared to synchronous ERA-Interim Reanalysis, NCEP Reanalysis 1 and 2 for the region Franconia (Fig. 18) according to a CWT-frequency classification; records classified as half circular and half directional are counted as directional only; C: cyclonic, A: anticyclonic.

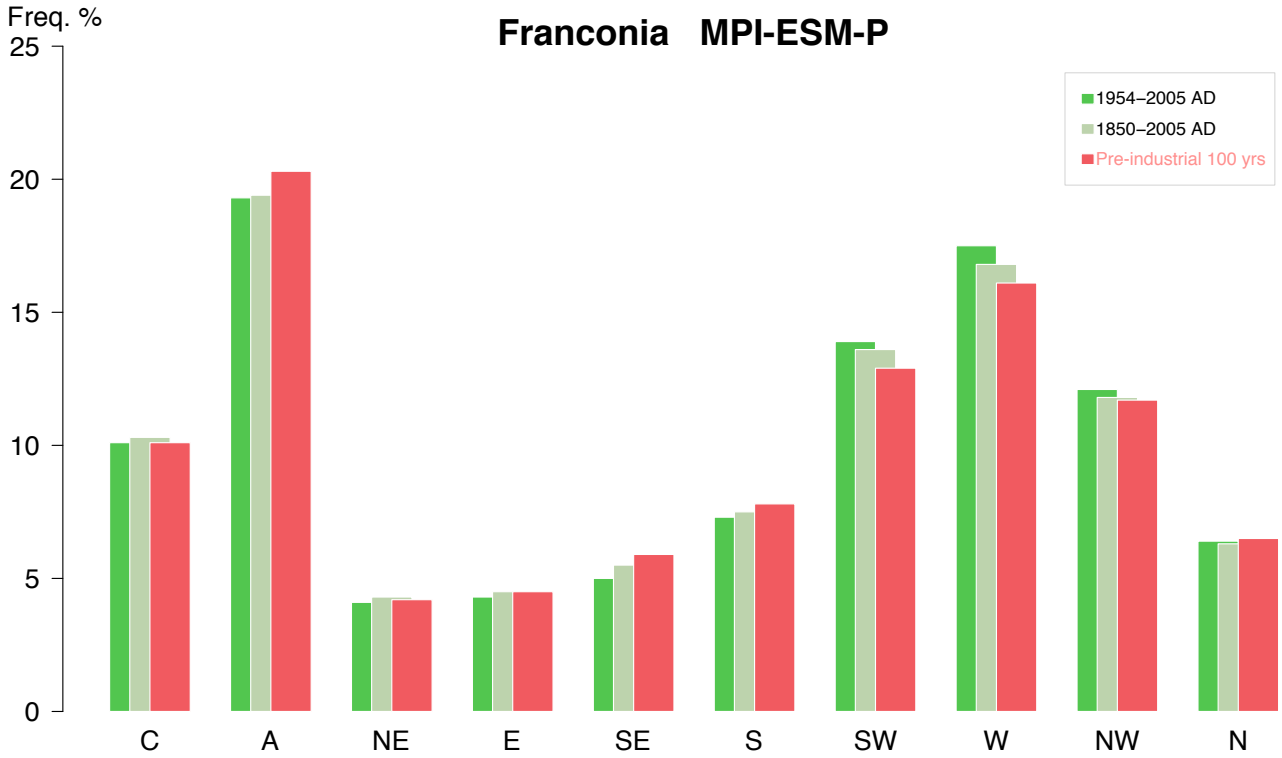

Figure 23: Circulation Weather Type occurrence frequencies decomposing the transient MPI-ESM-P-Hist 1850–2005 run, a subset (1954–2005) thereof, and the stationary MPI-PI (100 years) run.

Dominant wind patterns over Europe during the LGM and today To understand the general characteristics of the European climate during the LGM and its differences to today, the NCEP/NCAR Reanalysis 1 (NCEP1)[231], the PMIP-PI and the PMIP-LGM are compared for four European regions. A fifth region, labeled Transdanubia, is discussed in Sec. 7.4 (p. 98).

In this section (6.4), NCEP1 encompasses the time from 1970-Jan-1 to 1999-Dec-31, i.e. our recent transient, globally warming climate. To evaluate the four GCMs, from each of them a 30-year time slice of their PI and LGM simulation was classified using CWT. Then, the average CWT frequency distribution over the four GCM-dependent GCM distributions was calculated for each of the two analyzed climate states (PI and LGM) of the Earth. This resulted in two GCM ensemble mean distributions, called PMIP-PI and PMIP-LGM. To improve readability, the full identifier of an individual model simulations is shortened, i.e. MPI-PI and MPI-LGM are shortened to MPI-PI and MPI-LGM, respectively.

Franconia: NCEP, present-day and LGM CWT frequencies For Franconia (Fig. 24), CWT-A occurs the most often (24%), followed by CWT-W (17%) and -SW (11%) according to NCEP1. On the contrary, CWT-NE and -N are scarcest. In sum, high pressure systems and the western winds prevailed 60% of the times between 1970 and 2000. The general tendency of dominant CWT-A, -W, and -SW classes is reproduced by the PMIP-PI. However, the PMIP-PI considerably underestimates the CWT-A (6 pp), -E and -SE, whereas it overestimates all western winds, e.g. the CWT-SW (~3 pp).

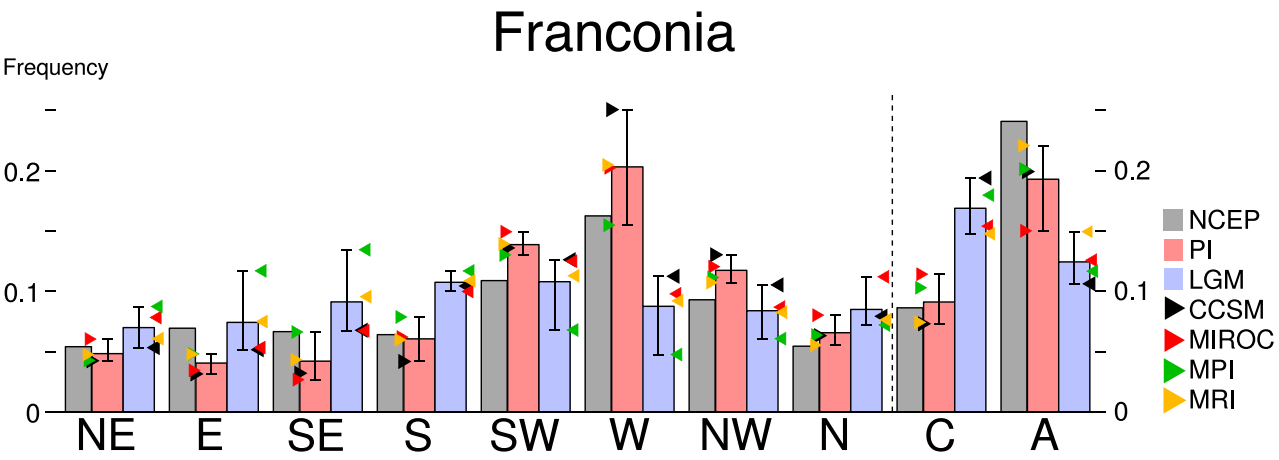

Figure 24: Circulation Weather Type occurrence frequencies for Franconia, based on the classification of the NCEP Reanalysis 1 (1970–1999; 'NCEP'), the PMIP-PI-30 ('PI'), and the PMIP-LGM-30 ('LGM'). All data sets span 30 years. Triangles indicate the frequencies resulting from the individual global climate model simulations that form the PMIP ensemble. *Adapted from Ludwig, Schaffernicht, Shao, and Pinto*[36] *© Wiley (p. 195).*

Regarding the sum of deviations over all classes, the MPI-PI reproduces the CWT frequencies of the NCEP1 much better than the PMIP-PI. It reproduces the frequencies of westerlies and southeasters considerably better, however, it slightly overestimates cyclones by 1 pp. The second best individual model in reproducing NCEP1 (after the MPI-PI) is the MRI-PI. It still reproduces NCEP1 slightly better than the PMIP-PI, especially its frequency for anticyclones is closest of all models to that of the NCEP1. The spread (the variance) of the four model-dependent occurrence frequencies within one GCM PMIP-PI class is largest for CWT-W (15–25%) and -A (15–22%).

According to the CWT frequency distribution that is based on the PMIP-LGM, cyclonic regimes prevailed (17%), consistent with significant contributions of cyclonic wind anomalies to surface cooling that were found[190] in simulations of an intermediate-complexity ocean-atmosphere model. Anticyclonic regimes prevailed the second most often (12%), followed by the southerlies and southwesters, each of them prevailing 11% of the time during the LGM (Fig. 24).

Regarding the individual changes per class for the LGM, CWT-SE more than doubles whereas -W diminishes to less than half of its original frequency compared to the PI. Also, CWT-E, -S and -C double, while -N and -NE increase, whereas the western classes and CWT-A diminish distinctly. Thus, the dominance of western winds over Franconia ceased in favor of cyclones, southerlies and eastern winds.

As the MPI-PI has been already better in reproducing the NCEP1, it is congruent that the MPI-LGM frequencies of several classes also differ from those of the PMIP-LGM: Easterlies and southeasters were more frequent (+4 pp, each) during the LGM according to the MPI, whereas the abundance of southwesters and westerly was reduced (−4 pp, each). Considering only the directional wind classes, southeasters, easterlies and southerlies prevailed over Franconia much more often than the western wind classes, according to the MPI-LGM. In total, the directional, non-western winds prevailed during 53% of the times, almost a doubling (+23 pp) compared to the MPI-PI. Correspondingly, the western winds prevailed only during 18% of the times, less than half of their MPI-PI occurrence frequency (−22 pp). As stated previously (Sec. 6.4, p. 78), the MPI-PI and -Hist underestimate eastern winds. Therefore, the all directional, non-western winds more likely prevailed 58 to 60% of the times during the LGM, and the western winds only about 13% of the times. This is approximately estimated taking into account the assumed bias of the MPI-LGM. The assumed bias bases on the reanalyses to MPI-PI comparison.

The enhanced frequencies of the northerlies, northeasters, and easterlies possibly occurred due to the semi permanent glacial anticyclone over the EIS[73,112], while more southeasters, southerlies, and cyclones likely resulted from the southward shift of the jet stream[110,191] and the storm tracks.

For the glacial atmospheric circulation over central Europe, an east (high pressure) to west (low pressure) sea level pressure gradient[228] supported the increased frequencies of CWT-SE and -S during the LGM.

The more frequent CWT-C result from the EIS topography that effectively constrained the path of the cyclones. Most likely, three paths remained open: One along and off the western and northwestern EIS margin, the other between its southern margin and north of the Alps–Carpathians-latitude[36], and the third along and over the Mediterranean region[143]. Regarding the zonally oriented storm tracks of the cyclones over the Mediterranean, in particular during winter, a northward branch likely[143] split off over Tyrrhenian Sea to cross the Adriatic, to then pass between the Alps and the Carpathians, to reach the south and southeastern EIS margin. It disappeared over the topographic gradient of the EIS that covered northeastern Poland and the adjacent Baltic Sea. Under the assumption that some of the cyclones along this branch followed a track that was slightly more oriented northwestwards over central Europe, this branch also supports the increased occurrence frequency of cyclones over Franconia during the LGM. For the inherent cyclone track of the recent climate, the northeastward passage over and across Scandinavia was blocked or at least inhibited due to the persistence of the high elevated EIS surfaces. According to most studies, the LGM jet stream shifted southward passing along lower latitudes, which also results from the PMIP-LGM and the MRI (Fig. 4 and 5), assuming that the atmospheric velocities between the 300 to 200 hPa level describe its variability reasonably. However, according to the MPI-LGM, the jet stream bended northeastwards and continued along the American east coast, then along and off the east coast of the GIS where it steadily weakens (Fig. 5, left panel). There, over the Nordic Seas and over the topographic gradient of the southeast LIS margin, the jet stream velocity increased the most, according to the MPI-LGM. Thus, the erstwhile zonally propagating jet stream (a westerly flow) turned into a latitude-crossing (southwester) flow directed towards the outermost western edge of the EIS, then possibly continuing with less than 20 m/s along and over the Nordic Seas.

Generally, the individual, model-dependent PMIP-LGM frequency spread is much larger than in the PMIP-PI, particularly the classes E (5–12%), SE (7–13%), SW (7–13%) and W (5–11%) have large spreads, because of the MPI-LGM and MRI-LGM, in which the easterlies and southeasters occur more often, while the southwesters and westerlies are less often, than in the MIROC- and CCSM-LGM. Therefore, the PMIP-LGM encompasses only the mean value of divergent original frequencies per class. This effect is most pronounced for Franconia and Galicia (Fig. 24 and 25). Likely, the numerical representation of the topographic gradient and the total elevation of the EIS, Alps, and Carpathians, which are part of Franconia (at least to a certain extent), differs widely from one GCM to another, given, e.g., their distinct grid size resolutions. Related to this, parametrizations for sub-grid scale processes could be (partly) inadequate in the surroundings of steep topographic gradients. Besides the fact that each GCM uses different default parametrization schemes, which approximate the atmospheric processes over such gradients distinctly well. Possibly, the distance of the analyzed region to the nearest Atlantic shore is also a critical factor, i.e. during the LGM, Franconia is located in the transition zone of a maritime to a continental climate and to capture frequently changing winds correctly might be challenging for the GCMs. All of these factors can result into diverging CWT occurrence frequency values.

Galicia For Galicia (Fig. 25), anticyclones are by far the dominant class according to NCEP1. They prevail 26% of the times during the recent climate, followed by 16% westerlies, 12% southwesters, and 10% northwesters. These four most frequent wind classes prevail about two thirds of the times over Galicia. Hence, western winds and anticyclones dominate the Galician climate during the 20th century.

The PMIP-PI captures the observed frequency distribution trend, yet it overestimates the western winds at the expense of the CWT-A and the eastern winds, i.e. westerlies (25%, +9 pp), anticyclones (21%, −5 pp), south- (15%, +3 pp), and northwesters (12%, +2 pp) prevail in total 72% of the times with a total overestimation of western winds by 14 pp. The overestimation of western winds is a general GCM problem[225]. The MPI-PI reproduces better than the PMIP-PI the westerlies and southeasters. The MRI-PI is closer to the observations for westerlies, northwesters, all eastern winds and the anticyclonic flows. For the other classes, their frequencies tend to be as near to the observations as those of the PMIP-PI.

The frequency distribution of the PMIP-LGM is almost identical (±1 pp per class) to that of the PMIP-PI, with the same order of prevailing regimes. This would imply that western winds and anticyclonic regimes also prevailed during the LGM, yet with frequencies that are oriented at the NCEP1 distribution to avoid the over- and underestimations found in the PMIP-PI. However, when the LGM frequencies are compared class-wise, the inter GCM spread increases distinctly. Though none of the four GCMs reproduces the Galician NCEP1 perfectly, the MRI- and MPI-PI outperform the other two models. Considering this fact, a reduction of westerlies and anticyclonic regimes accompanied by more cyclones, N-, NE-, E-, and SE-winds is more likely in Galicia during the LGM. Consequently, the frequencies of all directional winds were distributed more equally, anticyclonic regimes still prevailed most of the times, followed by either by southwesters as second and northeasters as third most frequent, or the other way round. Even though this shift to more northerlies, northeasters, and easterlies was less pronounced compared to Franconia, still, the same wind classes were more frequent during the LGM. This finding substantiates the Franconian LGM wind regime shift.

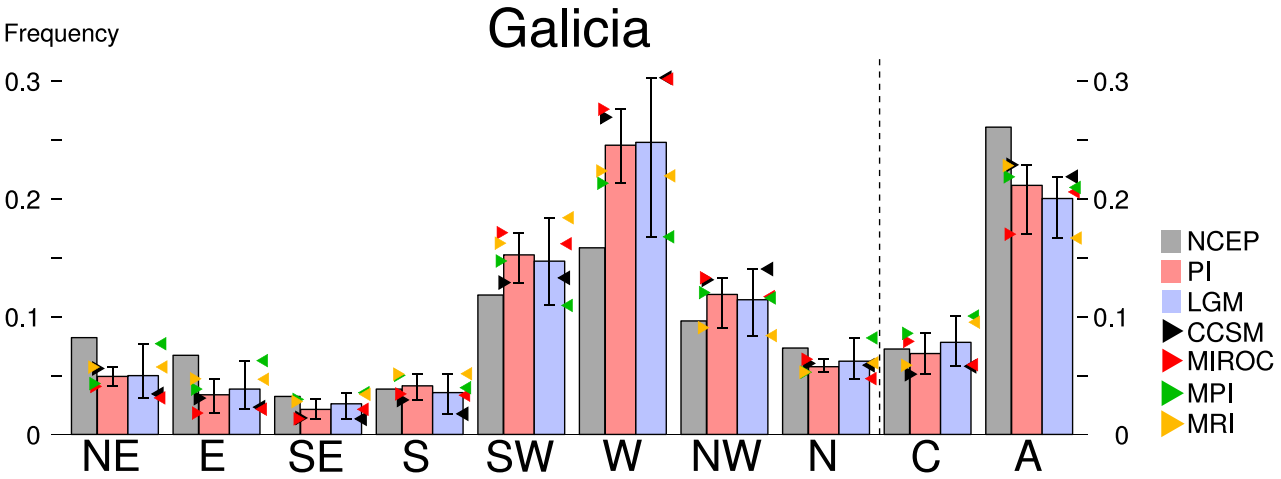

Figure 25: Circulation Weather Type occurrence frequencies for Galicia. Data sources and labels as in Fig. 24. *Adapted from Ludwig,* Schaffernicht*, Shao, and Pinto*[36] *© Wiley (p. 195).*

Campania For Campania (Fig. 26), according to NCEP1 and in contrast to the observations for Franconia and Galicia, the occurrence frequency distribution over all ten circulation weather type classes is more equally, i.e. it approaches more than those for the other two regions a uniform distribution. Anticyclonic regimes prevail mostly (18%), followed by about equally frequent CWT-C and -NE, while the west sector winds occur, with about 6% each, the least of all. The overall shape of the PMIP-PI occurrence frequency distribution differs distinctively from the reanalysis. While the anticyclonic regime frequency, obtained from the simulations as the most frequent regime (16%, −2 pp), still approximates well NCEP1, the second (northerlies) and third (westerlies) most frequent GCM deviate from the NCEP1. Also, the least frequent classes, i.e. easterlies and southeasters, are inconsistent with NCEP1. The MIROC-PI deviates from the NCEP1, thereby causing these inconsistency and amplifying the inter model spread. All GCMs overestimate the west sector winds, partly by more than 100%, and to a lesser extent the northerlies. At the same time, they markedly underestimate the easterlies, southeasters and cyclones. Regarding all ten classes, the MPI- and the MRI-PI reproduce NCEP1 best, and they also outperform the PMIP-PI.

According to the PMIP-LGM, cyclones were the most dominant class (15%). Compared with PMIP-PI, cyclones were 5 pp more while anticyclones were 5 pp less frequent during the LGM. The slightly more frequent west wind sector combined with less frequent northerlies and northeasters. The cyclone dominance over Campania agrees with a southward shifted jet stream, as well as with an amplified and southeastward extended storm track from the North Atlantic to the western Mediterranean[36,110,143]. During the LGM, frequent polar air incursions into the northwest Mediterranean likely caused increased cyclogenesis[66]. Evidence for such incursions was revealed using biological proxies and glacier equilibrium altitude lines[66]. This increased cyclogenesis is in line with the more frequent CWT-C over Campania (Fig. 26).

Based on the bias-corrected (according to NCEP1) interpretation of the MPI- and MRI-LGM, cyclones dominated by far (20%) in Campania, This dominance is in line with the extended storm track over the Mediterranean[110]. Anticyclonic regimes were the second most (about 13%), followed by southerlies and northeasters (each about 10%), while CWT-W, -NW, and -N are the least (7%). Southerlies being the third most is supported also by the assumption of a storm track branch splitting off over the Tyrrhenian Sea and turning northwards to pass between the Alps and Carpathians[143].

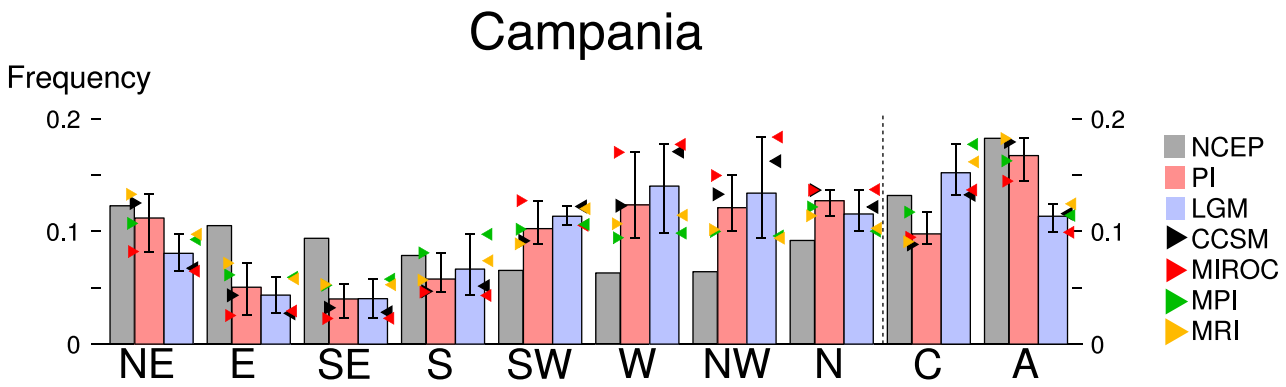

Figure 26: Circulation Weather Type occurrence frequencies for Campania. Data sources and labels as in Fig. 24. *Adapted from Ludwig,* Schaffernicht*, Shao, and Pinto*[36] *© Wiley (p. 195).*

Volgograd For Volgograd (Fig. 27), according to NCEP1, anticyclonic regimes prevail by far the most (20.5%), followed by southeasters (11%) and westerlies (10%). Northerlies and northeasters (7% each) occur least, hence, apart from the CWT-A, the total frequency distribution for Volgograd during the last third of the 20$^{\text{th}}$ century is close to a uniform distribution. As already found for the other regions, the PMIP-PI underestimates the occurrence frequencies of eastern winds, here accompanied by the overestimation of the west sector winds (in sum by 5 pp), the southerlies, and northerlies. Additionally, it overestimates the cyclones markedly by 5 pp while underestimating the anticyclonic regimes seriously by −6 pp. The anticyclonic regime is still its most frequent class (about 15%), then, the PMIP-PI deviates from NCEP1 as its cyclonic class is second most frequent (13%), followed by the westerlies (13%). Yet, it can reproduce one of NCEP1 least frequent classes, the northeasters.

Again, the MPI-PI does better than the PMIP-PI, as its anticyclonic regimes occur during about 17% of the times, followed by the cyclones (12%), and southeasters (11%). Its least frequent classes correspond to those of NCEP1, as well. It reproduces 6 of the 8 directional classes exceptionally well: the west sector winds, the CWT-N, -NE, and -SE. Its largest deviations occur in both circular classes, i.e. it overestimates the cyclones by 4 pp going hand in hand with the underestimation by 4 pp of the anticyclonic regime.

According to the PMIP-LGM and compared to the -PI, cyclones prevailed with a frequency of 18% most of the times (+5 pp) during the LGM, followed by anticyclonic regimes (12%, −2 pp) and southerlies (11%, +2 pp). Considering only the MPI-LGM and interpreting its results including a rough approximative correction using its known class dependent MPI-PI to NCEP1 offsets, anticyclonic regimes prevailed the most (17.5%) during the LGM, followed by the equally frequent southeasters and cyclones (12.5%, each), and the easterlies (12%). For the mineral dust cycle over the continental European regions during the LGM, the prevailing dry winds are particularly important. For Volgograd, these are the dry east sector winds and northerlies. They prevailed there during at least 41% of the times.

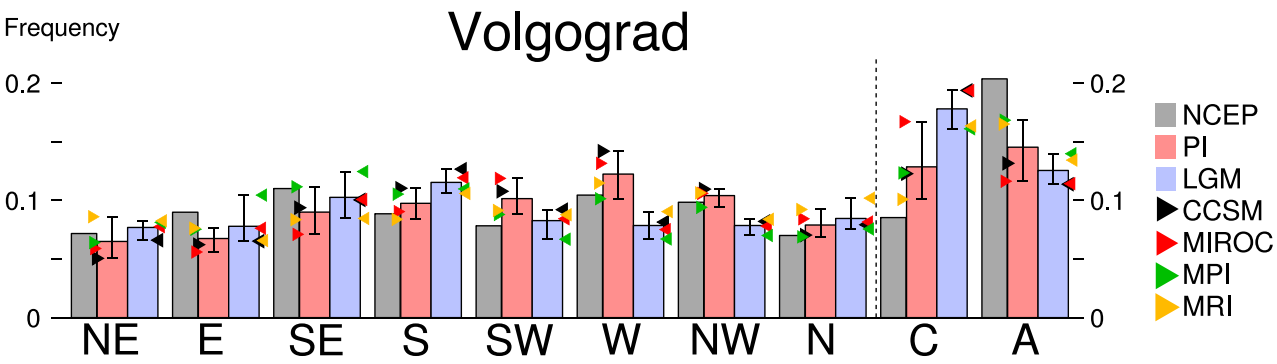

Figure 27: Circulation Weather Type occurrence frequencies for Volgograd. Data sources and labels as in Fig. 24. *Adapted from Ludwig, Schaffernicht, Shao, and Pinto*[36] © *Wiley (p. 195).*

Summary In summary (Fig. 28) during the LGM, the occurrence frequencies of CWT-N, -NE, -E, -SE, and -S of Franconia and Volgograd increased, at the expense of the west sector winds. For Galicia, more CWT-C, -N, -NE, -E, and -SE prevailed at the expense of westerlies and anticyclones. For Campania, CWT-S, -SW, -W, and -C likely increased at the expense of CWT-A, -N, and -NE, which is likely related to the southward shifted storm track[69,73,110,191] and its split-off branch over the Tyrrhenian Sea[143]. More eastern winds and northerlies over Franconia, Volgograd, and Galicia likely occurred due to the cold, semi-permanent EIS High centered over the eastern EIS, more precisely over about the former location of the Baltic Sea (Fig. 6a). The increased probability for blocking over Europe because of its increased topography also favors these four wind directions. Also, katabatic winds that likely descended from the EIS margin in eastern and central Europe support more frequent northerlies and northeasters which likely turned into easterlies (because of the Coriolis effect) as they cross the unglaciated parts of of central and eastern Europe. Over all four regions, more cyclones prevailed at the expense of anticyclones, with the most pronounced change found over Franconia, and least over Galicia (Fig. 28). These more frequent cyclones over all four (south of the EIS located) regions can be attributed to the harsher LGM climate, during which the EIS caused atmospheric blocking and the pressure gradients as well as the polar front jet stream were stronger[36,141] (Sec. 4.2, p. 29). The strengthened gradients occurred particularly over the North Atlantic[141]

Likely, the cyclones penetrated more easily further eastwards into continental Europe and persisted longer over Europe, as there were almost no roughness elements, i.e. obstacles such as woods and trees that absorbed their energy. Though there were large topographic obstacles in Europe, such as the EIS, the Alps, and the Carpathians, still, the unglaciated parts of the European Plain offered a zonal, hardly elevated corridor from the French Atlantic coast to western Russia with little drag for cyclones and zonal winds. Franconia and to a lesser extent also Volgograd encompassed at least parts of this corridor.

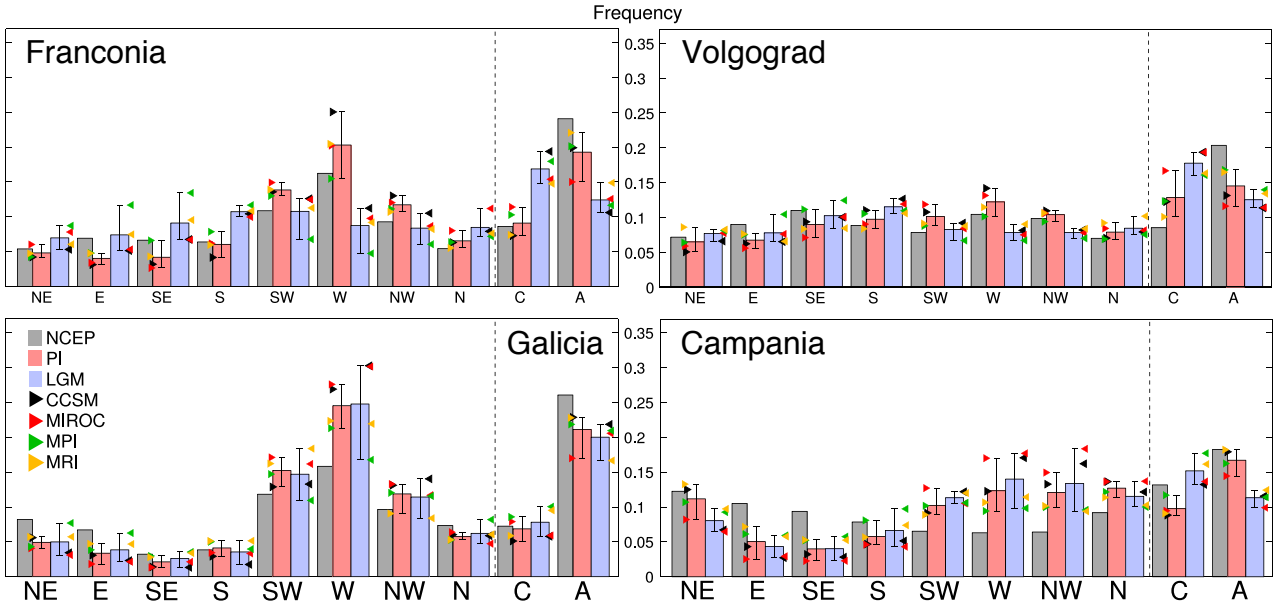

Figure 28: Juxtaposition of the Circulation Weather Type frequencies resulting from the analyses in this section. Data sources and labels as in Fig. 24. *Adapted from Ludwig,* Schaffernicht, *Shao, and Pinto*[36] © *Wiley (p. 195).*

6.5 Conclusions

The present European climate and wind dynamics are dominated by the western wind sector. However, all GCM simulations for the PI overestimate the western wind sector. Regarding the obtained similarity of the frequency distribution of the transient MPI-Hist and the steady state MPI-PI, the simulations for the PI represent the present climate about as good as the transient simulations (Hist). Thus, the PI simulations are considered as the reference to compare the steady state LGM simulations with. During the LGM, the NAO pressure gradient was larger (+4 hPa) than it is in the present climate. The wind dynamics were successfully obtained by classifying reanalyzed and simulated pressure data according to the CWT method. It has been shown that the CWT results for the present and the LGM pressure data are supported by and coherent with independent findings. Thus, the CWT method is also capable to successfully classify the regional European atmospheric circulation dynamics of the LGM. During the LGM and in contrast to the present, the eastern wind sector prevailed in Franconia, i.e. its frequency doubled. It was also more frequent over the other three European regions. Also, cyclones were more frequent over all four European regions accompanied by less frequent anticyclones. The quasi-stationary EIS High and the southward shifted jet stream likely contributed to these modified atmospheric dynamics. The EIS High likely blocked the passage of the west sector winds over Scandinavia. The MPI-PI (followed by the MRI-PI) is most capable to reproduce the present European climate. It outperformed the other simulations and the PMIP-PI. Hence, following the concept that the present can be at least to some extent the key to the past, i.e. the actualism[226,227] (historical inference) principle of geology, the MPI-LGM most likely provides the most realistic approximation of the European LGM climate of all four individual LGM simulations and also of the PMIP-LGM.

7 Linkage of the European Dust Cycle and Loess Records

7.1 Introduction

Importance of mineral dust in Earth system science Mineral dust is a core theme[56] in Earth system science: It affects the Earth's energy balance; carries organic material; contributes to the carbon cycle; fertilizes the oceans by depositing iron on them[233]; evidences changes of paleo wind systems and aridity[58]; suppresses or enhances precipitation[57]; scatters light; takes part in atmospheric photochemistry; and provides cloud condensation and ice nuclei that cause indirect radiation effects[57]. Dust serving as an ice nuclei likely cooled the LGM further.

Its diameters range from ~0.02 (measured) to ~100 µm, though cases of particles greater than 400 µm diameter were observed over the Pacific, and found in the Amazon basin[234,235]. The minimum modeled dust diameter varies, e.g. one model used[235] 0.8 µm. Small silt, 2–20 µm *(Large silt, 20–50 µm)*, has an atmospheric lifetime of days *(hours)*. This makes silt interesting for regional paleoclimate simulations, which are important to understand the loess deposits[51].

The LGM is particularly appropriate for the analysis of the mineral dust cycle because its cold climate enhanced the surface erosion by lowering the dust emission friction velocity threshold[236]. In addition, colder winds can entrain and carry more and larger particles[236]. During the LGM, our ancestors' mobility and remain were likely disfavored in regions where frequent dust storms dropped the visibility to almost zero[63].

Effects of the pleniglacial bio- and atmosphere on the dust cycle During the cold period 37–16 ka ago, central and eastern Europe were partly covered by taiga or montane woodland containing isolated pockets of temperate trees[164], while ice-sheet free regions in Denmark, northern France, Germany, western Poland, the United Kingdom, and Benelux were mainly polar deserts during the LGM[167]. These conditions probably resulted in more intensive high-latitude dust transport and frequent dust storms over Europe[237].

During the LGM, the atmospheric circulation over Europe differed substantially from its modern state[36]. The EIS High was a major feature, a semi-permanent high-pressure system over the EIS[73]. This blocked the North Atlantic cyclones over Europe and deflected the storm tracks causing them to run either along a lower latitude or towards the Arctic along the Nordic Seas, according to GCM simulations[36]. Although storms were probably more frequent[36], the European climate was drier[73,116,140,143], as both the summer westerlies and the polar front[66] were located at lower latitudes during the LGM. For the more complete picture refer to Sec. 6.4 (p. 74) for the LGM wind directions analysis, to Sec. 4 (p. 28) and Sec. 5 (p. 45) for the comprehensive analysis of the LGM climate in Europe and its surroundings.

Review of paleo dust simulations Considering the fund of peer-reviewed results on the Europe-wide dust cycle (from Portugal to the Urals) with a 50 km or higher horizontal resolution for the LGM, no results have been published up to the submission of this dissertation. For continental sized and sub-European domains, climate-dust simulation results have been published; however, either their environmental conditions had been set to glacial climates, which did not represent all LGM conditions, or their domain did not encompass the whole area from Portugal to the Urals.

Several global climate-dust emission and transport simulations for the LGM have been published[92–98]. Yet, among them, the represented dust process elaborateness differs considerably, for example some calculate the dust transport and emissions separately and offline[93]. All GCM-simulated dust loads[92–96] (and thus depositions) in Europe are, compared to most of the independently reconstructed European fieldwork-based MARs (Tab. 1), by orders of magnitude too low. To address this deficiency of appropriate LGM dust simulations, the standard WRF-Chem[102], which is capable to simulate present-day dust[238–240], has been developed further by the author to respect additionally those environmental conditions that were relevant for the LGM dust cycle.

Evidence for glacial dust from loess distribution Loess is a climate and mineral dust proxy resulting from aeolian dust deposits[63]. It provides the most complete, important, and widespread past climate record and dust archive located on the continents[63,79,241]. It is a clastic sediment of aeolian origin, consisting mainly of ex-aeolian silt (6.3–63 μm) but possibly containing ex-aeolian clay (< 6.3 μm) and sand (> 630 μm)[79]. Loess is tightly related to erosion, wind, and dust, because a dust source, adequate wind for dust transport, and an accumulation site are needed for its existence[242]. It records climatic changes[63], in particular aeolian activity during glaciations[79,236].

In Europe, loess covers large areas[79] (Fig. 41). Its creation in Europe began 75 kyr ago, followed by the enhanced built-up during the last glacial 30 to 15 kyr ago, and ended 15 kyr ago[80]. Its thickest layers form the European loess belt at about 50°N. They extend from France to the eastern European Plain[82], which stretches from Slovakia to the Caspian Mountains. This belt includes the large loess sheets of the southern proglacial EIS regions, which are optimal for studying the paleoclimate[79,83–85]. Aeolian, but also till, glaciofluvial, glaciolacustrine, and alluvial deposits—all partly cryogenically overprinted—capped the eastern European Plain[85]. In Europe, mineral dust storms occurred more often and were stronger during the glaciations than today[237]. The LGM represents the most substantial phase of loess accumulation in the eastern European history[81].

The spatial distribution, composition, and thickness of loess sequences within sediments furthers the understanding of the paleoclimatic conditions. Loess records are also one of, if not *the* major fieldwork-based reference to evaluate paleo climate-dust simulations[17]. According to the global LGM dust simulations[92–94], the European deposition rates ranged between 1 and 100 g m^{-2} yr^{-1}. However, even rates close to the upper limit of this range still underestimate substantially[57] the on average reconstructed European MAR of 800 g m^{-2} yr^{-1} (MAR_{avg}). This MAR_{avg} takes into account all fieldwork-based, peer-reviewed MARs (Tab. 1) that were reconstructed from sites between Lisbon and Moscow (Fig. 43).

Although a LGM-dated sequence exists in numerous European loess-paleosol profiles, its origin and its formation are not well understood. This has seriously compromised its value as a climate proxy. By analyzing the Nussloch loess record, Antoine et al.[82] suggested that rapid and cyclic aeolian deposition due to eastward-traveling transient cyclones played a major role[82] in the European loess formation during the LGM (Fig. 29). Yet, the results that led to this dissertation show as well different directions and drivers for the LGM dust transport and deposition over Europe.

All the mentioned discrepancies and unknowns show the need for state-of-the-art paleo dust modeling, which this dissertation contributes to. The therefore implemented regional climate-dust modeling serves to establish the linkage between the LGM dust cycle and the loess records, leading to an improved understanding of the paleoclimate in Europe.

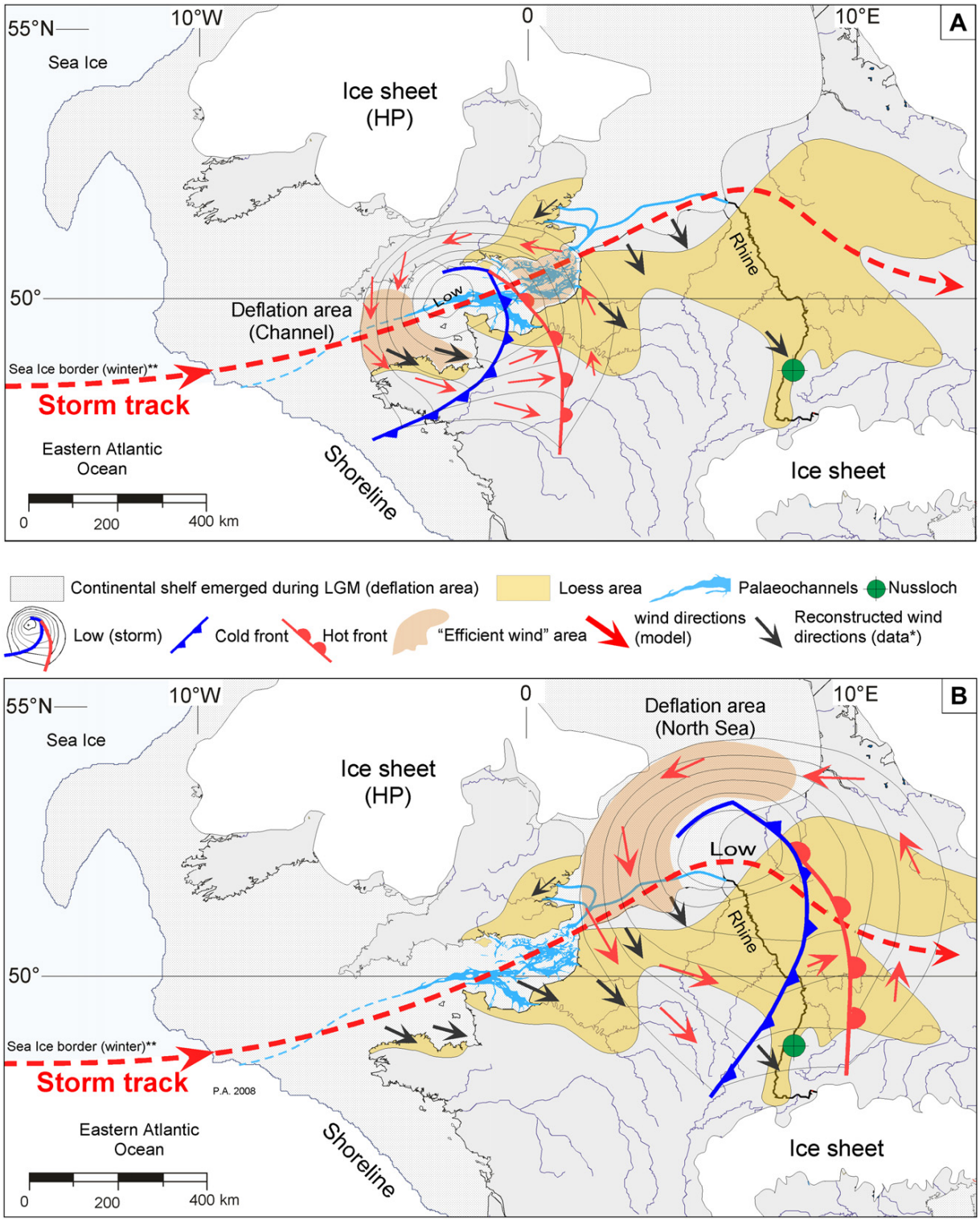

Figure 29: Antoine et al.[82] published a concept of the LGM dust cycle shown on this map (reprinted here from Antoine et al.[82] © Elsevier, p. 195). According to them[82], during the Late Pleniglacial (the LGM), the dust cycle between the European Atlantic shore and western Poland based only on northwesters, westerlies, and cyclones. Antoine et al.[82] published that the loess in the marked areas, i.e. including western and central Europe up to about the present German-Polish border, originated only from the Channel and the North Sea Basin (cf. marked "Efficient wind" areas).

7.2 Hypothesis on the Glacial European Dust Cycle

The following hypothesis on the LGM dust cycle in Europe is proposed by this dissertation: Northeasters and easterlies dominated over eastern and central Europe during the LGM and contributed considerably to the mineral dust transport to eastern and central Europe (Fig. 30). The origin of these winds was most likely over the EIS and related to the prevailing EIS High. These winds flowed down the slopes of the EIS while turning gradually into northeasters and easterlies. They played a significant role in the dust cycle over Europe because they were strong and dry — optimal preconditions to entrain dust into the atmosphere. The prevailing winds, which included cyclonic regimes over Europe, found a high potential for dust emissions on the bare, partly proglacial, eastern and central European surfaces. From there, the northeasters and easterlies but also the northern flank of the cyclones carried the dust westwards. Consequently, most dust was deposited west of its sources. The largest deposition rates prevailed in Poland, on the North German Plain, and in the dry-fallen German Bight. In summary, the east sector winds (NE, E, SE) and cyclonic regimes over central Europe contributed most to the aeolian dust transport and the formation of loess during the LGM.

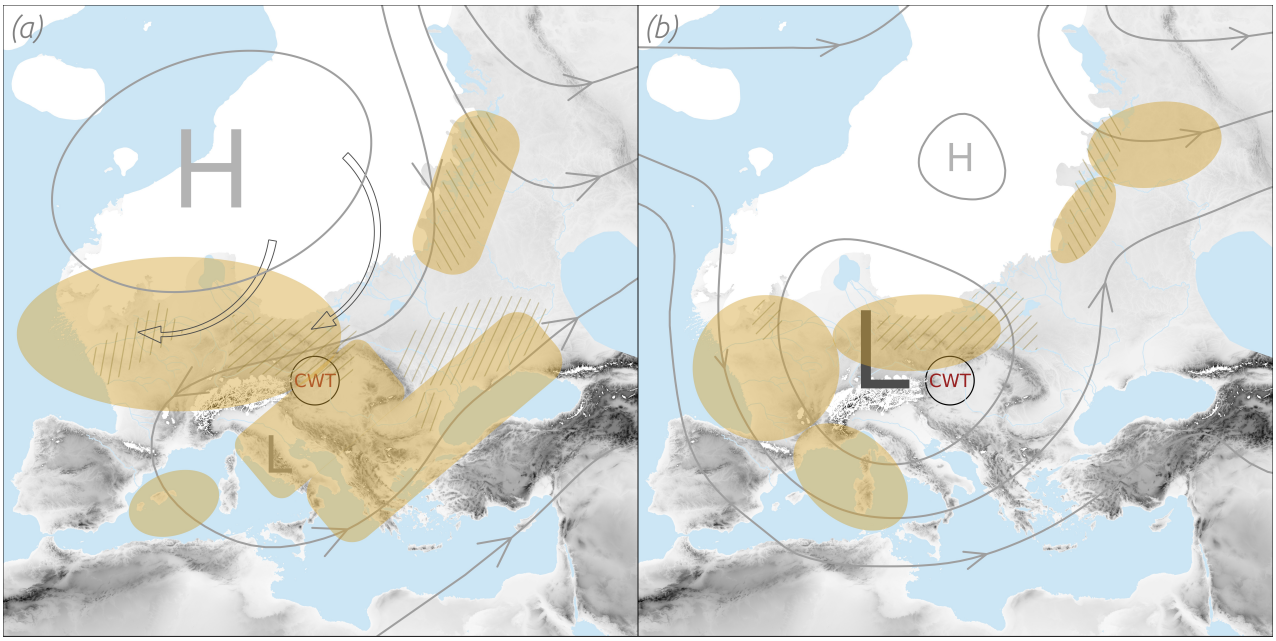

Figure 30: Conceptual model of the linkage between the European dust cycle during the Last Glacial Maximum and present-day loess deposits. The main dust deposition (filled), emission areas (hatched) and the Mediterranean low (L) are highlighted. The center of the region for the Circulation Weather Type analysis is denoted by CWT. (a) The easterly weather type regimes (NE, E, SE; black arrows) caused by the semi-permanent high-pressure (H) over the Eurasian ice sheet (white) prevailed 36% of the time over central Europe (Tab. 11). (b) The cyclonic weather type regime, which prevailed 22% of the time over central Europe (Tab. 11).

The east sector winds most likely dominated the dust cycle. The source regions of the dust carried by the cyclones to central and eastern Europe were more likely the southern margins of the EIS than the dry-fallen Channel–North Sea region, which was located west of the loess deposits.

In agreement with the hypothesis, a glacial simulation[243] calculated katabatic winds over the slope of the EIS. Also, GCM simulations[17,36] for the LGM confirmed prevailing easterlies over central and eastern Europe.

This hypothesis was tested using the LGM-adapted version of the Weather Research and Forecasting Model coupled with Chemistry[102–105] (WRF-Chem-LGM) for regional high-resolution climate-dust modeling. The WRF-Chem-LGM boundary conditions were derived from the LGM simulation of the Max Planck Institute Earth System Model in paleo mode[18–20] (MPI-LGM). The resulting simulation-based dust deposition rates were compared with mass accumulation rates — each of them independently reconstructed from and for one European loess site. The consistency between the climate model results and these proxy records supports the hypothesis.

7.3 Methods — Statistic Dynamic Downscaling

The regional climate model WRF-Chem-LGM, a refined version (Tab. 9) of the WRF-Chem[102], was applied to simulate the dust cycle in Europe during the LGM, taking into account the reconstructed PMIP3 and CLIMAP LGM conditions[17,178]. The atmosphere, surface, air chemistry, and the mineral dust[106] are fully coupled in the WRF-Chem-LGM. The specific setup (Tab. 8) enables the appropriate LGM climate and dust cycle modeling for Europe (Fig. 75).

Table 8: Modules and domain parameters applied to run the WRF-Chem-LGM simulations. University of Cologne (UC)

WRF-Chem version	3.5.1
Time step	3 min
Horizontal resolution	50 km
Vertical levels	35
MPI-LGM boundary data input interval	6 h
Microphysics	Lin Scheme[244]
Longwave, Shortwave Radiation	RRTMG[245]
Surface Layer	MM5 Similarity Scheme[246]
Land Surface Model	Unified Noah[247–249]
Planetary Boundary layer	Yonsei Univ. Scheme[250]
Cumulus convection parameter	Tiedtke Scheme[251]
Non hydrostatic	Yes
Chemistry modules active	Dust-only
Dry deposition	Yes[252]
Vertical turbulent mixing	Yes
Dust option	GOCART[253]
Dust emissions	UC Simplified Scheme[106]
Wet deposition	Enabled[107]

To respect LGM-specific environmental conditions, the global 1° PMIP3-LGM land-sea mask and the topography offsets[17] were interpolated to 50 km horizontal resolution and added to the WRF-Chem default land-sea mask and topography (Fig. 75). To implement the LGM land use affecting the top soil exposition, the 2° CLIMAP (Climate: Long range Investigation, Mapping, and Prediction[178]) LGM land-use reconstruction (including glaciers) was interpolated to 50 km resolution and converted (see Supplementary[37]) to United States Geological Survey 24 categories (USGS-24). The spatial distribution of the relative seasonality of the vegetation cover is assumed to be the same for the LGM and the present. Hence, based on the actualism[226,227] hypothesis, the 2° CLIMAP maximum vegetation cover for the LGM was interpolated to 50 km resolution and, using the factors of today's WRF-Chem vegetation cover seasonality, the monthly LGM vegetation cover was calculated.

The erodibility E (eq. 7.3.2), which defines the potential dust emission areas, results from the dust source function S:

$$S(z, z_{\min}, z_{\max}) = \left(\frac{z_{\max} - z}{z_{\max} - z_{\min}} \right)^5 \tag{7.3.1}$$

S is a local, non-linear probability measure based on neighboring terrain height differences to estimate the aeolian erodible alluvium fraction[234]. To calculate S, the 50 km resolved LGM topography is interpolated to 0.1°. For each of the resulting unglaciated land surface grid cells c, z is the height of c, and $z_{\min/\max}$ are the minimal/maximal heights within the square of 10° horizontal edge length centered at c.

For areas, in which the CLIMAP-LGM bare soil fraction b (interpolated to 0.1°) was larger than 0.5, E depends linearly on S, otherwise $E = 0$ (eq. 7.3.2). Potentially prevailing vegetation and snow covers, both hindering dust emissions, are considered to be mutually independent and uniformly distributed within a grid cell. To obtain the remaining erodible area, their potential effect was taken into account by reducing S by their coverage percentage (eq. 7.3.2). To avoid any effect of small physically meaningless artifacts due to the interpolation of the static boundary condition data, a filter was added that allowed for emissions only if the erodibility exceeds 9%.

$$E(z_i, z_{\max}, z_{\min}, c_{\text{snow}}, c_{\text{veg}}) = \begin{cases} S\,(1 - c_{\text{snow}})\,(1 - c_{\text{veg}}) & \text{if } b(z_i) > 0.5 \\ 0 & \text{otherwise} \end{cases} \tag{7.3.2}$$

The WRF-Chem-LGM ran in the dust-only mode using the simplified University of Cologne dust emissions module[106], the dry and wet deposition modules[107,252], embedded in GOCART (Global Ozone Chemistry Aerosol Radiation Transport) module[253]. The UC emission scheme[106,254] simulates size-resolved dust emissions — an advantage compared to other models.

Table 9: PMIP3 setup for global LGM simulations (first column) and its adapted implementation that refines the WRF-Chem to become the WRF-Chem-LGM. Default values listed for comparison to the right of the slash (second column).

	PMIP3-LGM[17]	WRF-Chem-LGM / WRF-Chem
Earth's orbit:		
Eccentricity	0.018994	0.018994 / 0.014
Obliquity	22.949°	22.949° / 23.5°
Gas concentrations:		
CO_2 (10^{-6})	185	185 / 379
CH_4 (10^{-9})	350	350 / 1774
N_2O (10^{-9})	200	200 / 319
CFCs, misc. (10^{-12})	0	0 / 169, 251, 538
Mineral dust	Computed or CMIP5-PI[255]	Shao et al.[106]
Land-sea mask	1° PMIP3-LGM[17]	1° PMIP3-LGM-based
Orography	Offsets added (1° PMIP3-LGM)	Offsets added (1° PMIP3-LGM-based)
Ice sheets	1° PMIP3-LGM	2° CLIMAP-LGM[178]-based
Land use	Same as in CMIP5-PI	2° CLIMAP-LGM-based
Vegetation cover	Same as in CMIP5-PI	Deduced from 2° CLIMAP-LGM and WRF geo-data[102]
Soil types	Not specified	Present-day WRF geo-data, EIS adapted
Erodibility	Not specified	Deduced[234] from 1° PMIP3-LGM topography and 2° CLIMAP-LGM bare soil
Sea surface temperatures	Not specified	MPI-LGM[18–20]

To reconstruct the dust cycle of the LGM, the 100-year time slice of the daily resolved and 2.5° interpolated MPI-LGM was statistically-dynamically downscaled using the CWT[36,53–55] analysis. This implied the classification of each MPI-LGM record according to its sea level pressure distribution in Transdanubia (Fig. 1, 18, and 30). Records classified as both, rotational and directional, were counted as directional only. Per CWT class (Tab. 11), 13 WRF-Chem-LGM simulations were run, each consisting of eight days. Each of these episodes was driven by distinct MPI-LGM initial and boundary conditions (Tab. 10). This resulted in an ensemble of 130 regionally-resolved episodic paleo-climate-dust simulations, in total encompassing 1040 days. For each episode, the first two days were considered as spin-up time and excluded from all subsequent analyses.

The weather type ensemble mean of a quantity Q is defined[55] as the weighted average

$$\langle Q \rangle = \sum_i \frac{f_i}{T} \int_T Q dt \tag{7.3.3}$$

where i represents the i^{th} CWT, f_i is the occurrence frequency of the i^{th} CWT in the MPI-LGM, and T is the duration of the CWT. To assess the capability of the statistic dynamic downscaling for dust simulations, the last 30 years of the MPI-LGM are dynamically downscaled using an identically configured WRF-Chem-LGM, which resulted in a continuous 30-year spanning simulation.

Independently reconstructed MARs from loess deposits in the domain are compiled for comparison (Tab. 1). Given the numerous, widespread present-day loess deposits all across Europe (Fig. 41 and 42) and their independently reconstructed MARs (Tab. 1 on p. 27; mutually independent and independent of the climate-dust simulations), the quantitative comparison of the dust deposition rates with these MARs is sound and suitable for evaluating the simulation-based depositions discerningly.

Table 10: Temporal setup for each regional dust episode simulation that must consist of 8 consecutive days according to the MPI-LGM calendar. If there are less than 13 separate 8-day episodes per CWT in the MPI-LGM, days with a different CWT are accepted according to the priorities ($^+$ = higher, $^-$ = lower)

	Consecutive days$^{\text{Priority}}$	Constraint
Spin-up	2^-	If available, of the same class as Main
↓		
Main	3	Must be of the same CWT class
↓		
Tracking	3^+	If available, of the same class as Main

7.4 Results and Discussions

7.4.1 Prevailing Eastern Sector Winds and Cyclones over Central Europe

Though the MPI-Hist CWT frequency proportions do not quantitatively reproduce those of the NCEP1, the MPI-Hist reproduces the relative relation among the ten CWT classes well (Fig. 31). For instance, from the categorical perspective, the same least frequent (E, SE) and most frequent (A) types resulted for the MPI-Hist and the NCEP1. The about sinusoidal (wavelike) shaped NCEP1 frequency distribution of the directional classes is generally reproduced by the MPI-Hist. CWT-SE and -E are the least frequent (~6%) in NCEP1, coherent with the MPI-Hist. Yet, the MPI-Hist underestimates them by −2.1 pp and −1.5 pp, respectively. The MPI-Hist reproduces best the CWT-C (+0.8 pp) and -N (+0.7 pp). CWT-SW and -W are the most frequent (~10%) directional classes in the NCEP1. They are also the most frequent in the MPI-Hist, however, overestimated by 2.8 pp and 2.3 pp, respectively.

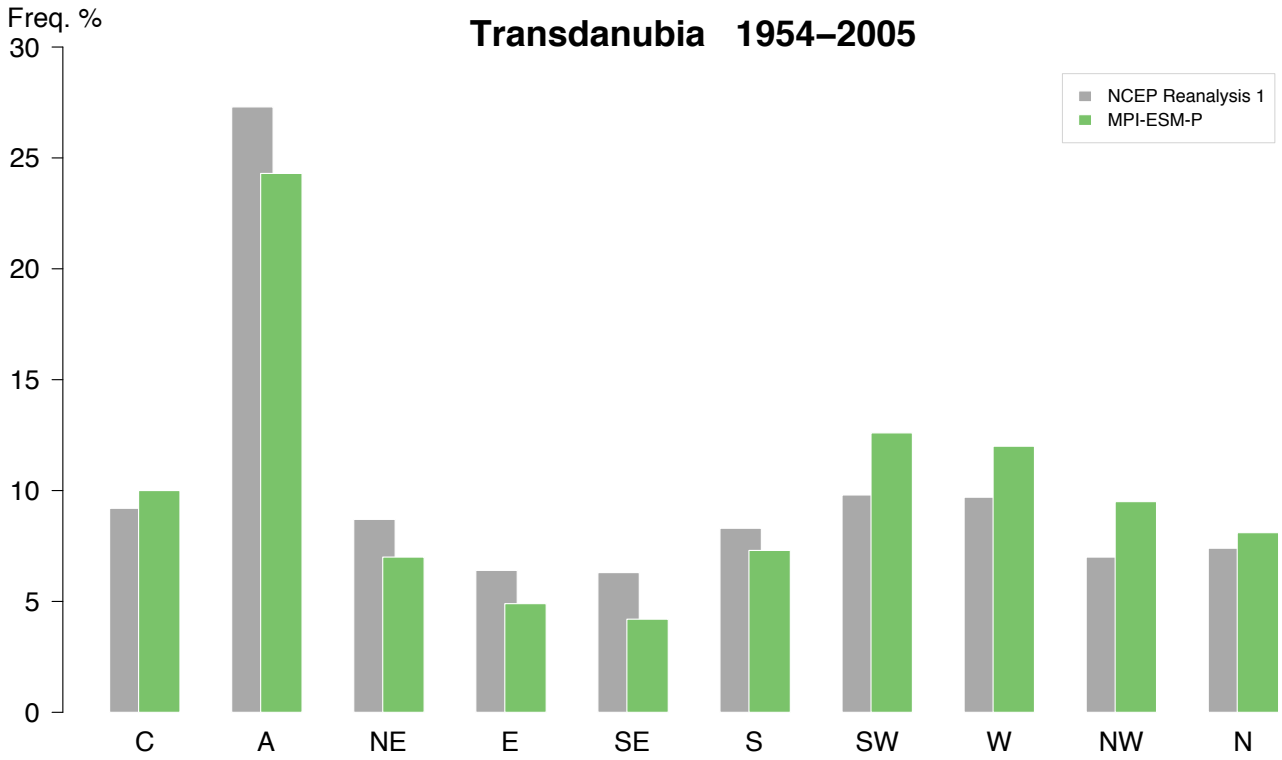

Figure 31: Transdanubian (Fig. 18) Circulation Weather Type occurrence frequencies for 1954–2005. Transient MPI-Hist simulation in green, NCEP Reanalysis 1 in grey. Records classified as half circular and half directional are counted as directional only. Circular regimes: cyclonic (C) and anticyclonic (A).

The NCEP1 spread between the most (CWT-SW) and least (CWT-SE) frequent directional CWT (3.5 pp) was not reproduced particularly well by the MPI-Hist: it (8.4 pp) is more than twice as large as the NCEP1 value. The west sector winds were disproportionately often (7.6 pp) simulated along with too few anticyclones and east sector winds. In total, 5.3 pp of the eastern wind sector occurrence in NCEP1 is not represented in the MPI-Hist. The western wind sector overestimation is not a unique MPI-Hist problem but a general problem of the GCMs. They underestimate blocking at high latitudes — especially over Europe[225]. For example, the MPI-Hist underestimates[225] the number of blocked days by 4% compared to ERA40 Reanalysis. This bias in the transient MPI-Hist likely occurs also in the MPI-LGM based Transdanubian CWT distribution. There, the presumably underestimated east sector winds reduces the quality of the LGM dust cycle reconstruction for Europe.

Generally, the NCEP1 based CWT results for 1979–2005 are coherent with the NCEP-DOE Reanalysis 2 (NCEP2)[176] and ERA-Interim results (Fig. 32). Taking the average over the NCEP2 and ERA-Interim as the best available approximation of the real atmosphere from 1979 to 2005, then the NCEP1 overestimates markedly (~3 pp) the occurrence frequency of the anticyclones, while it underestimates (−2.6 pp) the eastern wind sector.

On the contrary, the MPI-Hist underestimates the anticyclonic regimes (−4 pp), the southerlies (−1.5 pp) and the eastern wind sector (−7 pp) distinctly. Correspondingly, it overestimates the remaining CWT occurrence frequencies. In particular, the cyclonic regimes and western wind sector are simulated too frequent. Based on the NCEP1 MPI-Hist comparison result for 1954–2005, it is very likely that the MPI-LGM overestimates the occurrence frequencies of the western wind sector and the cyclones at the expense of the anticyclones, the southerlies, and the eastern wind sector. The occurrence frequency of the east sector winds is particularly relevant for the quality of the LGM dust cycle reconstruction for Europe.

Coherent, almost identical CWT occurrence frequencies resulted from the transient MPI-Hist (Fig. 33) when basing the CWT calculation only on its last 50 years compared to basing it on its complete time span (1850–2005). This shows that being transient, which is the unique property of MPI-Hist, hardly leads to distinct CWT occurrence frequency distributions for different periods extracted from the MPI-Hist.

The comparison of the MPI-Hist based and the MPI-ESM-P Preindustrial (MPI-PI) based CWT occurrence frequencies results in almost identity — though the MPI-PI was forced by the stationary *Preindustrial* boundary conditions. The MPI-PI differs most from the MPI-Hist by less frequent southwesters and westerlies (~1%); whereas southeasters were more frequent (~1%; Fig. 33). Consequently, it represents the NCEP and the ERA-Interim CWT frequency distributions better (Fig. 32 and 33). Therefore, the MPI-PI is even more appropriate than the MPI-Hist to approximate the real atmosphere over central Europe (Transdanubia) during 1954–2005 and 1974–2005. The stationary MPI-PI was thus selected as the best MPI-based approximation of present-day conditions and constitutes an adequate reference to compare the stationary MPI-LGM with (Fig. 34).

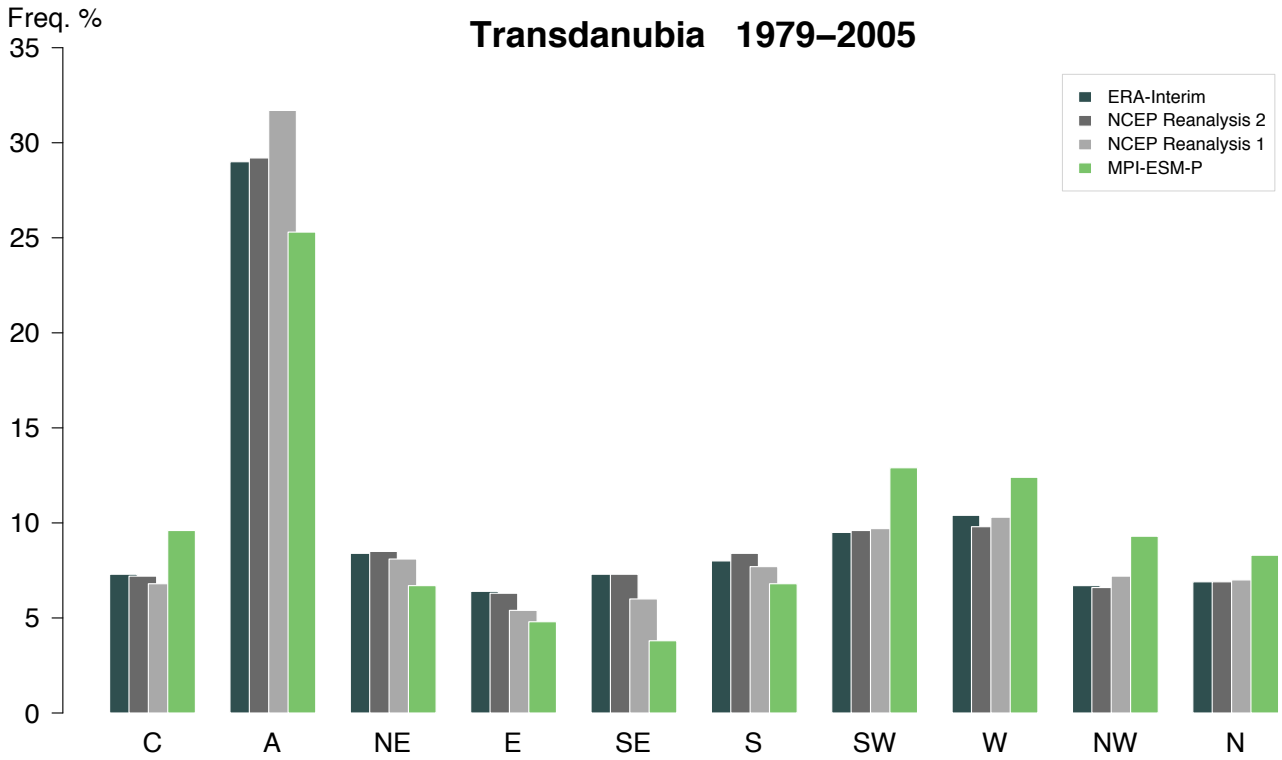

Figure 32: Comparison of the Transdanubian Circulation Weather Type occurrence frequencies based on MPI-Hist, NCEP, and ERA-Interim for 1979–2005. Hybrid records are classified according to their directional component. Circular regimes: cyclonic (C) and anticyclonic (A).

The Transdanubian MPI-LGM and -PI CWT frequency distributions differ considerably (Fig. 34, Tab. 11 on p. 101). The LGM east sector winds frequency was more than twice that of the present (+18.6 pp), dominating the near-surface atmosphere 36% of the times. The cyclonic regime doubled (+11.6 pp); it was the single most frequent (22%) LGM CWT class. Southerlies occurred more often (+2.1 pp). On the contrary, the western wind sector (16%, −16 pp), the anticyclones (−15.2 pp), and the northerlies (−1.3 pp) were less frequent during the LGM. The overall shape of the Transdanubian and the Franconian MPI-LGM frequency distribution correspond well (Fig. 34 and 24).

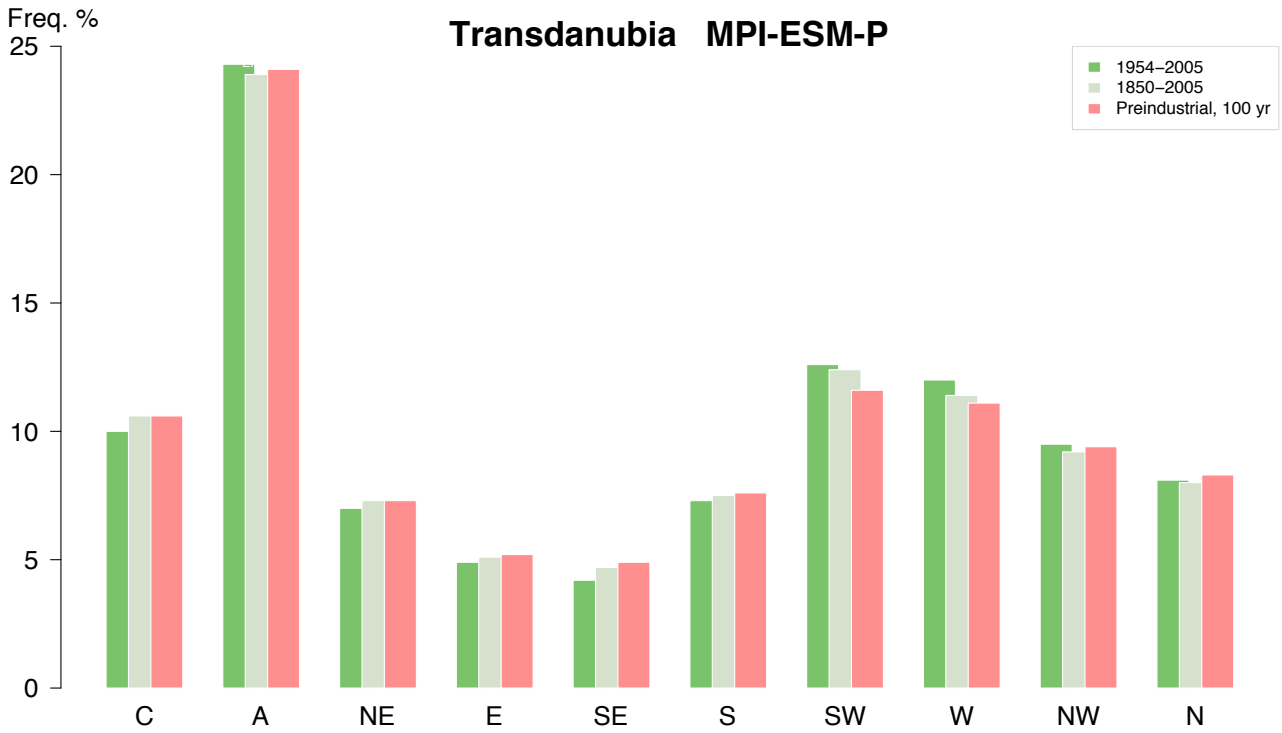

Figure 33: Transdanubian (Fig. 18) Circulation Weather Type occurrence frequency distribution of the transient MPI-Hist (MPI-ESM-P) 1850–2005 run, its transient 1954–2005 subset, and the stationary 100-year MPI-ESM-P Preindustrial simulation (MPI-PI). Half circular and half directional classified records are counted as directional only. Circular regimes: cyclonic (C) and anticyclonic (A).

In the recent climate (PI in Tab. 11, Fig. 34), the western wind sector and the anticyclones prevail 32% and 24% of the times, respectively. In contrast thereto, during the LGM, the eastern wind sector and the cyclones dominated with 58% the LGM weather types over central Europe (Transdanubia). Their glacial dominance is in line with the Franconian PMIP3 ensemble and the COHMAP results[36,73] (Fig. 24). The latter[73] indicated northeasters and easterlies along the southern EIS margin. During the LGM, easterly wind regimes associated with the EIS High[73] (Fig. 30a) developed frequently.

Table 11: Central European (Transdanubian) Circulation Weather Type occurrence frequencies (%) based on the MPI-ESM-P-LGM, -PI (Preindustrial), and -Hist (1850–2005, transient) simulations. Circular regimes: cyclonic (C), anticyclonic (A).

	C	A	NE	E	SE	S	SW	W	NW	N
LGM	22.2	8.9	12.4	13.4	10.2	9.7	6.8	4.3	5.0	7.0
PI	10.6	24.1	7.3	5.2	4.9	7.6	11.6	11.1	9.4	8.3
1850–2005	10.6	23.9	7.3	5.1	4.7	7.5	12.4	11.4	9.2	8.0

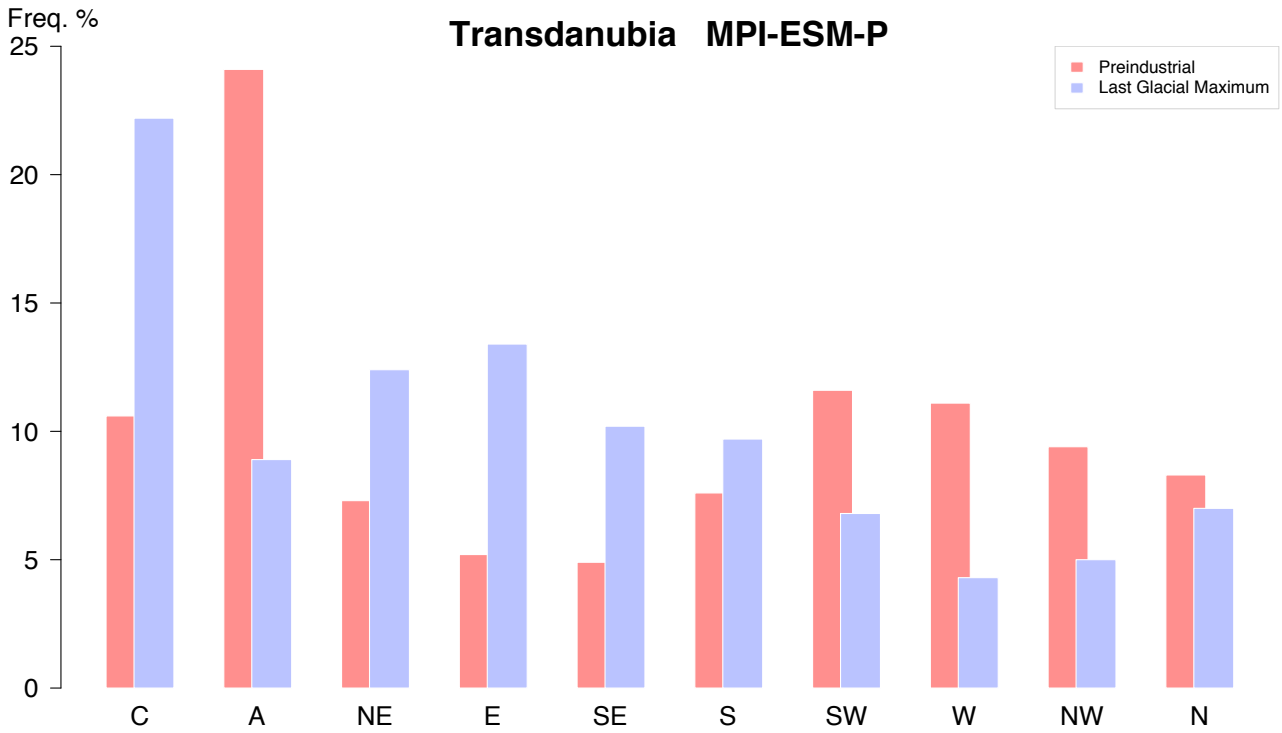

Figure 34: Central European (Transdanubian, Fig. 18) Circulation Weather Type occurrence frequency distribution, based on the MPI-LGM and -PI. Hybrid events are counted by neglecting their circular component. Circular regimes: cyclonic (C), anticyclonic (A)

The LGM storm tracks diverged from today's[69], running either along the Nordic Seas, or over central Europe, or over southern Europe[36,143] (Fig. 5). Alpine, western, and southern European climate proxies indicate that the LGM storm tracks ran along the Mediterranean Sea, splitting over the Adriatic Basin with one branch heading north and then passing over central Europe[143]. These findings, as well as the reconstructed surface winds for central and eastern Europe with dominantly northern component[46], support the notion of the EIS High and the prevailing easterly CWTs over central Europe.

The jet stream, which was shifted to the Spanish latitudes[143], is in line with the CWT results. The same is true for the westerlies. They blew along the zonal Mediterranean corridor much more often[143].

The EIS High, or more precisely the High over the Scandinavian part of the EIS (SIS High), favoured a clockwise surface wind circulation around the SIS. This implied northeasters along the eastern European SIS margin and agrees with the conically shaped dust plume deposits along the eastern EIS margin (Fig. 43 and 56).

The increased cyclonic regime occurrence frequency over central Europe (Tab. 11) during the LGM agrees with the storm frequency enhancement inferred from magnetic susceptibility and grain size records[82] for western Europe as far as western Germany. The frequent cyclones over central Europe (Transdanubia) were possibly related to the northern branch of the Mediterranean storm track[143] and the deflection effect of the EIS elevation[36]. More frequent cyclones might have occurred due to the strengthened polar-front jet stream over the Mediterranean[36].

However, directional wind regimes need to be incorporated, in particular, the easterlies that more than doubled in frequency (36%), compared with 17% during the PI (Tab. 11). Only then, a more complete LGM portrayal results of the central European aeolian dust cycle.

Northern-central European grain size records of the Late Pleniglacial indicate easterlies[46]. Eifel sediments[47] (6.5°E, 50.3°N) that accumulated 36 to 18 kyr ago, indicate more frequent (up to 19%) easterly dust storms. Increased dust accumulation[47] and strong easterlies over northern, central, and western Germany (23 to 20 kyr ago), which deposited heavy minerals from remote sources[48], support my findings. Likewise, a shift to prevailing easterlies can be deduced from the Harz Foreland loess record (51.9°N, 11.2°E, 150 m asl) for the LGM[49] and from the proxies located near the southern and eastern margins of the EIS[45]. For example, the wind-polished rocks there indicate easterlies, presumably of katabatic origin[45]. In addition to the easterlies, southeasters were inferred[45] from proxies in Denmark (22 to 17 kyr ago).

During the LGM winters, NNE winds prevailed in the Carpathian Basin (CB), according to simulations[57]. However, in the course of a LGM year, the prevailing CB winds possibly alternated[46,51,52] (N, NW, SE) as an effect of the surrounding mountain ranges. For Hungary, northerlies and northeasters were found during the LGM summer, and westerlies during the winter[50]. The former conforms with my findings on the prevailing eastern wind sector, the latter might be related to the increased cyclonic regime frequency (Tab. 11). For Katymar (Hungary), the main wind direction possibly varied during the LGM[46].

Over northern Serbia NNW and SE winds and over the Danube-Tisza confluence SW winds were inferred from loess[57]. Over northeastern and eastern Romania, NNE- and NNW-winds prevailed, according to geochemical and mineralogical analyses[46]. They were likely forced by northerly katabatic winds from the SIS. Over the lower Danube basin including Dobruja (Dobrogea, Romania), strong northerly winds advected dust, in addition to dust from the WNW[81,170], from the SIS margin.

Katabatic northerlies and northeaster from the EIS dominated over Dobrudja (44.32°N, 28.18°E, Mircea Voda), the eastern Walachian Plain (both Romania), and Stary Kaydaky (Dniepropetrovsk, Ukraine, 48.37°N, 35.12°E), according to sand deposits all over Ukraine[52]. In western Ukraine, the Carpathians deflected[52] them, possibly leading to northwesters there in agreement with eight loess sections[46].

The high aridity and grain size variations of the Surduk (Serbia) and Stari Bezradychy (Ukraine, Tab. 1) records indicate prevailing dry, periodically strong northeasters and easterlies[46,91]. The central and eastern European loess was created to some extent from glacial dust originating from the Aral and Caspian Sea[86], which fell dry partly during the LGM. This indicates dust transport by easterlies and southeasters[46].

According to a simulation[43], the main dust sources for the loess in Stayky (50.09°N, 30.9°E) were located in Stayky's west-northwest, suggesting that dust was transported by WNW winds to Stayky. This result could be related to my finding of the western wind sector prevailing 16% of the times (Tab. 11). Possibly, short but strong and large dust amount carrying (north-)western wind episodes existed (Fig. 58), though the occurrence frequency of the western wind sector was significantly reduced (Tab. 11). Yet, the suggested WNW winds deviated clearly from the finding of dominant east sector winds (Fig. 37) that prevailed 36% of the times during the LGM over central Europe (Tab. 11). My results (Tab. 11) contradict that during the LGM winters southwesters, westerlies, and northwesters should have dominated[45] in central Europe (*here*[45]*:* 0–30°E, 40–55°N).

7.4.2 Major Erosion from the Fringes of the Eurasian Ice Sheet

During the LGM, large dust amounts resulted from aeolian erosion occurring within the corridor that was southwards confined by the Alps, Danube, and Black Sea, and northwards by the EIS margin (Fig. 35 and 36). The simulation-based LGM reconstruction shows that the emission corresponds to the predefined potential dust sources (Fig. 75), implying that winds are strong enough to erode the surface irregardless of other limiting factors such as the vegetation and the snow cover.

In particular, the erosion north and east of the Alps and near the Carpathians (Fig. 35 and 36) is spatially consistent with the loess-inferred dust source reconstructions[46,57]. The Alpine erosion is in line with the fieldwork-inferred existence of erodible material generated by the Alpine ice cap[88]. The highest emission rates (10^5–10^6 g m^{-2} yr^{-1}) occurred at the southern EIS margins, within 15–18°E and 51–53°N (Fig. 35). North of the Carpathians (~50°N, 25°E; Fig. 35), the emission range resulting from my simulations includes the range found in a 'Greenland stadial' GCM simulation[43] (80–140 g m^{-2} yr^{-1}). Yet, their range is at the lower limit of my results.

Most of the erosion was glacial (Fig. 35). The largest occurred at the southern and southeastern margin of the EIS, conforming to dust flux estimates based on loess deposits[57]. From the dry-fallen Channel up to the German Bight, emissions were high as well (Fig. 35). For the dry-fallen German Bight, they agree considerably with a GCM simulation[84], according to which the average emission from the Channel up to the German Bight was 140 g m^{-2} yr^{-1} and the maximum was more than 200 g m^{-2} yr^{-1}.

Dust emissions from topographic corridors, such as the German-Polish border region, were strong (Fig. 35 and 75). Strong emissions occurred as well from the plains near the foothills of the Caucasus, the east Carpathians, the Massif Central and from the Channel and North Sea Basins. This correlation between low-sloped or low-laying environments and high dust emissions is also found today, e.g. in the dust source regions of Mali, Mauritania, and the Bodélé Basin[256]. According to this finding, the assumption that the present-day dust sources are mainly hydrological basins, which contain large amounts of alluvium[234], would also apply to the LGM.

The reduced LGM vegetation cover facilitated, compared to the interstadial climate[43], a 30–50% increase of the dust emission rates particularly from the western European deflation areas.

The Carpathian Basin synchronously was a source and sink[57] (Fig. 35 and 47). Coherent with loess-inferred results[46,57], my results (Fig. 35) provide evidence for major dust sources of silt-size particles surrounding the Carpathians and Eastern Alps. The dust emissions from the Danube Basin, located between the Black Sea and the Carpathians (Fig. 35), are consistent with strong winds reconstructed for Urluia[81] (15 km away from the Danube, near the west coast of the Black Sea). The dry-fallen Black Sea littoral zone emissions agree with mineralogical results[90] (Fig. 35).

Apart from the proglacial surfaces south of the EIS, the east sector winds eroded areas almost all over Ukraine, in southern Russia, in northern France, in the unglaciated part of the North Sea Basin, in the lower Danube basin, and at the Eastern Alps (Fig. 37). On the contrary and though they were the single most frequent central European CWT (Tab. 11), the cyclonic regimes eroded only a few areas: near the southernmost EIS margin around the German-Polish border, at southeastern England, and along the southeastern EIS margin (55–63°N; Fig. 38).

The statistic dynamic downscaling (Fig. 35) and the dynamic downscaling (Fig. 36) result in largely conforming dust emission rate estimates. Though, according to the dynamic downscaling, much higher emission occurred in the Middle East (Levant), this region is far beyond the scope of the CWT analysis for central Europe (Transdanubia, Fig. 18). For western Europe in particular in French regions, the statistic dynamic downscaling estimated higher rates than the dynamic downscaling; the reverse is found from southern Ukraine to the Volgograd region (southwest Russia).

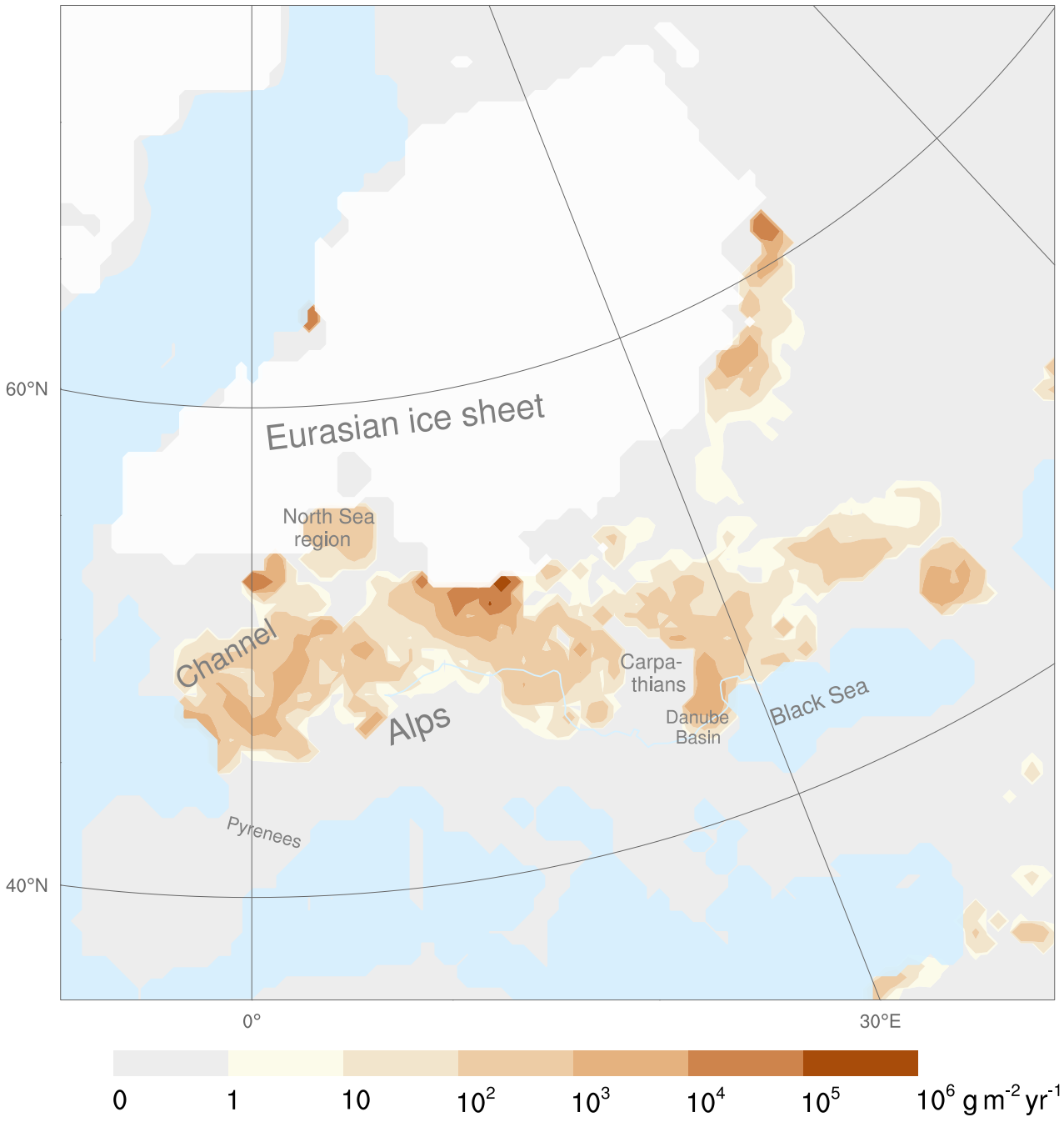

Figure 35: Simulated European dust emission rates for the LGM, based on the statistic dynamic downscaling of the complete, i.e. 100-year long, MPI-LGM. Ice sheet extents in white.

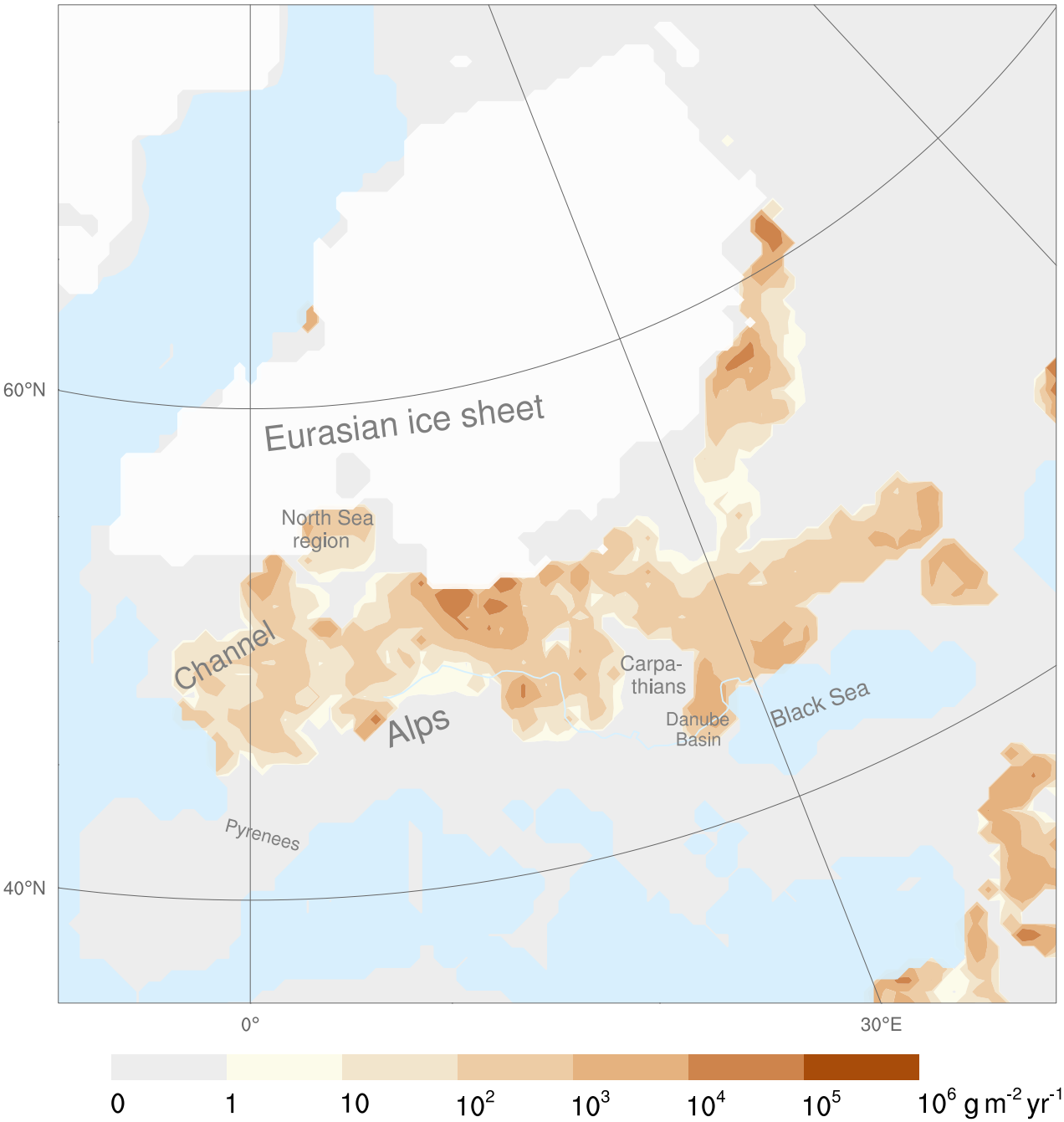

Figure 36: Simulated European dust emission rates for the LGM, based on the dynamic downscaling of 30 consecutive MPI-LGM years. Ice sheet extents in white.

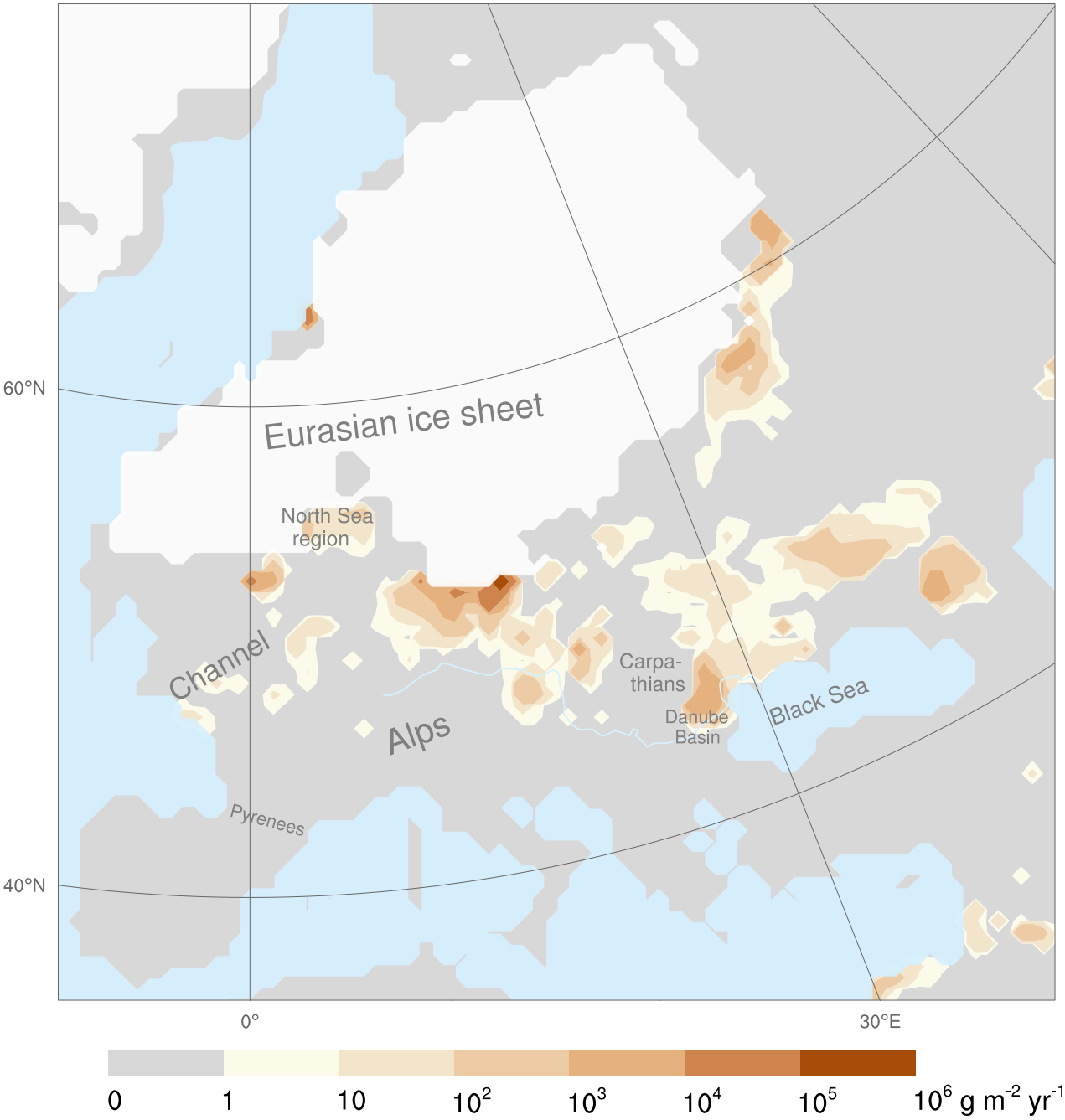

Figure 37: Contributions to the total LGM dust emission rates only by northeasters, easterlies, and southeasters

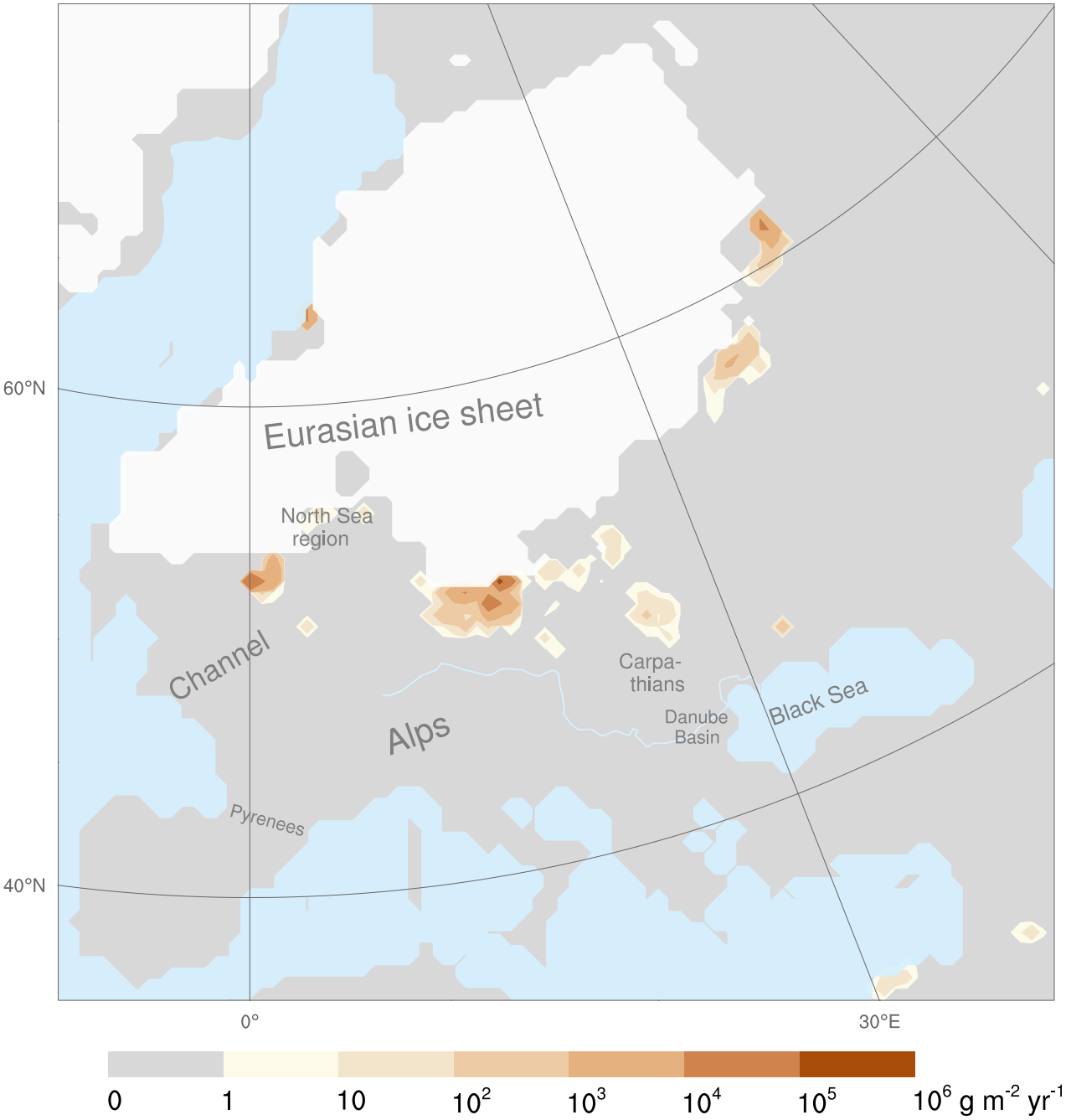

Figure 38: Contributions to the total LGM dust emission rates only by cyclonic regimes.

7.4.3 Dust Emission to Deposition Comparison within Europe

The LGM dust emissions dominated the depositions in the southern and eastern proglacial EIS areas, according to the WRF-Chem-LGM simulation based reconstruction (Fig. 39). This applies in particular to Saxony, Poland, Czechia, and the western CB. There, the dust emission rates were partly larger than 10^5 g m^{-2} yr^{-1}. The emissions dominated also in the Moscow region and north of Vologda (10^5 g m^{-2} yr^{-1}; Fig. 39), in eastern England (east of London), in the proglacial North Sea Basin, in the Danube Basin, and from the Danube Basin eastwards along southern Ukraine to Volgograd (Russia) and the northern Caucasian foreland. The EIS covered Norway entirely; thus, the emission spot at the Norwegian coast is a numerical artifact resulting from an interpolation discrepancy of PMIP3 and CLIMAP data.

Most of the dominant emission regions were located inland, several 100 km away from the Atlantic and Mediterranean Sea. There, the vegetation and snow covers were likely sparse—at least seasonally—and cold dry winds prevailed. These properties enhanced aeolian surface erosion and dust transport.

The EIS cast its rain shadow over the proglacial Moscow and Vologda regions. Consequently, the prevailing northerlies and westerlies were exceptionally dry there (Fig. 39). Similarly, the western CB is covered by the Alpine rain shadow, and the area from the Danube Basin to southwestern Ukraine by the Balkans and Carpathian rain shadows (Fig. 39). These rain shadows prohibited the moisture advection by the west sector winds. The LGM east sector winds and northerlies—prevailing 43% of the times (Tab. 11)—favored dust emissions, as neither their origin nor track were located over extended water surfaces before these winds reached erodible surfaces.

In contrast to the Middle East, dominant emissions were absent in the Mediterranean area (Spain, Italy, the Balkans, Greece, and Turkey), probably due to the prevailing year-round vegetation cover (Fig. 39, 78, and 79).

Applying dynamic downscaling, the dust emissions dominated the depositions in fewer but larger spatial clusters, particularly in the southern proglacial EIS area, and between the Danube Basin and the Caucasian foreland (Fig. 40 and 39). On the contrary, according to the statistic dynamic downscaling, the dominant dust emissions were more sparsely distributed over Europe (Fig. 39 and 40). Nevertheless, the estimated dominant emission centers, based on statistic dynamic downscaling and dynamic downscaling, are congruent.

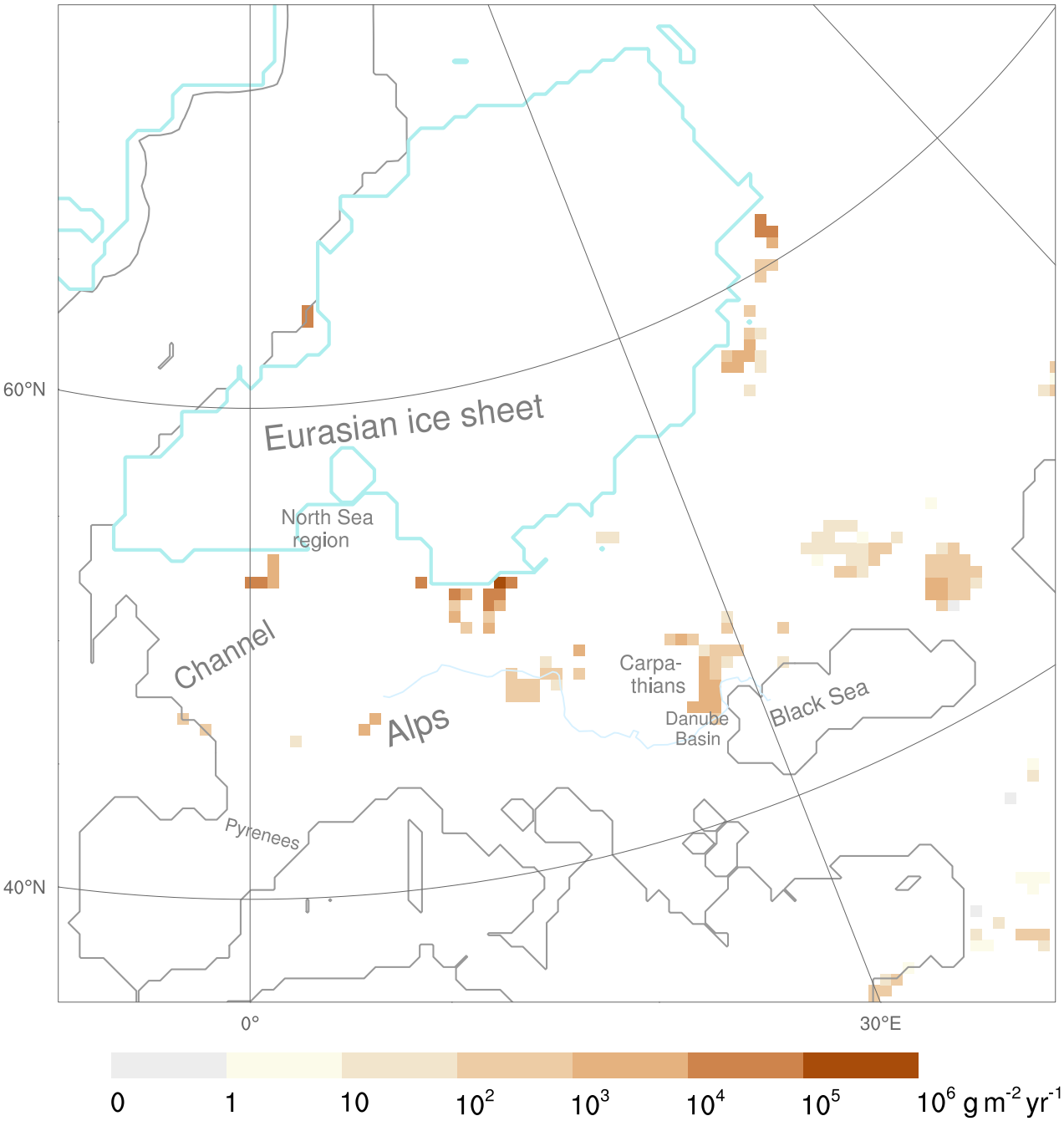

Figure 39: Net LGM dust emission rates based on the statistic dynamic downscaling dust cycle reconstruction. Obtained by subtracting the deposition from the emission rates. Negative net emission areas masked (white).

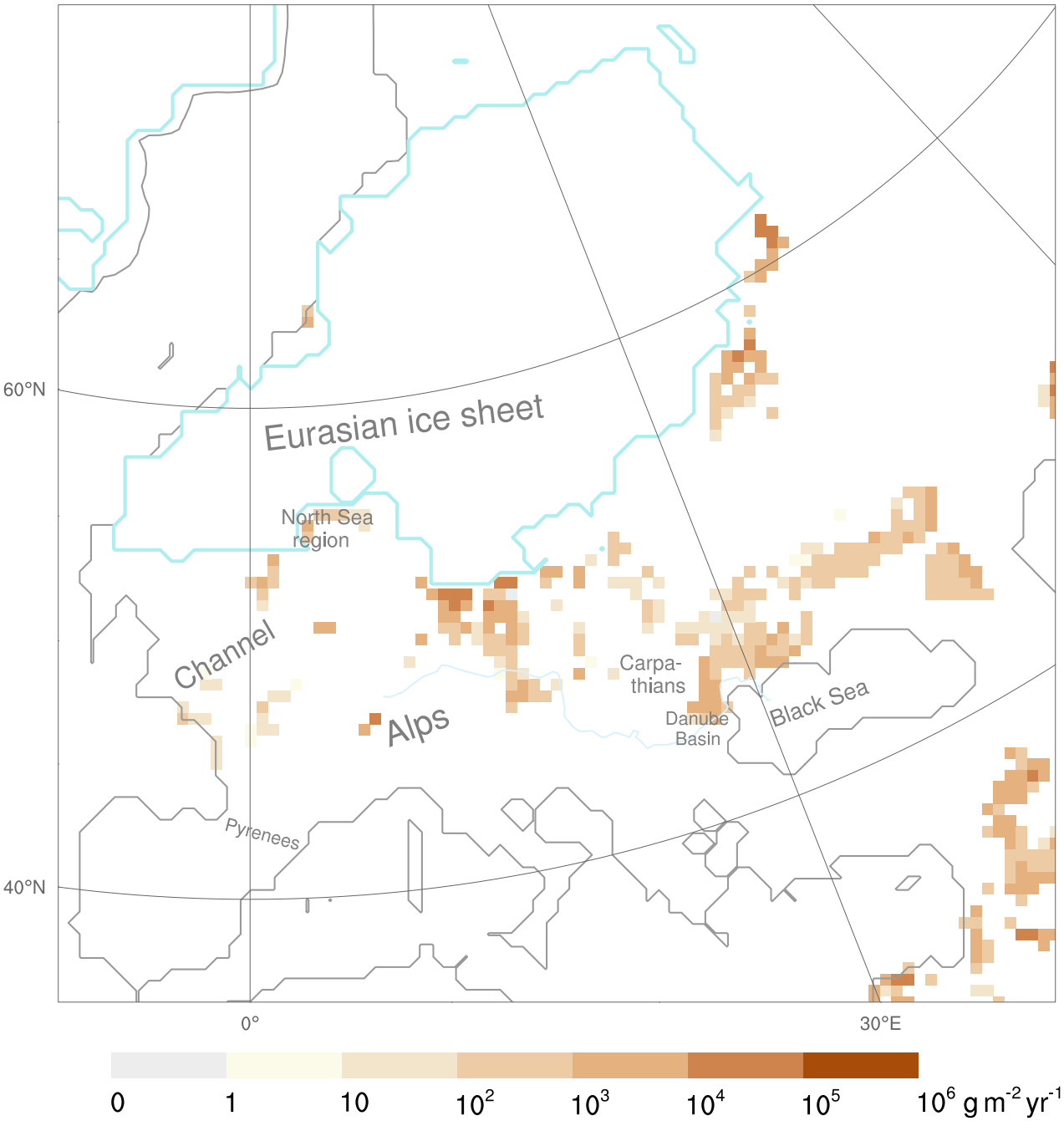

Figure 40: Net LGM dust emission rates based on the dynamic downscaling dust cycle reconstruction. Obtained by subtracting the deposition from the emission rates. Negative net emission areas masked (white).

7.4.4 Consistency of Simulated Dust Depositions and Loess Accumulation Rates

The European loess belt (Fig. 41) consists of extensive paleo dust deposits that enable the validation of paleodust simulations for Europe[79,83–85] (Fig. 42 and 41). During the LGM, its area was unglaciated and northwards confined by the EIS. Subsequently, F_D refers to the simulated LGM deposition rates that take into account all aeolian dust depositions processes: the gravitational settling, the dry, and the wet deposition.

During the LGM, dust was transported over central Europe by cyclonic regimes, scarcely occurring western, and dominant east sector winds (Tab. 11) according to my simulations (Fig. 56, 57, and 60). Consistently, present-day loess sites west of the Meuse (Maas) were caused by dust deposited by northerlies, northeasters, and easterlies[45]. My findings are also supported for central Europe, where LGM wind proxies evidence easterlies[46]. Wind proxies in the Benelux indicate westerlies, northwesters, and northerlies for the LGM[46].

The F_D and the mass accumulation rates (MARs, Tab. 1) that were inferred from various sites in the European loess belt agree quantitatively well (Fig. 43, 45, and 47). The spatial F_D distribution is congruent to the loess distribution in Europe today (Fig. 43, 44, 41, and 42).

For example, the locations of substantial LGM F_D (Fig. 43 and 44) are congruent with today's loess presence (Fig. 41 and 42) in the CB, along the Danube Basin, and in most of the—back then unglaciated—areas of the European Plain.

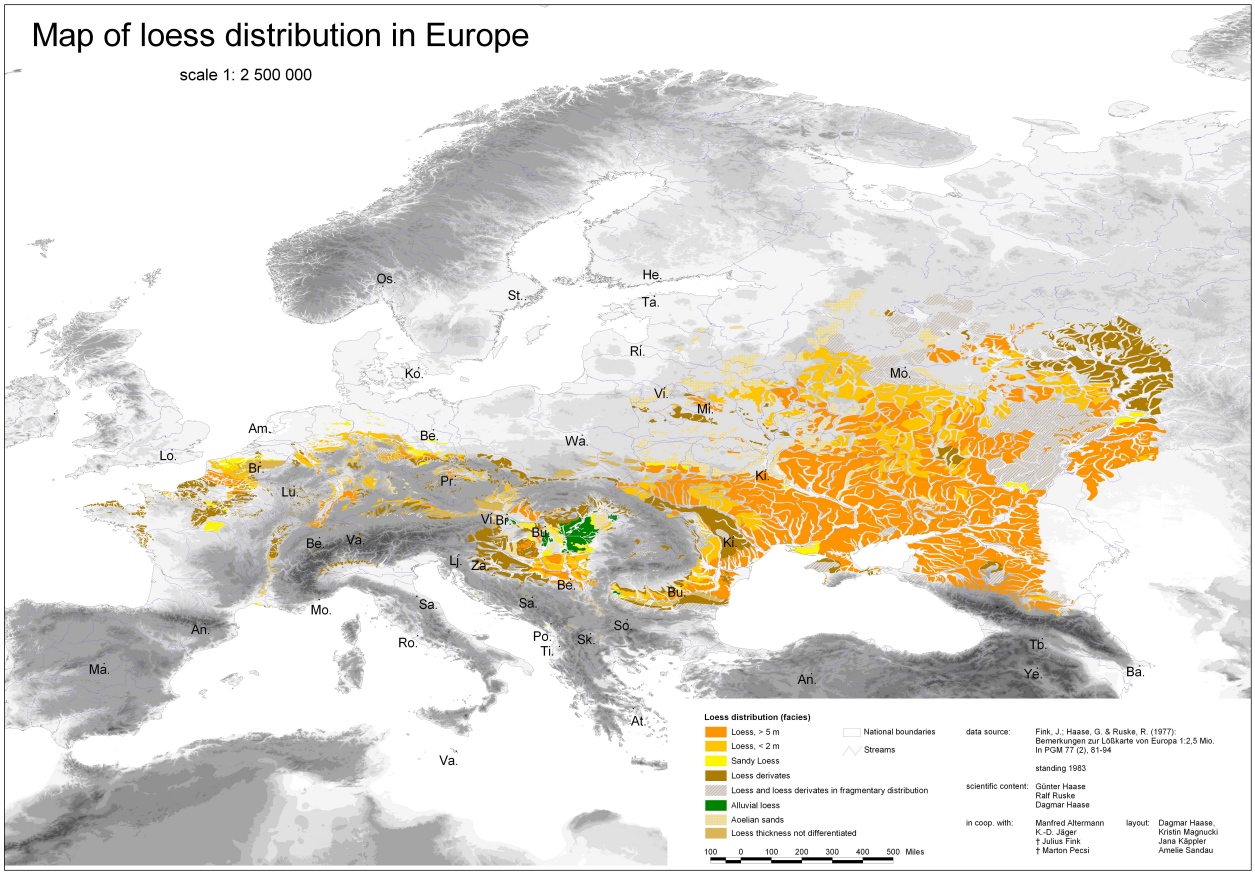

Figure 41: Loess distribution in Europe today (peer-reviewed). Map bases only on fieldwork data. From from Haase et al.[79] © Elsevier (p. 195)

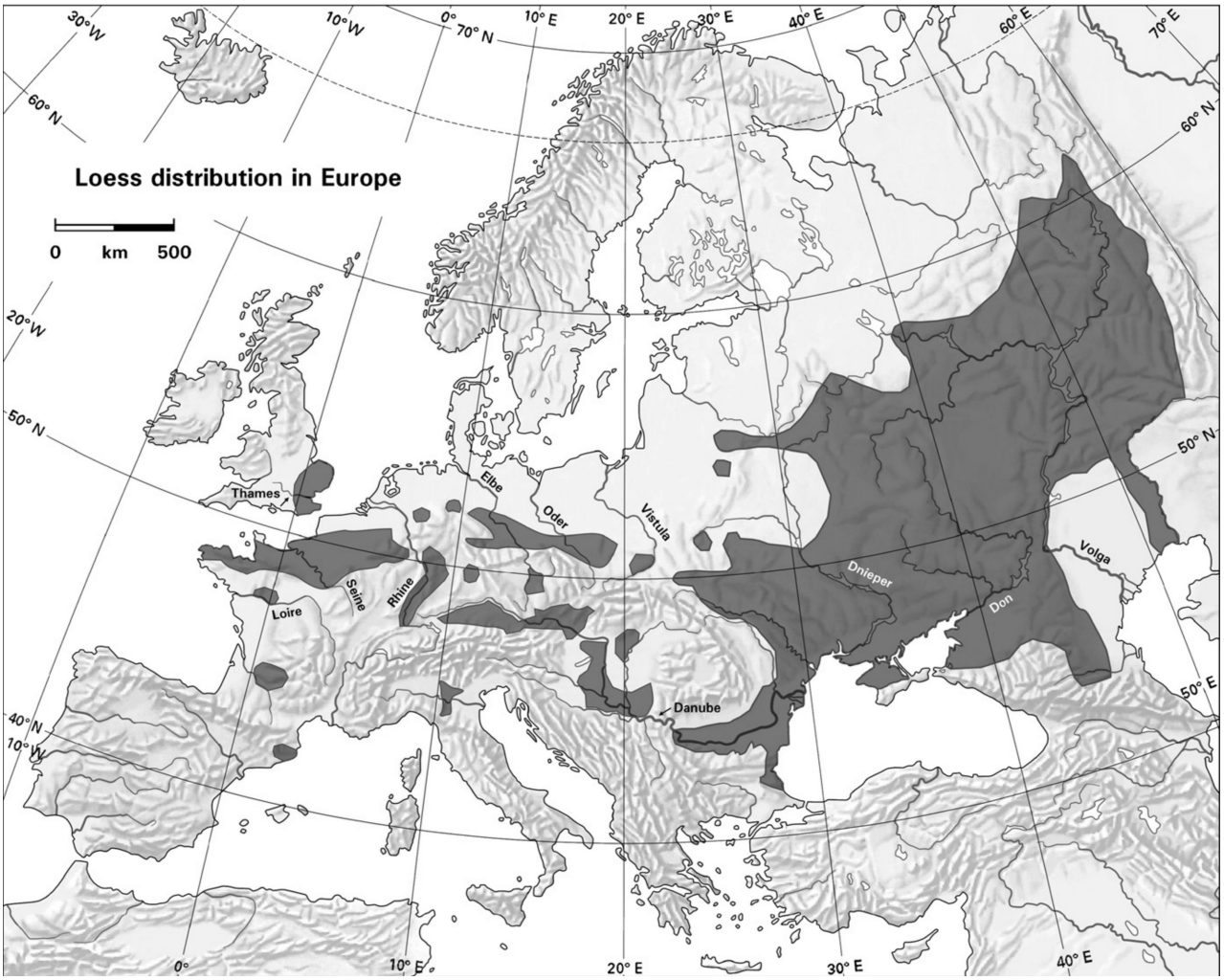

Figure 42: Loess distribution in Europe today (peer-reviewed). Map bases only on fieldwork data. From Smalley et al.[89] © Elsevier (p. 195)

F_{D12} denotes the deposition rate of particles up to 12 µm and F_{D20} of particles up to 20 µm diameter. Both (Fig. 47) were estimated either from dynamic ($F_{D20\,\mathrm{DD}}$, $F_{D12\,\mathrm{DD}}$) or statistic dynamic downscaling simulations ($F_{D20\,\mathrm{SD}}$, $F_{D12\,\mathrm{SD}}$). The dynamic and statistic dynamic downscaling resulted in similar F_D for central Europe, though the dynamic downscaling potential for varying MPI-LGM boundary conditions is 14 times larger. This similarity confirms the effectiveness and efficiency of the statistic dynamic downscaling for simulating dust (Fig. 47).

Proglacial of the southernmost EIS, the $F_{D20\,\mathrm{SD}}$ are at least ten times larger ($F_{D20\,\mathrm{SD}} > 10^4$ g m^{-2} yr^{-1}) than the $F_{D20\,\mathrm{DD}}$ maxima. In westernmost Europe (on the partly EIS-covered British Isles and the Bay of Biscay) the $F_{D20\,\mathrm{SD}}$ is about ten times larger than the $F_{D20\,\mathrm{DD}}$, while it is about ten times smaller on the southeastern proglacial EIS plain and in western Russia. These differences result most likely from the different LGM reconstruction methods: The statistic dynamic downscaling bases on selecting long and unambiguously prevailing prototypical episodes of each CWT regime, while the dynamic downscaling implies a sequence of unclassified boundary conditions that induces more frequent atmospheric changes. The consecutiveness (30 years) of the dynamic downscaling likely enables more atmospheric and dust intra-domain interaction than during the ensemble of isolated 8-day simulations. As this dissertation mainly focuses on the statistic dynamic downscaling, the statistic dynamic downscaling results are discussed subsequently (Fig. 43, 44, 45, and 46).

Sediment accumulation rates are commonly published as MARs and MAR10s; MAR10s base only on less than 10 µm diameter particles. For the most reasonable comparison of the simulation-based results and the available independent reconstructions, it makes sense to compare the F_{D20} with the MARs (Fig. 43 and 44) and the F_{D12} with the MAR10 (Fig. 45 and 46).

The highest F_{D20} (larger than 10^5 g m^{-2} yr^{-1}) occurred in western Poland (Fig. 43 and 44), slightly smaller F_{D20} of 10^4–10^5 g m^{-2} yr^{-1} were found in the adjacent areas, e.g. eastern Germany. On most of the North European Plain, extended by the dry-fallen German Bight, eastern England, and areas southeast of the Carpathians, F_{D20} reached 10^3–10^4 g m^{-2} yr^{-1}. Regional deposition maxima of 10^3–10^4 g m^{-2} yr^{-1} occurred along the French Atlantic coast (46–48°N), on the eastern side of the Carpathians (44–47°N) including the Lower Danube Plain, and near the Caucasus (44–45°N) (Fig. 43 and 44). They coincide with today's extensive loess derivates[79] along the French Atlantic coast, at the European foothills north of 42°N, and with the loess thickness maximum in the Romanian Danube Plain[90].

The high quality of the simulations is recognizable, e.g. in the CB, of which loess covers almost half[257]. The loess and its underlying red clay are both of aeolian origin[257]. There, the simulated F_{D20} (100–1000 g m^{-2} yr^{-1}; Fig. 43 and 44) coincide with the bulk MARs[257] (200–500 g m^{-2} yr^{-1}). In Ukraine and at the eastern EIS margins, the F_{D20} of 100–1000 g m^{-2} yr^{-1} agree with the bulk MARs (Fig. 43 and 44).

The European deposition rates that resulted from GCM dust simulations for the LGM range between 1 and 100 g m^{-2} yr^{-1}. They are at least ten to one hundred times lower than both, the WRF-Chem-LGM simulated deposition rates and the reconstructed MARs. Thus, a detailed comparison with GCM simulations is omitted, because it would not yield additional understanding nor insight beyond the fact that the GCMs considerably underestimate the dust cycle.

The bulk MAR of a few loess deposits is higher than their respective F_{D20}. This finding does not question the F_{D20} validity, as the WRF-Chem-LGM simulations exclude silt and sand with more than 20 µm diameters, while the bulk MAR encompasses them. Thus, if the bulk MAR deviates from the F_{D20}, it is expected according to the theoretical reasoning to overestimate the F_{D20}. This is confirmed by the simulation-to-bulk-MAR comparison (Fig. 43 and 44). Bulk MARs among nearby sites vary over orders of magnitude. In some cases even for the same site, e.g. along the Rhine and in Belgium between 10^2 and 10^4 g m^{-2} yr^{-1} (Fig. 43 and 44). Possible reasons are strong MAR variations over small distances, loess-paleosol dating uncertainties[241], and age model inaccuracies[258].

For western Germany, a transition resulted from larger F_{D20} (10^3–10^4 g m^{-2} yr^{-1}) near the North German Plain to lower F_{D20} (10^2–10^3 g m^{-2} yr^{-1}) at Baden and Rhineland-Palatine (Fig. 43 and 44).

For a few sites in Austria, Ukraine, southwestern Germany, and along the Danube, F_{D20} are ten times smaller than their respective bulk MARs (Fig. 43 and 44). Possible reasons are: The reconstructed MARs overestimate the real values. The topographical resolution dependent erodibility definition could have neglected erodible surfaces that existed at scales far below 50 km. The simulations do neither take into account larger than 20 µm diameter particles nor seasonal hydrological dust sources.

Sima et al.[43] (in short: *Sima*) published that the loess at Stayky (50.1°N, 30.9°E) resulted from dust that was transported by westerlies and northwesters to Stayky. Sima's study[43] also finds that westerlies and northwesters prevailed over central Europe during the glacial climate. They[43] state that the loess at Stayky originated from dust sources located between 49–54°N and 15–29°E, named here *the Sima Sources*.

However, while dust transport from the Sima Sources to Stayky by northwesters (i.e. CWT-NW) was possible (Fig. 61), the northwesters occurred scarcely — only 5% of the times (Tab. 11). Even if potential contributions by westerlies (CWT-W 4%) and northerlies (CWT-N 7%) are added, these three wind directions did not prevail either. In sum, they occurred only during 16% of the times. Each of these three directional occurrence frequencies is even below the 10% expectation value, in case one does not consider any physical properties of the wind field and classification algorithm but the discrete uniform distribution that treats all classes as equally likely.

In summary, the westerlies, northwesters, and/or northerlies did not prevail during the LGM between the Sima Sources[43] and Stayky. This contradicts Sima's finding on prevailing northwesters over central Europe. Nevertheless, it is likely that these—however scarcely occurring—northwesters transported large amounts of dust to Stayky (Fig. 60, 61, and 62). Yet, according to my WRF-Chem-LGM-based results, the complete picture encompasses as well dust transports to Stayky by the east sector winds (Fig. 56).

For three west Russian sites (46–54°N and 38–45°E, Tab. 1) the $F_{D20\,\mathrm{SD}}$ are ten times smaller than their bulk MARs (Fig. 47a). The dynamically downscaled $F_{D20\,\mathrm{DD}}$ performs better, since the orders of magnitude of the $F_{D20\,\mathrm{DD}}$and of the three bulk MARs are identical (Fig. 47b). The same applies to the F_{D20} for the three westernmost French sites (Tab. 1); yet, the differences between the $F_{D20\,\mathrm{SD}}$ and the $F_{D20\,\mathrm{DD}}$ are smaller. Considering the F_{D12} MAR10 comparison, the statistic dynamic downscaling performs slightly better, because the $F_{D12\,\mathrm{SD}}$ do not underestimate any MAR10, which the $F_{D12\,\mathrm{DD}}$ do for three sites (Fig. 47c and d).

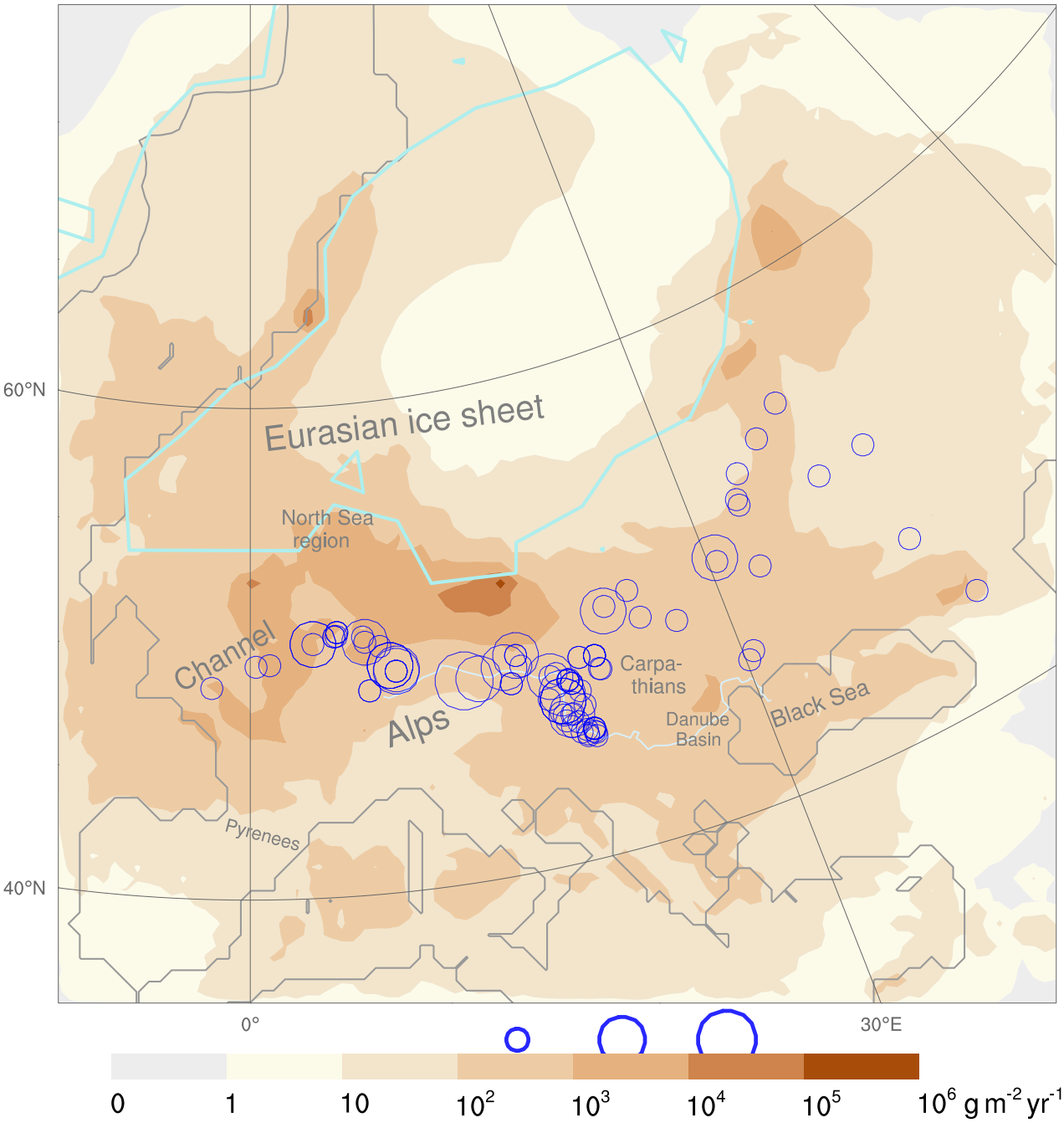

Figure 43: LGM dust deposition rates (smoothed) comprising simulated particles of up to 20 µm diameter (F_{D20} in g m^{-2} yr^{-1}) using statistic dynamic downscaling. Each blue circle size represents one bulk mass accumulation rate (MAR). The F_{D20} and the MARs base on independent data. MAR values compiled in Tab. 1. Eurasian ice sheet extent[178] (turquoise), Danube (light blue), and coastlines[17] (grey) delineated.

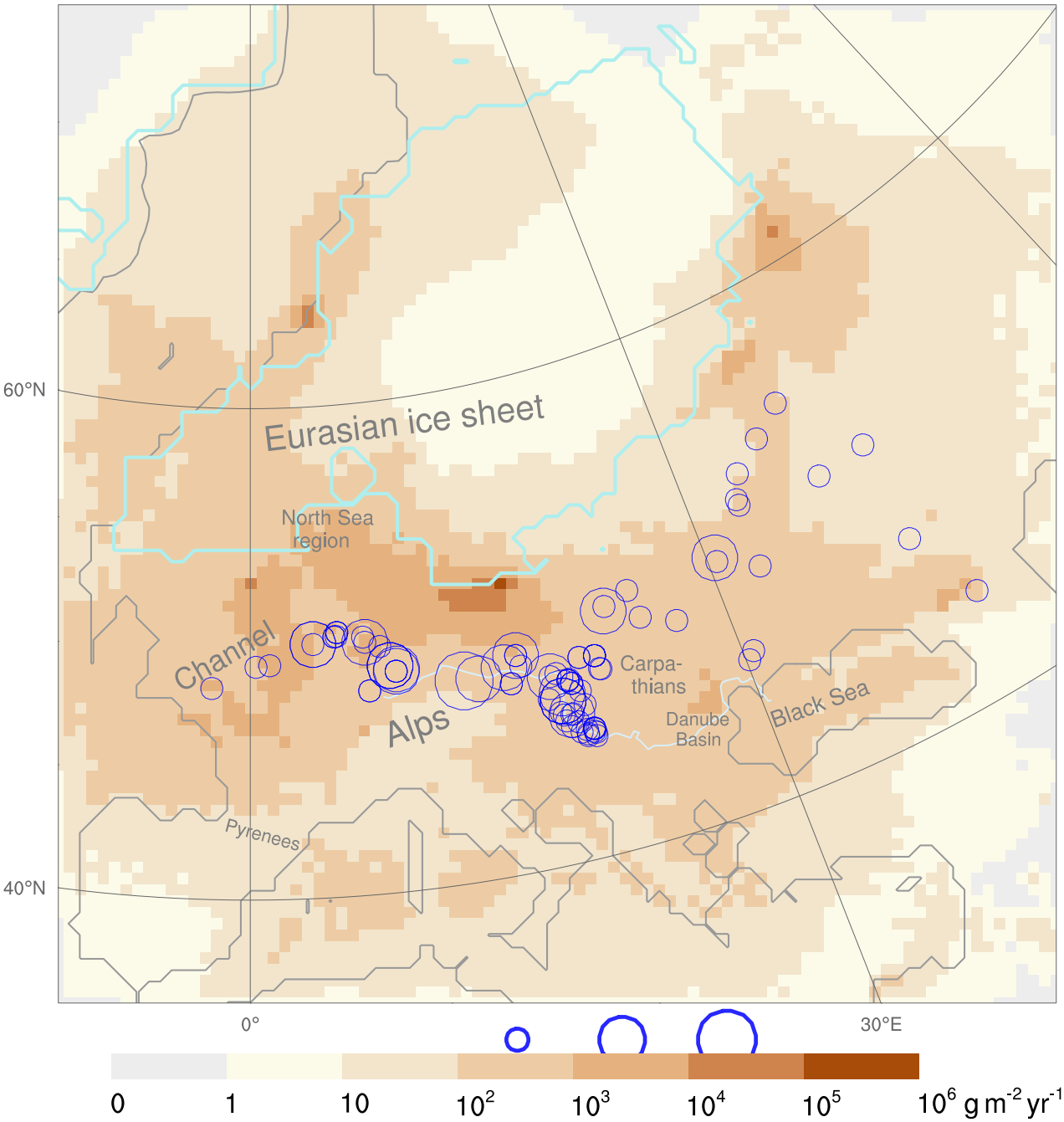

Figure 44: LGM dust deposition rates comprising simulated particles of up to 20 µm diameter (F_{D20} in g m^{-2} yr^{-1}) using statistic dynamic downscaling. Other explanations as in caption of Fig. 43

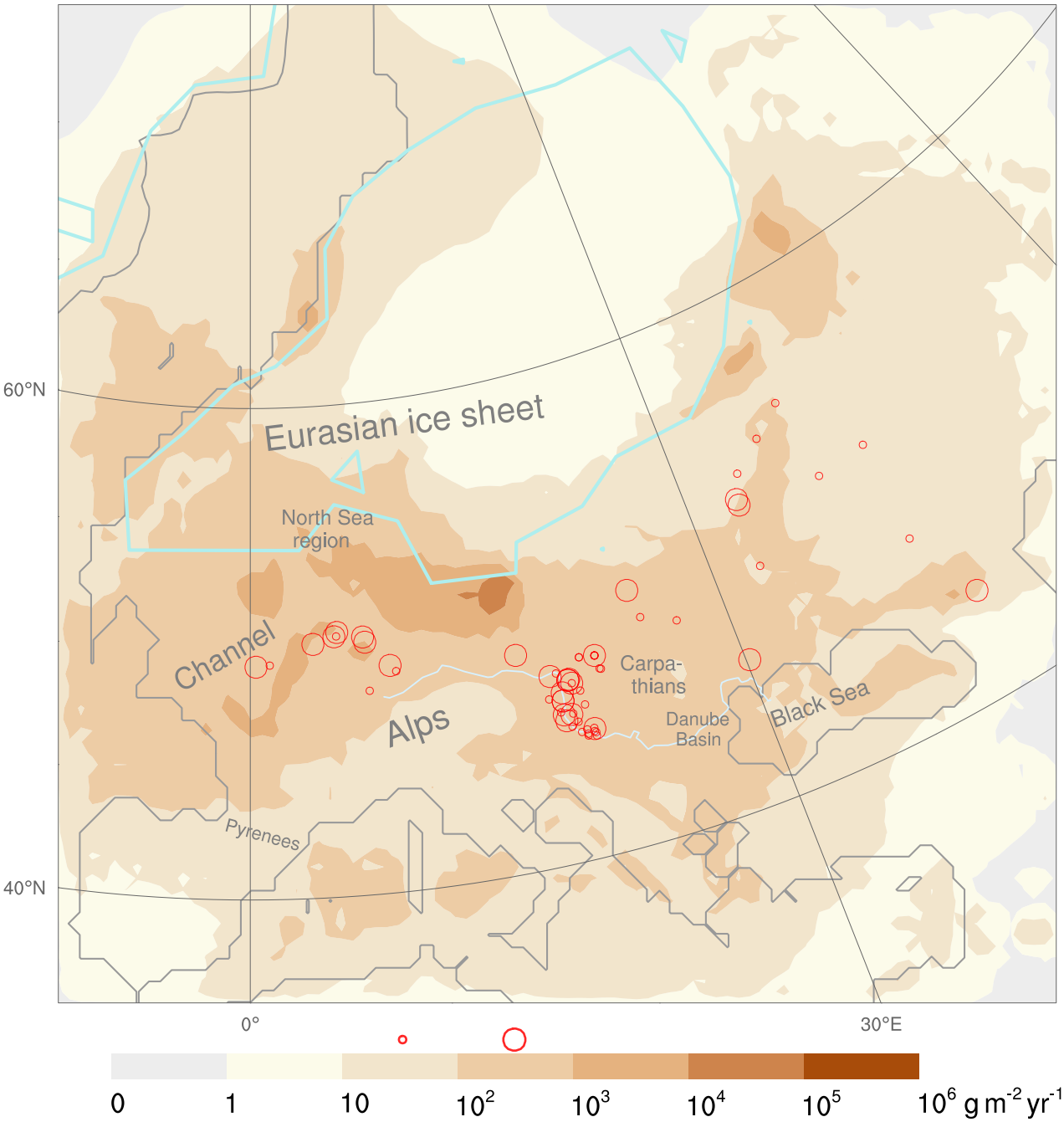

Figure 45: LGM dust deposition rates (smoothed) comprising simulated particles of up to 12 µm diameter (F_{D12} in g m^{-2} yr^{-1}) using statistic dynamic downscaling. Each red circle size represents one reduced mass accumulation rate (MAR10). The MAR10s encompass only particles up to 10 µm diameter. The F_{D12} and the MAR10s base on independent data. MAR10 values given in Tab. 1. Other explanations as in caption of Fig. 43

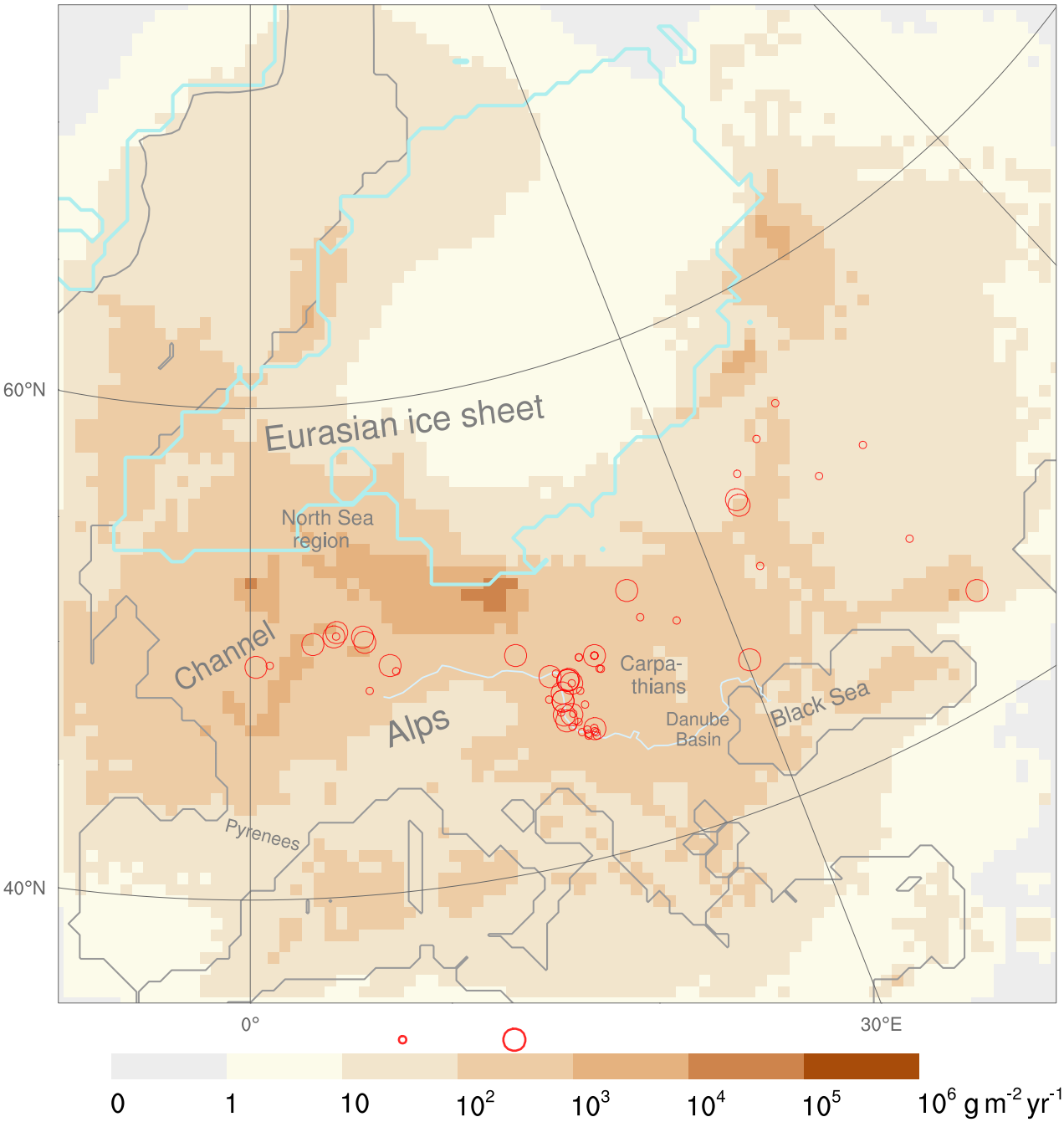

Figure 46: LGM dust deposition rates comprising simulated particles of up to 12 µm diameter (F_{D12} in g m^{-2} yr^{-1}) using statistic dynamic downscaling. Other explanations as in caption of Fig. 45

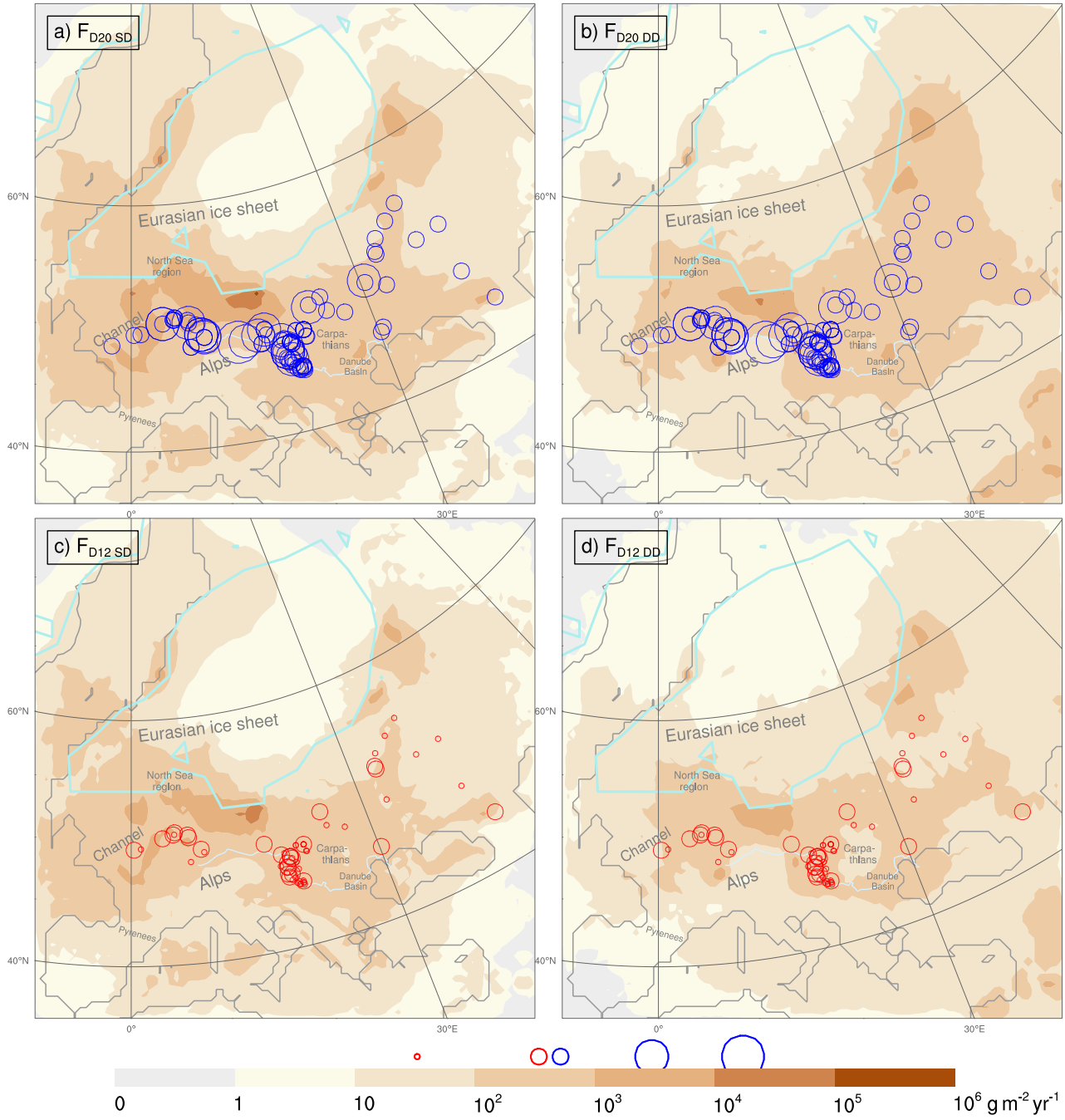

Figure 47: LGM dust deposition rates comprising particles of up to 20 µm diameter (F_{D20}) using (a) statistic dynamic downscaling ($F_{D20\ SD}$) and (b) dynamic downscaling ($F_{D20\ DD}$). (c) and (d) as (a) and (b), but for particles up to 12 µm (F_{D12}). Each blue circle size represents one bulk mass accumulation rate (MAR) magnitude. Each red circle size represents one reduced mass accumulation rate (MAR10) magnitude. MAR and MAR10 values compiled in Tab. 1. The simulation-based (F_{D20}, F_{D12}) and the fieldwork-based (MAR, MAR10) rates base on independent data. Eurasian ice sheet extent[178] (turquoise), Danube (light blue), and coastlines[17] (grey) delineated.

Fit between simulated depositions of fine particles and reduced MARs Consistent with the F_{D20}, the $F_{D12\,\mathrm{SD}}$ (10^4 to 10^5 g m^{-2} yr^{-1}) were largest on the southernmost proglacial Polish area (Fig. 45 and 46). The remaining *plume pattern* of $F_{D20\,\mathrm{SD}}$ and $F_{D12\,\mathrm{SD}}$ over central-western Europe is also almost congruent (Fig. 47). High F_{D12} (10^3 to 10^4 g m^{-2} yr^{-1}) covered also northern and eastern Germany. In particular for central Europe, the $F_{D12\,\mathrm{SD}}$ and $F_{D12\,\mathrm{DD}}$ patterns agree. The $F_{D12\,\mathrm{SD}}$ are ten times larger on the Carpathians, in central, and in western Europe, whereas they are one order of magnitude smaller than the $F_{D12\,\mathrm{DD}}$ on parts of the East European Plain (Fig. 47). These parts were confined southwards by the Black Sea and the Caucasus, and northwards by the eastern EIS margin.

The spatial distribution of the $F_{D12\,\mathrm{SD}}$ and MAR10s is consistent (Fig. 45 and 46), because the necessary condition that the order of magnitude of the $F_{D12\,\mathrm{SD}}$ and MAR10 is either identical or that the $F_{D12\,\mathrm{SD}}$ is larger, is met for all sites. For example, along the Rhine and Danube, the MAR10 of each site was either between 10 and 100 g m^{-2} yr^{-1} or between 100 and 1000 g m^{-2} yr^{-1}, and the MAR10 of equal magnitude did not cluster. Thus, if these MAR10s are reliable, then high MAR10 variability existed on small spatial scales. The $F_{D12\,\mathrm{SD}}$ (between 100 and 1000 g m^{-2} yr^{-1}) and most of the MAR10s agree in their order of magnitude. Sites with smaller MAR10s (10 to 100 g m^{-2} yr^{-1}) potentially conform, as the $F_{D12\,\mathrm{SD}}$ also allows for particles between 10 and 12 µm, which are neglected in the MAR10. To address this substantial fieldwork-inferred MAR10-variability at almost the same locations, spatially higher resolved simulations comprising time-dependent dust sources are required.

Lacking dust transport across domain boundary Apart from the already mentioned restrictions (limited particle size, MAR estimation uncertainties), the domain boundary proximity effect could have biased the F_{D20}. This affected particularly areas in the east of the domain, where the F_{D20} likely underestimate the real LGM dust deposition rates. Easterlies and/or southeasters likely wafted dust from the dry-fallen parts of the Caspian and Aral Sea to these areas during the LGM[46]. Yet, these sources are outside of the domain, which had to be sized within the high performance computing time limitations. Thus, the effect on the European dust cycle by potential dust sources located outside of the WRF-Chem-LGM domain had to be neglected.

Spatial distributions of gravitational settling, dry, and wet deposition Mineral dust is removed from the atmosphere by gravitational settling, dry and wet deposition[106] (Fig. 48, 49, 50, 51, 52, and 53). During the LGM, dust was mainly removed from the atmosphere by gravitational settling and wet deposition (Fig. 50 and 52). Their rates peaked (10^4 to 10^5 g m^{-2} yr^{-1}) proglacially of the southernmost EIS margin corresponding to about Poland. The highest continuous dry deposition rates occurred there as well. This conforms to the expectation[62] that the dry deposition may remove 50% or more of the dust load near the dust sources, where the average dust particle size is the largest. Yet, the dry depositions (10^3 to 10^4 g m^{-2} yr^{-1}) are one order of magnitude smaller than the other two removal processes (Fig. 48 and 49), which is supported by the finding[62] that dry deposition removes dust less effective than wet deposition.

The spatial distribution of the gravitational settling and of the dry deposition rates result in equal dust removal magnitudes for large homogeneous areas. On the contrary, the wet deposition values cluster to heterogeneous, fragmented, multi-angular polygons indicating variations of their orders of magnitude on very small spatial scales (Fig. 52 and 53), likely correlating with the precipitation rate patterns. On western to northern France including the Bay of Biscay, the Mediterranean and the eastern Black Sea, the wet depositions are about ten times larger than the other deposition processes (Fig. 52 and 53).

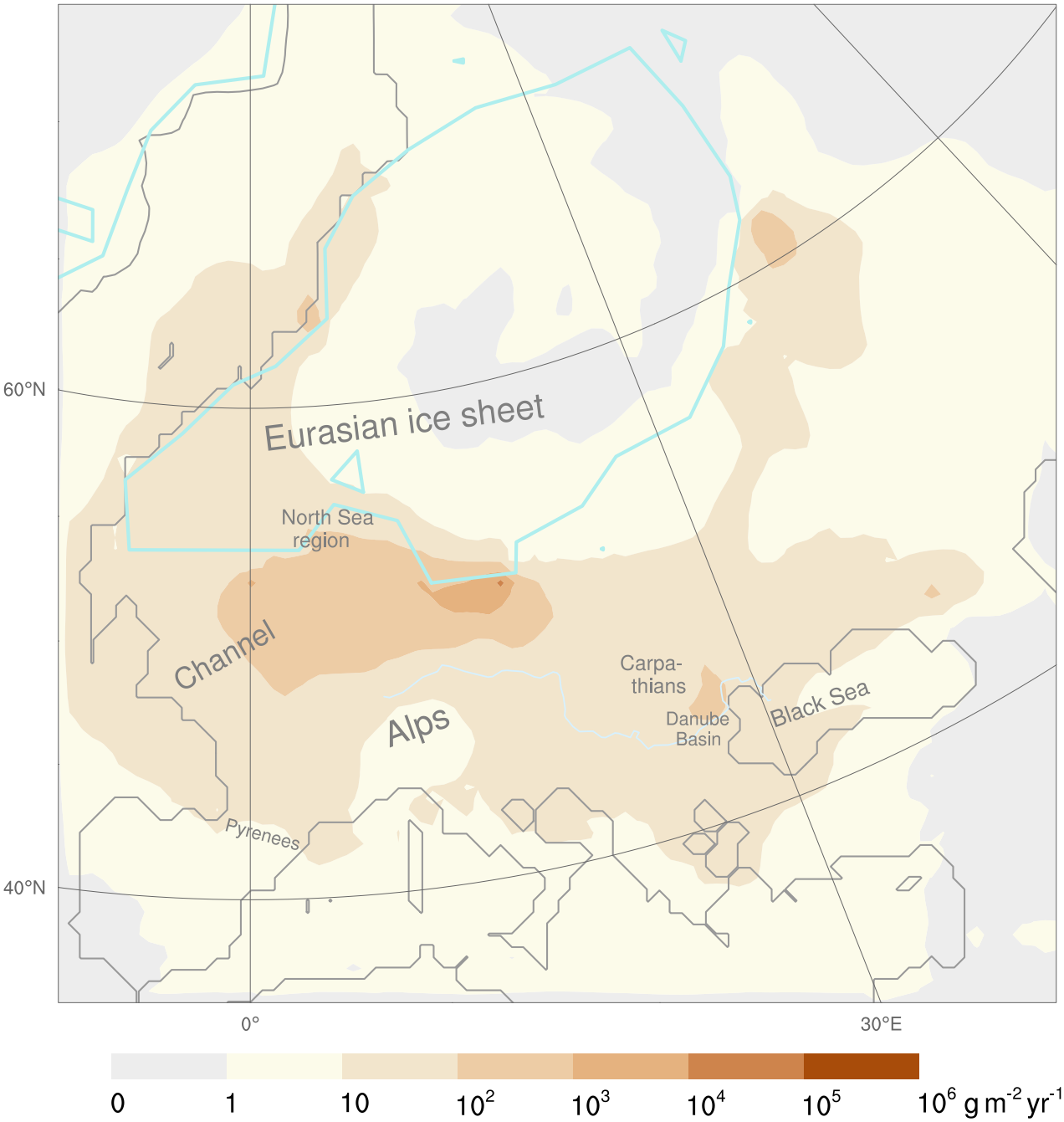

Figure 48: Dry deposition rates for the LGM using statistic dynamic downscaling

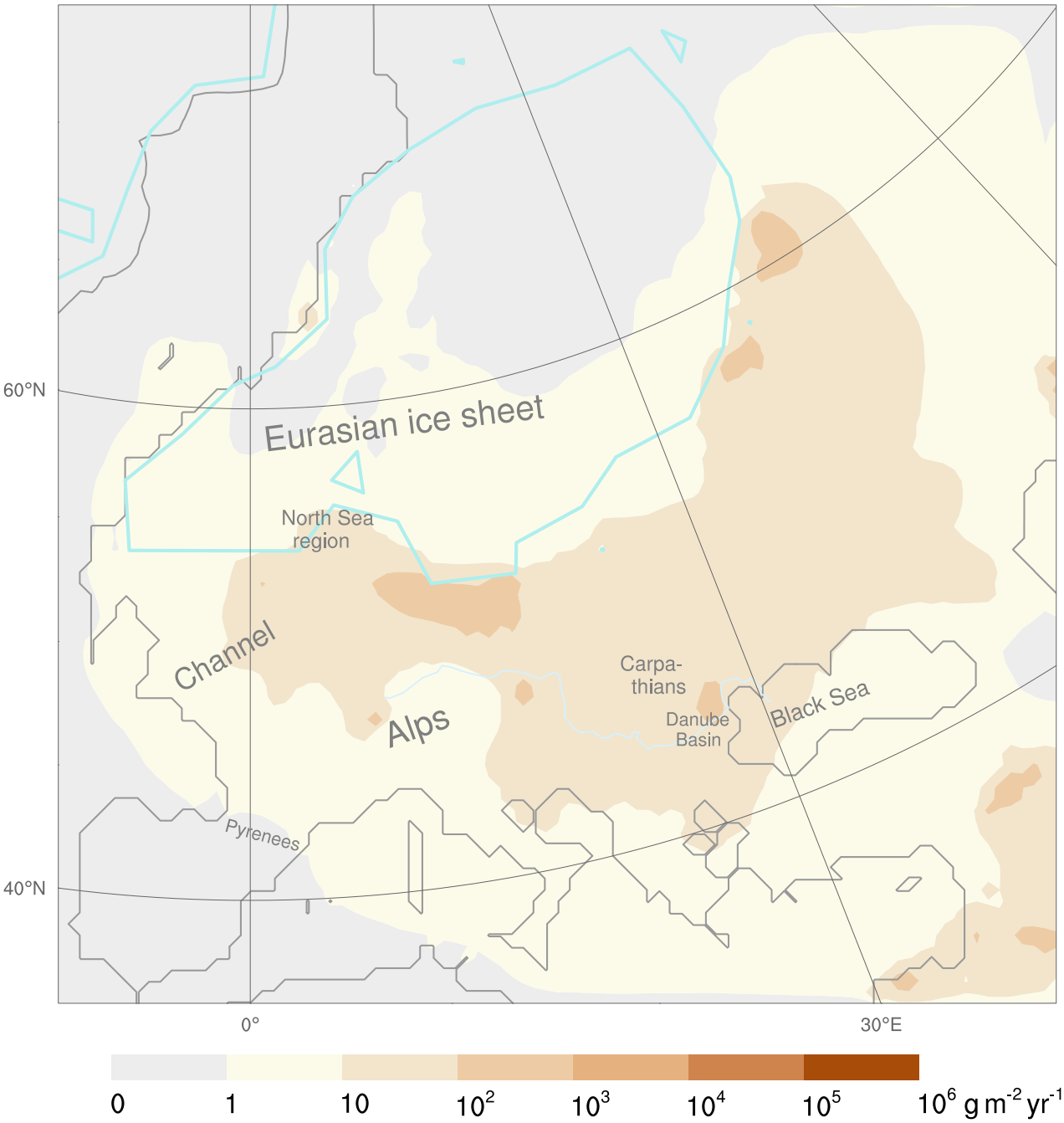

Figure 49: Dry deposition rates for the LGM using dynamic downscaling

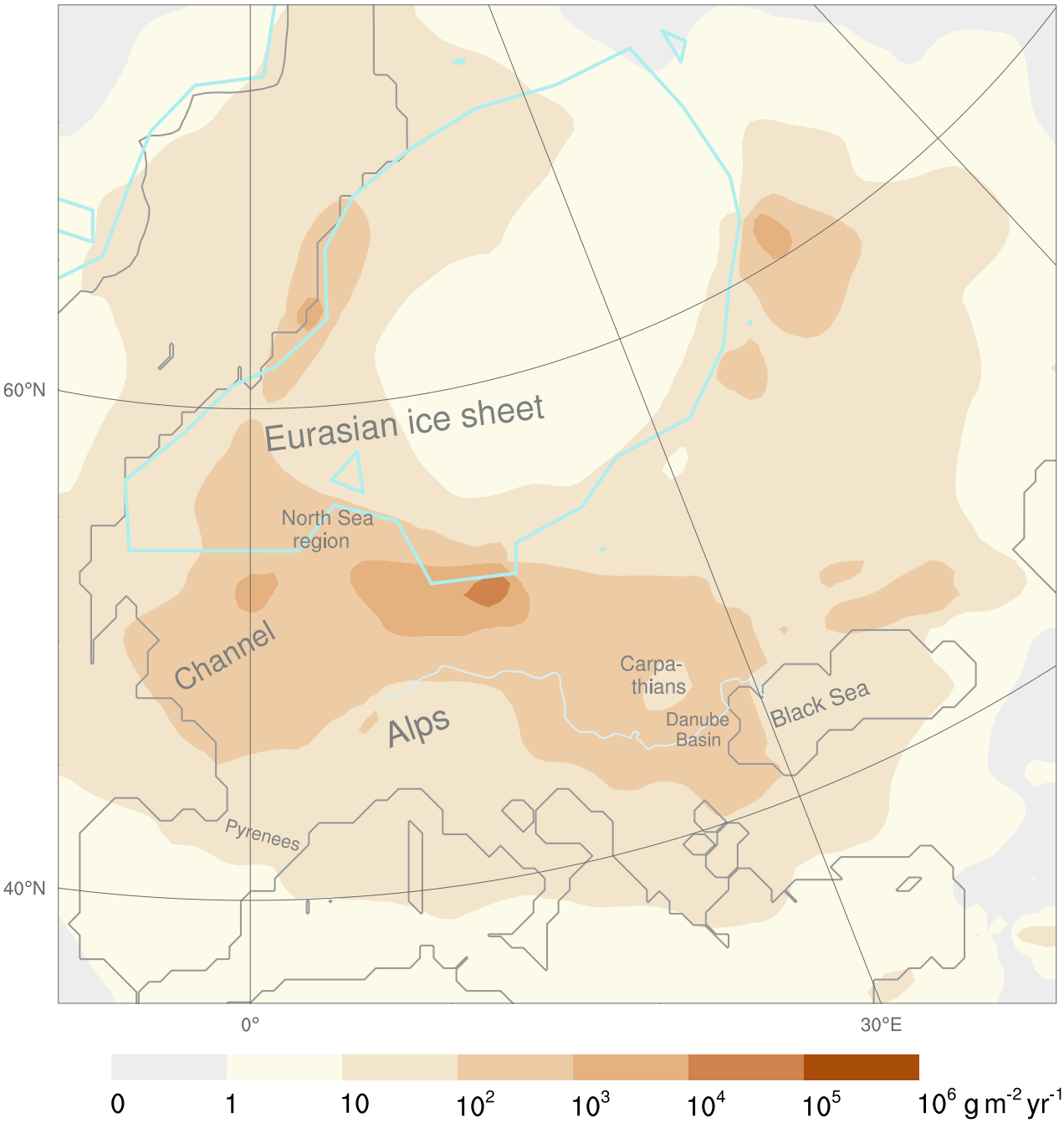

Figure 50: Gravitational settling rates for the LGM using statistic dynamic downscaling

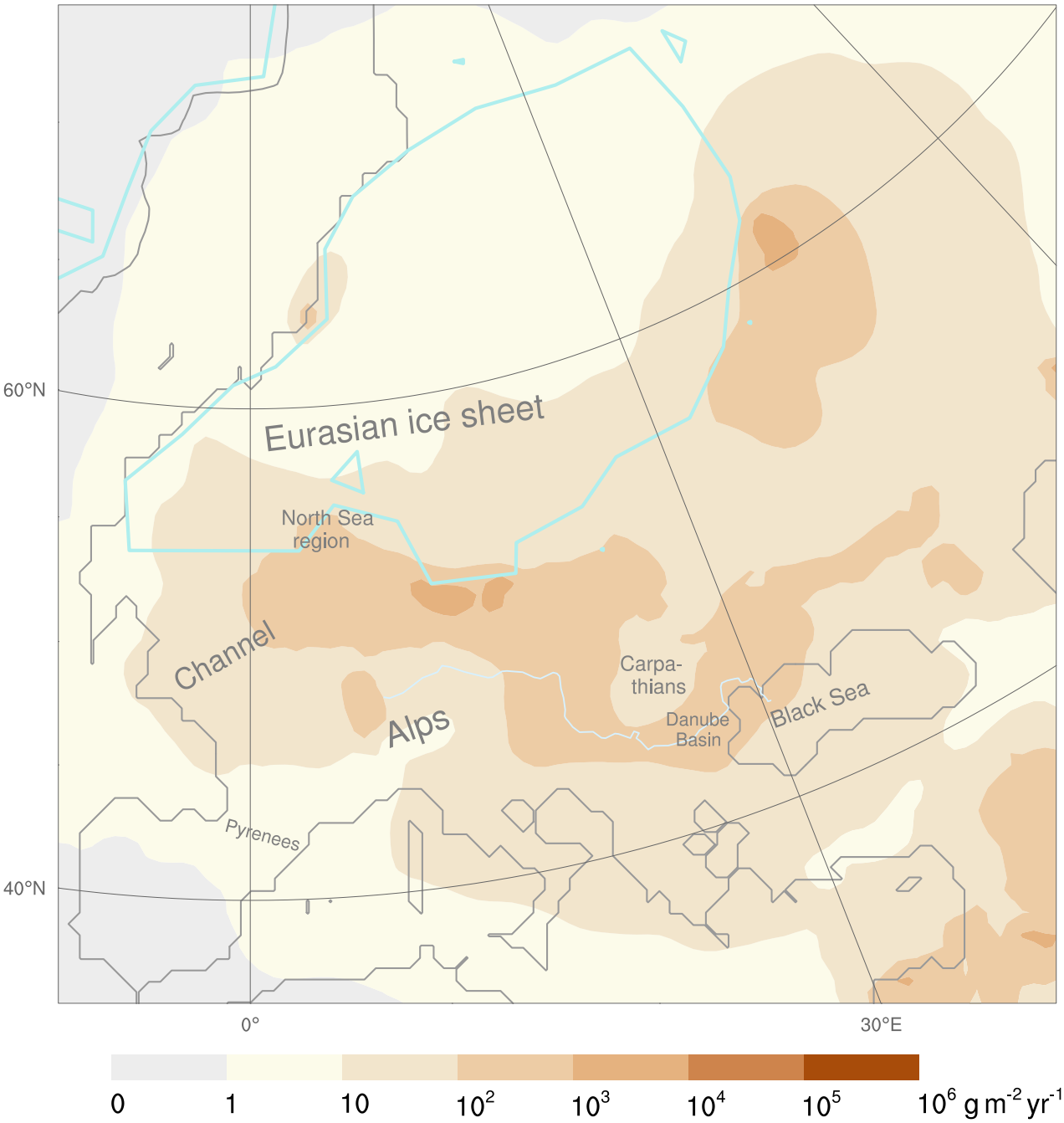

Figure 51: Gravitational settling rates for the LGM using dynamic downscaling

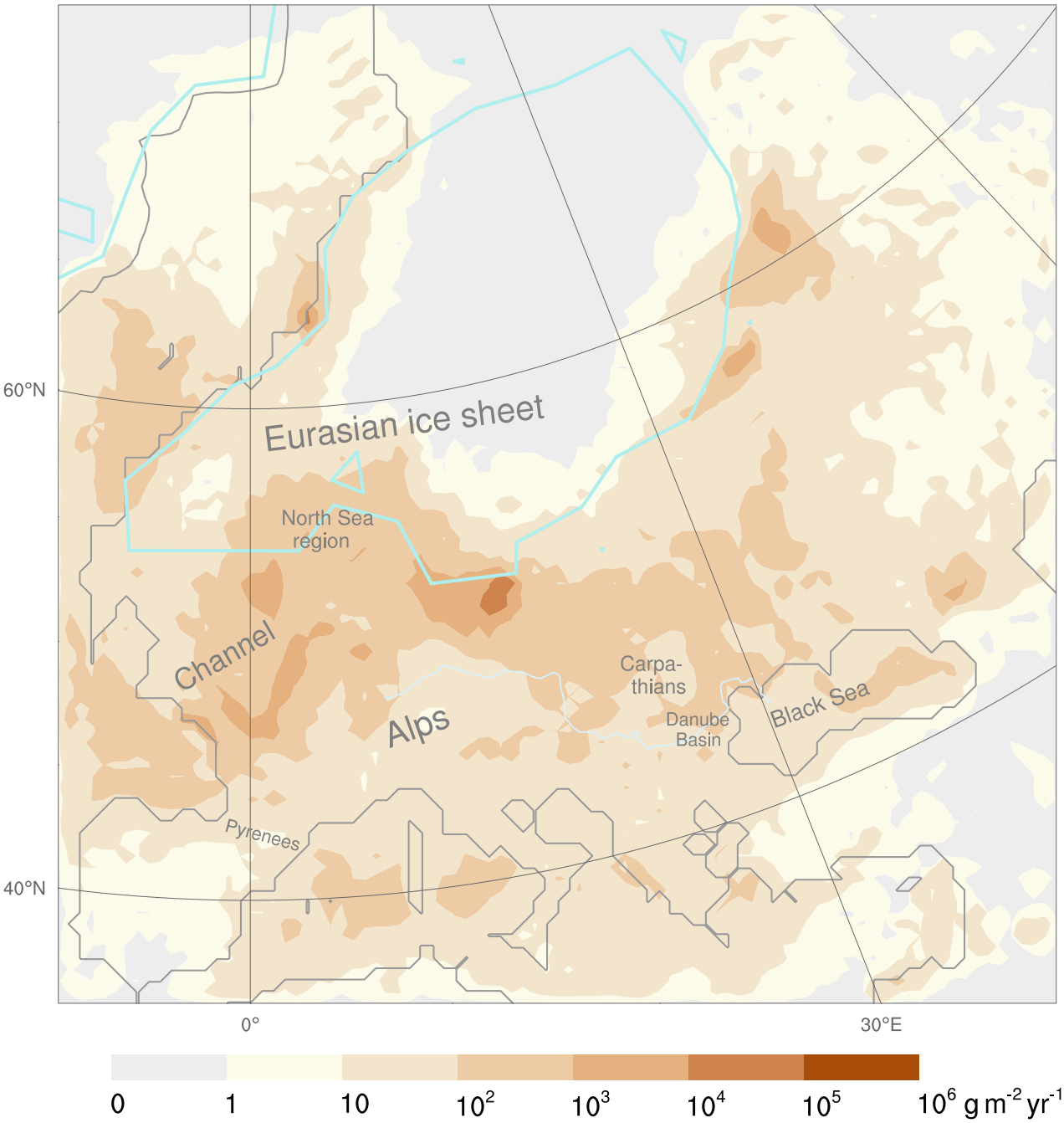

Figure 52: Wet deposition rates for the LGM using statistic dynamic downscaling

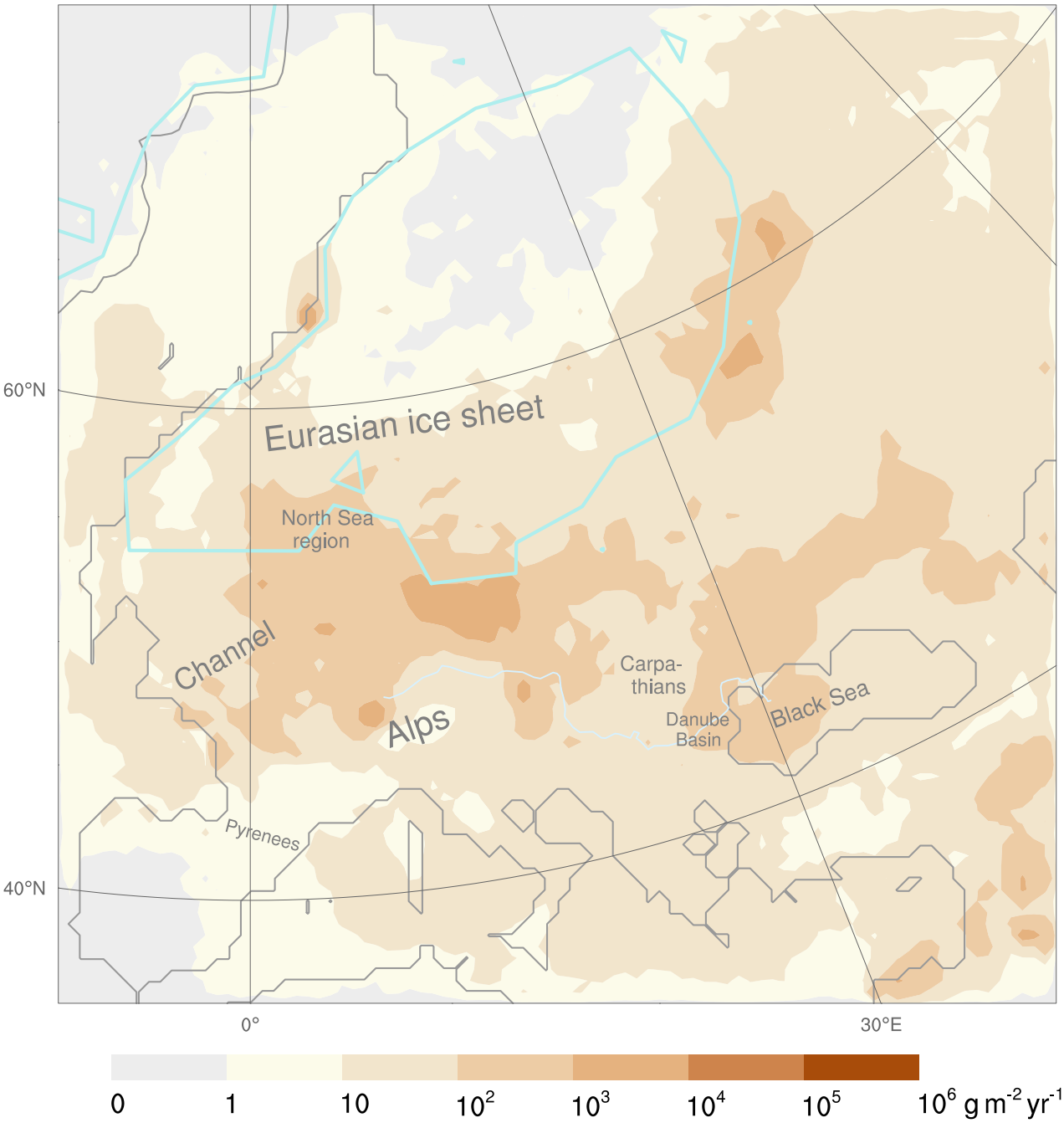

Figure 53: Wet deposition rates for the LGM using dynamic downscaling

Dominant deposition and emission areas The dust deposition dominated on most of the European areas (Fig. 54 and 55). Based on the statistic dynamic downscaling, only seven dominant emission rate clusters existed: Western England, the southern and eastern proglacial EIS areas, western Hungary, the area north of the Danube Basin, and two areas north of the eastern Black Sea and the Caucasus (Fig. 54). Almost all loess sites (Tab. 1) are located in areas, where the LGM deposition dominated the emission rates (Fig. 54). Only three sites near the upper Danube deviate from that. For them, the aeolian dust budget approach at 50 km resolution could be too coarse, as the emissions and depositions likely occurred at distinct places within the about 2500 km^2 large area that one grid cell represents. Possibly, the Danube and its tributaries could have contributed alluvium. Yet, at the current state, the hydrology is not represented in the WRF-Chem-LGM.

Using dynamic downscaling, the spatial dominance of the deposition rates is considerably reduced (Fig. 55 versus 54). Dominant emission rates extended southwards from the southernmost proglacial EIS region up to the Danube. The emissions dominated also more extensively in the regions north of the Black Sea and Caucasus (Fig. 55 versus 54). In sum, six sites with published bulk MARs are —rather arbitrarily— distributed (western France, Caucasus foreland) over all emission-dominated areas. Yet, they do not contradict the validity of the simulations (the explanation, given for the statistic dynamic downscaling based results, applies)

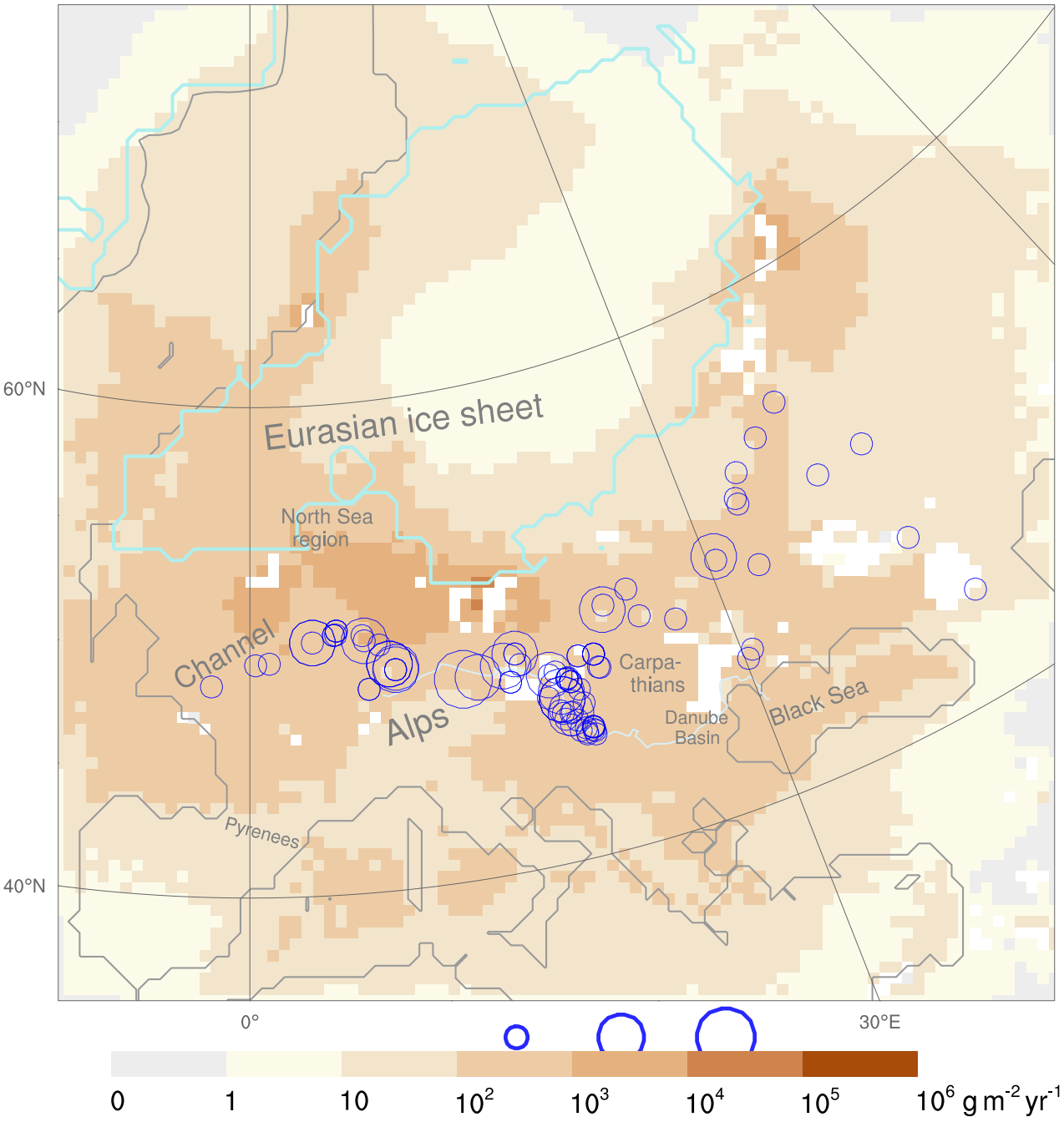

Figure 54: Net LGM dust deposition rates based on statistic dynamic downscaling. Obtained by subtracting the emission from the deposition rates. Emission-dominated areas are masked (white). The orders of magnitude (blue circle sizes, size-to-value reference at the color bar) of the independently reconstructed fieldwork-based bulk MARs (Tab. 1) are shown.

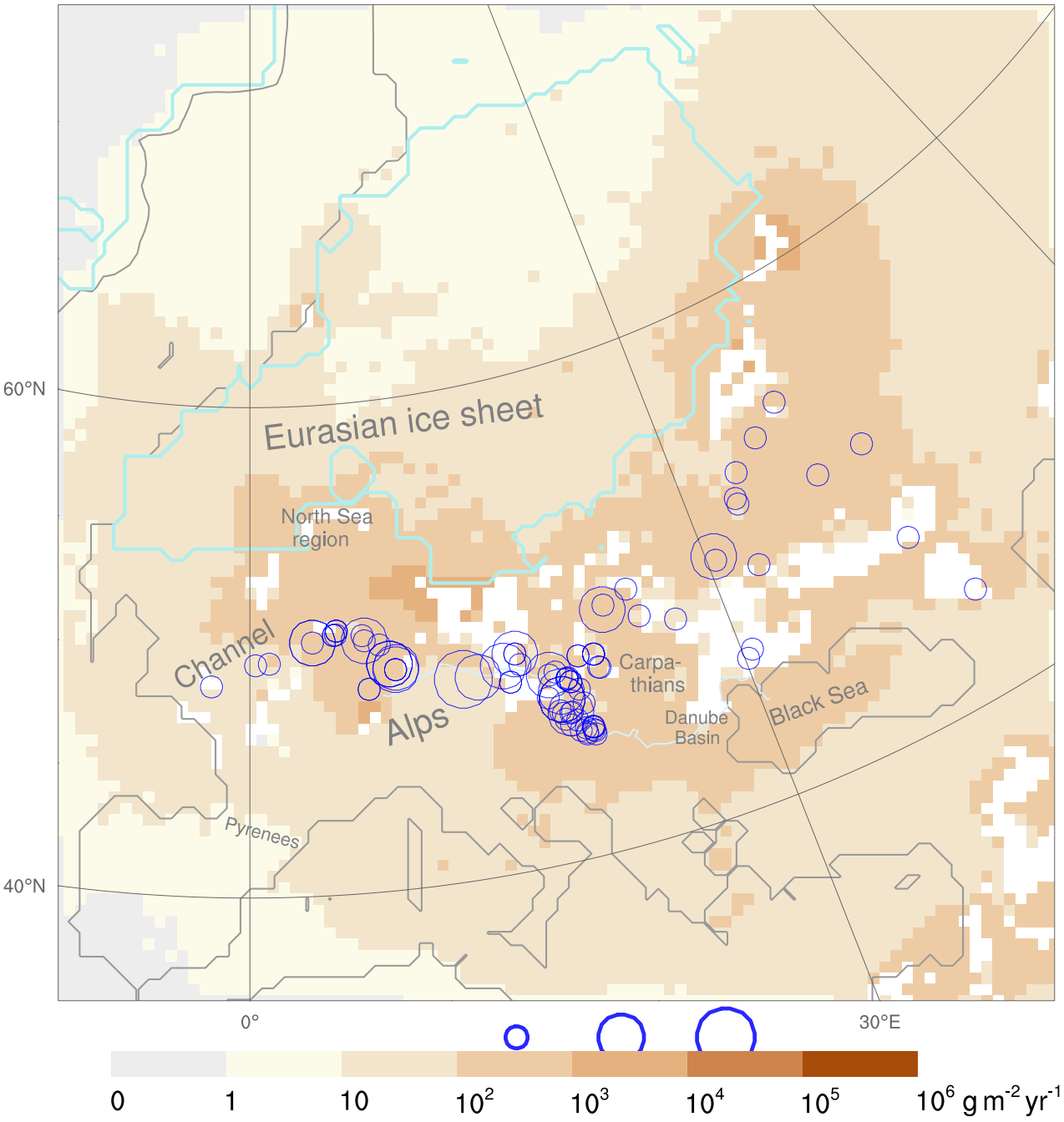

Figure 55: Net LGM dust deposition rates based on dynamic downscaling. Obtained by subtracting the emission from the deposition rates. Negative net deposition areas masked (white). The orders of magnitude (blue circle sizes, size-to-value reference at the color bar) of the independently reconstructed fieldwork-based bulk MARs (Tab. 1) are shown.

While the east sector winds (NE, E, SE) prevailed over central Europe (Transdanubia), the shapes and gradients of the F_{D20} distribution (Fig. 56) provide evidence for anticyclonic dust-carrying winds circulating around the SIS. This conforms with the SIS High, the main part of the EIS High, whose importance became already evident in the preceding sections. The east sector winds led to the highest average domain deposition rates compared with the other directional wind (sector) rates (Fig. 58, 59, and 62) and the cyclonic regimes (Fig. 57). Eastern dust (Fig. 56), mainly from Poland, deposited on Poland and Germany (10^4 to 10^5 g m^{-2} yr^{-1}), as well as on Denmark, north and west France, England, the Benelux, and the North Sea Basin (10^3 to 10^4 g m^{-2} yr^{-1}). This agrees with dominant easterlies and southeasters between 22 and 17 kyr ago over Denmark, which were inferred from wind-polished Danish boulders[45].

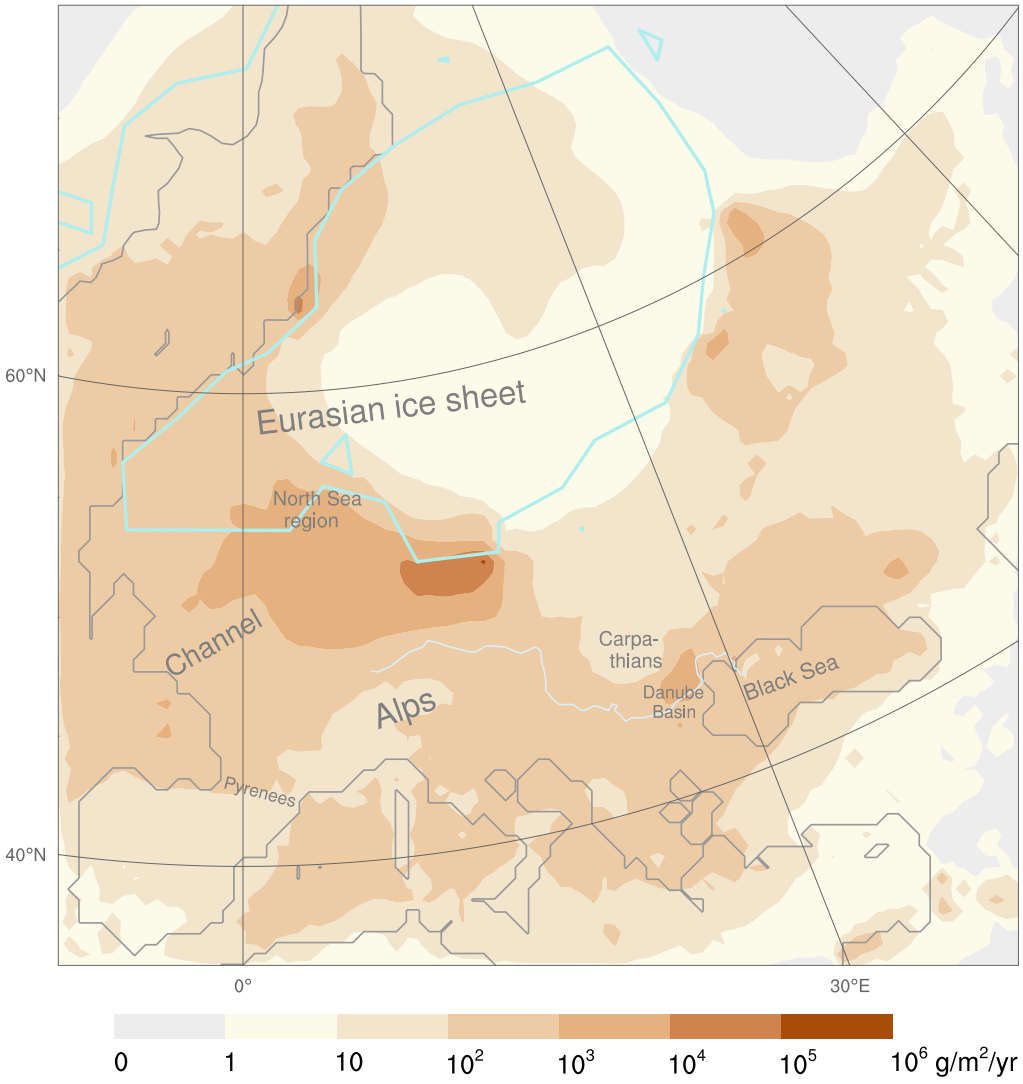

Figure 56: Dust deposition rates occurring while the east sector winds (NE, E, SE) prevailed over Transdanubia (central Europe). These average rates based on 312 WRF-Chem-LGM-simulated days, i.e. 13 episodes of 8 days were simulated per Circulation Weather Type.

Over the proglacial areas in central Europe (Fig. 57), the cyclonic regimes (the most frequent LGM CWT class, Tab. 11) transported dust along the southern EIS margin from the east to the west. This is inferred from the shape of F_{D20} shadings with the highest F_{D20} (10^4 to 10^5 g m^{-2} yr^{-1}) in the east and a gradually decreasing F_{D20} *plume* running from there westwards on the proglacial areas.

From England and the northern dry-fallen Channel, dust was transported during cyclonic regimes southwards along the zero meridian up to the northern Pyrenean foreland (Fig. 57). Evidence for this is provided by the high F_{D20} on England (10^3 to 10^4 g m^{-2} yr^{-1}) and their subsequent decrease along France (10^2 to 10^3 g m^{-2} yr^{-1}). On the contrary, almost no dust was deposited during cyclonic regimes over Transdanubia (central Europe) on large parts of Ukraine, the Black Sea, the Caucasus region, Turkey, southwestern Russia, the eastern Mediterranean Sea, Greece, and the Balkans.

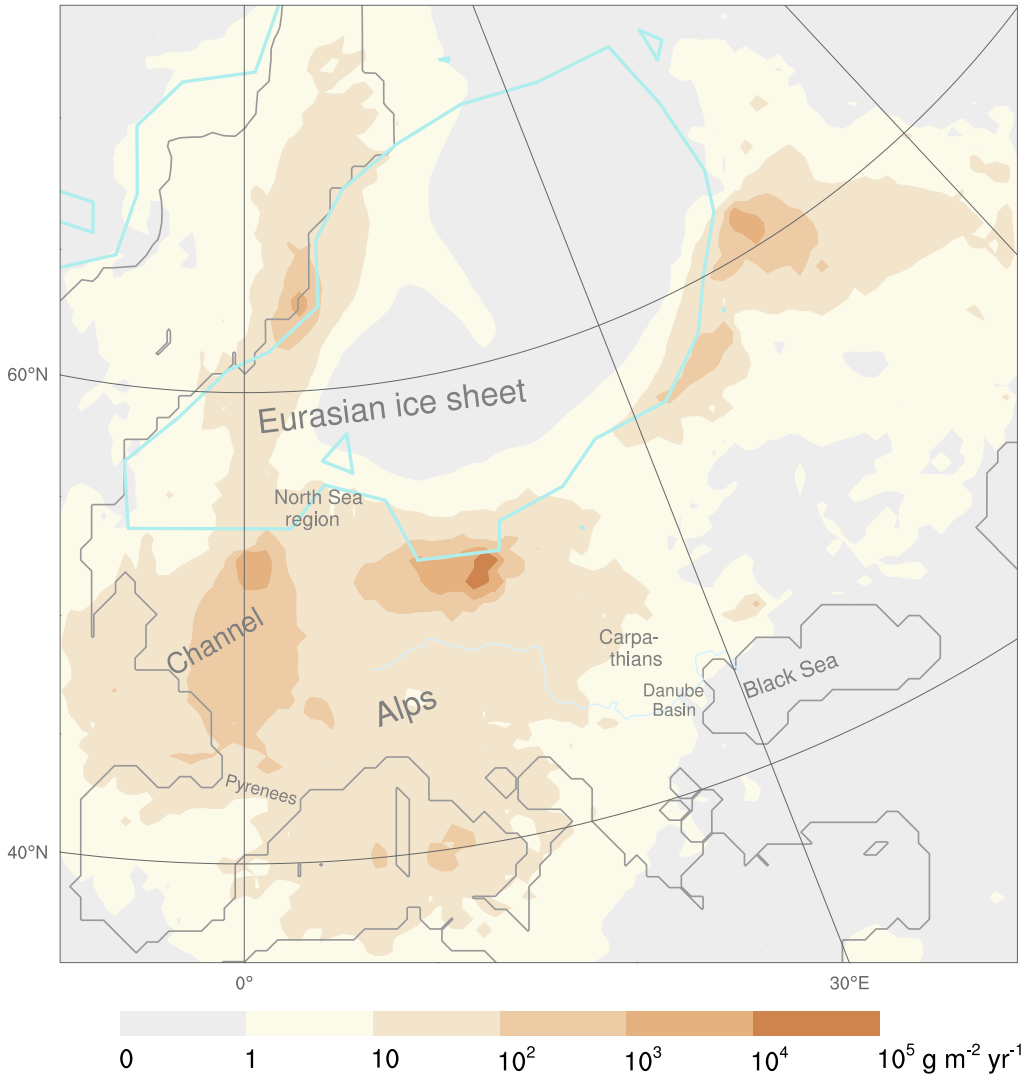

Figure 57: Dust deposition rates occurring while cyclonic regimes prevailed over Transdanubia (central Europe). These average rates base on 104 WRF-Chem-LGM-simulated days, i.e. 13 CWT-C episodes of 8 days were simulated.

During west sector winds (SW, W, and NW) over Transdanubia, the maximum of the in sum occurring dust deposition rates ranges between 10^3 and 10^4 g m^{-2} yr^{-1} (Fig. 58). This is about ten times smaller than the maxima during most other CWT regimes and wind sectors (e.g. Fig. 56, 57, and 59).

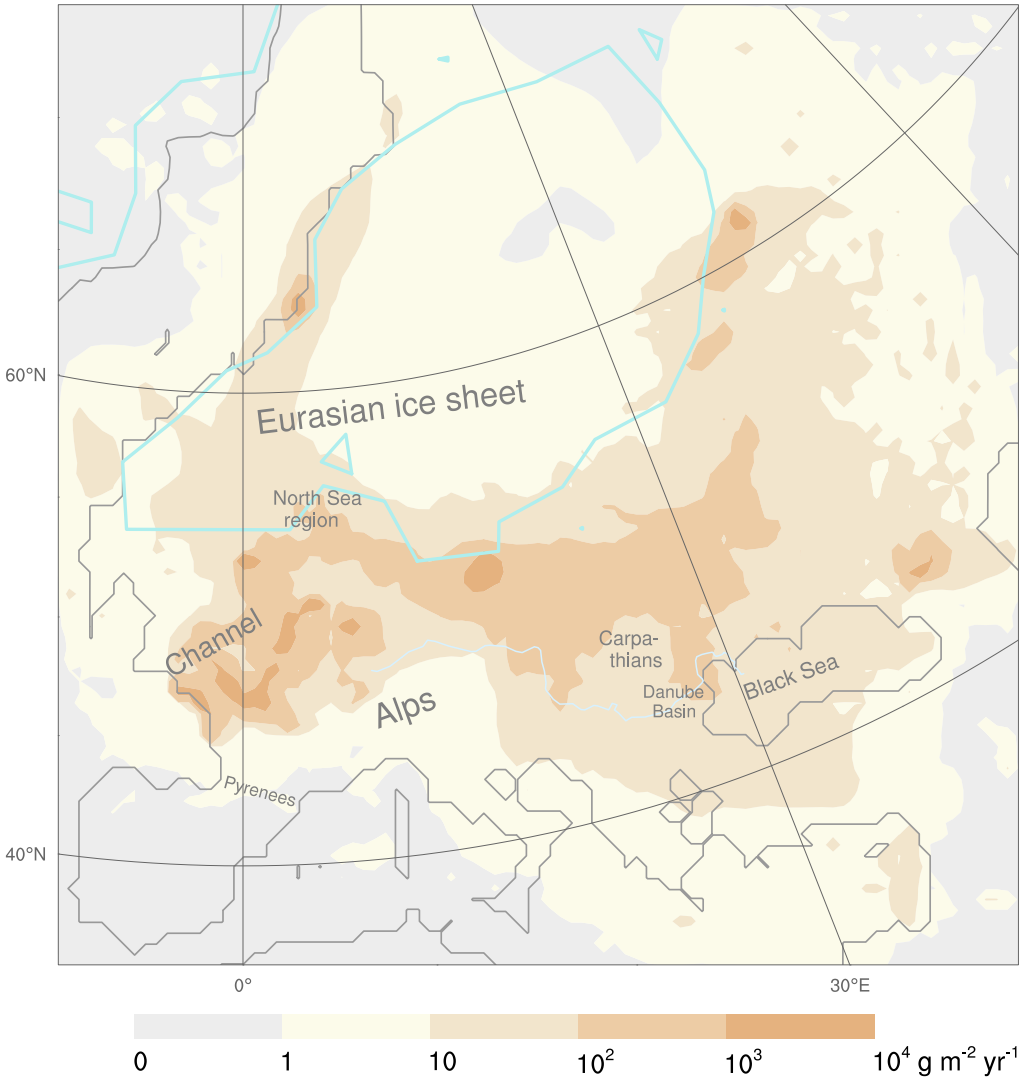

Figure 58: Dust deposition rates that occurred while the west sector winds (SW, W, NW) prevailed over Transdanubia (central Europe). These average rates based on 312 WRF-Chem-LGM-simulated days, i.e. 13 episodes of 8 days were simulated per Circulation Weather Type.

During prevailing southerlies over Transdanubia, about three quarters of the domain were hardly affected by any dust transport and deposition (Fig. 59). This concerned mainly the areas south of the Alps and east of the Carpathians. Given the orientation and gradient of the colored shapes (Fig. 59), dust was mainly transported northwestwards from the Carpathian Basin and from the proglacial area between the EIS and Danube. It deposited on the North German Plain, Denmark, and the North Sea Basin. The southeasters, which were inferred from dust deposition rates for Denmark (Fig. 59), agree with the dominant easterlies and southeasters between 22 and 17 kyr ago, that were inferred from wind-polished Danish boulders[45]. In the northwestern Alps foreland and France, the orientation of the F_{D20} shape and gradient suggests southerlies transporting dust in ~100 km steps northwards.

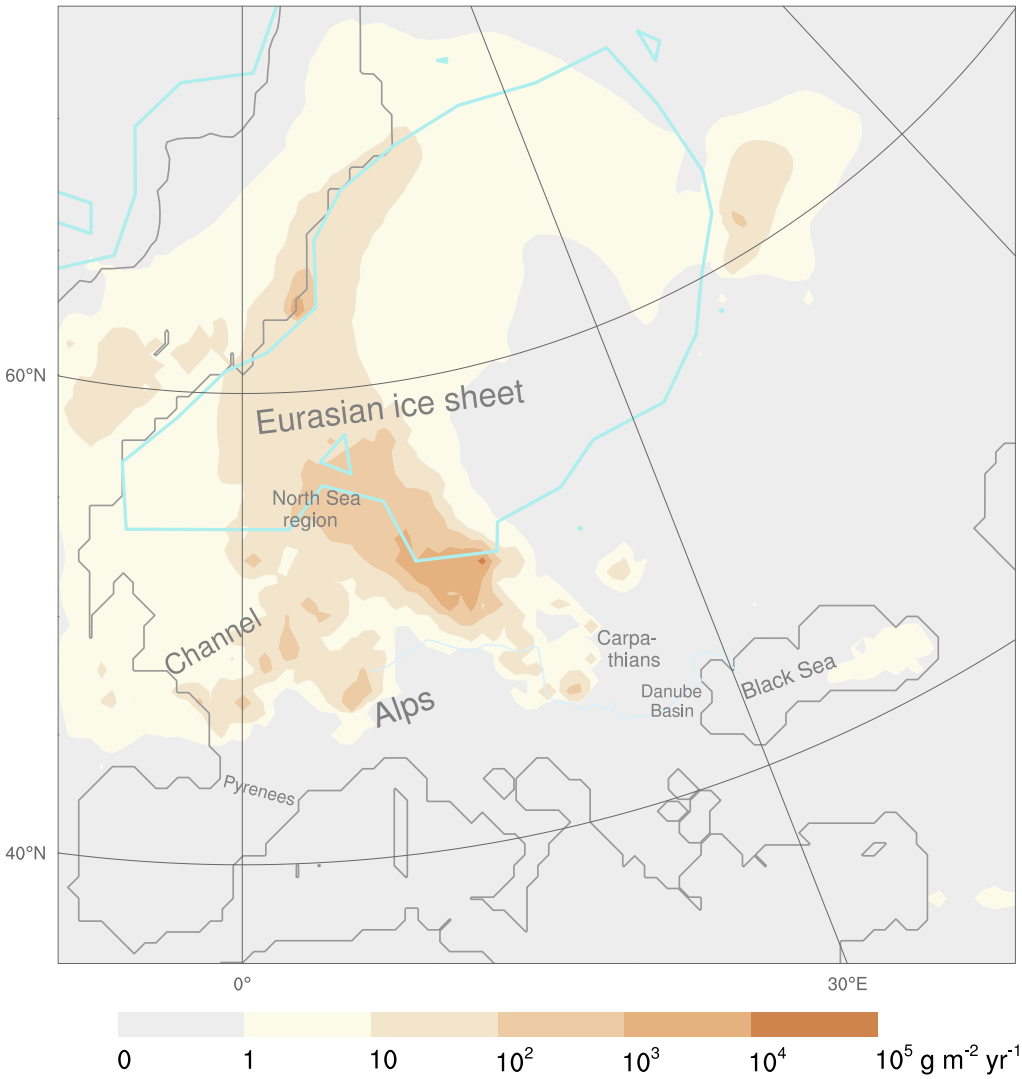

Figure 59: Dust deposition rates occurring while southerlies prevailed over Transdanubia (central Europe). These average rates base on 104 WRF-Chem-LGM-simulated days, i.e. 13 CWT-C episodes of 8 days were simulated.

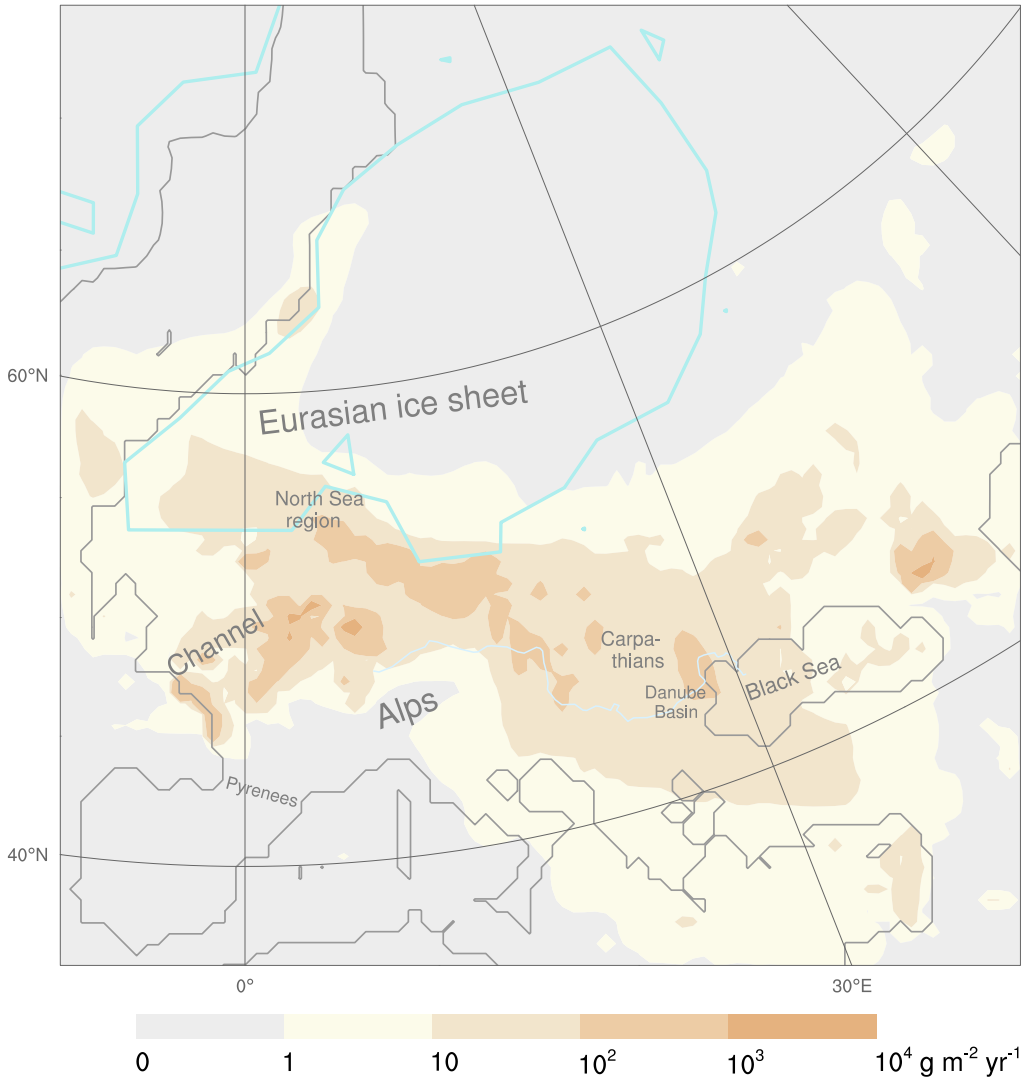

Figure 60: Dust deposition rates occurring while westerlies prevailed over Transdanubia (central Europe). These average rates base on 104 WRF-Chem-LGM-simulated days, i.e. 13 CWT-C episodes of 8 days were simulated.

During prevailing northwesters over Transdanubia, the orientation of the F_{D20} shape (Fig. 61) provides evidence for the southward and southeastward dust transport from England across the Channel (100 to 1000 g m^{-2} yr^{-1}) to France (10 to 100 g m^{-2} yr^{-1}). The orientation of the F_{D20} shape and its gradient suggests that dust was transported by westerlies from the southernmost proglacial EIS area up to western Russia. Yet, the F_{D20} ranged between only 100 and 1000 g m^{-2} yr^{-1} in the main deposition zone north of the Carpathians.

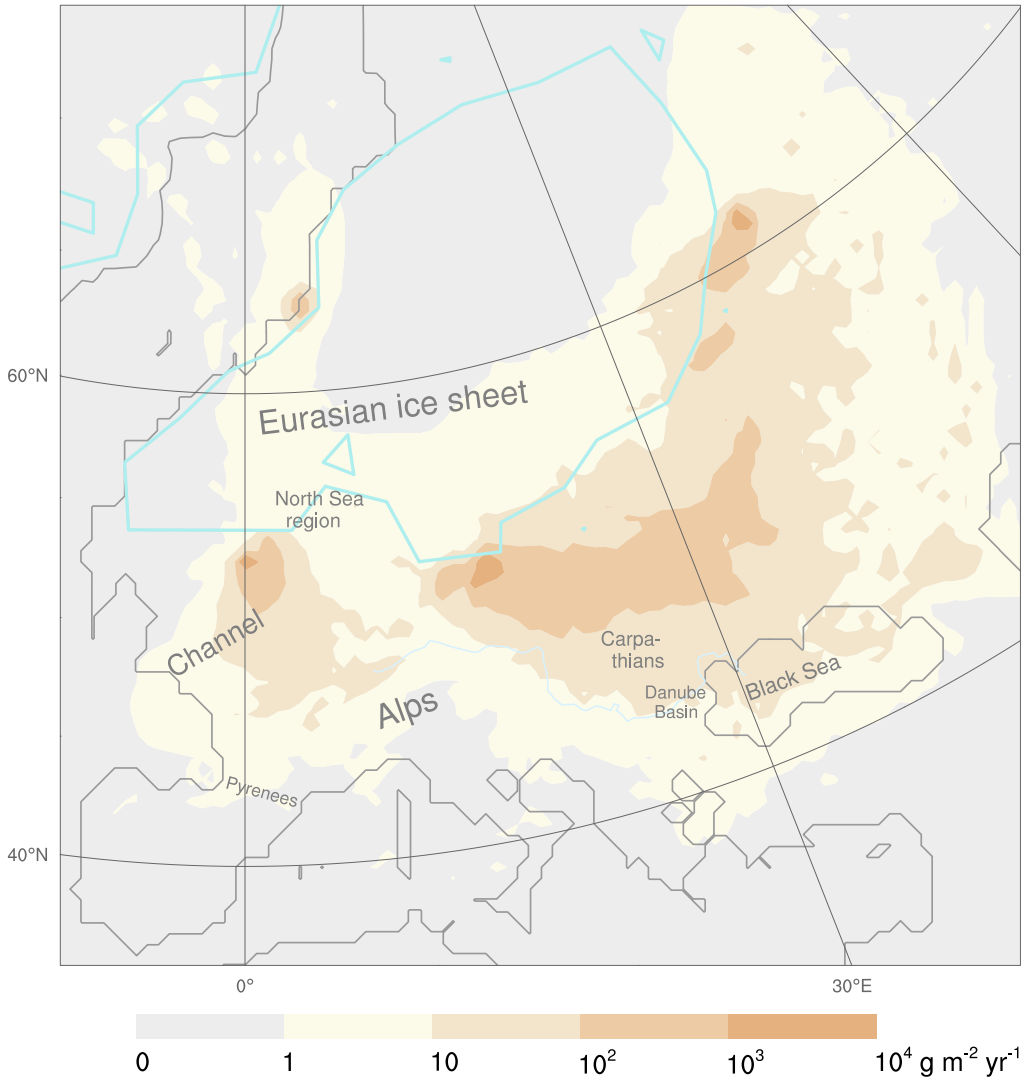

Figure 61: Dust deposition rates occurring while northwesters prevailed over Transdanubia (central Europe). These average rates base on 104 WRF-Chem-LGM-simulated days, i.e. 13 CWT-C episodes of 8 days were simulated.

During prevailing northerlies over Transdanubia (Fig. 62), the orientation of the F_{D20} shape and gradient provides evidence for dust-carrying northwesters from England to southwestern Germany (10 to 100 g m^{-2} yr^{-1}), and from the Polish EIS margin to the CB, to western Ukraine, to Moldova, and to the northwestern Black Sea (100 to 1000 g m^{-2} yr^{-1}).

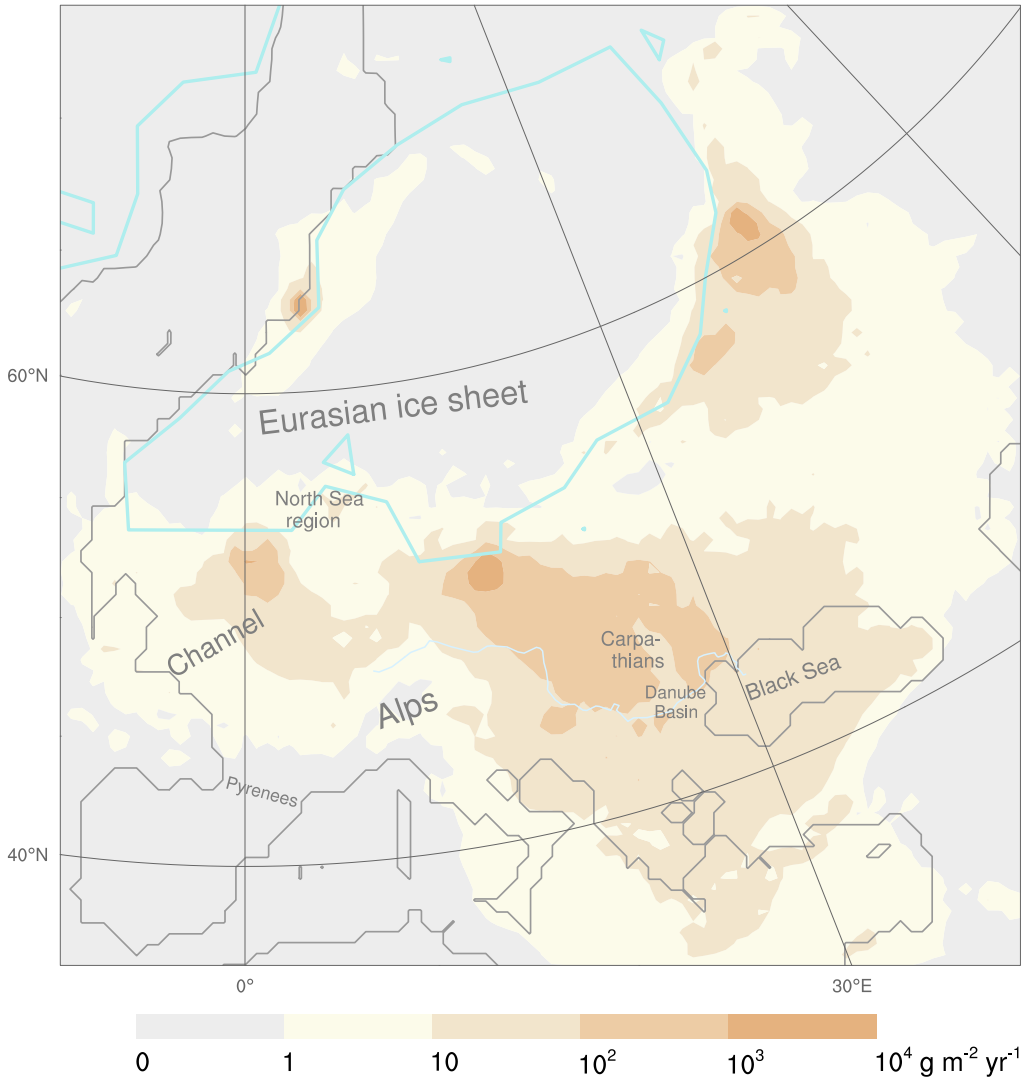

Figure 62: Dust deposition rates occurring while northerlies prevailed over Transdanubia (central Europe). These average rates base on 104 WRF-Chem-LGM-simulated days, i.e. 13 CWT-C episodes of 8 days were simulated.

7.4.5 Intra-Annual Distribution of Episodes

To reconstruct the LGM, the statistic dynamic downscaling bases on 1040 simulated days comprised of 13 eight-day episodes per CWT (Tab. 11). The criteria for selecting an appropriate daily record (ADR) from the MPI-LGM to force the WRF-Chem-LGM boundaries are described in Tab. 10. In total, 1040 potentially distinct ADRs were selected.

It is unlikely that these 1040 ADRs are uniformly or randomly distributed over the complete MPI-LGM. Instead, due to the selection criteria that seek to extract consecutive sequences of eight ADRs, deviations from the uniform and random distributions are likely: Considerably more January, December, and July ADRs were selected (Fig. 63) than expected in the case of an intra-annually uniformly distributed number necessitating between 79 and 89 ADRs per month. Thus, according to the MPI-LGM, the early winter (December and January) and the mid summer (July) contain more ADR sequences. More specifically, 161 ADRs resulted from the 3100 January MPI-LGM records and more than 141 ADRs from the December records. In contrast, only 56 and 43 ADRs resulted for August and September respectively (Fig. 63).

Thus, the per se reasonable preference to choose the ADR sequences in decreasing order of duration from the MPI-LGM over-represents the early winter and July in the ADR ensemble, while it under-represents August and September. This indicates that the day by day LGM pressure variability in central Europe (Transdanubia) was—compared to the remaining months—on the one hand much lower during the early winter and July, on the other much higher during August–September. The ADR distribution (Fig. 63) indicates that March, May, and October were closest to the number of ADRs presupposed by the uniform distribution.

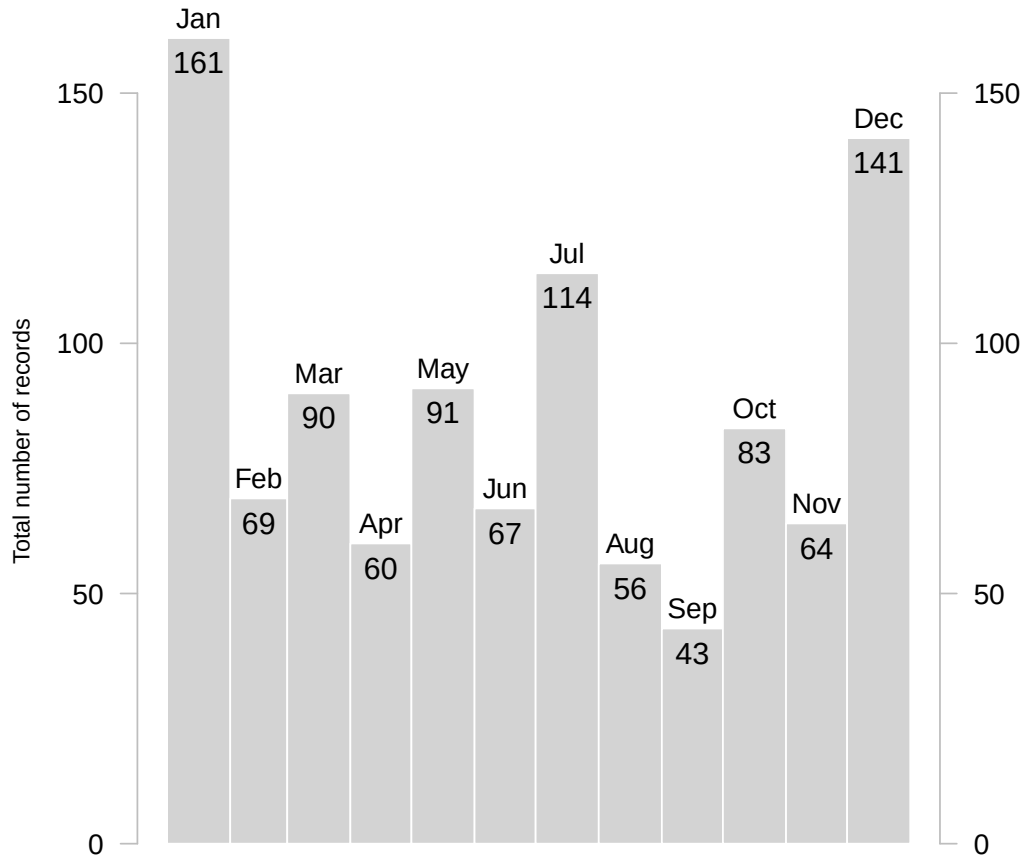

Figure 63: Intra-annual distribution of the 1040 selected appropriate daily records (ADR; according to (Tab. 10)) to statistical dynamical downscale the MPI-LGM.

Circulation Weather Type-wise intra-annual distribution of episodes All of the 13 longest LGM cyclonic CWT episodes over central Europe occurred between late spring and mid summer (Fig. 64). More precisely, about two thirds of them prevailed in May (~61%), the remaining were distributed over the two subsequent months, i.e. June (~28%) and July (~10%).

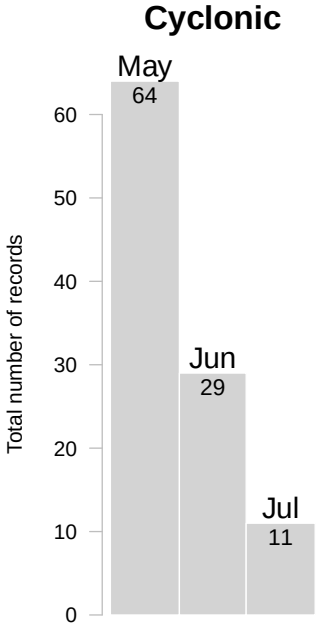

Figure 64: Intra-annual distribution of the selected records (Tab. 10) to simulate the required 13 cyclonic episodes over central Europe for the statistic dynamic LGM reconstruction. These MPI-LGM records forced the regional WRF-Chem-LGM boundaries.

The 13 longest anticyclonic CWT episodes mostly occurred between November and January and slightly less often in March and August (Fig. 65). During February, September, and from April until July, they occurred hardly or not at all.

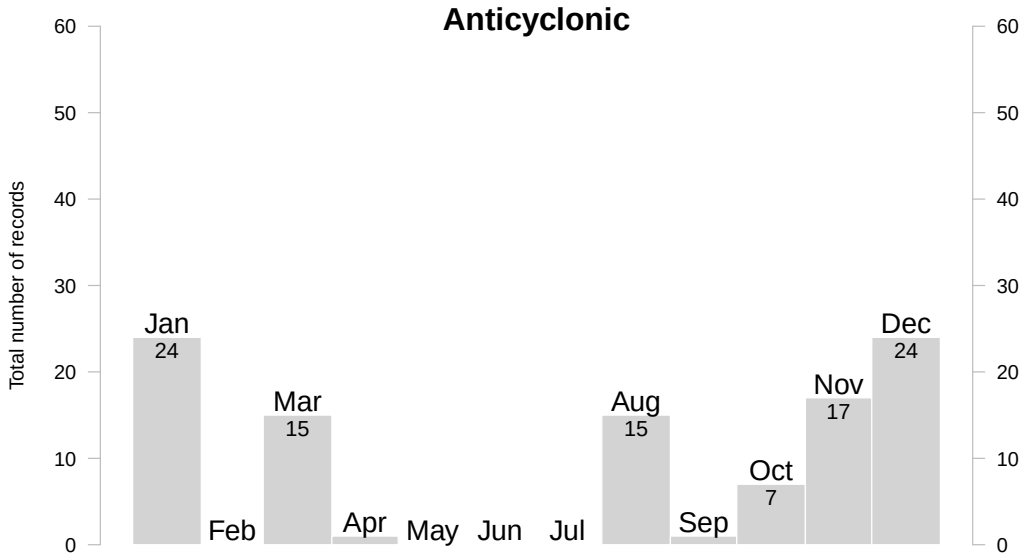

Figure 65: Intra-annual distribution of the selected records (Tab. 10) to simulate the required 13 anticyclonic episodes over central Europe for the statistic dynamic LGM reconstruction.

The 13 longest northeaster episodes over central Europe during the LGM occurred most often during August (24%), then June, and October (Fig. 66). None or only a few occurred in March, April, and July.

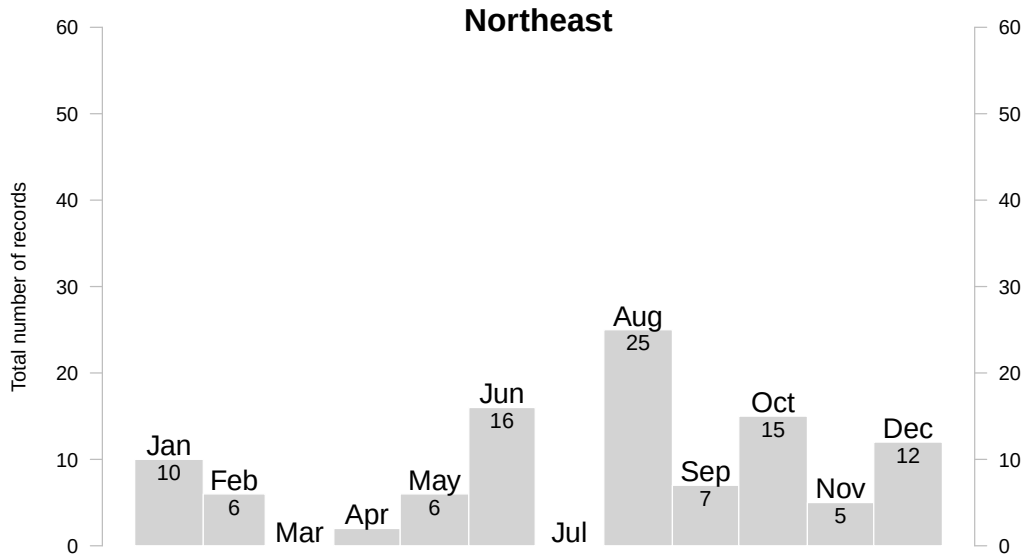

Figure 66: Intra-annual distribution of the selected records (Tab. 10) to simulate the required 13 northeaster episodes over central Europe for the statistic dynamic LGM reconstruction.

Most of the 13 longest easterly episodes occurred in October (23%), then April (22%), and March (19%) (Fig. 67). None occurred during summer and September.

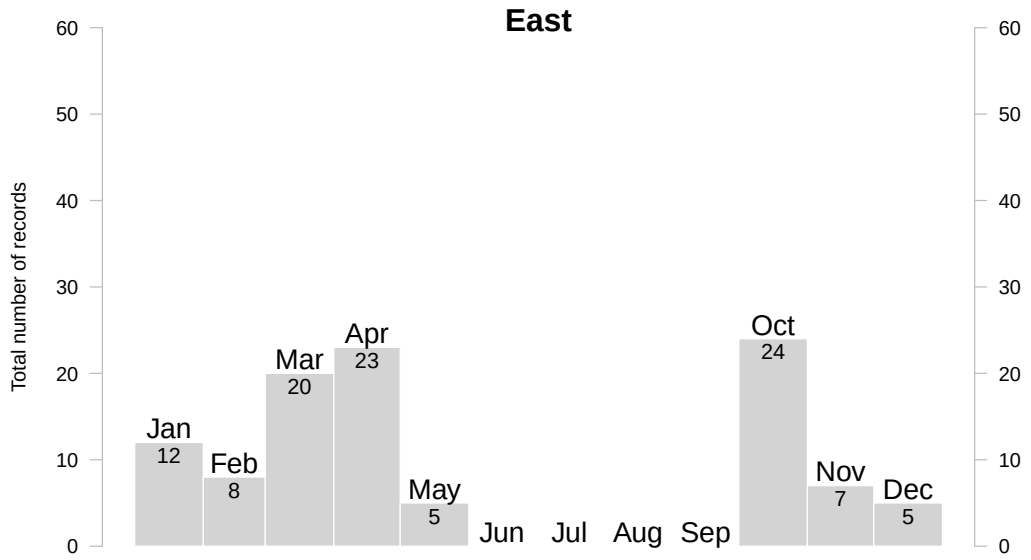

Figure 67: Intra-annual distribution of the selected records (Tab. 10) to simulate the required 13 easterly episodes over central Europe for the statistic dynamic LGM reconstruction.

All of the 13 longest southeasterly episodes occurred during the winter half-year, between October and April. Most of them occurred in March (25%), slightly less during the mid–late winter (Fig. 68).

About 40% of the 13 longest southerly episodes occurred during December, the remaining were distributed from autumn to spring; none occurred in summer (Fig. 69).

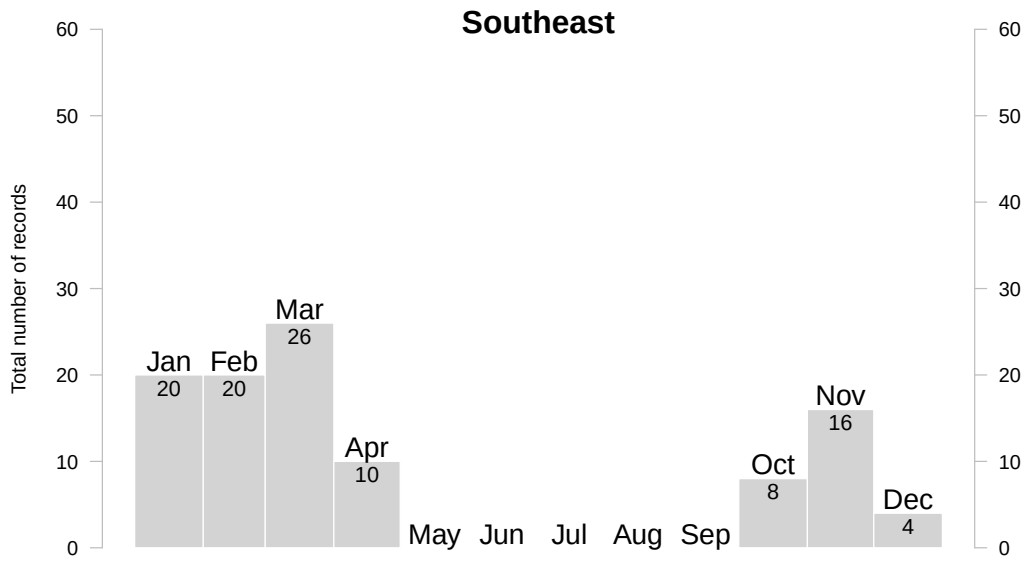

Figure 68: Intra-annual distribution of the selected records (Tab. 10) to simulate the required 13 southeaster episodes over central Europe for the statistic dynamic LGM reconstruction.

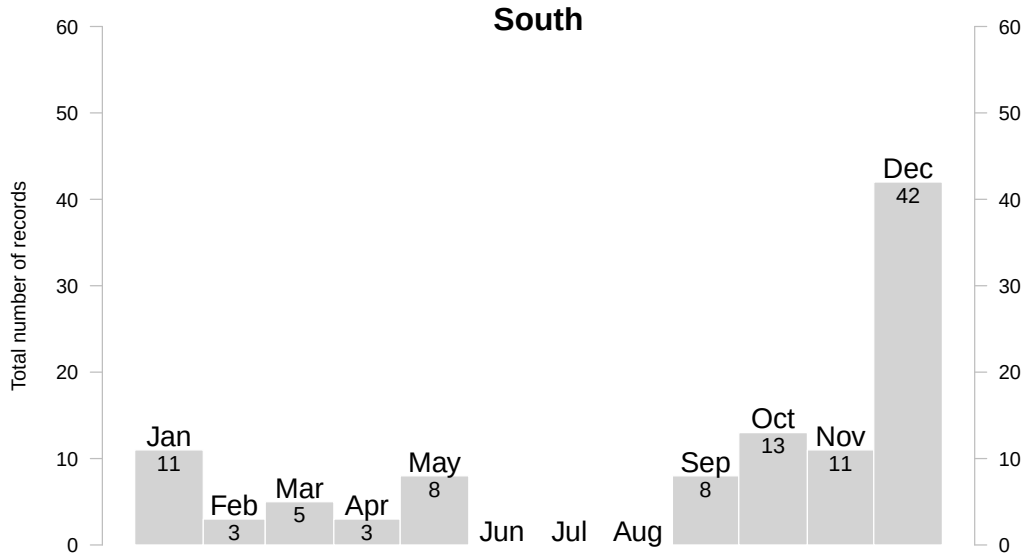

Figure 69: Intra-annual distribution of the selected records (Tab. 10) to simulate the required 13 southerly episodes over central Europe for the statistic dynamic LGM reconstruction.

Most of the 13 longest southwesterly episodes occurred over central Europe in the LGM winter (Fig. 70): in January (33%), December (20%), and February (15%). Thus, more than two thirds of the CWT-SW episodes typically occurred only during the winter according to the MPI-LGM. In contrast, during summer including September, southwesterly episodes were absent.

All of the 13 longest westerly LGM episodes occurred between early winter and mid spring, more than 80% between December and March (Fig. 71). More specifically, about half (48%) of them occurred in January, followed by March (~20%) and December (~15%, Fig. 71).

About 80% of the 13 longest LGM northwester episodes over central Europe occurred between mid summer and early autumn (Fig. 72). Almost half of them occurred in July (45%), followed by the subsequent months August (15%) and September (18%). None occurred during November to January and in spring.

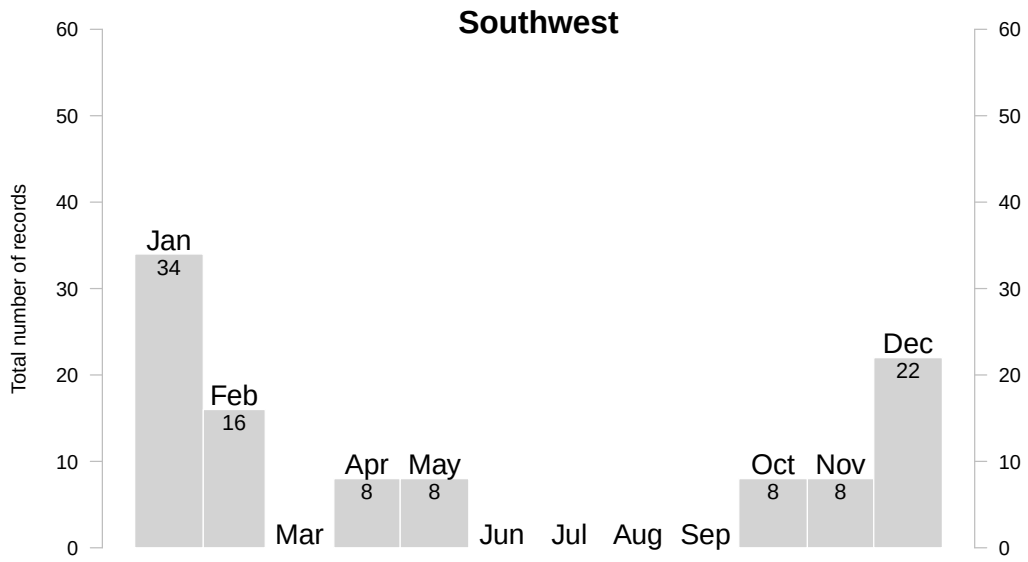

Figure 70: Intra-annual distribution of the selected records (Tab. 10) to simulate the required 13 southwester episodes over central Europe for the statistic dynamic LGM reconstruction.

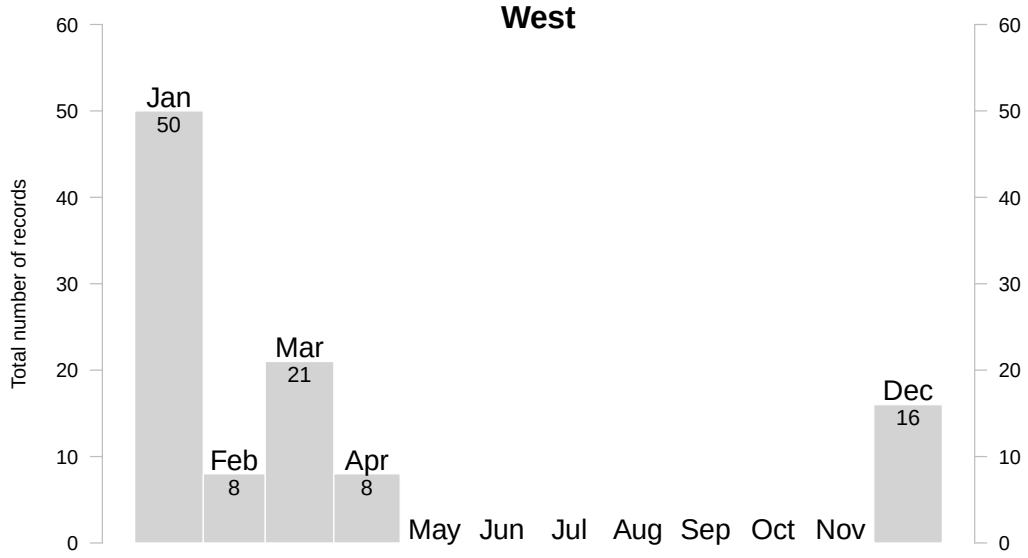

Figure 71: Intra-annual distribution of the selected records (Tab. 10) to simulate the required 13 westerly episodes over central Europe for the statistic dynamic LGM reconstruction.

More than half of the 13 longest northerly episodes over central Europe during the LGM (Fig. 73) occurred in July (54%). On the contrary, none occurred between October and mid March, except for the second most frequent monthly occurrence in December (15%).

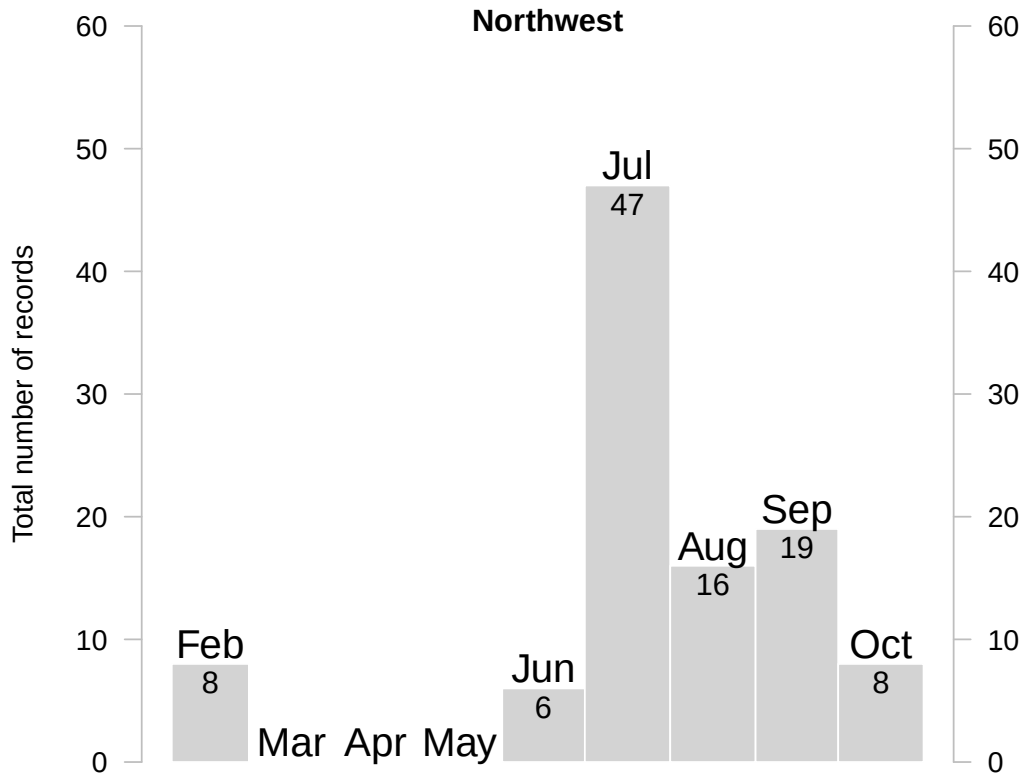

Figure 72: Intra-annual distribution of the selected records (Tab. 10) to simulate the required 13 northwester episodes over central Europe for the statistic dynamic LGM reconstruction.

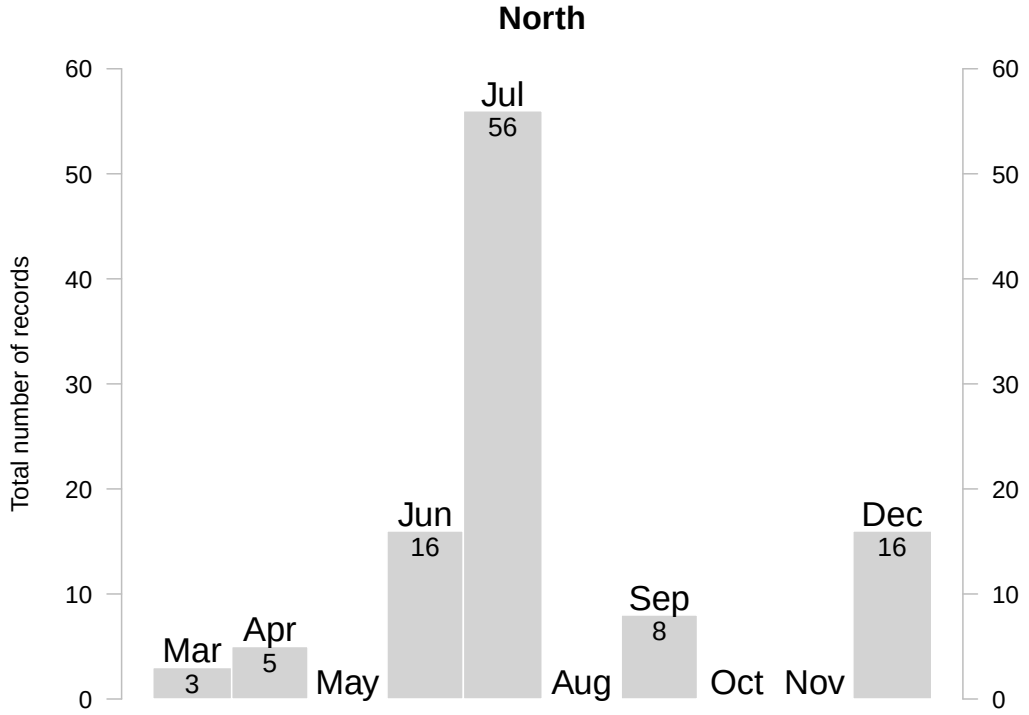

Figure 73: Intra-annual distribution of the selected records (Tab. 10) to simulate the required 13 northerly episodes over central Europe for the statistic dynamic LGM reconstruction.

7.4.6 Seasonally resolved Atmospheric Circulation and Dust Distribution

The daily-resolved LGM CWT occurrence frequencies over central Europe (Transdanubia, Tab. 7) based on the MPI-LGM were seasonally heterogeneously distributed (Tab. 12 and Fig. 74). During spring, the eastern wind sector (NE, E, SE) prevailed almost half of the time (45%) over central Europe. During summer, cyclonic regimes (30%) prevailed the most, followed by the eastern wind sector (23%), the western wind sector (22%), and the northerlies (11%). During fall, the east sector dominated (39%), followed by cyclonic regimes (20%). During winter, the occurrence frequencies among all ten CWT classes were distributed the most uniformly, compared to the other seasons. Still, the east sector winds dominated (38%), reinforced by frequent southerlies (13%). This results in an extended eastern–southeast sector prevailing more than 50% of the times. The anticyclones occurred the most frequent (13%) during the LGM winter. Though the cyclonic regimes occurred the least during winter (14%), they were still the second most prevailing individual class following the easterlies (15%).

Table 12: Seasonal Circulation Weather Type frequencies (%, rounded) for central Europe (Transdanubia) during the LGM, based the daily-resolved MPI-LGM. December, January, and February (DJF); Cyclonic (C) and Anticyclonic (A) regimes; northeasters (NE), etc.

	C	A	NE	E	SE	S	SW	W	NW	N
DJF	14.0	13.0	11.7	14.5	12.1	12.5	8.4	4.7	3.8	5.3
MAM	25.0	6.0	12.8	19.0	12.8	8.9	5.2	2.8	2.9	4.6
JJA	30.2	6.8	12.0	5.9	4.7	7.4	7.2	5.8	8.8	11.4
SON	19.5	10.0	13.3	14.3	11.3	10.3	6.6	3.8	4.3	6.7
Year	22.2	8.9	12.4	13.4	10.2	9.7	6.8	4.3	5.0	7.0

As previously discussed (Sec. 7.3, p. 94), the statistic dynamic downscaling requires a reasonably large number of episodes for the reconstructed dust cycle period. For each CWT and each period, corresponding episodes consisting of consecutive ADRs are necessary (Tab. 10). It has also been discussed in this dissertation that the intra annual episode distribution is not uniform (Sec. 7.4.5, p. 141). Thus, the rigorous seasonally-resolved LGM reconstruction according to the respective seasonal CWT frequencies (Tab. 12) is impossible based on the 130 prototypical episodes that were extracted from the MPI-LGM. If the statistic dynamic downscaling rigorously sticks to the criterion of episodes consisting of at least eight consecutive records of the same CWT, then a longer MPI-LGM would probably be able to provide such a number of episodes. However, this can fail, if the seasonally influenced climate model dynamic per-se suppresses longer mono CWT episodes during the respective seasons.

Alternatively, it would be possible to lower the selection criteria for the CWT episodes, i.e. accepting also (much) shorter episodes of the same CWT. Using this less rigorous method, it would be necessary to assess if each episode is long enough to allow the complete representation of the dust emissions, transport, and depositions.

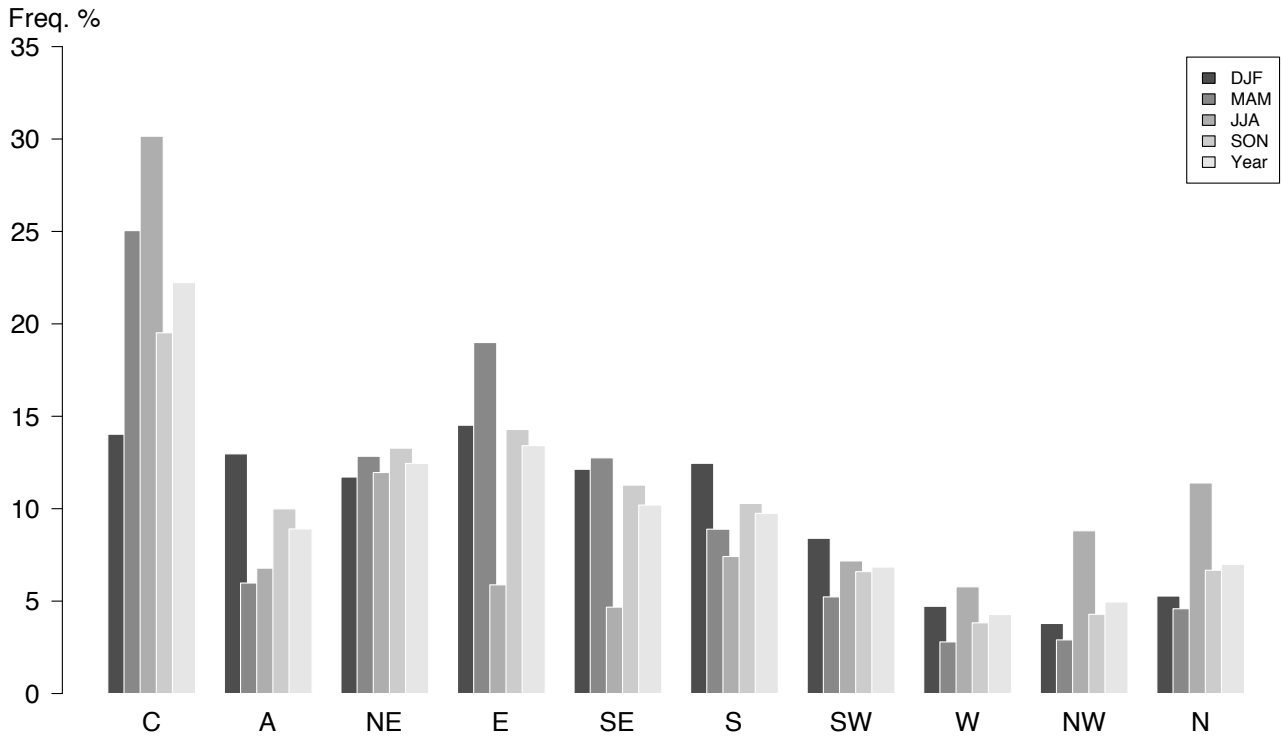

Figure 74: Seasonal LGM Circulation Weather Type occurrence frequencies for central Europe (defined by Transdanubia). The simulated sea level pressure fields of the MPI-LGM serve as input data to the performed analyses.

It has also been thought of seasonally resolved LGM dust reconstructions that base at least partly on CWT episodes of the other three seasons. However, this likely induces season-specific bias due to, for example, the inappropriate effect of the radiative forcing, the sea ice, the vegetation, the precipitation, and the snow cover.

7.4.7 Static LGM Boundary Conditions for Regional Dust Simulations

The subsequent figures show the results of creating a set of LGM environment data that were used as static boundary conditions in the WRF-Chem-LGM climate-dust simulations. The data and the methods on which these boundary condition reconstructions are based are detailed in Tab. 9.

The LGM-adapted topography for Europe takes into account the significant elevations of the EIS over northern and central Europe including the British Isles; along with the lower global mean sea level and dry-fallen areas such as the northern Adriatic (Fig. 75). As the definition of the potential dust source areas has been closely linked to the topography gradients, the calculated areas are depicted on the same map (Fig. 75).

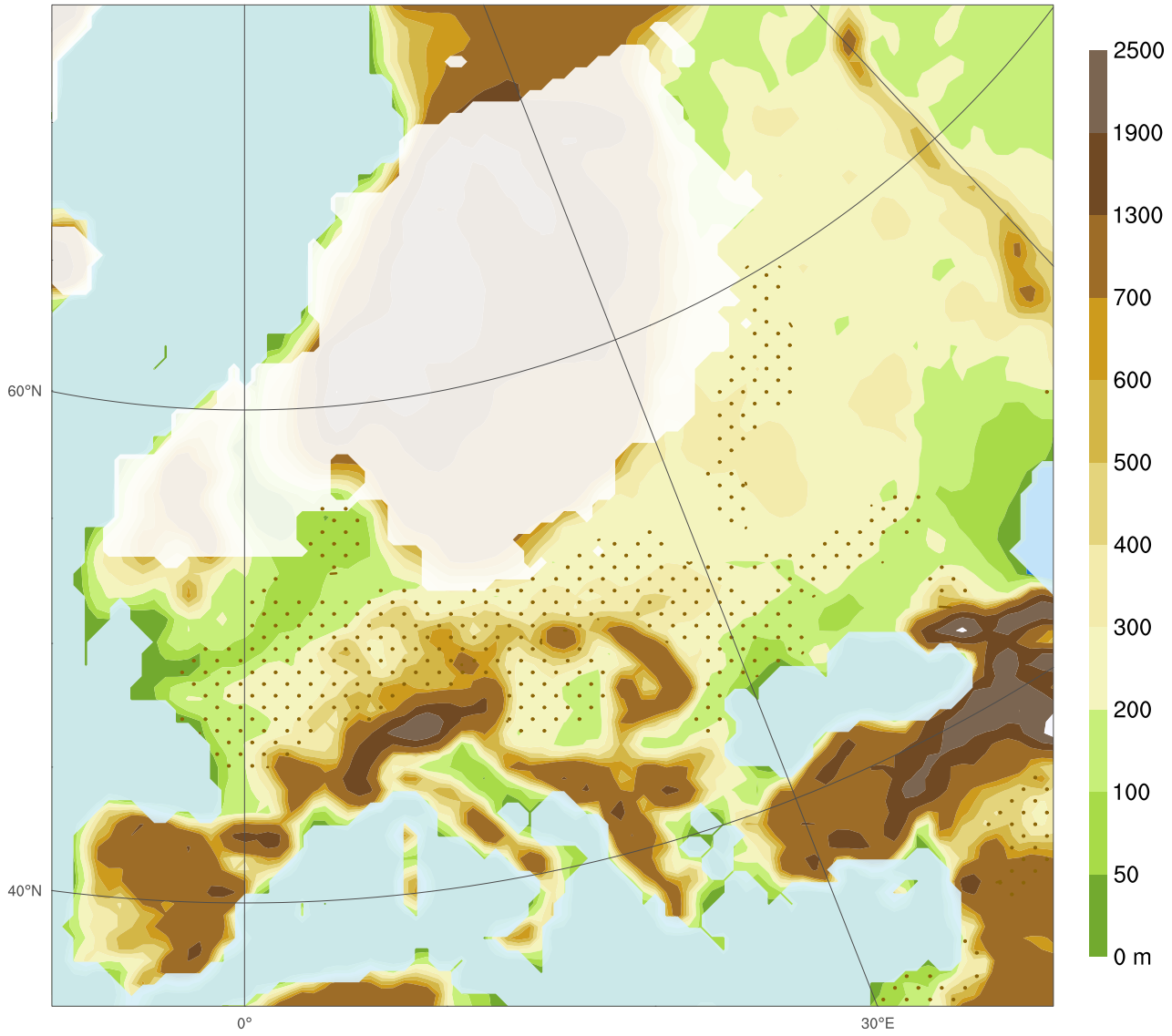

Figure 75: Adapted topography at 50 km horizontal resolution applied for all WRF simulations. Potential dust source regions (dotted) and the EIS[178] (white) are marked. Data sources specified in Tab. 9

During the LGM, the reconstructed vegetation cover for December is the sparsest of all months (Fig. 76), whereas it is densest for June (Fig. 77).

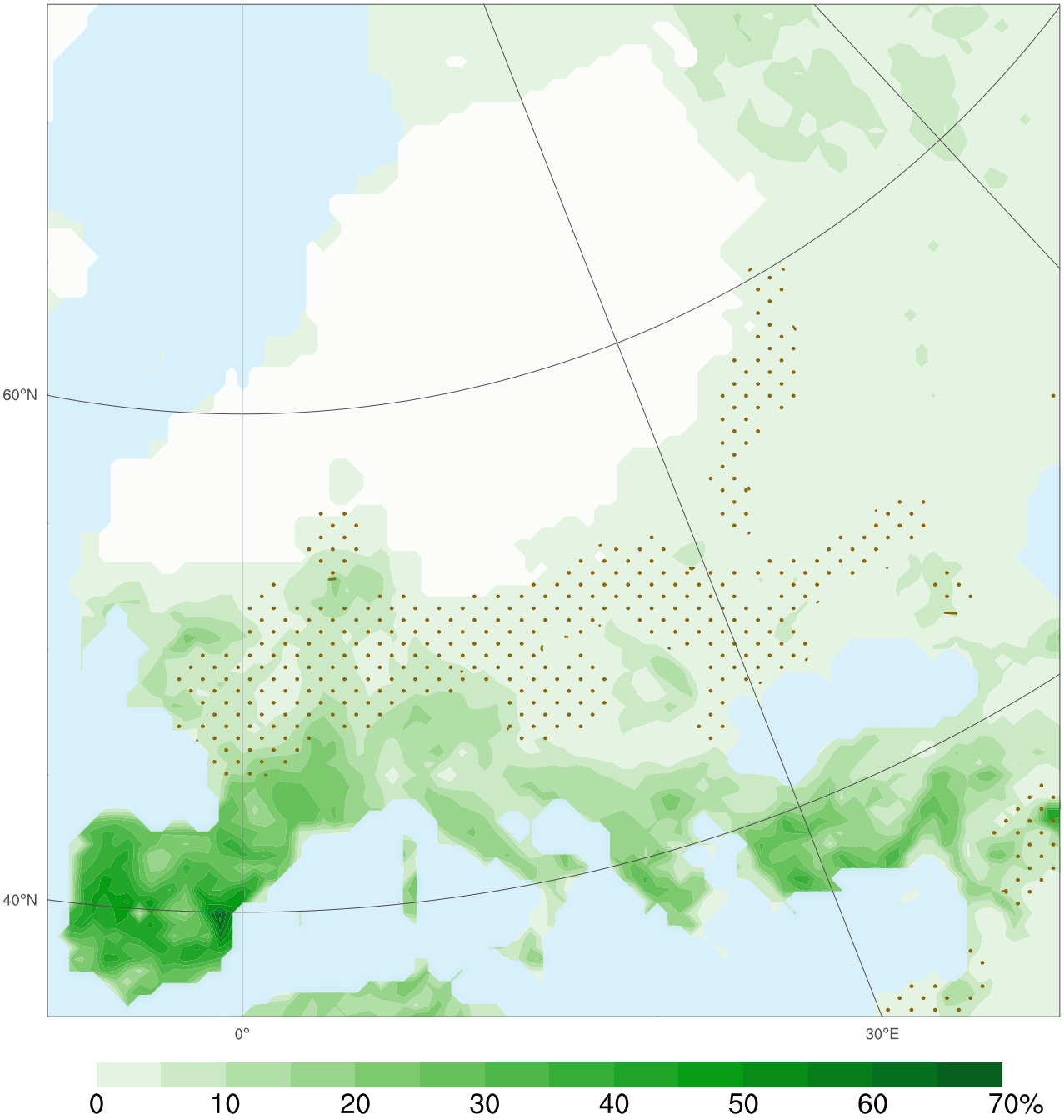

Figure 76: Sparsest monthly LGM vegetation cover. It existed—according to the reconstruction[178]—during December.

Parts of the Mediterranean region, such as Iberia, Greece and the coastal areas of Turkey, were covered the whole year long by vegetation, preventing dust emission (almost) completely there (Fig. 78 and 79). During the LGM winter and early spring (Dec to Apr, Fig. 78), below average vegetation covered the southern and eastern proglacial EIS regions. This favored high dust emissions there; in line with the erodibility distribution (Fig. 75).

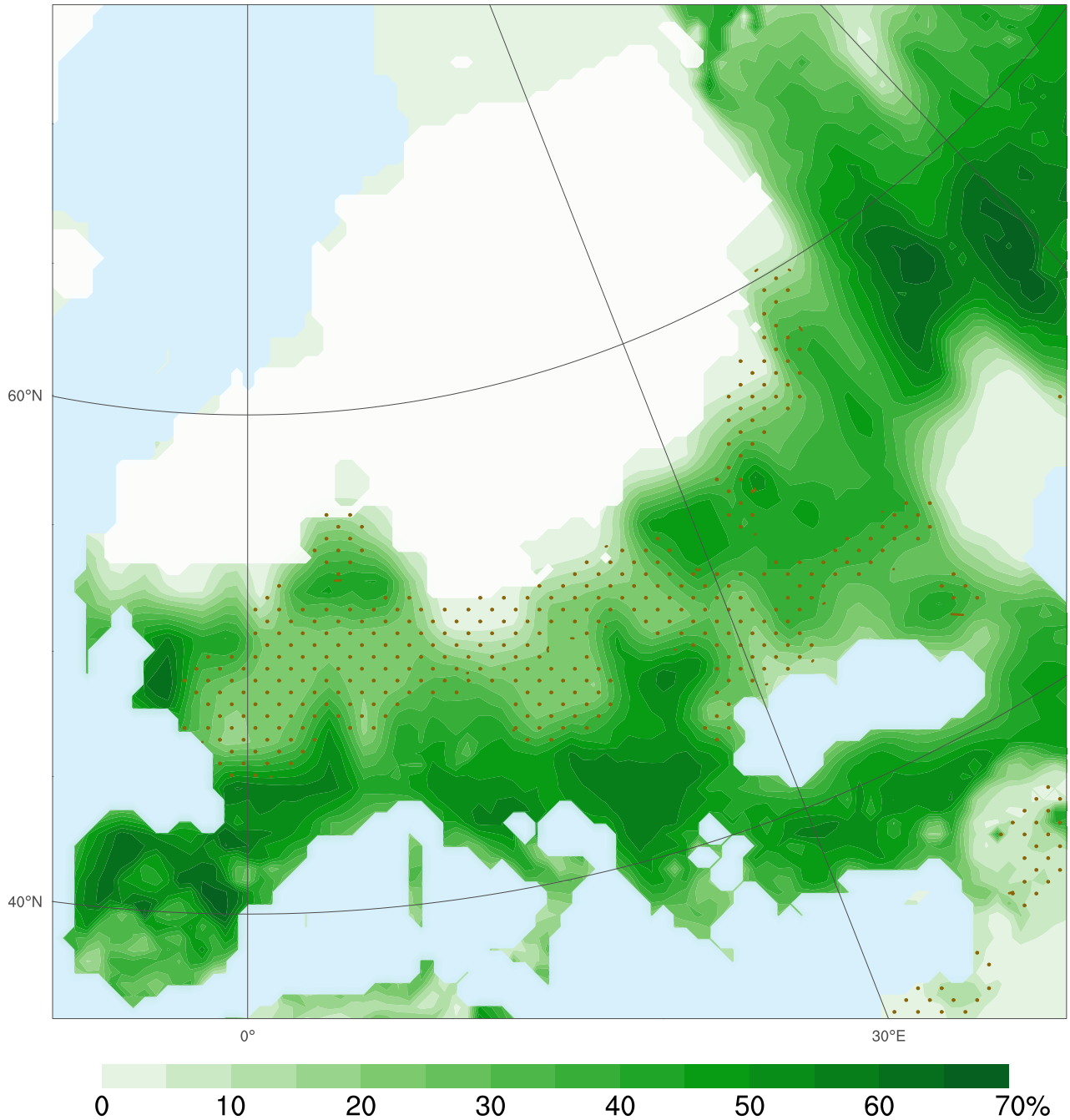

Figure 77: Maximum monthly vegetation cover, reconstructed for the LGM. The maximal cover prevailed—according to this reconstruction—during June. Remaining shapes as in Fig. 75. Data sources specified in Tab. 9.

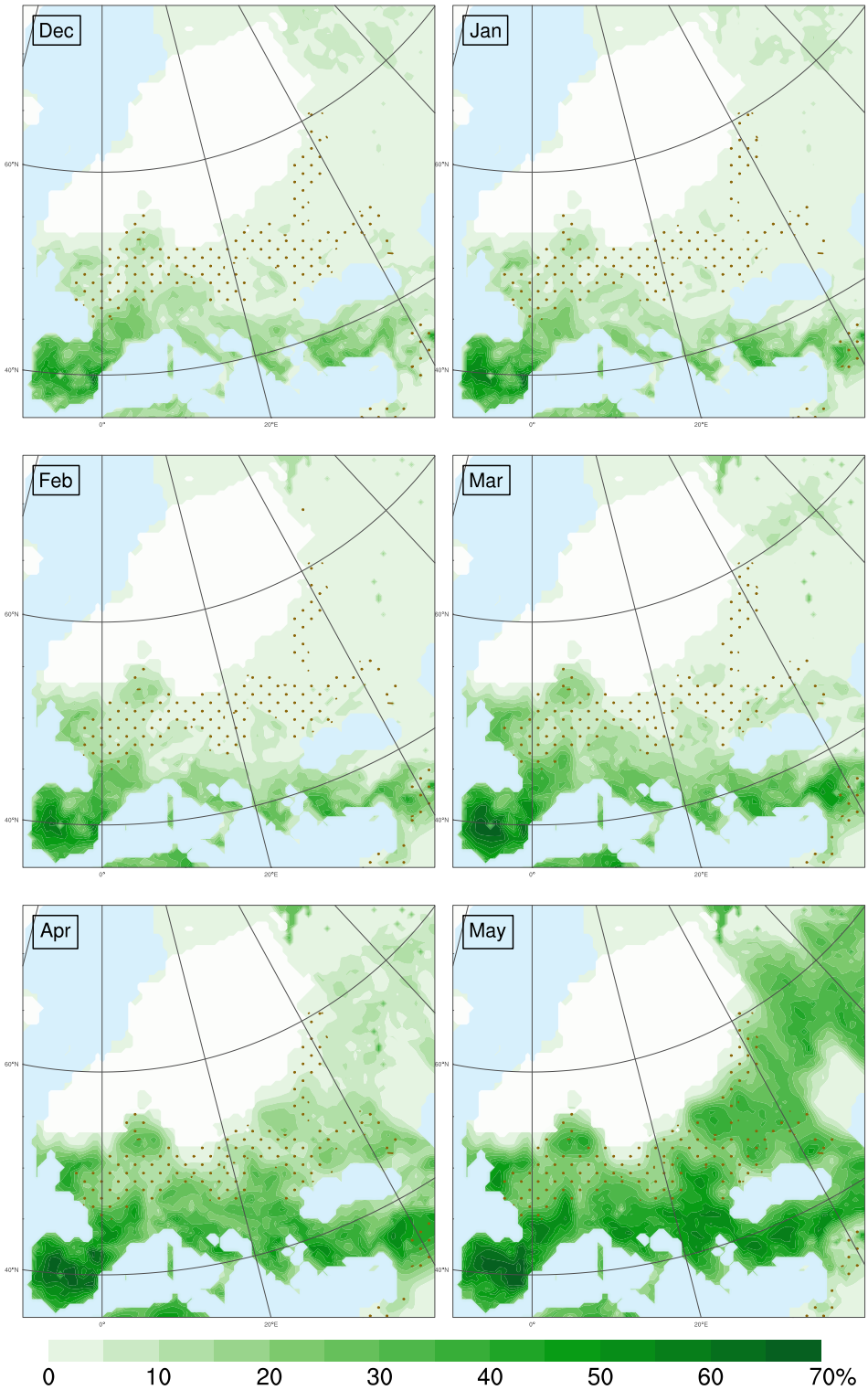

Figure 78: Average vegetation covers, reconstructed for the LGM winter and spring (Dec. to May)

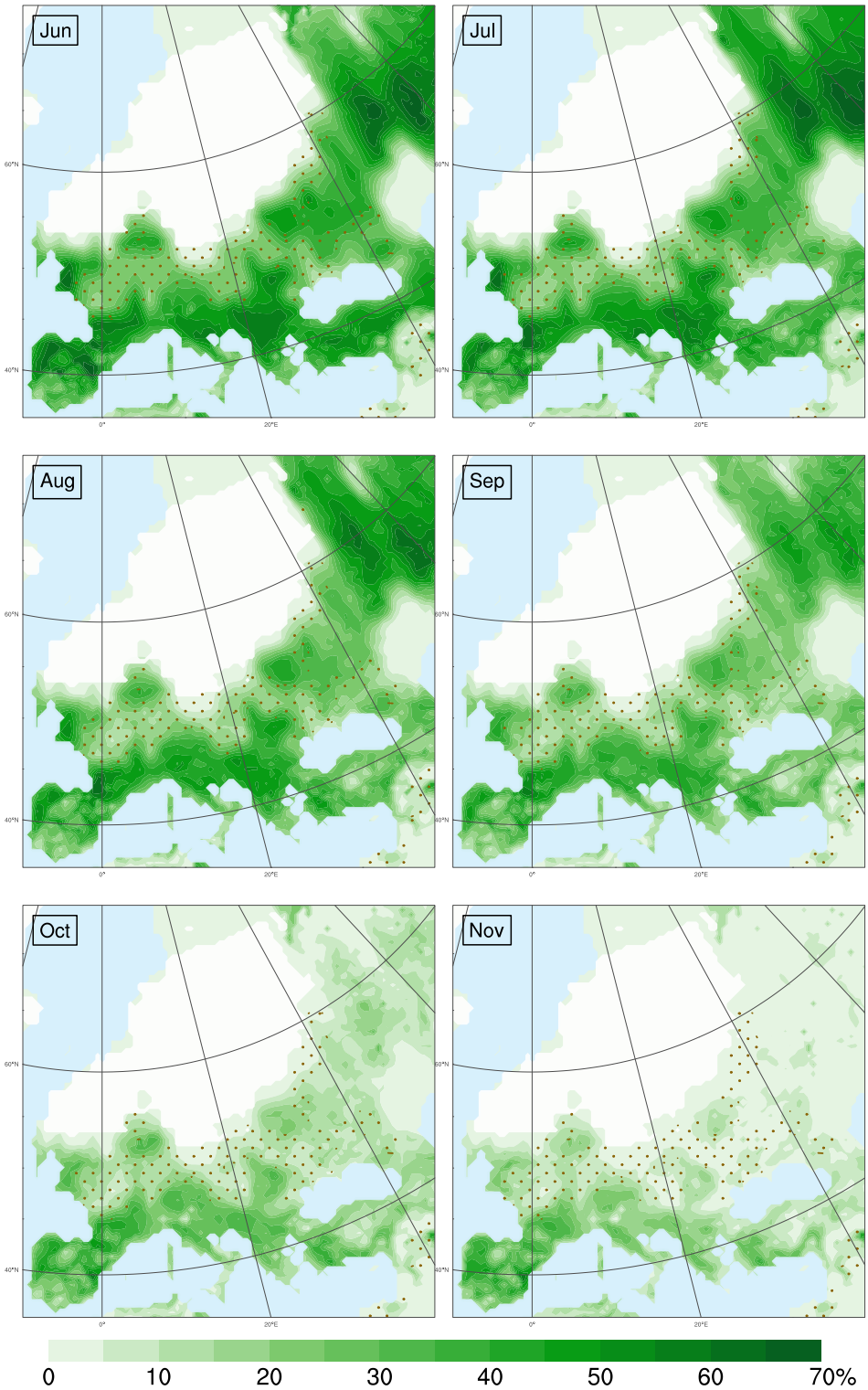

Figure 79: Average vegetation covers, reconstructed for the LGM summer and autumn (June to Nov.)

According to the LGM land use reconstruction for Europe, vast areas in western, central, and eastern Europe were dominated by herbaceous tundra (Fig. 80). These areas eroded more easily, compared to the southwestern Mediterranean that was dominated by shrubs. This applied in particular to the southern and eastern margins of the EIS, where dry and strong wind prevailed, most likely of katabatic origin. In the Carpathian Basin, lower amounts of dust emissions were probably a consequence of the mixed forest cover that prevailed there during the LGM.

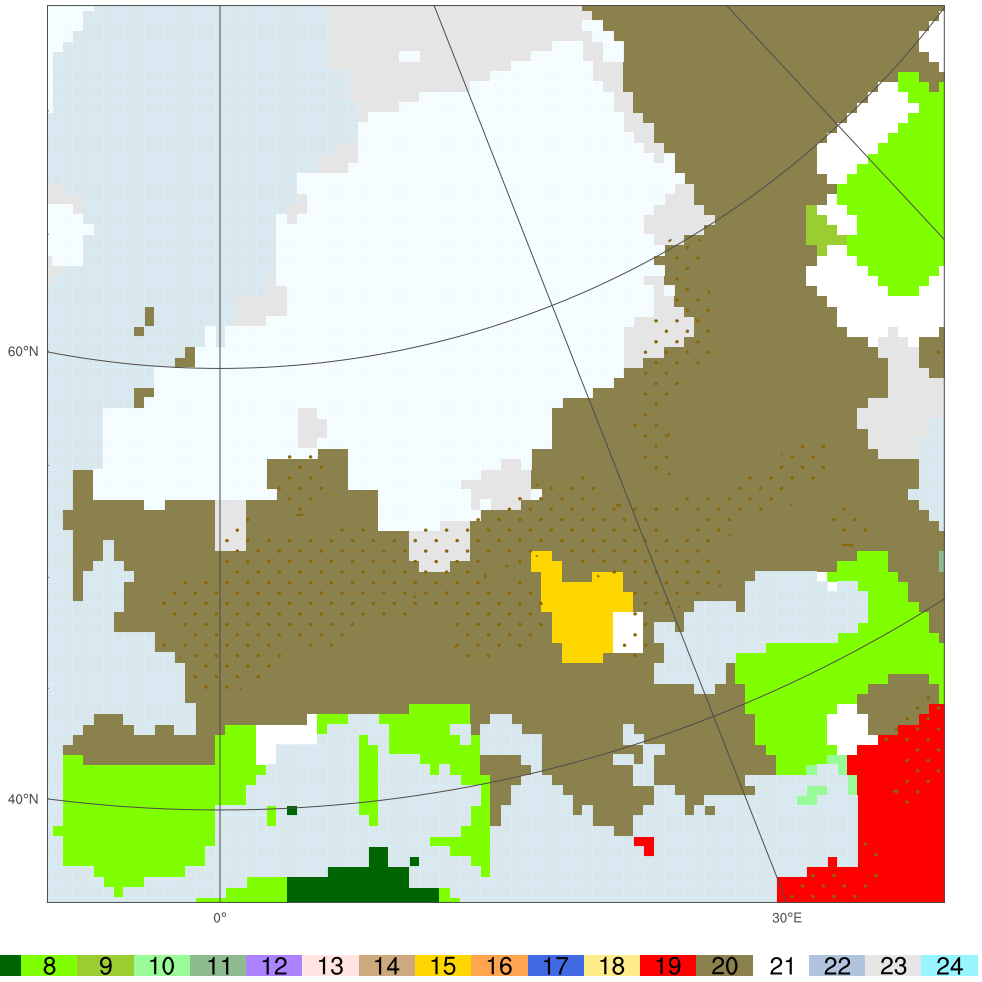

7	Grassland	8	Shrub
9	Mixed Shrubland/Grassland	10	Savanna
11	Deciduous Broadleaf Forest	12	Deciduous Needleleaf Forest
13	Evergreen Broadleaf	14	Evergreen Needleleaf
15	Mixed Forest	16	-
17	Herbaceous Wetland	18	Wooden Wetland
19	Barren or Sparsely Vegetated	20	Herbaceous Tundra
21	Wooded Tundra	22	Mixed Tundra
23	Bare Ground Tundra	24	-

Figure 80: Reconstructed[178] land use index for the Last Glacial Maximum. Categories according to the United States Geological Survey, apart from *Water Bodies* colored in light blue and *Snow or Ice* colored in light cyan. Erodible areas dotted.

Until now, a peer-reviewed compilation of the spatial distribution of top soil types in Europe is missing. Due to this deficiency, today's distribution of top soil types adapted to the EIS extent is used as the best available approximation for the LGM top soil type distribution (Fig. 81).

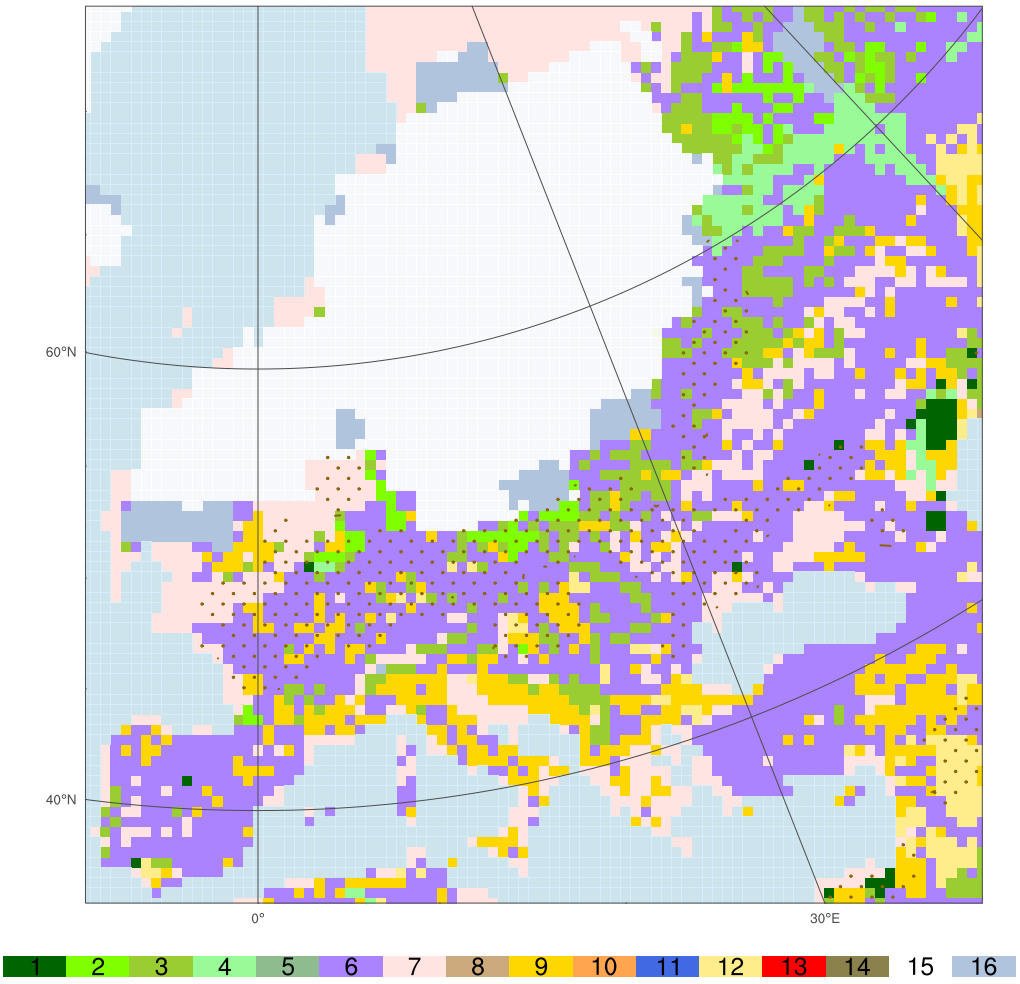

1	Sand	2	Loamy Sand
3	Sandy Loam	4	Silt Loam
5	Silt	6	Loam
7	Sandy Clay Loam	8	Silty Clay Loam
9	Clay Loam	10	Sandy Clay
11	Silty Clay	12	Clay
13	-	14	-
15	-	16	Other

Figure 81: Distribution of the dominant top soil types, reconstructed for the Last Glacial Maximum. The top soil distribution uses present-day WRF geo-data for all areas that are not otherwise determined by published LGM surface data. The dominant top soil type is assumed to be *Sandy Clay Loam* in the areas that were dry-fallen during the LGM. Water surfaces colored in light blue. Extents of the ice sheets colored in light cyan, almost white. *Other* (category 16) includes all remaining, non-listed Earth surface types including ice but excluding bedrock, water surfaces, and organic material.

7.5 Limitations

MPI-LGM The proportion of the zonal west sector winds (CWT-NW, -W, and -SW) is too large over Europe in most of the GCM simulations[259]. Consequently, these simulations underestimate the real number of blocking days. A GCM-to-reanalysis comparison[225] found that the MPI underestimates 4% of the number of blocked days. Blocking was most likely underestimated for the LGM as the simulations for the recent and the LGM climate base on the same model. In this case, the proportion of the east sector winds and of their dust transport underestimates their real importance during the LGM in Europe.

Results based on Polar-WRF[260] simulations suggest that the MPI-LGM possibly overestimated the LGM sea surface temperatures near Europe[37].

Saharan and Arabian Dust African and Arabian Peninsula dust possibly contributed to the depositions in Europe. Yet, the potential dust emissions and transports from there could only be represented in a negligible way, given the chosen domain (Fig. 75). The domain includes Syrian, west Iraqi, and Sinaitic dust sources (Fig. 75). Thus, the enhanced aeolian dust supply from the Sahara to the eastern Mediterranean[237] that was inferred from marine sediments[257] is hardly verifiable here.

The same argument applies to the possible deposition of North African silty 2–8 µm admixture in the Carpathian Basin[57,261]. However, the supposed contribution of North African dust to the loess in the Carpathian Basin is rather subordinate according to grain size analyses.

The effect of long-term variations of the African summer monsoon as well as possibly increased Saharan dust emissions during glacial phases due to the more seasonally distributed precipitation[257] are beyond the scope of this study.

Hybrid record counting According to the classification of the MPI-LGM records for central Europe, the sea level pressure field of certain records corresponds simultaneously to a circular and a directional weather type. These records are called hybrid and each of them is assigned to two CWTs. If all possible kinds of hybrid records were taken into account, 26 different CWT classes would potentially have resulted. Yet, 26 CWTs would have resulted in a high segmentation of the MPI-LGM records. Then, each CWT-class would most likely have represented on average too few consecutive records to extract a reasonable number of prototypical CWT-episodes. This, in turn, would have made it impossible to simulate enough independent appropriate eight-day episodes required to statistically-dynamically downscale the GCM. For the scope of this study, the CWT classification is therefore limited to ten classes (Tab. 11) and hybrid records were classified by considering only their directional weather type. This kind of counting may have resulted in an overestimated occurrence frequency for each directional class at the expense of underestimated occurrence frequencies for both circular classes.

Most limiting representations in climate-dust models Numerical climate-dust models only approximate the reality. Thus, it is important to determine which numerically represented or not-yet represent process in the Earth's climate system limits the most the validity of the model outcome. The improvement of these processes will create the largest benefits to the scientific understanding of nature.

Dust particles larger than 20 µm In the applied UC dust scheme of the WRF-Chem-LGM (Tab. 8), the 20 µm dust particle diameter limit could be increased in future to represent more completely the real dust particle size distribution. In the current UC dust scheme range, only clay and small-sized silt particles are represented, i.e. large-sized silt[79] and all kinds of sand particles lack. Nevertheless, particles up to 20 µm are the most important for global, continental and supra regional scale aeolian dust transport.

In the Carpathian Basin (CB), fieldwork-based loess grain size distributions usually peak at or above 20 µm. This implies that particles larger than 20 µm potentially participated in the aeolian LGM dust cycle, e.g.forming LGM dust storms[63]. Thus, the WRF-Chem-LGM simulations potentially underestimated the real emission, transport, and deposition rates.

Erodibility and European surface soil types Satellite observations show that large dust storms emanate from pointlike sources[58] implying that local, site-specific wind and land surface conditions control dust emission. They mostly affect dust emission (highly) non-linearly. Thus, to simulate dust emission well, the climate models require high-resolved terrain and surface soil data[262]. However, high-resolved surface soil distribution data is missing for vast parts of the Earth even for the present[58]. This shortcoming is even larger for the LGM, for which it applies in particular also to Europe. In this dissertation, the LGM distribution of the soil types in Europe was approximated by its present-day standard analogue; however, adapted to the EIS extent and the dry-fallen areas. The WRF-Chem evaluates the numerical value of the erodibility as a Boolean variable, which can be considered as a rather coarse representation. The WRF-Chem-LGM uses the same equations as the WRF-Chem, except for the additional LGM cut-off filter requiring setting a threshold of 0.09. Nevertheless, the WRF-Chem dust simulations have been validated successfully[238–240].

Intra-annual distribution of LGM episodes Given the constraints of the CWT-controlled statistic dynamic downscaling, the intra-annual distribution of episodes did not result uniformly based on the available MPI-LGM. The requirement of continuous 8-day episodes of the same CWT in the MPI-LGM resulted unintentionally in an above average number of appropriate episodes that occurred in January, July, and December. Possibly, these episodes caused an above average annual snow or vegetation cover in the ensemble mean of the WRF-Chem-LGM simulations. Nevertheless, the outcomes of statistic dynamic downscaling and dynamic downscaling were almost identical implying that this intra-annual deviation hardly matters.

Furthermore, the potential improvement of a shift towards more intra-annual uniformity would imply e.g. relying on fewer episodes per CWT, shorter episodes, or inventing longer episodes by concatenating disjunct shorter episodes found in the MPI-LGM. Whether one of these approaches generates a more realistic representation of the LGM dust cycle is not per se evident. To answer this, these approaches would likely need to be tested and evaluated against each other as well as against independent present-day measurements and e.g. LGM dust proxies. Beyond that, the priority of potential improvements in this aspect ought to be set in context to potential improvements in the other deficiencies such as e.g. the spatiotemporal resolution, meltwater effects, and dry-fallen riverbed dust sources.

Spatiotemporal simulation resolution The maximum possible spatiotemporal resolution and the maximum possible number of performed simulations were limited by the capacity of the high performance computing system. This limitation hindered reviewing certain fieldwork results by complementary simulations. For example, lower MARs were reconstructed for alluvial plains and hill slopes, whereas higher MARs were reconstructed for plateaus and river terraces, all of them located in the CB[57]. The review of these fieldwork results using WRF-Chem-LGM simulations requires a much higher than the current 50 km domain resolution, probably combined with nesting. Yet, it has been impossible to simulate the climate including dust at a 1 or 0.1 km resolution for Europe within the available computing time. To numerically review sites whose MARs had been determined by the local conditions[46] such as topography, climate and/or hydrology, nesting of climate-dust simulations and improved computing performance are necessary.

Hydrological dust cycle The land model of the WRF-Chem-LGM includes neither meltwater runoff nor lakes, torrents or rivers. Several fieldwork-based studies describe river-related effects on the European dust cycle during the LGM. Yet, given the current WRF-Chem-LGM constraints, their findings and assumptions were not verifiable.

River-shaped dust source locations and alluvial sediments According to loess-based dust flux estimates[57], the LGM dust sources were located, apart from in the proglacial southeastern EIS areas, along the Rhine and the Danube. For example, on the alluvial Danubian fans, silt-sized sediments were eroded[50,52,57] and reworked by winds[90]. The regimes of the periglacial braided rivers, such as of the Danube and the Rhine, highly contrasted over the year: These rivers transported huge amounts of sand and silt during short but strong meltwater discharge periods, while they remained almost completely dry for the rest of the year[84]. During the latter state, their river beds and valleys were exposed to deflation and likely provided the coarse material found in aeolian deposits[84]. The main sources of loess in Hungary must have been on the Danube catchment, according to isotopic signatures and detrital zircon U–Pb ages[57].

Hydrological erosion, transport, and deposition The thickest loess and coversands deposits are along or nearby major rivers, such as the Rhine and Danube[57,84]. Some of these deposits result from the Alps[51] and the Carpathians[57]. These glacial materials were carried, additionally to the aeolian dust transport, by the Danube and it tributaries to the alluvial fans[51,57]. For example, the Danube affected the loess formation in the CB and the supply of silt and of fine-grained material to the CB. The Danube presumably also fined material downstream, resulting in silt that forms part of today's Dobruja plateau loess (Romania)[52,170].

8 Conclusions

8.1 Climatology of the Last Glacial Maximum

For Europe and the North Atlantic, the LGM climatologies for pressure, temperature, and precipitation based on MPI-ESM-P simulations are consistent with independent global and regional simulations as well as with climate proxies (Sec. 4.4).

Jet stream, North Atlantic Oscillation, pressure systems, and surface winds In the EurAt Domain, the jet stream was narrower and faster during the LGM than at present; partly by more than $\Delta v = 10\,\mathrm{m/s}$. According to the PMIP-LGM, its fastest section was over the LIS coast (v = 40–45 m/s) . The—likely more realistic—MPI and MRI indicate a slightly lower velocity, v_{MPI} = 35–40 m/s and v_{MRI} =30–35 m/s. Its shape and propagation directions were affected by the LGM topography. Compared to the recent climate, it either bent west of the British Isles and continued northeastwards along the Nordic Seas, or it flowed along more southern latitudes over one of two topographic corridors: the Mediterranean or the southern part of the North German Plain.

The Azores High was larger, stationary lows were confined over the northwestern Atlantic, the NAO was stronger, and, during NAO plus phases, northwesters were most likely stronger over the North Atlantic. Moreover, quasi-stationary highs over the LIS and EIS prevailed favoring proglacial east sector surface winds. The storm tracks and the westerly flow over Scandinavia and the Baltic was blocked — most likely due to the EIS High.

Temperatures The temperature range in the EurAt Domain was larger during the LGM (−45 to 30 °C) than during the recent climate (−35 to 30 °C). The LGM temperatures differed most from their recent analogues over the LIS and EIS. East of the EIS, the temperatures allowed large-scale permafrost. There, the temperature difference to their recent values is second largest (ΔT between 8 and 26 °C). The LGM temperatures indicate large-scale sea ice in Baffin Bay, on the Labrador and Nordic Seas. They also indicate northward heat advection up to the northern Norwegian Sea. This non latitude-conform heat surplus most likely evidences that the North Atlantic Current reached up to there during the LGM. The spatial distribution of the LGM temperatures is supported by independent Mg/Ca-, foraminifera-, or alkenone-based temperature reconstructions. Particularly for central eastern Europe, the simulated temperatures are corroborated by biotic proxies such as pollen.

Precipitation The precipitation maxima of the LGM and the recent climate occurred over the Gulf Stream (7–8 mm/d) and the eastern shore of southern Greenland. The latter maxima was caused by moist winds forced to lift along the GIS gradient. Medium sized rates occurred over the subpolar gyre, the North Atlantic Current, and the remaining lift-causing topographic gradients in the EurAt Domain, such as the Norwegian west coast. Precipitation was (almost) absent over Baffin Bay and the top plateaus of the ice sheets due to previous lifting and cooling of the incoming air. Therefore, surplus moisture had condensed and precipitated before reaching the plateaus. The simulated LGM precipitation reduction over Europe is corroborated by independent biotic proxies. Low precipitation rates favored the aeolian erosion in proglacial central Europe and in unglaciated Eurasian regions north of 55°N.

8.2 Subclimatological Atmospheric Patterns

The cumulative explained variability of the first three and of the first 60 CEOFs for the EurAt Domain resulted to be higher for the LGM than for the recent climate. This raises the question whether the atmospheric variability during the LGM possibly had fewer degrees of freedom than during the recent climate, which implies a smaller LGM phase space of atmospheric states.

The strength of the glacial NAO varied distinctly. Related thereto, the temperatures varied over the Labrador Sea and the subpolar gyre. This temperature variability was synchronous but antiphased with the EIS coast temperature variability. Arctic winds, less precipitation, and freezing contrasted with southerlies, more precipitation, and melting.

The LGM precipitation variability between the Azores and Iberia (predominantly above-average rates) was probably related to the southwards shifted westerlies — particularly during NAO minus phases.

A distinct pressure variability seesaw resulted with one pole over the EIS and the other over southern Baffin Bay. During large positive EIS High anomalies, the EIS High likely merged with the Azores High. Synchronously, strong dry katabatic northerlies, northeasters, and easterlies prevailed over central eastern Europe while cyclones dominated the northwestern Sahara including the adjacent southern Mediterranean areas. These katabatic winds could explain the cooling between eastern France and Ukraine. Synchronously, warm anomalies occurred over the GIS, Iceland, and the Nordic Seas. Most likely, southerlies advected heat to there, coherent with the enforced pressure gradient between the EIS High and the Labrador Sea Low.

Phases of high precipitation over the northernmost Mediterranean Sea are consistent with independently reconstructed glacier equilibrium lines and biotic climate proxies. Over the southeastern GIS, the precipitation anomalies were large and mainly positive during the LGM. Synchronously with them, mainly negative anomalies prevailed over northeastern France, Germany, and the adjacent regions. The positive anomalies are coherent with the warming; both were consequences of the southerlies. The negative anomalies likely were an effect of katabatic winds.

Compared to the recent climate, larger subclimatological temperature variabilities prevailed over the easternmost LIS, the EIS-covered British Isles, and the subpolar gyre while the pressure variability was larger over Iceland, where the precipitation variability even doubled. The anti-phased precipitation variability between the Nordic Seas on the one and Labrador, the Azores, and eastern central Europe on the other hand was more pronounced during the LGM.

During the recent climate, the analogue of the EIS-Labrador pressure variability seesaw was less extended and dominated by negative anomalies over eastern Finland complemented by positive anomalies over the southern GIS. The recent temperatures varied most from Poland to central Asia with the highest variability at the Urals; its synchronous anti-phased variability centered over the Nordic Seas. Thus, the locations of the PI and LGM temperature variabilities contrasted. During the PI, central Europe varied anti-phased to Iceland. The Icelandic LGM variability encompassed a larger area because it extended over Iceland and almost the whole GIS. Among other, these PI to LGM differences resulted from their distinct topographies.

The third LGM CEOF suggests four synchronously varying pressure anomaly poles. Each pair of these in west-east direction neighboring poles is characterized by anti-phased anomaly amplitudes. The positive Franco-Iberian Anomalies were the strongest. They likely hindered westerlies to propagate over France and Germany; instead probably redirecting them towards the Nordic Seas.

Synchronously with the positive Franco-Iberian Anomalies, positive Bermuda, negative Azores, and negative Caspian Anomalies occurred. The combination of the EIS High, the negative Caspian, and the positive Franco-Iberian Anomalies favored cold-advecting northeasters from the Urals and the Arctic via eastern Europe up to the Hoggar Mountains. Proxies for the LGM confirm corresponding cold outbreaks over the northern Mediterranean.

Synchronously, western Iberia was warmer; likely due to warmer and drier southerlies that were favored by the Positive Pyrenees Anomalies and replaced colder and wetter westerlies. Coterminously, below average precipitation occurred also over France, Italy, the southeastern EIS, and the west Maghreb coasts; most likely due to the positive Franco-Iberian Anomalies. This likely favored dust emission — particularly from bare soil areas such as the proglacial southeastern EIS regions

Synchronously, above average precipitation occurred over the Azores, the subpolar gyre, western Iceland, the EIS coast, the Black Sea, Turkey, and the southern Mediterranean. Most likely, the required moisture had been advected by south sector winds to the three former areas, by westerlies to the EIS coast, and by northerlies to Turkey. The synchronous positive east Atlantic Anomalies favored warmer and wetter southerlies in their west, and colder and drier northerlies from the Labrador Sea in their east.

The less frequent negative Franco-Iberian Anomalies likely indicate approximately latitude-parallel propagating low pressure systems over France.

In contrast, according to the third LGM CEOF for the PI, above average pressure was most frequent over the British Isles (positive British Anomalies) synchronous with negative Urals Anomalies. Most likely, the lower topography favors this distribution, resulting in a weaker PI NAO.

Positive temperature anomalies over the GIS and the subpolar gyre (particularly southwest of Iceland) occurred most frequently and synchronous with negative temperature anomalies over eastern Europe. Analogously to the northward-shifted PI pressure anomalies, the temperature anomalies also shifted 15° to the north, i.e. they center north of the Carpathians. Positive precipitation anomalies prevailed over the southern GIS and the Norwegian west coast synchronously with negative precipitation anomalies in the neighboring areas of the British Isles. These GIS anomalies (absent during the LGM) were likely favored by the positive British Anomalies. The missing present-day precipitation anomaly synchrony between Norway and southern Turkey could relate to the negative Urals Anomalies, which are—compared to the Caspian LGM Anomalies—more distant from the Mediterranean.

8.3 Dominant Eastern Sector Winds over Central and Eastern Europe

While the anticyclones and the west sector winds prevailed during the recent climate, the east sector winds and the cyclones were more frequent in Europe during the LGM. In particular over central Europe (Transdanubia and Franconia), the east sector wind frequency doubled implying the dominance of east sector winds. Different reanalyses resulted in coherent, almost identical CWT frequencies. With regard to the (reference) CWT frequencies of the NCEP1 reanalysis, the MPI-PI reproduces best the recent climate in all four European regions. It outperforms the other three PMIP PI simulations as well as the PMIP-PI ensemble average. The CWT frequencies of the Preindustrial and of the recent atmosphere are almost identical to those of the reanalyses. In addition to classifying reanalyses (NCEP1 and 2, ERA-Interim) and recent climates (Preindustrial, transient 1850–2005), the CWTs were successfully applied for the first time to classify the LGM atmosphere. Their successful LGM applicability is corroborated by consistent independent proxy results. In analogy to the geological concept of actualism the MPI-LGM is thus most likely the best LGM climate approximation for Europe among all global PMIP LGM simulations including the PMIP-LGM ensemble mean.

8.4 Linkage of the European Dust Cycle and the Loess records

The LGM dust cycle in Europe, including emission, transport, and deposition, was successfully simulated using the WRF-Chem-LGM. Part of the research that resulted in this dissertation was the creation of the WRF-Chem-LGM. The implementation of two distinct GCM downscaling methods, the statistic dynamic downscaling (1040 days simulated) and the dynamic downscaling (10950 days simulated), was proven by their concordant results. This indicates the quality and efficiency of the statistic dynamic downscaling even for dust modeling and glacial boundary conditions, which is a new result that is neither known in the scientific community nor has been published yet.

The linkage between the LGM dust cycle and the present-day sediments of aeolian origin in Europe has been established. The CWT analysis of the MPI-LGM revealed dominant east sector winds (NE, E, SE; 36%) and cyclonic regimes (22%) over central Europe (centered at Transdanubia) during the LGM. Independent evidence for the prevailing east sector winds was found in numerous LGM wind proxies, such as loess, sand deposits, and wind-polished rocks.

This dissertation shows that the LGM dust originated mainly from the proglacial zonal corridor bounded in its north by the EIS margin and in its south by the Alps, the Danube, and the Black Sea. During the LGM, the highest dust emission rates ($>10^4$ g m^{-2} yr^{-1}) occurred at the EIS margins, the mountain foothills, and the dry-fallen flats. The highest LGM dust deposition rates (~10^5 g m^{-2} yr^{-1}) occurred at the southern EIS margins between 12° and 19°E. Considerable dust amounts deposited west of their sources. Dust deposited in particular on the North German Plain and in the North Sea Basin. Most LGM deposition areas correspond to today's loess sites. The simulated deposition rates are largely consistent across Europe with the independently reconstructed sediment-based MARs.

Simulation-based studies by others suggested that only westerlies and northwesters dominated over central Europe and that dust was transported only from west (or northwest) to east (or southeast) during the LGM. On the contrary, this dissertation presents the more complete LGM dust cycle by taking into account the dominant east sector winds (36%) that were favored by the EIS High. Both, the east sector winds and the cyclonic regimes (22%) eroded the proglacial cryogenic and alluvial LGM fans near the southern and eastern margins of the EIS. The resulting dust was deposited along the eastern and central European loess belt. Rare (16%) but presumably strong episodes of west sector winds (SW, W, NW) carried dust eastwards. The agreement between the simulation-based results and the fieldwork-based MARs supports the linkage between the dust cycle during the LGM and the present-day loess deposits in Europe.

9 References

1. Hershkovitz, I. *et al.* The earliest modern humans outside Africa. *Science* **359**, 456–459 (2018). URL http://science.sciencemag.org/content/359/6374/456. http://science.sciencemag.org/content/359/6374/456.full.pdf. 8

2. Campbell, M. C., Hirbo, J. B., Townsend, J. P. & Tishkoff, S. A. The peopling of the African continent and the diaspora into the new world. *Current Opinion in Genetics & Development* **29**, 120 – 132 (2014). URL http://www.sciencedirect.com/science/article/pii/S0959437X14000987. Genetics of human evolution. 8

3. Groucutt, H. S. *et al.* Rethinking the dispersal of Homo sapiens out of Africa. *Evolutionary Anthropology: Issues, News, and Reviews* **24**, 149–164 (2015). 8

4. Isaji, Y., Kawahata, H., Ohkouchi, N., Murayama, M. & Tamaki, K. Terrestrial environmental changes around the Gulf of Aden over the last 210 kyr deduced from the sediment n-alkane record: Implications for the dispersal of Homo sapiens. *Geophysical Research Letters* **42**, 1880–1887 (2015).

5. Oppenheimer, S. A single southern exit of modern humans from Africa: Before or after Toba? *Quaternary International* **258**, 88–99 (2012).

6. Maier, A. *et al.* Demographic estimates of hunter-gatherers during the Last Glacial Maximum in Europe against the background of palaeoenvironmental data. *Quaternary International* **425**, 49–61 (2016). 8, 38

7. Richter, J., Melles, M. & Schäbitz, F. Temporal and spatial corridors of Homo sapiens sapiens population dynamics during the Late Pleistocene and early Holocene. *Quaternary International* **274**, 1–4 (2012). 8

8. Schmidt, I. *et al.* Rapid climate change and variability of settlement patterns in Iberia during the Late Pleistocene. *Quaternary International* **274**, 179–204 (2012). 8

9. McClure, S. B. & Schmich, S. Local Actions in Global Context: The Pleistocene-Holocene Transition in Iberia. *J. of Anthropological Research* **65**, 179–184 (2009). URL https://doi.org/10.3998/jar.0521004.0065.201. 8

10. Stuart, A. J., Kosintsev, P. A., Higham, T. F. G. & Lister, A. M. Pleistocene to Holocene extinction dynamics in giant deer and woolly mammoth. *Nature* **431**, 684–689 (2004). 8, 10

11. Hughes, A. L. C., Gyllencreutz, R., Lohne, O. S., Mangerud, J. & Svendsen, J. I. The last Eurasian ice sheets - a chronological database and time-slice reconstruction, DATED-1. *Boreas* **45**, 1–45 (2015). URL http://dx.doi.org/10.1111/bor.12142. 8, 16, 18

12. Clark, P. U. *et al.* The Last Glacial Maximum. *Science* **325**, 710–714 (2009). URL http://dx.doi.org/10.1126/science.1172873. 8, 11, 16, 17

13. Straus, L. G. The human occupation of southwestern Europe during the Last Glacial Maximum: Solutrean cultural adaptations in France and Iberia. *J. of Anthropological Research* **71**, 465–492 (2015). 8

14. Hewitt, G. The genetic legacy of the Quaternary ice ages. *Nature* **405**, 907–913 (2000). 8

15. Jorde, L. B., Bamshad, M. & Rogers, A. R. Using mitochondrial and nuclear DNA markers to reconstruct human evolution. *Bioessays* **20**, 126–136 (1998). 8

16. Barnosky, A. D., Koch, P. L., Feranec, R. S., Wing, S. L. & Shabel, A. B. Assessing the Causes of Late Pleistocene Extinctions on the Continents. *Science* **306**, 70–75 (2004). 8, 10, 188

17. Braconnot, P. *et al.* Evaluation of climate models using palaeoclimatic data. *Nature Climate Change* **2**, 417–424 (2012). URL `http://dx.doi.org/10.1038/nclimate1456`. 8, 11, 23, 24, 75, 90, 94, 95, 96, 118, 122

18. Stevens, B. *et al.* Atmospheric component of the MPI-M Earth System Model: ECHAM6. *J. of Advances in Modeling Earth Systems* **5**, 146–172 (2013). 15, 23, 29, 94, 96

19. Jungclaus, J. H. *et al.* Characteristics of the ocean simulations in the Max Planck Institute Ocean Model (MPIOM) the ocean component of the MPI-Earth system model. *J. of Advances in Modeling Earth Systems* **5**, 422–446 (2013). URL `http://dx.doi.org/10.1002/jame.20023`.

20. Jungclaus, J. *et al.* CMIP5 simulations of the Max Planck Institute for Meteorology (MPI-M) based on the MPI-ESM-P model: The lgm experiment, served by ESGF. WDCC at DKRZ (2012). 8, 15, 23, 29, 94, 96

21. IPCC, . *Climate Change 2001: The Scientific Basis. Contribution of Working Group I to the Third Assessment Report of the Intergovernmental Panel on Climate Change* (Cambridge Univ. Press, 2001). 9

22. IPCC, . *Climate Change 2007: The Physical Science Basis. Contribution of Working Group I to the Fourth Assessment Report of the Intergovernmental Panel on Climate Change* (Cambridge Univ. Press, 2007). 20

23. IPCC Intergovernmental Panel on Climate Change. *Climate Change 2013: The Physical Science Basis* (Cambridge University Press, 2013). URL `http://dx.doi.org/10.1017/CBO9781107415324`. 9, 20

24. Barnosky, A. D. *et al.* Has the Earth's sixth mass extinction already arrived? *Nature* **471**, 51–57 (2011). 9

25. Pereira, H. M. *et al.* Scenarios for Global Biodiversity in the 21st Century. *Science* **330**, 1496 (2010).

26. Hallmann, C. A. *et al.* More than 75 percent decline over 27 years in total flying insect biomass in protected areas. *PloS one* **12**, e0185809 (2017). 9

27. Schulte, P. *et al.* The Chicxulub Asteroid Impact and Mass Extinction at the Cretaceous-Paleogene Boundary. *Science* **327**, 1214 (2010). 9

28. Alvarez, L. W., Alvarez, W., Asaro, F. & Michel, H. V. Extraterrestrial Cause for the Cretaceous-Tertiary Extinction. *Science* **208**, 1095–1108 (1980). 9

29. Ceballos, G. *et al.* Accelerated modern human–induced species losses: Entering the sixth mass extinction. *Science Advances* **1** (2015). URL http://dx.doi.org/10.1126/sciadv.1400253. 9

30. IPCC Intergovernmental Panel on Climate Change. *Climate Change 2014: Impacts, Adaptation and Vulnerability. Part A: Global and Sectoral Aspects.* (Cambridge University Press, 2014). 9

31. IPCC Intergovernmental Panel on Climate Change. *Climate Change 2014: Impacts, Adaptation and Vulnerability. Part B: Regional Aspects* (Cambridge University Press, 2014).

32. Rosenzweig, C. *et al.* Assessing agricultural risks of climate change in the 21st century in a global gridded crop model intercomparison. *Proceedings of the National Academy of Science* **111**, 3268–3273 (2014). 9

33. Tallavaara, M., Luoto, M., Korhonen, N., Järvinen, H. & Seppä, H. Human population dynamics in Europe over the Last Glacial Maximum. *Proceedings of the National Academy of Science* **112**, 8232–8237 (2015). URL http://adsabs.harvard.edu/abs/2015PNAS..112.8232T. 10

34. Burke, A. *et al.* Risky business: The impact of climate and climate variability on human population dynamics in Western Europe during the Last Glacial Maximum. *Quaternary Science Reviews* **164**, 217–229 (2017). URL http://adsabs.harvard.edu/abs/2017QSRv..164..217B. 10

35. Maher, B. *et al.* Global connections between aeolian dust, climate and ocean biogeochemistry at the present day and at the last glacial maximum. *Earth-Science Reviews* **99**, 61–97 (2010). URL http://dx.doi.org/10.1016/j.earscirev.2009.12.001. 10, 11, 14

36. Ludwig, P., Schaffernicht, E. J., Shao, Y. & Pinto, J. G. Regional atmospheric circulation over Europe during the Last Glacial Maximum and its links to precipitation. *J. of Geophysical Research: Atmospheres* **121**, 2130–2145 (2016). URL http://dx.doi.org/10.1002/2015JD024444. 10, 15, 22, 28, 31, 32, 71, 75, 77, 81, 83, 84, 85, 86, 87, 88, 89, 94, 97, 101, 102, 103, 193, 195

37. Ludwig, P., Pinto, J. G., Raible, C. C. & Shao, Y. Impacts of Surface Boundary Conditions on Regional Climate Model Simulations of European Climate during the Last Glacial Maximum. *Geophysical Research Letters* (2017). URL http://dx.doi.org/10.1002/2017GL073622. 38, 70, 95, 155

38. Ravazzi, C. Late Quaternary history of spruce in southern Europe. *Review of Palaeobotany and palynology* **120**, 131–177 (2002).

39. Akçar, N. *et al.* Glacier response to the change in atmospheric circulation in the eastern Mediterranean during the Last Glacial Maximum. *Quaternary Geochronology* **19**, 27–41 (2014).

40. Janská, V. *et al.* Palaeodistribution modelling of European vegetation types at the Last Glacial Maximum using modern analogues from Siberia: Prospects and limitations. *Quaternary Science Reviews* **159**, 103–115 (2017). 10

41. Sommer, R. S., Kalbe, J., Ekström, J., Benecke, N. & Liljegren, R. Range dynamics of the reindeer in Europe during the last 25,000 years. *J. of Biogeography* **41**, 298–306 (2014). 10

42. Hofreiter, M. *et al.* Lack of phylogeography in European mammals before the last glaciation. *Proceedings of the National Academy of Science* **101**, 12963–12968 (2004). 10

43. Sima, A. *et al.* Modeling dust emission response to North Atlantic millennial-scale climate variations from the perspective of East European MIS 3 loess deposits. *Climate of the Past* **9**, 1385–1402 (2013). URL http://dx.doi.org/10.5194/cp-9-1385-2013. 11, 14, 15, 104, 105, 116

44. Rousseau, D.-D. *et al.* European glacial dust deposits: Geochemical constraints on atmospheric dust cycle modeling. *Geophysical Research Letters* **41**, 7666–7674 (2014). URL http://dx.doi.org/10.1002/2014GL061382. 11, 14

45. Renssen, H., Kasse, C., Vandenberghe, J. & Lorenz, S. J. Weichselian Late Pleniglacial surface winds over northwest and central Europe: a model–data comparison. *J. of Quaternary Science* **22**, 281–293 (2007). URL http://dx.doi.org/10.1002/jqs.1038. 11, 13, 15, 24, 70, 103, 104, 113, 133, 136

46. Bokhorst, M. *et al.* Atmospheric circulation patterns in central and eastern Europe during the Weichselian Pleniglacial inferred from loess grain-size records. *Quaternary International* **234**, 62–74 (2011). URL http://dx.doi.org/10.1016/j.quaint.2010.07.018. 11, 13, 14, 15, 25, 26, 27, 70, 102, 103, 104, 105, 113, 123, 157

47. Dietrich, S. & Seelos, K. The reconstruction of easterly wind directions for the Eifel region (Central Europe) during the period 40.3 to 12.9 ka BP. *Climate of the Past* **6**, 145–154 (2010). URL http://dx.doi.org/10.5194/cp-6-145-2010. 11, 13, 70, 103

48. Römer, W., Lehmkuhl, F. & Sirocko, F. Late Pleistocene aeolian dust provenances and wind direction changes reconstructed by heavy mineral analysis of the sediments of the Dehner dry maar (Eifel, Germany). *Global and Planetary Change* **147**, 25–39 (2016). URL http://dx.doi.org/10.1016/j.gloplacha.2016.10.012. 11, 70, 103

49. Krauß, L. *et al.* A Multi-Proxy Analysis of two Loess-Paleosol Sequences in the Northern Harz Foreland, Germany. *Palaeogeography, Palaeoclimatology, Palaeoecology* **461**, 401–417 (2016). URL http://dx.doi.org/10.1016/j.palaeo.2016.09.001. 11, 18, 70, 103

50. Újvári, G., Varga, A. & Balogh-Brunstad, Z. Origin, weathering, and geochemical composition of loess in southwestern Hungary. *Quaternary Research* **69**, 421–437 (2008). URL http://dx.doi.org/10.1016/j.yqres.2008.02.001. 11, 70, 103, 157

51. Novothny, A., Frechen, M., Horváth, E., Wacha, L. & Rolf, C. Investigating the penultimate and last glacial cycles of the Süttő loess section (Hungary) using luminescence dating, high-resolution grain size, and magnetic susceptibility data. *Quaternary International* **234**, 75–85 (2011). URL http://dx.doi.org/10.1016/j.quaint.2010.08.002. 18, 27, 70, 89, 103, 158

52. Buggle, B. *et al.* Geochemical characterization and origin of Southeastern and Eastern European loesses (Serbia, Romania, Ukraine). *Quaternary Science Reviews* **27**, 1058–1075 (2008). URL http://dx.doi.org/10.1016/j.quascirev.2008.01.018. 11, 13, 15, 70, 103, 157, 158

53. Jones, P. D., Hulme, M. & Briffa, K. R. A comparison of Lamb circulation types with an objective classification scheme. *International J. of Climatology* **13**, 655–663 (1993). URL http://dx.doi.org/10.1002/joc.3370130606. 11, 15, 71, 72, 97

54. Jones, P. D., Harpham, C. & Briffa, K. R. Lamb weather types derived from reanalysis products. *International J. of Climatology* **33**, 1129–1139 (2013). URL http://dx.doi.org/10.1002/joc.3498. 74

55. Reyers, M., Pinto, J. G. & Moemken, J. Statistical-dynamical downscaling for wind energy potentials: evaluation and applications to decadal hindcasts and climate change projections. *International J. of Climatology* **35**, 229–244 (2014). URL http://dx.doi.org/10.1002/joc.3975. 11, 15, 71, 97

56. Shao, Y. *et al.* Dust cycle: An emerging core theme in Earth system science. *Aeolian Research* **2**, 181–204 (2011). URL http://dx.doi.org/10.1016/j.aeolia.2011.02.001. 11, 89

57. Újvári, G., Kovács, J., Varga, G., Raucsik, B. & Marković, S. B. Dust flux estimates for the Last Glacial Period in East Central Europe based on terrestrial records of loess deposits: a review. *Quaternary Science Reviews* **29**, 3157–3166 (2010). URL http://dx.doi.org/10.1016/j.quascirev.2010.07.005. 11, 13, 14, 15, 22, 25, 26, 27, 70, 89, 90, 103, 104, 105, 155, 157, 158

58. Prospero, J. M. Environmental characterization of global sources of atmospheric soil dust identified with the NIMBUS 7 Total Ozone Mapping Spectrometer (TOMS) absorbing aerosol product. *Reviews of Geophysics* **40** (2002). URL http://dx.doi.org/10.1029/2000RG000095. 11, 89, 156

59. Kohfeld, K. E. & Harrison, S. P. DIRTMAP: the geological record of dust. *Earth Science Reviews* **54**, 81–114 (2001). URL http://adsabs.harvard.edu/abs/2001ESRv...54...81K. 11, 14

60. Shin, S.-I. *et al.* A Simulation of the Last Glacial Maximum climate using the NCAR-CCSM. *Climate Dynamics* **20**, 127–151 (2002). 11

61. Bush, A. B. G. & Philander, S. G. H. The climate of the Last Glacial Maximum: Results from a coupled atmosphere-ocean general circulation model. *J. of Geophysics Research* **104**, 24509–24526 (1999). 11

62. Harrison, S. P., Kohfeld, K. E., Roelandt, C. & Claquin, T. The role of dust in climate changes today, at the last glacial maximum and in the future. *Earth-Science Reviews* **54**, 43–80 (2001). URL https://dx.doi.org/10.1016/S0012-8252(01)00041-1. 11, 123

63. Varga, G., Kovács, J. & Újvári, G. Late Pleistocene variations of the background aeolian dust concentration in the Carpathian Basin: an estimate using decomposition of grain-size distribution curves of loess deposits. *Netherlands Journal of Geosciences* **91**, 159–171 (2012). URL http://dx.doi.org/10.1017/S0016774600001566. 11, 89, 90, 156

64. Clark, P. U., Alley, R. B. & Pollard, D. Northern Hemisphere Ice-Sheet Influences on Global Climate Change. *Science* **286**, 1104–1111 (1999). URL http://dx.doi.org/10.1126/science.286.5442.1104. 11, 18, 37

65. Hayes, A., Kucera, M., Kallel, N., Sbaffi, L. & Rohling, E. J. Glacial Mediterranean sea surface temperatures based on planktonic foraminiferal assemblages. *Quaternary Science Reviews* **24**, 999–1016 (2005). 35, 37

66. Kuhlemann, J. *et al.* Regional Synthesis of Mediterranean Atmospheric Circulation During the Last Glacial Maximum. *Science* **321**, 1338–1340 (2008). URL http://dx.doi.org/10.1126/science.1157638. 15, 18, 24, 28, 32, 35, 37, 38, 45, 50, 53, 55, 85, 89

67. Bartlein, P. J. *et al.* Pollen-based continental climate reconstructions at 6 and 21 ka: a global synthesis. *Climate Dynamics* **37**, 775–802 (2011). URL http://dx.doi.org/10.1007/s00382-010-0904-1. 21, 37, 38, 42

68. Tarasov, P. E. *et al.* Last Glacial Maximum climate of the former Soviet Union and Mongolia reconstructed from pollen and plant macrofossil data. *Climate Dynamics* **15**, 227–240 (1999). 37, 38, 42

69. Hofer, D., Raible, C. C., Dehnert, A. & Kuhlemann, J. The impact of different glacial boundary conditions on atmospheric dynamics and precipitation in the North Atlantic region. *Climate of the Past* **8**, 935–949 (2012). URL http://dx.doi.org/10.5194/cp-8-935-2012. 13, 14, 15, 31, 37, 38, 87, 102

70. Wu, H., Guiot, J., Brewer, S. & Guo, Z. Climatic changes in Eurasia and Africa at the last glacial maximum and mid-Holocene: reconstruction from pollen data using inverse vegetation modelling. *Climate Dynamics* **29**, 211–229 (2007). URL http://dx.doi.org/10.1007/s00382-007-0231-3. 15, 21, 38

71. Kasse, C., Huijzer, A. S., Krzyszkowski, D., Bohncke, S. J. P. & Coope, G. R. Weichselian Late Pleniglacial and Late-glacial depositional environments, Coleoptera and periglacial climatic records from central Poland (Bełchatów). *J. of Quaternary Science* **13**, 455–469 (1998). URL http://dx.doi.org/10.1002/(SICI)1099-1417(199809)13:5<455::AID-JQS398>3.0.CO;2-T. 11, 15, 18, 24

72. Peltier, W. R., Argus, D. F. & Drummond, R. Space geodesy constrains ice age terminal deglaciation: The global ICE-6G_C (VM5a) model. *J. of Geophysical Research: Solid Earth* **120**, 450–487 (2015). 11, 18

73. Cooperative Holocene Mapping (COHMAP) Project Members & Anderson, P. M. Climatic Changes of the Last 18,000 Years: Observations and Model Simulations. *Science* 1043–1052 (1988). URL http://science.sciencemag.org/content/241/4869/1043. 11, 16, 18, 28, 82, 87, 89, 101

74. Lambeck, K., Rouby, H., Purcell, A., Sun, Y. & Sambridge, M. Sea level and global ice volumes from the Last Glacial Maximum to the Holocene. *Proceedings of the National Academy of Science* **111**, 15296–15303 (2014). 11, 17

75. Austermann, J., Mitrovica, J. X., Latychev, K. & Milne, G. A. Barbados-based estimate of ice volume at Last Glacial Maximum affected by subducted plate. *Nature Geoscience* **6**, 553–557 (2013). 17

76. Clark, P. U. & Mix, A. C. Ice sheets and sea level of the Last Glacial Maximum. *Quaternary Science Reviews* **21**, 1–7 (2002). 17

77. Yokoyama, Y., Lambeck, K., De Deckker, P., Johnson, P. & Fifield, K. Timing for the maximum of the Last Glacial constrained by lowest sea-level observations. *Nature* **406**, 713–716 (2000). 11, 17

78. Monnin, E. *et al.* Atmospheric CO2 Concentrations over the Last Glacial Termination. *Science* **291**, 112–114 (2001). URL http://science.sciencemag.org/content/291/5501/112. http://science.sciencemag.org/content/291/5501/112.full.pdf. 11, 19, 20, 195

79. Haase, D. *et al.* Loess in Europe—its spatial distribution based on a European Loess Map, scale 1:2,500,000. *Quaternary Science Reviews* **26**, 1301–1312 (2007). URL http://dx.doi.org/10.1016/j.quascirev.2007.02.003. 12, 90, 113, 115, 156, 195

80. Gasse, F., Vidal, L., Develle, A.-L. & Van Campo, E. Hydrological variability in the Northern Levant: a 250 ka multiproxy record from the Yammoûneh (Lebanon) sedimentary sequence. *Climate of the Past* **7**, 1261–1284 (2011). URL http://dx.doi.org/10.5194/cp-7-1261-2011. 12, 13, 18, 21, 90

81. Fitzsimmons, K. E. & Hambach, U. Loess accumulation during the last glacial maximum: Evidence from Urluia, southeastern Romania. *Quaternary International* **334-335**, 74–85 (2014). URL http://dx.doi.org/10.1016/j.quaint.2013.08.005. 12, 70, 90, 103, 105

82. Antoine, P. *et al.* Rapid and cyclic aeolian deposition during the Last Glacial in European loess: a high-resolution record from Nussloch, Germany. *Quaternary Science Reviews* **28**, 2955–2973 (2009). URL http://dx.doi.org/10.1016/j.quascirev.2009.08.001. 12, 90, 91, 92, 103, 190, 195

83. Kukla, G. Pleistocene land—sea correlations I. Europe. *Earth-Science Reviews* **13**, 307–374 (1977). URL http://dx.doi.org/10.1016/0012-8252(77)90125-8. 12, 90, 113

84. Sima, A. *et al.* Imprint of North-Atlantic abrupt climate changes on western European loess deposits as viewed in a dust emission model. *Quaternary Science Reviews* **28**, 2851–2866 (2009). URL http://dx.doi.org/10.1016/j.quascirev.2009.07.016. 104, 157, 158

85. Little, E. C. *et al.* Quaternary stratigraphy and optical dating of loess from the east European Plain (Russia). *Quaternary Science Reviews* **21**, 1745–1762 (2002). URL http://dx.doi.org/10.1016/S0277-3791(01)00151-2. 12, 15, 25, 26, 90, 113

86. Avramov, V. I., Jordanova, D., Hoffmann, V. & Roesler, W. The role of dust source area and pedogenesis in three loess-palaeosol sections from North Bulgaria: A mineral magnetic study. *Studia Geophysica et Geodaetica* **50**, 259–282 (2006). URL http://dx.doi.org/10.1007/s11200-006-0015-y. 13, 70, 104

87. Lehmkuhl, F., Zens, J., Krauß, L., Schulte, P. & Kels, H. Loess-paleosol sequences at the northern European loess belt in Germany: Distribution, geomorphology and stratigraphy. *Quaternary Science Reviews* **153**, 11–30 (2016). URL http://dx.doi.org/10.1016/j.quascirev.2016.10.008. 13

88. Marković, S. B. *et al.* Late Pleistocene loess-palaeosol sequences in the Vojvodina region, north Serbia. *J. of Quaternary Science* **23**, 73–84 (2007). URL http://dx.doi.org/10.1002/jqs.1124. 13, 104

89. Smalley, I. *et al.* Rivers and loess: The significance of long river transportation in the complex event-sequence approach to loess deposit formation. *Quaternary International* **198**, 7–18 (2009). URL http://dx.doi.org/10.1016/j.quaint.2008.06.009. 13, 114, 195

90. Jipa, D. C. The conceptual sedimentary model of the Lower Danube loess basin: Sedimentogenetic implications. *Quaternary International* **351**, 14–24 (2014). URL http://dx.doi.org/10.1016/j.quaint.2013.06.008. 13, 105, 115, 157

91. Antoine, P. *et al.* High-resolution record of the last climatic cycle in the southern Carpathian Basin (Surduk, Vojvodina, Serbia). *Quaternary International* **198**, 19–36 (2009). URL http://dx.doi.org/10.1016/j.quaint.2008.12.008. 13, 22, 104

92. Mahowald, N. M. *et al.* Change in atmospheric mineral aerosols in response to climate: Last glacial period, preindustrial, modern, and doubled carbon dioxide climates. *J. of Geophysical Research: Atmospheres* **111** (2006). URL http://dx.doi.org/10.1029/2005JD006653. 14, 15, 25, 26, 90

93. Werner, M. Seasonal and interannual variability of the mineral dust cycle under present and glacial climate conditions. *J. of Geophysical Research* **107** (2002). URL http://dx.doi.org/10.1029/2002JD002365. 90

94. Sudarchikova, N. *et al.* Modelling of mineral dust for interglacial and glacial climate conditions with a focus on Antarctica. *Climate of the Past* **11**, 765–779 (2015). URL http://dx.doi.org/10.5194/cp-11-765-2015. 90

95. Takemura, T. *et al.* A simulation of the global distribution and radiative forcing of soil dust aerosols at the Last Glacial Maximum. *Atmospheric Chemistry and Physics* **9**, 3061–3073 (2009). URL http://dx.doi.org/10.5194/acp-9-3061-2009.

96. Albani, S. *et al.* Improved dust representation in the Community Atmosphere Model. *J. of Advances in Modeling Earth Systems* **6**, 541–570 (2014). URL http://dx.doi.org/10.1002/2013MS000279. 14, 15, 90

97. Hopcroft, P. O., Valdes, P. J., Woodward, S. & Joshi, M. M. Last glacial maximum radiative forcing from mineral dust aerosols in an Earth system model. *J. of Geophysical Research: Atmospheres* **120**, 8186–8205 (2015).

98. Yue, X., Wang, H., Liao, H. & Jiang, D. Simulation of the Direct Radiative Effect of Mineral Dust Aerosol on the Climate at the Last Glacial Maximum. *J. of Climate* **24**, 843–858 (2011). 14, 15, 90

99. Frechen, M. Loess in Europe—mass accumulation rates during the Last Glacial Period. *Quaternary Science Reviews* **22**, 1835–1857 (2003). URL http://dx.doi.org/10.1016/S0277-3791(03)00183-5. 14, 15, 25, 26, 27

100. Evan, A. T., Flamant, C., Fiedler, S. & Doherty, O. An analysis of aeolian dust in climate models. *Geophysical Research Letters* **41**, 5996–6001 (2014). URL http://adsabs.harvard.edu/abs/2014GeoRL..41.5996E. 14

101. Kok, J. F. A scaling theory for the size distribution of emitted dust aerosols suggests climate models underestimate the size of the global dust cycle. *Proceedings of the National Academy of Science* **108**, 1016–1021 (2011). URL http://adsabs.harvard.edu/abs/2011PNAS..108.1016K. 1012.5818. 14

102. Grell, G. A. *et al.* Fully coupled "online" chemistry within the WRF model. *Atmospheric Environment* **39**, 6957–6975 (2005). URL http://dx.doi.org/10.1016/j.atmosenv.2005.04.027. 14, 15, 90, 94, 96

103. Fast, J. D. *et al.* Evolution of ozone, particulates, and aerosol direct radiative forcing in the vicinity of Houston using a fully coupled meteorology-chemistry-aerosol model. *J. of Geophysical Research: Atmospheres* **111**, n/a–n/a (2006). URL http://dx.doi.org/10.1029/2005JD006721. D21305.

104. Su, L. & Fung, J. C. H. Sensitivities of WRF-Chem to dust emission schemes and land surface properties in simulating dust cycles during springtime over East Asia. *J. of Geophysical Research: Atmospheres* **120**, 11 (2015). URL http://adsabs.harvard.edu/abs/2015JGRD..12011215S.

105. Kumar, R., Barth, M. C., Pfister, G. G., Naja, M. & Brasseur, G. P. WRF-Chem simulations of a typical pre-monsoon dust storm in northern India: influences on aerosol optical properties and radiation budget. *Atmospheric Chemistry & Physics* **14**, 2431–2446 (2014). 14, 15, 94

106. Shao, Y. Simplification of a dust emission scheme and comparison with data. *J. of Geophysical Research* **109** (2004). URL http://dx.doi.org/10.1029/2003JD004372. 14, 94, 96, 123

107. Jung, E., Shao, Y. & Sakai, T. A study on the effects of convective transport on regional-scale Asian dust storms in 2002. *J. of Geophysical Research: Atmospheres* **110** (2005). URL http://dx.doi.org/10.1029/2005JD005808. D20201. 14, 94, 96

108. Mahowald, N., Albani, S., Engelstaedter, S., Winckler, G. & Goman, M. Model insight into glacial-interglacial paleodust records. *Quaternary Science Reviews* **30**, 832–854 (2011). 14

109. Annan, J. D. & Hargreaves, J. C. A new global reconstruction of temperature changes at the Last Glacial Maximum. *Climate of the Past* **9**, 367–376 (2013). 15, 37, 38

110. Laîné, A. *et al.* Northern hemisphere storm tracks during the last glacial maximum in the PMIP2 ocean-atmosphere coupled models: energetic study, seasonal cycle, precipitation. *Climate Dynamics* **32**, 593–614 (2009). URL http://dx.doi.org/10.1007/s00382-008-0391-9. 30, 31, 39, 82, 85, 87

111. Strandberg, G., Brandefelt, J., Kjellström, E. & Smith, B. High-resolution regional simulation of last glacial maximum climate in Europe. *Tellus Series A* **63**, 107–125 (2011). 18, 39

112. Kageyama, M. *et al.* Mid-Holocene and Last Glacial Maximum climate simulations with the IPSL model—part I: comparing IPSL_CM5A to IPSL_CM4. *Climate Dynamics* **40**, 2447–2468 (2013). URL http://dx.doi.org/10.1007/s00382-012-1488-8. 32, 34, 37, 39, 41, 42, 52, 74, 82

113. Zhang, Y., Dulière, V., Mote, P. W. & Salathé, E. P. Evaluation of WRF and HadRM Mesoscale Climate Simulations over the U.S. Pacific Northwest*. *J. of Climate* **22**, 5511 (2009). 15, 39

114. Barker, S., Cacho, I., Benway, H. & Tachikawa, K. Planktonic foraminiferal Mg/Ca as a proxy for past oceanic temperatures: a methodological overview and data compilation for the Last Glacial Maximum. *Quaternary Science Reviews* **24**, 821–834 (2005). 15, 24, 35

115. Tarasov, P. E. *et al.* Last glacial maximum biomes reconstructed from pollen and plant macrofossil data from northern Eurasia. *J. of Biogeography* **27**, 609–620 (2000). URL http://dx.doi.org/10.1046/j.1365-2699.2000.00429.x. 15, 22, 24

116. Peyron, O. *et al.* Climatic Reconstruction in Europe for 18,000 YR B.P. from Pollen Data. *Quaternary Research* **49**, 183–196 (1998). URL http://dx.doi.org/10.1006/qres.1997.1961. 18, 21, 89

117. Allen, J. R. M. *et al.* Rapid environmental changes in southern Europe during the last glacial period. *Nature* **400**, 740–743 (1999). URL http://dx.doi.org/10.1038/23432. 15, 21, 24

118. Novothny, A., Horváth, E. & Frechen, M. The loess profile at Albertirsa, Hungary—improvements in loess stratigraphy by luminescence dating. *Quaternary International* **95-96**, 155–163 (2002). URL http://dx.doi.org/10.1016/S1040-6182(02)00036-8. 15, 25

119. Łanczont, M. & Madeyska, T. Environment of the East Carpathian Foreland during periods of Palaeolithic man's activity. *CATENA* **59**, 319–340 (2005). URL http://dx.doi.org/10.1016/j.catena.2004.09.003. 26

120. van den Haute, P., Vancraeynest, L. & De Corte, F. The Late Pleistocene loess deposits and palaeosols of eastern Belgium: new TL age determinations. *J. of Quaternary Science* **13**, 487–497 (1998). URL http://dx.doi.org/10.1002/(SICI)1099-1417(1998090)13:5<487::AID-JQS405>3.0.CO;2-Z. 26

121. Rutter, N. W. *et al.* Correlation and interpretation of paleosols and loess across European Russia and Asia over the last interglacial–glacial cycle. *Quaternary Research* **60**, 101–109 (2003). URL http://dx.doi.org/10.1016/S0033-5894(03)00069-3. 26

122. Haesaerts, P. *et al.* The east Carpathian loess record: a reference for the middle and late pleniglacial stratigraphy in central Europe [La séquence loessique du domaine est-carpatique: une référence pour le Pléniglaciaire moyen et supérieur d'Europe centrale.]. *Quaternaire* **14**, 163–188 (2003). URL http://dx.doi.org/10.3406/quate.2003.1740. 26

123. Rousseau, D. *et al.* Abrupt millennial climatic changes from Nussloch (Germany) Upper Weichselian eolian records during the Last Glaciation. *Quaternary Science Reviews* **21**, 1577–1582 (2002). URL http://dx.doi.org/10.1016/S0277-3791(02)00034-3. 26

124. Molodkov, A. N. & Bolikhovskaya, N. S. Eustatic sea-level and climate changes over the last 600 ka as derived from mollusc-based ESR-chronostratigraphy and pollen evidence in Northern Eurasia. *Sedimentary Geology* **150**, 185–201 (2002). URL http://dx.doi.org/10.1016/S0037-0738(01)00275-5. 26

125. Sümegi, P. & Rudner, Z. E. In situ charcoal fragments as remains of natural wild fires in the upper Würm of the Carpathian Basin. *Quaternary International* **76-77**, 165–176 (2001). URL http://dx.doi.org/10.1016/S1040-6182(00)00100-2. 15, 26, 27

126. Bretherton, C. S., Smith, C. & Wallace, J. M. An Intercomparison of Methods for Finding Coupled Patterns in Climate Data. *J. of Climate* **5**, 541–560 (1992). 15, 45

127. Giorgetta, M. A. *et al.* Climate and carbon cycle changes from 1850 to 2100 in MPI-ESM simulations for the Coupled Model Intercomparison Project phase 5. *J. of Advances in Modeling Earth Systems* **5**, 572–597 (2013). URL http://dx.doi.org/10.1002/jame.20038. 15, 23

128. Berger, A. & Loutre, M. F. Insolation values for the climate of the last 10 million years. *Quaternary Science Reviews* **10**, 297–317 (1991). 16

129. Berger, A. Milankovitch Theory and climate. *Reviews of Geophysics* **26**, 624 (1988). URL http://dx.doi.org/10.1029/RG026i004p00624. 16, 18

130. Berger, A. & Loutre, M. F. Astronomical solutions for paleoclimate studies over the last 3 million years. *Earth and Planetary Science Letters* **111**, 369–382 (1992). 16

131. Berger, A. L. Long-Term Variations of Daily Insolation and Quaternary Climatic Changes. *J. of the Atmospheric Sciences* **35**, 2362–2367 (1978). URL http://dx.doi.org/10.1175/1520-0469(1978)035<2362:LTVODI>2.0.CO;2. 16

132. Wikimedia Commons contributors. Europe relief — Wikimedia Commons, the free media repository (2017). URL https://commons.wikimedia.org/w/index.php?title=File:{E}urope_relief_laea_location_map.jpg&oldid=245722164. 17

133. Abe-Ouchi, A. *et al.* Ice-sheet configuration in the CMIP5/PMIP3 Last Glacial Maximum experiments. *Geoscientific Model Development* **8**, 3621–3637 (2015). URL http://dx.doi.org/10.5194/gmd-8-3621-2015. 18

134. Hughes, P. D., Gibbard, P. L. & Ehlers, J. Timing of glaciation during the last glacial cycle: evaluating the concept of a global "Last Glacial Maximum" (LGM). *Earth-Science Reviews* **125**, 171–198 (2013). URL http://dx.doi.org/10.1016/j.earscirev.2013.07.003. 18

135. Harrison, S. P., Bartlein, P. J. & Prentice, I. C. What have we learnt from palaeoclimate simulations? *J. of Quaternary Science* **31**, 363–385 (2016). URL http://dx.doi.org/10.1002/jqs.2842. 18

136. Hubberten, H. W. *et al.* The periglacial climate and environment in northern Eurasia during the Last Glaciation. *Quaternary Science Reviews* **23**, 1333–1357 (2004). URL http://www.sciencedirect.com/science/article/pii/S0277379103003469. Quaternary Environments of the Eurasian North (QUEEN). 18, 22

137. Gasse, F., Chalié, F., Vincens, A., Williams, M. A. J. & Williamson, D. Climatic patterns in equatorial and southern Africa from 30,000 to 10,000 years ago reconstructed from terrestrial and near-shore proxy data. *Quaternary Science Reviews* **27**, 2316–2340 (2008).

138. Rojas, M. *et al.* The Southern Westerlies during the last glacial maximum in PMIP2 simulations. *Climate Dynamics* **32**, 525–548 (2009).

139. Hesse, P. P. & McTainsh, G. H. Last Glacial Maximum to Early Holocene Wind Strength in the Mid-latitudes of the Southern Hemisphere from Aeolian Dust in the Tasman Sea. *Quaternary Research* **52**, 343–349 (1999).

140. Heyman, B. M., Heyman, J., Fickert, T. & Harbor, J. M. Paleo-climate of the central European uplands during the last glacial maximum based on glacier mass-balance modeling. *Quaternary Research* **79**, 49–54 (2013). URL http://dx.doi.org/10.1016/j.yqres.2012.09.005. 18, 89

141. Pausata, F. S. R., Li, C., Wettstein, J. J., Kageyama, M. & Nisancioglu, K. H. The key role of topography in altering North Atlantic atmospheric circulation during the last glacial period. *Climate of the Past* **7**, 1089–1101 (2011). URL http://dx.doi.org/10.5194/cp-7-1089-2011. 18, 32, 37, 87

142. Shakun, J. D. & Carlson, A. E. A global perspective on Last Glacial Maximum to Holocene climate change. *Quaternary Science Reviews* **29**, 1801–1816 (2010). 18

143. Florineth, D. & Schlüchter, C. Alpine Evidence for Atmospheric Circulation Patterns in Europe during the Last Glacial Maximum. *Quaternary Research* **54**, 295–308 (2000). URL http://dx.doi.org/10.1006/qres.2000.2169. 18, 70, 83, 85, 87, 89, 102, 103

144. Hoogakker, B. A. A., Elderfield, H., Schmiedl, G., McCave, I. N. & Rickaby, R. E. M. Glacial-interglacial changes in bottom-water oxygen content on the Portuguese margin. *Nature Geoscience* **8**, 40–43 (2015). 19

145. Betts, R. A., Jones, C. D., Knight, J. R., Keeling, R. F. & Kennedy, J. J. El Niño and a record CO_2 rise. *Nature Climate Change* **6**, 806–810 (2016). URL https://www.nature.com/articles/nclimate3063. 19, 20, 21, 195

146. Ruddiman, W. F. The Anthropogenic Greenhouse Era Began Thousands of Years Ago. *Climatic Change* **61**, 261–293 (2003). URL https://doi.org/10.1023/B:CLIM.0000004577.17928.fa. 20

147. Siegenthaler, U. & Oeschger, H. Biospheric CO2 emissions during the past 200 years reconstructed by deconvolution of ice core data. *Tellus B: Chemical and Physical Meteorology* **39**, 140–154 (1987). 20

148. MacFarling Meure, C. *et al.* Law Dome CO_2, CH_4 and N_2O ice core records extended to 2000 years BP. *Geophysical Research Letters* **33**, L14810 (2006). 20

149. Cicerone, R. J. & Shetter, J. D. Sources of atmospheric methane - Measurements in rice paddies and a discussion. *J. of Geophysics Research* **86**, 7203–7209 (1981). 20

150. Howarth, R. W., Santoro, R. & Ingraffea, A. Methane and the greenhouse-gas footprint of natural gas from shale formations. *Climatic Change* **106**, 679 (2011). 20

151. Hoegh-Guldberg, O. *et al.* Coral Reefs Under Rapid Climate Change and Ocean Acidification. *Science* **318**, 1737 (2007). 20

152. Anthony, K. R. N., Kline, D. I., Diaz-Pulido, G., Dove, S. & Hoegh-Guldberg, O. Ocean acidification causes bleaching and productivity loss in coral reef builders. *Proceedings of the National Academy of Science* **105**, 17442–17446 (2008).

153. Pandolfi, J. M., Connolly, S. R., Marshall, D. J. & Cohen, A. L. Projecting Coral Reef Futures Under Global Warming and Ocean Acidification. *Science* **333**, 418 (2011).

154. Orr, J. C. *et al.* Anthropogenic ocean acidification over the twenty-first century and its impact on calcifying organisms. *Nature* **437**, 681–686 (2005).

155. Parker, L. M. *et al.* Ocean acidification narrows the acute thermal and salinity tolerance of the Sydney rock oyster Saccostrea glomerata. *Marine Pollution Bulletin* **122**, 263–271 (2017).

156. Albright, R. *et al.* Reversal of ocean acidification enhances net coral reef calcification. *Nature* **531**, 362–365 (2016). 20

157. Ehleringer, J. R., Cerling, T. E. & Helliker, B. R. C 4 photosynthesis, atmospheric CO 2 , and climate. *Oecologia* **112**, 285–299 (1997). 21

158. Sage, R. F. The evolution of C4 photosynthesis. *New Phytologist* **161**, 341–370 (2004). URL http://dx.doi.org/10.1111/j.1469-8137.2004.00974.x. 21

159. Huang, Y. *et al.* Climate Change as the Dominant Control on Glacial-Interglacial Variations in C_3 and C_4 Plant Abundance. *Science* **293**, 1647–1651 (2001). 21

160. Galy, V. *et al.* C4 plants decline in the Himalayan basin since the Last Glacial Maximum. *Quaternary Science Reviews* **27**, 1396–1409 (2008).

161. Crucifix, M., Betts, R. A. & Hewitt, C. D. Pre-industrial-potential and Last Glacial Maximum global vegetation simulated with a coupled climate-biosphere model: diagnosis of bioclimatic relationships. *Global and Planetary Change* **45**, 295–312 (2005). 21

162. Zhang, Z., Zhao, M., Lu, H. & Faiia, A. M. Lower temperature as the main cause of C_4 plant declines during the glacial periods on the Chinese Loess Plateau. *Earth and Planetary Science Letters* **214**, 467–481 (2003). 21

163. Prentice, I. C. & Harrison, S. P. Ecosystem effects of CO_2 concentration: evidence from past climates. *Climate of the Past* **5**, 297–307 (2009). URL http://dx.doi.org/10.5194/cp-5-297-2009. 21

164. Willis, K. & van Andel, T. Trees or no trees? The environments of central and eastern Europe during the Last Glaciation. *Quaternary Science Reviews* **23**, 2369–2387 (2004). URL http://dx.doi.org/10.1016/j.quascirev.2004.06.002. 21, 89

165. Kaplan, J. O. *et al.* Climate change and Arctic ecosystems: 2. Modeling, paleodata-model comparisons, and future projections. *J. of Geophysical Research: Atmospheres* **108** (2003). URL http://dx.doi.org/10.1029/2002JD002559. 21

166. Cheddadi, R. & Bar-Hen, A. Spatial gradient of temperature and potential vegetation feedback across Europe during the late Quaternary. *Climate Dynamics* **32**, 371–379 (2008). URL http://dx.doi.org/10.1007/s00382-008-0405-7. 21

167. Ugan, A. & Byers, D. Geographic and temporal trends in proboscidean and human radiocarbon histories during the late Pleistocene. *Quaternary Science Reviews* **26**, 3058–3080 (2007). URL http://dx.doi.org/10.1016/j.quascirev.2007.06.024. 21, 89

168. Elenga, H. *et al.* Pollen-based biome reconstruction for southern Europe and Africa 18,000 yr BP. *J. of Biogeography* **27**, 621–634 (2000). URL http://dx.doi.org/10.1046/j.1365-2699.2000.00430.x. 21

169. Simakova, A. N. The vegetation of the Russian Plain during the second part of the Late Pleistocene (33–18ka). *Quaternary International* **149**, 110–114 (2006). URL http://dx.doi.org/10.1016/j.quaint.2005.11.024. 22

170. Fitzsimmons, K. E., Marković, S. B. & Hambach, U. Pleistocene environmental dynamics recorded in the loess of the middle and lower Danube basin. *Quaternary Science Reviews* **41**, 104–118 (2012). URL http://dx.doi.org/10.1016/j.quascirev.2012.03.002. 22, 70, 103, 158

171. Magyari, E. K. *et al.* Late Pleniglacial vegetation in eastern-central Europe: are there modern analogues in Siberia? *Quaternary Science Reviews* **95**, 60–79 (2014). URL http://dx.doi.org/10.1016/j.quascirev.2014.04.020. 22

172. Gent, P. R. *et al.* The Community Climate System Model Version 4. *J. of Climate* **24**, 4973–4991 (2011). URL http://dx.doi.org/10.1175/2011jcli4083.1. 23

173. Sueyoshi, T. *et al.* Set-up of the PMIP3 paleoclimate experiments conducted using an Earth system model, MIROC-ESM. *Geoscientific Model Development* **6**, 819–836 (2013). URL http://dx.doi.org/10.5194/gmd-6-819-2013. 23

174. Yukimoto, S. *et al.* A New Global Climate Model of the Meteorological Research Institute: MRI-CGCM-Model Description and Basic Performance. *J. of the Meteorological Society of Japan* **90A**, 23–64 (2012). URL http://dx.doi.org/10.2151/jmsj.2012-A02. 23, 29

175. Kalnay, E. *et al.* The NCEP/NCAR 40-Year Reanalysis Project. *Bull. of the American Meteorological Society* **77**, 437–471 (1996). 23, 70, 78

176. Kanamitsu, M. *et al.* NCEP–DOE AMIP-II Reanalysis (R-2). *Bull. of the American Meteorological Society* **83**, 1631–1643 (2002). URL http://dx.doi.org/10.1175/BAMS-83-11-1631. 23, 78, 99

177. Dee, D. P. *et al.* The ERA-Interim reanalysis: configuration and performance of the data assimilation system. *Quarterly J. of the Royal Meteorological Society* **137**, 553–597 (2011). URL http://dx.doi.org/10.1002/qj.828. 23, 70, 78

178. Climate, Long-Range Investigation, Mapping and Prediction (CLIMAP) Project Members & Ruddiman, W. F. The Last Interglacial Ocean. *Quaternary Research* **21**, 123–224 (1984). URL http://dx.doi.org/10.1016/0033-5894(84)90098-X. 24, 94, 95, 96, 118, 122, 148, 149, 153

179. Rousseau, D.-D., Zöller, L. & Valet, J.-P. Late Pleistocene Climatic Variations at Achenheim, France, Based on a Magnetic Susceptibility and TL Chronology of Loess. *Quaternary Research* **49**, 255–263 (1998). URL http://dx.doi.org/10.1006/qres.1998.1972. 25

180. Frechen, M., Zander, A., Cílek, V. & Ložek, V. Loess chronology of the Last Interglacial/Glacial cycle in Bohemia and Moravia, Czech Republic. *Quaternary Science Reviews* **18**, 1467–1493 (1999). URL http://dx.doi.org/10.1016/S0277-3791(98)00087-0. 25

181. Frechen, M., van Vliet-Lanoë, B. & van den Haute, P. The Upper Pleistocene loess record at Harmignies/Belgium — high resolution terrestrial archive of climate forcing. *Palaeogeography, Palaeoclimatology, Palaeoecology* **173**, 175–195 (2001). URL http://dx.doi.org/10.1016/S0031-0182(01)00319-4. 26

182. Frechen, M., Horváth, E. & Gábris, G. Geochronology of Middle and Upper Pleistocene Loess Sections in Hungary. *Quaternary Research* **48**, 291–312 (1997). URL http://dx.doi.org/10.1006/qres.1997.1929. 26

183. Nawrocki, J., Bakhmutov, V., Bogucki, A. & Dolecki, L. The paleo- and petromagnetic record in the Polish and Ukrainian loess-paleosol sequences. *Physics and Chemistry of the Earth, Part A: Solid Earth and Geodesy* **24**, 773–777 (1999). URL http://dx.doi.org/10.1016/S1464-1895(99)00113-1. 26

184. Wintle, A. G. Thermoluminescence dating of loess at Rocourt, Belgium. *Geologie en Mijnbouw* **66**, 35–42 (1987). 27

185. Antoine, P., Rousseau, D.-D., Lautridou, J.-P. & Hatté, C. Last interglacial-glacial climatic cycle in loess-palaeosol successions of north-western France. *Boreas* **28**, 551–563 (1999). URL http://dx.doi.org/10.1111/j.1502-3885.1999.tb00241.x. 27

186. Virina, E. I. *et al.* Palaeoclimatic record in the loess-palaeosol sequence of the Strelitsa type section (Don glaciation area, Russia) deduced from rock magnetic and palynological data. *J. of Quaternary Science* **15**, 487–499 (2000). URL http://dx.doi.org/10.1002/1099-1417(200007)15:5<487::AID-JQS512>3.0.CO;2-F. 27

187. Frechen, M. Systematic thermoluminescence dating of two loess profiles from the Middle Rhine Area (F.R.G.). *Quaternary Science Reviews* **11**, 93–101 (1992). URL http://dx.doi.org/10.1016/0277-3791(92)90048-D. 27

188. Trofimov, V. T. (ed.) *Loess mantle of the Earth, and its properties.* (Moscow University Press, 2001). 27

189. Rousseau, D.-D., Gerasimenko, N., Matviischina, Z. & Kukla, G. Late Pleistocene Environments of the Central Ukraine. *Quaternary Research* **56**, 349–356 (2001). URL http://dx.doi.org/10.1006/qres.2001.2270. 27

190. Justino, F., Timmermann, A., Merkel, U. & Peltier, W. R. An Initial Intercomparison of Atmospheric and Oceanic Climatology for the ICE-5G and ICE-4G Models of LGM Paleotopography. *J. of Climate* **19**, 3–14 (2006). URL http://dx.doi.org/10.1175/JCLI3603.1. 30, 74, 82

191. Merz, N., Raible, C. C. & Woollings, T. North Atlantic Eddy-Driven Jet in Interglacial and Glacial Winter Climates. *J. of Climate* **28**, 3977–3997 (2015). URL http://dx.doi.org/10.1175/JCLI-D-14-00525.1. 30, 82, 87

192. Li, C. & Battisti, D. S. Reduced Atlantic Storminess during Last Glacial Maximum: Evidence from a Coupled Climate Model. *J. of Climate* **21**, 3561–3579 (2008). URL http://dx.doi.org/10.1175/2007JCLI2166.1. 30

193. Appenzeller, C., Stocker, T. F. & Anklin, M. North Atlantic Oscillation Dynamics Recorded in Greenland Ice Cores. *Science* **282**, 446 (1998). 32

194. Bader, J. & Latif, M. North Atlantic Oscillation response to anomalous Indian Ocean SST in a coupled GCM. *J. of Climate* **18**, 5382–5389 (2005).

195. Hoerling, M. *et al.* On the increased frequency of Mediterranean drought. *J. of Climate* **25**, 2146–2161 (2012). URL https://doi.org/10.1175/JCLI-D-11-00296.1.

196. Kucharski, F., Molteni, F. & Bracco, A. Decadal interactions between the western tropical Pacific and the North Atlantic Oscillation. *Climate Dynamics* **26**, 79–91 (2006).

197. Ninglian, W. *et al.* Influence of variations in NAO and SO on air temperature over the northern Tibetan Plateau as recorded by δ18O in the Malan ice core. *Geophysical Research Letters* **30** (2003).

198. Glueck, M. F. & Stockton, C. W. Reconstruction of the North Atlantic Oscillation, 1429-1983. *International J. of Climatology* **21**, 1453–1465 (2001).

199. Casty, C., Handorf, D. & Sempf, M. Combined winter climate regimes over the North Atlantic/European sector 1766-2000. *Geophysical Research Letters* **32**, L13801 (2005). URL http://dx.doi.org/10.1029/2005GL022431. 45, 52

200. Benedict, J. J., Lee, S. & Feldstein, S. B. Synoptic View of the North Atlantic Oscillation. *J. of the Atmospheric Sciences* **61**, 121–144 (2004).

201. Cassou, C., Terray, L., Hurrell, J. W. & Deser, C. North Atlantic Winter Climate Regimes: Spatial Asymmetry, Stationarity with Time, and Oceanic Forcing. *J. of Climate* **17**, 1055–1068 (2004). URL https://doi.org/10.1175/1520-0442(2004)017<1055:NAWCRS>2.0.CO;2. 32

202. Lindgren, A., Hugelius, G., Kuhry, P., Christensen, T. R. & Vandenberghe, J. GIS-based Maps and Area Estimates of Northern Hemisphere Permafrost Extent during the Last Glacial Maximum. *Permafrost and Periglacial Processes* **27**, 6–16 (2016). 34

203. Paul, A. & Schäfer-Neth, C. Modeling the water masses of the Atlantic Ocean at the Last Glacial Maximum. *Paleoceanography* **18** (2003). 35, 38

204. Pinardi, N. & Masetti, E. Variability of the large scale general circulation of the Mediterranean Sea from observations and modelling: a review. *Palaeogeography, Palaeoclimatology, Palaeoecology* **158**, 153–173 (2000). 35, 37

205. Banks, W. E. *et al.* Human ecological niches and ranges during the LGM in Europe derived from an application of eco-cultural niche modeling. *J. of Archaeological Science* **35**, 481–491 (2008). 35

206. Pflaumann, U. *et al.* Glacial North Atlantic: Sea-surface conditions reconstructed by GLAMAP 2000. *Paleoceanography* **18**, 10–1 (2003). 38

207. Kutzbach, J. *et al.* Climate and biome simulations for the past 21,000 years. *Quaternary Science Reviews* **17**, 473–506 (1998). 39

208. Jost, A. *et al.* High-resolution simulations of the last glacial maximum climate over Europe: a solution to discrepancies with continental palaeoclimatic reconstructions? *Climate Dynamics* **24**, 577–590 (2005). URL http://dx.doi.org/10.1007/s00382-005-0009-4. 39, 42, 45, 50

209. Hubbard, A., Sugden, D., Dugmore, A., Norddahl, H. & Pétursson, H. G. A modelling insight into the Icelandic Last Glacial Maximum ice sheet. *Quaternary Science Reviews* **25**, 2283–2296 (2006). 42

210. Harrison, S. P., Yu, G. & Tarasov, P. E. Late Quaternary Lake-Level Record from Northern Eurasia. *Quaternary Research* **45**, 138–159 (1996). URL http://dx.doi.org/10.1006/qres.1996.0016. 42

211. Beghin, P. *et al.* What drives LGM precipitation over the western Mediterranean? A study focused on the Iberian Peninsula and northern Morocco. *Climate Dynamics* **46**, 2611–2631 (2016). 42

212. Giorgi, F. & Gutowski Jr, W. J. Regional dynamical downscaling and the CORDEX initiative. *Annual Review of Environment and Resources* **40** (2015). 42

213. Fraedrich, K., Bantzer, C. & Burkhardt, U. Winter climate anomalies in Europe and their associated circulation at 500 hPa. *Climate Dynamics* **8**, 161–175 (1993). URL https://doi.org/10.1007/BF00207963. 45

214. Monahan, A. H., Fyfe, J. C., Ambaum, M. H. P., Stephenson, D. B. & North, G. R. Empirical Orthogonal Functions: The Medium is the Message. *J. of Climate* **22**, 6501 (2009). 45

215. Moore, G. W. K., Renfrew, I. A. & Pickart, R. S. Multidecadal Mobility of the North Atlantic Oscillation. *J. of Climate* **26**, 2453–2466 (2013). 45

216. Thiéblemont, R., Matthes, K., Omrani, N.-E., Kodera, K. & Hansen, F. Solar forcing synchronizes decadal North Atlantic climate variability. *Nature Communications* **6**, 8268 (2015).

217. Croci-Maspoli, M., Schwierz, C. & Davies, H. C. Atmospheric blocking: space-time links to the NAO and PNA. *Climate Dynamics* **29**, 713–725 (2007).

218. Blessing, S., Fraedrich, K., Junge, M., Kunz, T. & Lunkeit, F. Daily North-Atlantic Oscillation (NAO) index: Statistics and its stratospheric polar vortex dependence. *Meteorologische Zeitschrift* **14**, 763–769 (2005). 45

219. Trenberth, K. E., Fasullo, J. T., Branstator, G. & Phillips, A. S. Seasonal aspects of the recent pause in surface warming. *Nature Climate Change* **4**, 911–916 (2014). 45

220. Stuecker, M. F., Timmermann, A., Jin, F.-F., McGregor, S. & Ren, H.-L. A combination mode of the annual cycle and the El Niño/Southern Oscillation. *Nature Geoscience* **6**, 540–544 (2013). URL http://dx.doi.org/10.1038/NGEO1826. 45

221. UCAR, NCAR, CISL & TDD. The NCAR Command Language (NCL, v. 6.4.0). Software (2017). URL http://dx.doi.org/10.5065/D6WD3XH5. 47

222. Schulzweida, U., Kornblueh, L. & Mueller, R. Climate Data Operators (CDO, v. 1.7.2). Software, Max-Planck-Institute for Meteorology (2017). URL http://www.mpimet.mpg.de/cdo. 47

223. North, G. R., Bell, T. L., Cahalan, R. F. & Moeng, F. J. Sampling Errors in the Estimation of Empirical Orthogonal Functions. *Monthly Weather Review* **110**, 699 (1982). 48

224. Rohling, E. J. *et al.* Abrupt cold spells in the northwest Mediterranean. *Paleoceanography* **13**, 316–322 (1998). 53

225. Anstey, J. A. *et al.* Multi-model analysis of Northern Hemisphere winter blocking: Model biases and the role of resolution. *J. of Geophysical Research: Atmospheres* **118**, 3956–3971 (2013). URL http://dx.doi.org/10.1002/jgrd.50231. 70, 78, 84, 99, 155

226. Shea, J. H. Twelve fallacies of uniformitarianism. *Geology* **10**, 455 (1982). 71, 88, 95

227. Baker, V. R. Catastrophism and uniformitarianism: logical roots and current relevance in geology. *Geological Society of London Special Publications* **143**, 171–182 (1998). 71, 88, 95

228. Hofer, D., Raible, C. C., Merz, N., Dehnert, A. & Kuhlemann, J. Simulated winter circulation types in the North Atlantic and European region for preindustrial and glacial conditions. *Geophysical Research Letters* **39** (2012). URL http://dx.doi.org/10.1029/2012GL052296. 74, 82

229. Löfverström, M., Caballero, R., Nilsson, J. & Kleman, J. Evolution of the large-scale atmospheric circulation in response to changing ice sheets over the last glacial cycle. *Climate of the Past* **10**, 1453–1471 (2014). URL http://dx.doi.org/10.5194/cp-10-1453-2014. 74

230. Felzer, B. Climate impacts of an ice sheet in East Siberia during the Last Glacial Maximum. *Quaternary Science Reviews* **20**, 437–447 (2001). URL http://dx.doi.org/10.1016/S0277-3791(00)00106-2. 74

231. Kistler, R. *et al.* The NCEP–NCAR 50–Year Reanalysis: Monthly Means CD–ROM and Documentation. *Bull. of the American Meteorological Society* **82**, 247–267 (2001). URL http://dx.doi.org/10.1175/1520-0477(2001)082<0247:TNNYRM>2.3.CO;2. 78, 81

232. Uppala, S. M. *et al.* The ERA-40 re-analysis. *Quarterly J. of the Royal Meteorological Society* **131**, 2961–3012 (2005). 78

233. Mahowald, N. M. *et al.* Atmospheric Iron Deposition: Global Distribution, Variability, and Human Perturbations. *Annu. Rev. Mar. Sci.* **1**, 245–278 (2009). URL http://dx.doi.org/10.1146/annurev.marine.010908.163727. 89

234. Ginoux, P. *et al.* Sources and distributions of dust aerosols simulated with the GOCART model. *J. of Geophysical Research: Atmospheres* **106**, 20255–20273 (2001). URL http://dx.doi.org/10.1029/2000JD000053. 89, 95, 96, 104

235. Tegen, I. & Fung, I. Modeling of mineral dust in the atmosphere: Sources, transport, and optical thickness. *J. of Geophysical Research* **99**, 22897 (1994). URL http://dx.doi.org/10.1029/94JD01928. 89

236. Újvári, G., Kok, J. F., Varga, G. & Kovács, J. The physics of wind-blown loess: Implications for grain size proxy interpretations in Quaternary paleoclimate studies. *Earth-Science Reviews* **154**, 247–278 (2016). URL http://dx.doi.org/10.1016/j.earscirev.2016.01.006. 89, 90

237. Újvári, G. *et al.* Evaluating the use of clay mineralogy, Sr–Nd isotopes and zircon U–Pb ages in tracking dust provenance: An example from loess of the Carpathian Basin. *Chemical Geology* **304-305**, 83–96 (2012). URL http://dx.doi.org/10.1016/j.chemgeo.2012.02.007. 89, 90, 155

238. Kang, J.-Y., Yoon, S.-C., Shao, Y. & Kim, S.-W. Comparison of vertical dust flux by implementing three dust emission schemes in WRF/Chem. *J. of Geophysical Research: Atmospheres* **116**, D09202 (2011). 90, 156

239. Darmenova, K., Sokolik, I. N., Shao, Y., Marticorena, B. & Bergametti, G. Development of a physically based dust emission module within the Weather Research and Forecasting (WRF) model: Assessment of dust emission parameterizations and input parameters for source regions in Central and East Asia. *J. of Geophysical Research: Atmospheres* **114**, D14201 (2009).

240. Shao, Y., Ishizuka, M., Mikami, M. & Leys, J. F. Parameterization of size-resolved dust emission and validation with measurements. *J. of Geophysical Research: Atmospheres* **116**, D08203 (2011). URL https://agupubs.onlinelibrary.wiley.com/doi/10.1029/2010JD014527. 90, 156

241. Singhvi, A., Bluszcz, A., Bateman, M. & Rao, M. Luminescence dating of loess–palaeosol sequences and coversands: methodological aspects and palaeoclimatic implications. *Earth-Science Reviews* **54**, 193–211 (2001). URL http://dx.doi.org/10.1016/S0012-8252(01)00048-4. 90, 116

242. Pye, K. The nature, origin and accumulation of loess. *Quaternary Science Reviews* **14**, 653–667 (1995). URL http://dx.doi.org/10.1016/0277-3791(95)00047-X. 90

243. Krinner, G. *et al.* Enhanced ice sheet growth in Eurasia owing to adjacent ice-dammed lakes. *Nature* **427**, 429–432 (2004). URL http://dx.doi.org/10.1038/nature02233. 94

244. Lin, Y., Farley, R. & Orville, H. Bulk Parameterization of the Snow Field in a Cloud Model. *J. of Applied Meteorology and Climatology* **22**, 1065–1092 (1983). 94

245. Iacono, M. J. *et al.* Radiative forcing by long-lived greenhouse gases: Calculations with the AER radiative transfer models. *J. of Geophysical Research* **113** (2008). URL http://dx.doi.org/10.1029/2008JD009944. 94

246. Webb, E. K. Profile relationships: The log-linear range, and extension to strong stability. *Quarterly J. of the Royal Meteorological Society* **96**, 67–90 (1970). 94

247. Rosero, E., Yang, Z.-L., Gulden, L. E., Niu, G.-Y. & Gochis, D. J. Evaluating Enhanced Hydrological Representations in Noah LSM over Transition Zones: Implications for Model Development. *J. of Hydrometeorology* **10**, 600–622 (2009). URL http://dx.doi.org/10.1175/2009JHM1029.1. 94

248. Case, J. L., Crosson, W. L., Kumar, S. V., Lapenta, W. M. & Peters-Lidard, C. D. Impacts of High-Resolution Land Surface Initialization on Regional Sensible Weather Forecasts from the WRF Model. *J. of Hydrometeorology* **9**, 1249–1266 (2008). URL http://dx.doi.org/10.1175/2008JHM990.1.

249. Tewari, M. *et al.* Implementation and verification of the unified NOAH land surface model in the WRF model. *20th conference on weather analysis and forecasting/16th conference on numerical weather prediction* **1115**, 11–15 (2004). 94

250. Hong, S.-Y., Noh, Y. & Dudhia, J. A New Vertical Diffusion Package with an Explicit Treatment of Entrainment Processes. *Monthly Weather Review* **134**, 2318–2341 (2006). URL http://dx.doi.org/10.1175/MWR3199.1. 94

251. Zhang, C., Wang, Y. & Hamilton, K. Improved Representation of Boundary Layer Clouds over the Southeast Pacific in ARW-WRF Using a Modified Tiedtke Cumulus Parameterization Scheme. *Monthly Weather Review* **139**, 3489–3513 (2011). URL http://dx.doi.org/10.1175/MWR-D-10-05091.1. 94

252. Wesely, M. Parameterization of surface resistances to gaseous dry deposition in regional-scale numerical models. *Atmospheric Environment (1967)* **23**, 1293–1304 (1989). URL http://dx.doi.org/10.1016/0004-6981(89)90153-4. 94, 96

253. Chin, M., Rood, R. B., Lin, S.-J., Müller, J.-F. & Thompson, A. M. Atmospheric sulfur cycle simulated in the global model GOCART: Model description and global properties. *J. of Geophysical Research: Atmospheres* **105**, 24671–24687 (2000). URL http://dx.doi.org/10.1029/2000JD900384. 94, 96

254. Marticorena, B. & Bergametti, G. Modeling the atmospheric dust cycle: 1. Design of a soil-derived dust emission scheme. *J. of Geophysical Research* **100**, 16415 (1995). URL http://dx.doi.org/10.1029/95JD00690. 96

255. Taylor, K. E., Stouffer, R. J. & Meehl, G. A. An Overview of CMIP5 and the Experiment Design. *Bull. of the American Meteorological Society* **93**, 485–498 (2012). URL http://dx.doi.org/10.1175/BAMS-D-11-00094.1. 96

256. Koven, C. D. & Fung, I. Identifying global dust source areas using high-resolution land surface form. *J. of Geophysical Research* **113** (2008). URL http://dx.doi.org/10.1029/2008JD010195. 104

257. Varga, G., Kovács, J. & Újvári, G. Analysis of Saharan dust intrusions into the Carpathian Basin (Central Europe) over the period of 1979–2011. *Global and Planetary Change* **100**, 333–342 (2013). URL http://dx.doi.org/10.1016/j.gloplacha.2012.11.007. 115, 155

258. Bettis, E. A., Muhs, D. R., Roberts, H. M. & Wintle, A. G. Last Glacial loess in the conterminous USA. *Quaternary Science Reviews* **22**, 1907–1946 (2003). URL http://dx.doi.org/10.1016/S0277-3791(03)00169-0. 116

259. Brands, S., Herrera, S., Fernández, J. & Gutiérrez, J. M. How well do CMIP5 Earth System Models simulate present climate conditions in Europe and Africa? *Climate Dynamics* **41**, 803–817 (2013). URL https://doi.org/10.1007/s00382-013-1742-8. 155

260. Hines, K. M. *et al.* Sea Ice Enhancements to Polar WRF*. *Monthly Weather Review* **143**, 2363–2385 (2015). 155

261. Stuut, J.-B., Smalley, I. & O'Hara-Dhand, K. Aeolian dust in Europe: African sources and European deposits. *Quaternary International* **198**, 234–245 (2009). URL http://dx.doi.org/10.1016/j.quaint.2008.10.007. 155

262. Callot, Y. Geomorphologic approach for modelling the surface features of arid environments in a model of dust emissions: application to the Sahara desert. *Geodinamica Acta* **13**, 245–270 (2000). URL http://dx.doi.org/10.1016/S0985-3111(00)01044-5. 156

10 Abbreviations, Acronyms, Physical Units

Table 13: Abbreviations, acronyms, terms, and physical units used in this dissertation.

^{14}C yr BP	Carbon isotope based age dating unit
A	Anticyclonic. Or the capitalized indefinite article
ADR	Appropriate daily record
BIIS	British Irish ice sheet
BP	before present
C	Cyclonic
CB	Carpathian Basin
CCSM	Community Climate System Model (United States)
CCSM4	CCSM version 4
CEOF	Combined EOF
CLIMAP	Climate: Long-range Investigation, Mapping, and Prediction
CM	Climate Model, or: Coupled Model
CNRM	Centre National de Recherches Meteorologiques
COHMAP	Cooperative Holocene Mapping Project
CWT	Circulation Weather Type
CWT-N	Circulation Weather Type North (analogously other wind directions)
DFG	Deutsche Forschungsgemeinschaft
DJF	December, January, and February
E	East
ECMWF	European Centre for Medium-Range Weather Forecasts
EIS	Eurasian Ice Sheet
EIS High	High pressure system over the EIS
EOF	Empirical Orthogonal Function
ERA-Interim	ECMWF Re-Analysis Interim
GCM	Global climate model, *also:* general circulation model
GIS	Greenland Ice Sheet
GLAMAP	Glacial Atlantic Ocean Mapping
GOCART	Goddard Chemistry Aerosol Radiation and Transport model
HadCM	Hadley Centre Coupled Model
HadRM	Hadley Centre Regional Model
IPSL	Institut Pierre-Simon Laplace
IPSL-CM4	IPSL Coupled Model version 4
JJA	June, July, and August
ka	kilo anno, 1000 years, identical to kyr
kyr	kilo year, 1000 years, identical to ka
LGM	Last Glacial Maximum, about 21000 year ago
LIS	Laurentide ice sheet

Table continues

Table 13: continued

LIS High	High pressure system over the LIS
MAM	March, April, and May
MAR	Mass Accumulation Rate
MAR10	MAR of particles only up to 10 µm diameter
megafauna[16]	*here:* Species with individual mass > 44 kg
MIROC	Model for Interdisciplinary Research on Climate (Japan)
MIROC-ESM	MIROC Earth System Model
MPI	Max Planck Institute for Meteorology
MPI-ESM-P	Max Planck Institute Earth System Model Paleo
MPI-ESM-P-LGM	LGM simulation, version r1i1p1, run by the MPI-ESM-P
MPI-ESM-P-PI	Preindustrial simulation, version r1i1p1, run by the MPI-ESM-P
MPI-LGM	Identical to MPI-ESM-P-LGM
MPI-PI	Identical to MPI-ESM-P-PI
MRI	Meteorological Research Institute (Japan)
MRI-CGCM3	MRI Coupled Atmosphere-Ocean GCM version 3
N	North
NAO	North Atlantic Oscillation
NCAR	National Centers for Atmospheric Research (United States)
NCEP	National Centers for Environmental Prediction (United States)
NCEP1	NCEP/NCAR Reanalyses 1
NCEP2	NCEP-DOE Reanalysis 2
NE	Northeast
NW	Northwest
PI	Preindustrial or pre-industrial
PMIP	Paleoclimate Modeling Intercomparison Project Phase 3
PMIP2	Paleoclimate Modeling Intercomparison Project Phase 2
PMIP3	Paleoclimate Modeling Intercomparison Project Phase 3
pp	Percentage point(s)
PR	Precipitation rate
PSL	Sea level pressure, identical to SLP
r1i1p1	realization 1, initialization method 1, physics version 1
RCM	Regional climate model
S	South
SE	Southeast
SI	International System of Units
SIS	Scandinavian ice sheet
SLP	Sea level pressure, identical to PSL
SON	September, October, and November
spatiotemporal	With regard to both, space and time

Table continues

Table 13: continued

SST	Sea surface temperature
SW	Southwest
TAS	Near-surface air temperature
UC	University of Cologne
W	West
WMO	World Meteorological Organization
WRF-Chem	Weather Research and Forecasting model coupled with Chemistry
WRF-Chem-LGM	LGM-refined version of the WRF-Chem

11 List of Figures

12 Acknowledgments

Special thanks goes to Yaping Shao. He is professor at the Institute for Geophysics and Meteorology at the University of Cologne and an expert on mineral dust modeling. He supervised my research on the climate-dust modeling for the LGM, which resulted in this dissertation. He and professor Martin Melles were the principle investigators, responsible for the project that provided the framework for my research. Discussing scientific questions with Yaping has been inspiring and helpful. New ideas arose frequently from these discussions. I also like to thank Patrick Ludwig, a colleague of mine and former member of Yaping Shao's research group. Patrick worked on the same project "Collaborative Research Centre 806 (CRC806), Our Way to Europe, Project E6" as a post-doc. He was available to discuss upcoming questions on all kind of meteorological topics, on the software tools for scientific research including the high performance computing system, as well as on the results of my analyses. My thanks and gratitude includes also Martin; he is professor at the Institute of Geology and Mineralogy at the University of Cologne and was one of the chairmen of the CRC806, which provided the interdisciplinary framework that favored collaborating among different disciplines. He was available to discuss geological and geographical questions that came up during my research. Jointly with the other chairmen, he supported my research by providing funding for research equipment. Regarding this, I also thank Frank Schäbitz and Jürgen Richter, the other two chairmen of the CRC806. For offering discussions on fieldwork results my thanks goes to Frank Lehmkuhl, professor for physical geography at Aachen University (RWTH Aachen) and his group members. Among them, I like to mention Christian Zeeden, Janina Bösken, Igor Obrecht, and Lydia Krauss. Discussing my results with them always resulted in new perspectives, particularly regarding the comparison of my simulations with fieldwork-based results. I like to give thanks to Joaquim G. Pinto and Andreas Fink, both former members of the Institute for Geophysics and Meteorology at the University of Cologne and now professors at the Karlsruhe Institute of Technology. Joaquim, who is very experienced regarding Circulation Weather Type analysis and co-authored a joint publication[36] that partly based on my dissertation research, has been open to scientific discussions, which I appreciate. My thanks goes to Yaping, Martin, and Joaquim for joining my dissertation committee. I like to express my gratefulness to Andreas and Rita Hense. He, a professor at the Institute for Meteorology in Bonn, and Rita took the time to discuss my ideas on how to research on paleoclimate patterns using empirical orthogonal functions. I like to mention several members of Yaping Shao's research group sharing their expertise about specific questions that came up during my doctoral research. These are: Mark Reyers, Sven Ulbrich, Michael Hintz, Cedrick Ansorge, Martina Klose, Xia Qian, and Paul Tsui. Beyond my group members, my gratefulness extends to Philipp J. Griewank (office mate), Jan Chylik, Christian Willmes, Daniel Becker, Alexandre Wennmacher, Mario Mech, and Dagmar Janzen (secretary).

(continued)

Apart from my academic research and professional colleagues, there are many more that supported and facilitated the creation of this dissertation. First and foremost, I like to express gratefulness to my parents, Monika and Helmut Schaffernicht, who supported me by providing financial as well as housing/office space means to finish this dissertation, particularly during the year before I submitted my dissertation. In particular, I am very grateful that they opened and offered to me a quiet room in their home, which allowed me to concentrate on the writing of this thesis and of the manuscript that presents my reconstruction of the LGM dust cycle in Europe to the international scientific community.

There are many more friends and relatives that supported me by showing their interest for my work and by asking questions on my results, which in turn helped me to see my research from their, partly non-academic, perspective. This was useful to work out my main line of thought, arguments and conclusions very explicitly and to become able to explain my research even to non-scientists or non-meteorologists in a clear, concise, and easy understandable way. Last but not least, a healthy mind lives in a healthy body ("Ein gesunder Geist lebt in einem gesunden Körper"). I thank my Iyengar Yoga teachers, my beach volleyball and competitive ballroom dance trainers. They supported my research indirectly by either teaching me healthy physical activities, body stretching, and stress management methods. This thankfulness includes my dance partners and beach volleyball team mates. Sharing a joint laugh or smile is one of the greatest source of energy and motivation to accomplish a dissertation.

13 Supplementary

13.1 Legal Statements

Statement of Co-Authorship

Figure 4, 5, 19, 20, 24, 25, 26, 27, and 28 are modified versions of those that already appeared in one[36] of the primary publications that I co-authored.

My co-authorship of this peer-reviewed journal article[36] consisted of major contributions to data analysis, interpretation, and writing.

Permissions

Fig. 2 From Monnin et al.[78] Reprinted with permission from The American Association for the Advancement of Science © 2001.

Fig. 3 From Betts et al.[145] Reprinted with permission from Macmillan Publishing Ltd © 2016.

Fig. 29 From Antoine et al.[82] Reprinted with permission from Elsevier © 2009.

Fig. 41 From Haase et al.[79] Reprinted with permission from Elsevier © 2007.

Fig. 42 From Smalley et al.[89] Reprinted with permission from Elsevier © 2009.

13.2 Erklärung zur Dissertation

Ich versichere, dass ich die von mir vorgelegte Dissertation selbständig angefertigt, die benutzten Quellen und Hilfsmittel vollständig angegeben und die Stellen der Arbeit – einschließlich Tabellen, Karten und Abbildungen –, die anderen Werken im Wortlaut oder dem Sinn nach entnommen sind, in jedem Einzelfall als Entlehnung kenntlich gemacht habe; dass diese Dissertation noch keiner anderen Fakultät oder Universität zur Prüfung vorgelegen hat; dass sie – abgesehen von unten angegebenen Teilpublikationen – noch nicht veröffentlicht worden ist, sowie, dass ich eine solche Veröffentlichung vor Abschluss des Promotionsverfahrens nicht vornehmen werde. Die Bestimmungen der Promotionsordnung sind mir bekannt. Die von mir vorgelegte Dissertation ist von Prof. Dr. Yaping Shao betreut worden. Diese Arbeit habe ich eigenständig ohne zu Hilfe nahme von nicht gekennzeichneten Quellen angefertigt.

13.3 Teilpublikation

Ludwig, P., Schaffernicht, E. J., Shao, Y. and Pinto, J. G.

Regional atmospheric circulation over Europe during the Last Glacial Maximum and its links to precipitation

J. Geophys. Res. Atmos. 121, 2130–2145 (2016)

http://dx.doi.org/10.1002/2015JD024444